N/Z EQUILIBRATION

A Dissertation

by

ELIZABETH BELL

Submitted to the Office of Graduate Studies of
Texas A&M University
in partial fulfillment of the requirements for the degree of

DOCTOR OF PHILOSOPHY

May 2005

Major Subject: Chemistry

N/Z EQUILIBRATION

A Dissertation

by

ELIZABETH BELL

Submitted to Texas A&M University
in partial fulfillment of the requirements
for the degree of

DOCTOR OF PHILOSOPHY

Approved as to style and content by:

Sherry J. Yennello (Chair of Committee)	Joseph B. Natowitz (Member)
Che-Ming Ko (Member)	Rand L. Watson (Member)
	Emile A. Schweikert (Head of Department)

May 2005

Major Subject: Chemistry

ABSTRACT

N/Z Equilibration. (May 2005)

Elizabeth Bell, B.S., The University of Texas at San Antonio

Chair of Advisory Committee: Dr. Sherry J. Yennello

The N/Z, or ratio of neutron to proton, degree of freedom may be used to study intermediate energy nuclear collisions to give information about the origin of emitted collision fragments. Establishing under what conditions the onset of N/Z equilibrium occurs will give a better understanding of the physics of the equation of state through the use of simulation codes. If the nuclear equation of state can be elucidated in terms of the N/Z dependent component and how the N/Z dependent component varies with density, then the equilibrium ratio of protons to neutrons inside high density neutron stars can be inferred, allowing for prediction of cooling rates and supernovae mechanisms.

In the current study, isotopic and isobaric ratios at $\text{theta}_{\text{lab}}=40^{\circ}$ with cuts of 10% and 20% most central events, respectively, are studied for their N/Z equilibration signals. Light charged particles, or LCPs, are found to be emitted from systems which have not yet fully N/Z combined; the fragments with A=3 are emitted from the least equilibrated systems. Intermediate mass fragments, or IMFs, are seen to be emitted by N/Z equilibrated sources, within statistical error bars.

The N/Z tracer method is used with ratios of isotopes and isobars to see how the amount of nuclear stopping or N/Z mixing changes as a function of the centrality of the event. The N/Z observable is used to reinvestigate earlier findings of the isotope and isobar ratio observables and shows the progression (or lack of it, in some cases) of the N/Z equilibration. This observable has proven to be a clear and sensitive tool to use when considering the differences in N/Z mixing of the systems at two energies.

TABLE OF CONTENTS

Page

CHAPTER

LIST OF FIGURES

FIGURE Page

FIGURE Page

LIST OF TABLES

TABLE Page

CHAPTER I
INTRODUCTION

It is an exciting time to be involved in N/Z, or neutron to proton, equilibration research. The Rare Isotope Accelerator (RIA) is being planned [1] which will allow production and beam delivery of highly N/Z asymmetric unstable nuclei. RIA will open a new chapter in the study of the nuclear equation of state (EOS). Neutron-rich and proton-rich nuclei will be made with RIA and then used in heavy-ion nuclear collision experiments to probe the behavior of very N/Z asymmetric nuclei. RIA also will facilitate connections and collaborations between astrophysics and nuclear physics, strengthening them as the line between neutron star behavior and the N/Z dependent component of the nuclear equation of state is studied [2, 3, 4, 5]. If the N/Z dependent component of the nuclear equation of state and how it changes with density can be understood, then the equilibrium ratio of protons to neutrons inside the high density neutron stars can be extrapolated. This equilibrium ratio of protons to neutrons can then be incorporated into models that predict cooling rates and supernovae mechanisms.

The nuclear equation of state describes nuclei in terms of pressure, density and temperature. The nuclear equation of state also includes terms describing the mass, charge, energy, N/Z asymmetry, nucleon-nucleon interactions and cross sections, and the mean field. By colliding intermediate energy heavy-ions in nuclear physics experiments, a very small reproduction of high density nuclear matter (which may be found in neutron stars and type II supernovae) is seen for very short periods of time. Findings from these experiments may be extrapolated from normal nuclear density (ρ_o) and N/Z symmetry ($N = Z$) to the high densities ($4\ \rho_o$) and N/Z asymmetry ($N \approx 4\ Z$) seen in neutron stars [3].

The N/Z of excited nuclear systems becomes important in that it can give information about the origin of emitted collision fragments. Establishing under what

---

This dissertation follows the style of Physical Review C.

conditions the onset of N/Z equilibrium occurs will help to improve the accuracy of code predictions and deepen our understanding of the events occurring prior to fragment emission in hot nuclear matter.

Many studies of N/Z dependence of observables from fragmentation following heavy-ion collisions have been conducted in recent times [4-18]. In 1993, the reaction of 50 MeV/nucleon ^{4}He on $^{116, 124}$Sn is used to investigate the effect of the target N/Z ratio on the N/Z of the intermediate mass fragments [6]. Equilibrium and non-equilibrium-like fragments are studied as a function of the charge and isotopic content of fragments emitted from the two systems. Measured cross sections are higher for the neutron-poor system (^{4}He on ^{116}Sn) and this is seen most for equilibrium-like fragments. In the non-equilibrium-like fragments, the IMF yields are comparable for both targets, but as the fragment charge increases, the ratio of fragment yields from the neutron-poor to the neutron-rich increases. An interpretation for this result is as follows. Decay through neutron emission competes with IMF emission in the neutron-rich system and decreases IMF emission probability due to the lower average neutron binding energies in ^{124}Sn [6].

The N/Z dependence of transverse collective flow is well documented [7, 8, 9, 10, 11]. When intermediate energy nuclear collisions of heavy ions occur, the collision or interaction region formed is compressed. The nucleons, in response to the compression, are pushed away from the collision center or interaction area. The outward push from the interaction area is called transverse collective flow. Transverse collective flow is measured by plotting the mean transverse momentum per nucleon as a function of the normalized center of mass rapidity of a system.

BUU is used to model systems ^{48}Cr + ^{58}Ni, which has an $(N/Z)_{CS} = 1.04$, and ^{48}Ca + ^{58}Fe, which has an $(N/Z)_{CS} = 1.12$ [10]. The BUU model used is N/Z dependent in that it incorporates experimental nucleon-nucleon cross sections (which are inherently N/Z dependent), the symmetry energy and the nuclear mean field. The BUU prediction of the collective flow of the chromium nickel and calcium iron systems shows the N/Z dependence of collective flow could be attributed to many different parameters. They include the nucleon-nucleon cross sections, coulomb repulsion energy, the N/Z dependent part of the nuclear EOS or the symmetry energy. The relative importance of these parameters, however, could not be shown.

There have been numerous studies specifically related to N/Z equilibration in intermediate energy heavy-ion nuclear reactions [12, 13, 14, 15, 16, 17, 18]. Deep inelastic or damped collisions are examined in 1988 [12] in a study of N/Z equilibration, which showed that N/Z equilibration is dependent with the level of energy loss in the system; the highest energy losses correspond to the most N/Z equilibration. Also, it stated that with larger differences in target and projectile N/Z, N/Z equilibration is more rapid.

In 1987, the reactions of 84 MeV/nucleon ^{12}C and ^{18}O on $^{58,\,64}$Ni, ^{nat}Ag, and ^{197}Au are studied for their isotopic yield ratios [13], giving information about the origin of fragments. When plotting the isotope yield ratios as a function of the N/Z ratio of the combined system of the target and projectile, the values for two ratios that have different targets and projectiles but identical total system N/Z will be equal if the emitting systems are N/Z equilibrated before the fragments are emitted. In the case where the two systems with matching N/Z of the combined target and projectile have isotope yield ratios that do not match, the number of nucleons from the target and projectile in the combined emitting system are adjusted by a scaling factor and then the ratio values are plotted as a function of the scaled N/Z values. The scaling factor which gives matching ratio values indicates the extent of mixing which the target and projectile underwent before emitting fragments.

In 1993, the radioactive beam of 53 MeV/nucleon ^{40}Cl along with stable beams of ^{40}Ar and ^{40}Ca and the targets of ^{58}Fe, Ni are employed to study the N/Z degree of freedom using fragments' isotopic distributions [14]. Using isotope yield ratios, it is shown that N/Z equilibration is not reached for these systems at the projectile energy of 53 MeV/nucleon. In a related report published in 1998 [15], the time scale at which N/Z equilibrium is reached is studied using the isospin dependent BUU code using ^{40}Ca on ^{124}Sn at 25, 50, 150, and 300 MeV/nucleon. N/Z equilibrium is found to be possible below Fermi energies or below about 30 MeV/nucleon using the same “isospin” or N/Z dependent code, iBUU. The N/Z non-equilibrium in heavy-ion collisions at intermediate energies has likewise been studied [16] with the same type of BUU in 1995. The system of ^{40}Ar on ^{58}Ni at 25, 35, 45 and 55 MeV/nucleon are simulated in order to probe whether or not they achieve N/Z equilibrium. By looking at the number of protons and neutrons in front of and behind the center of mass over time, it is predicted that N/Z equilibrium is reached somewhere between 35 and 45 MeV/nucleon for the ^{40}Ar on ^{58}Ni system.

Isotope and isobar ratios are used to investigate N/Z equilibration by plotting them as a function of the N/Z of the combined system N/Z, $(N/Z)_{CS}$. Equation 1 shows how $(N/Z)_{CS}$ is calculated.

$$\left(\frac{N}{Z}\right)_{cs} = \frac{N_{projectile} + N_{t\arg et}}{Z_{projetile} + Z_{t\arg et}} \tag{1}$$

The equilibration of N/Z of ^{40}Ar, ^{40}Ca + ^{58}Fe, ^{58}Ni at the energies of 33 and 45 MeV/nucleon have been investigated [17] using isobaric ratios. When plotted as a function of the N/Z of the compound system $(N/Z)_{CS}$, the isobaric ratios of the detected yields of ^{7}Li to ^{7}Be, ^{10}Be to ^{10}B and ^{11}B to ^{11}C are seen to increase. Also, using ratios from the two systems with identical N/Z, Ca on Fe and Ar on Ni, N/Z equilibrium is seen to exist in the 33 MeV/nucleon data, but not in the 45 MeV/nucleon data.

If hot nuclear matter has become equilibrated before emitting fragments, then the isobaric ratios plotted for two different systems having identical (N/Z) content, such as the case in the Ar on Ni and Ca on Fe systems, will be equal to one another. In the 33 MeV/nucleon data in Ref. 17, the data suggest fragments are emitted from an equilibrated source because the ratios' points fall on top of one another. On the other hand, in the 45 MeV/nucleon data, the data suggest fragments are being emitted from a non-equilibrated source, with the Ca on Fe isobaric ratios falling above the Ar on Ni isobaric ratios. These findings point out that the N/Z equilibration is, again, dependent on energy of the projectile and that the onset of non-equilibration for these systems lies between 33 and 45 MeV/nucleon for these data.

The nuclear transparency and N/Z equilibration of ^{96}Ru and ^{96}Zr at 400 MeV/nucleon has been studied [18]. N/Z non-equilibrium is studied using the N/Z tracer method. The N/Z tracer method involves selecting a cell in momentum space and counting the number of protons within that cell. The collected charge in a cell from a Ru on Ru reaction should be higher than the collected charge in a cell from the Zr on Zr reaction because Ru has 44 protons while Zr has only 40. These systems are interesting because there is a large difference in N/Z values, with $(N/Z)_{Ru} = 1.18$ and $(N/Z)_{Zr} = 1.4$. The collected charge in a cell at the end of a mixed reaction of either Zr on Ru or Ru on Zr will have an intermediate value and give some indication of the amount of mixing between the nucleons of the projectile with the nucleons of the target. The authors came up with a value called R_Z, which measures the amount of mixing between projectiles and target nucleons. Using the symmetric systems as a calibration, the following factor of R_Z is calculated to determine the degree of transparency,

$$R_Z = \frac{2(Z_{\text{det}}) - Z_{\text{det}}^{Zr} - Z_{\text{det}}^{Ru}}{Z_{\text{det}}^{Zr} - Z_{\text{det}}^{Ru}}, \tag{2}$$

where Z_{det} is the total number of protons detected in a selected space after a collision of a mixed system (Z_{det}), Zr on Zr ($Z^{Zr}{}_{det}$), or Ru on Ru ($Z^{Ru}{}_{det}$). In the symmetric systems, R_Z takes the value of +1 for the Zr on Zr and -1 for Ru on Ru. R_Z takes a value of zero when the emitting source is in full N/Z equilibrium. As shown in Ref. 18, the mixed reactions of Zr and Ru at a projectile energy of 400 MeV/nucleon are never equilibrated and as the collisions become more peripheral, the system becomes less and less equilibrated.

Another way to use the N/Z tracer method is to use ratios of isotopes and isobars in place of the previous variables involving collected charge in momentum space [18]. Equation 3 shows how an example of an N/Z tracer term for the isotopic yield ratio of p/t is calculated for the two symmetric and two asymmetric reactions ^{58}Fe and ^{58}Ni on ^{58}Fe and ^{58}Ni.

$$N/Z\_tracer\_term = \frac{2*(p/t)_X - (p/t)_{NiNi} - (p/t)_{FeFe}}{(p/t)_{NiNi} - (p/t)_{FeFe}}, \tag{3}$$

where $(p/t)_X$ is the isotopic yield ratio of protons to deuterons from one of the four systems, $(p/t)_{NiNi}$ is the ratio of protons to deuterons from ^{58}Ni on ^{58}Ni and $(p/t)_{FeFe}$ is the proton to deuteron yield ratio from ^{58}Fe on ^{58}Fe. If X equals NiNi, the value of the N/Z tracer term is positive one. If X equals FeFe, then the value of N/Z tracer term equals negative one. If X equals NiFe or FeNi, then N/Z tracer term takes on an intermediate value between positive and negative one. As an example, take the (p/t) ratio values for each system and substitute the $(N/Z)_{CS}$ for each system, one gets the value of 1 for the NiNi = X, 0.0375 for FeNi = NiFe = X, and -1 for FeFe = X.

Simulations codes are run to predict nuclear collision experimental results using many different theories to account for the thermal, momentum and N/Z equilibration of excited nuclear systems produced in nuclear collisions. Simulation codes treat the excited nuclear matter created in nuclear collisions dynamically or statistically (or both consecutively) until cold fragments are created and can be compared after filtering for detector acceptance to experimental data. Simulation codes that are run to further understanding of the physics involved in N/Z dependence of nuclear reactions sometimes simply assume N/Z equilibration. The assumption of N/Z equilibration in simulation codes cannot be valid at all N/Z, energies, masses and densities. Establishing the onset or failure of N/Z equilibration is a laudable goal whose success will greatly improve simulation code predictions and understanding of the physics involved in N/Z asymmetric nuclear collisions, as well as supernovae and neutron star behaviors. The current study will investigate N/Z equilibration using the isotopic and isobaric ratios from 35 and 45 MeV/nucleon $^{54, 58}$Fe and $^{58, 64}$Ni on $^{54, 58}$Fe and $^{58, 64}$Ni and the N/Z tracer method [18].

CHAPTER II

NUCLEAR REACTIONS AND COMPUTER SIMULATIONS

Nuclear reactions

Heavy-ion nuclear reactions are reactions between target and projectiles with charge greater than two. Heavy-ion nuclear reactions can be split into four general groups by decreasing impact parameters [19,20]. The first group has the largest impact parameters and includes elastic and inelastic scattering and Coulomb excitations. The second group has slightly smaller impact parameters than the first and includes direct reactions and grazing collisions. The third group of heavy-ion nuclear reactions includes dissipative or damped collisions. And the fourth group of collisions involve the formation of a compound nucleus or composite system made up of some or all of the nucleons in the target and projectile.

When the projectile and target are not overlapping during the collision, as when the impact parameter is equal to or larger than the combined radii of the projectile and target, the type of heavy-ion nuclear reaction is called elastic scattering. In elastic scattering, as a result of the impact parameter is no smaller than the distance in which the projectile and target are just touching. Elastic scattering experimental data have given insights into the thickness of skins on neutron rich nuclei [21].

With a similar impact parameter as in elastic scattering, a heavy-ion nuclear reaction can occur in which a piece of the projectile's kinetic energy is transferred to the target nucleus' excitation energy. This type of heavy-ion nuclear reaction is called inelastic scattering. Experimental inelastic scattering data give information about high angular momenta leading to high-spin states [22]. Also, if the projectile does not carry enough energy to overcome the Coulomb barrier but excites the target solely by electromagnetic interactions, the type of heavy-ion nuclear reaction is Coulomb excitation. Coulomb excitation experimental data has yielded information about nuclear structure and is a type of inelastic scattering. A general schematic drawing of elastic scattering is seen in Fig. 1. The red nucleus is the projectile and the yellow nucleus is the target. The distance between the lines which are parallel to the initial direction of the projectile and which intersect the center of both nuclei is defined as the impact parameter. When the nuclei are just touching, the impact parameter is the sum of the two nuclei's radii. When they are not touching the impact parameter is larger than the radii sum. When the nuclei overlap, the impact parameter is less than the radii sum.

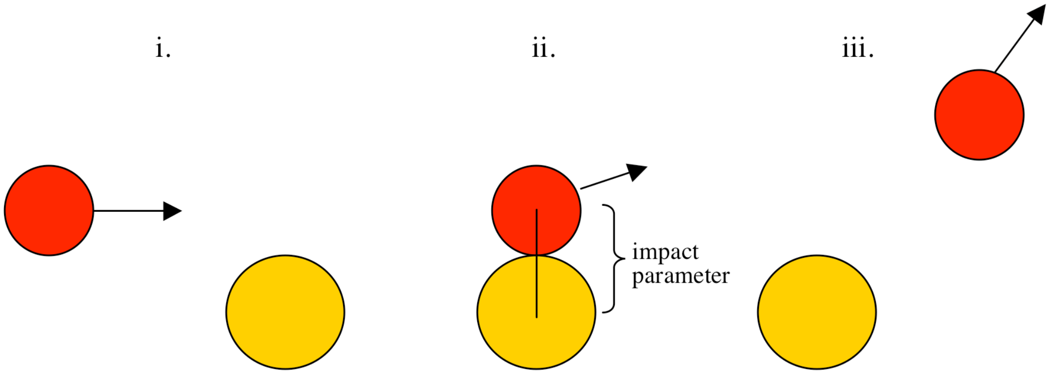

Fig. 1. A schematic of an elastic scattering nuclear collision.

As the impact parameter becomes smaller and projectile energies rise above the Coulomb barrier, the amount of overlap during the collision of the projectile and the target increases and the resulting distribution of scattering angles will begin to differ from those well predicted by Coulomb interaction. These are called direct reactions or grazing collisions. Grazing heavy-ion nuclear collisions include transfer reactions in which nucleons are picked up or stripped from the projectile or target. A schematic picture of a grazing nuclear collision can be seen in Fig. 2.

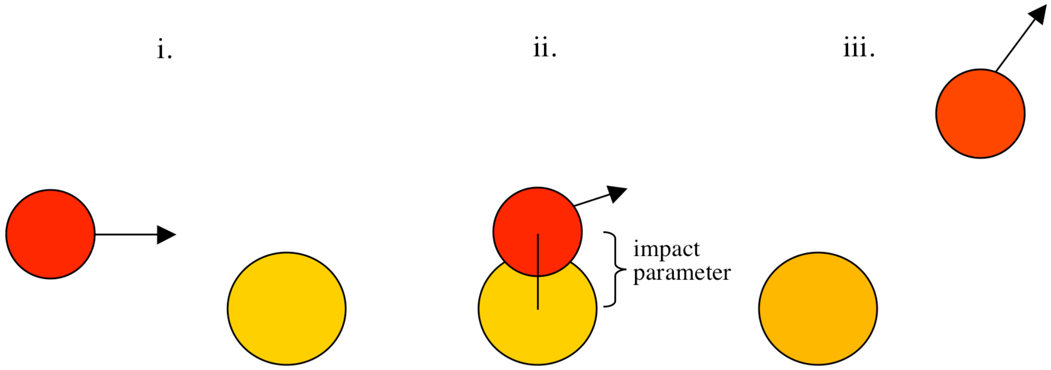

Fig. 2. A schematic of a grazing nuclear collision.

By reducing the impact parameter of a heavy-ion nuclear reaction even more, one sees a type of nuclear collision called a dissipative or damped collision. These collisions dissipate their initial kinetic energy, which is delivered by the projectile, into the intrinsic degrees of freedom of the projectile and target. Bridging the gap between the grazing collisions and compound nucleus forming collisions are deep inelastic collisions, in which a large amount of nucleons can be transferred between the target and projectile. A schematic drawing of a deep inelastic collision is seen in Fig. 3.

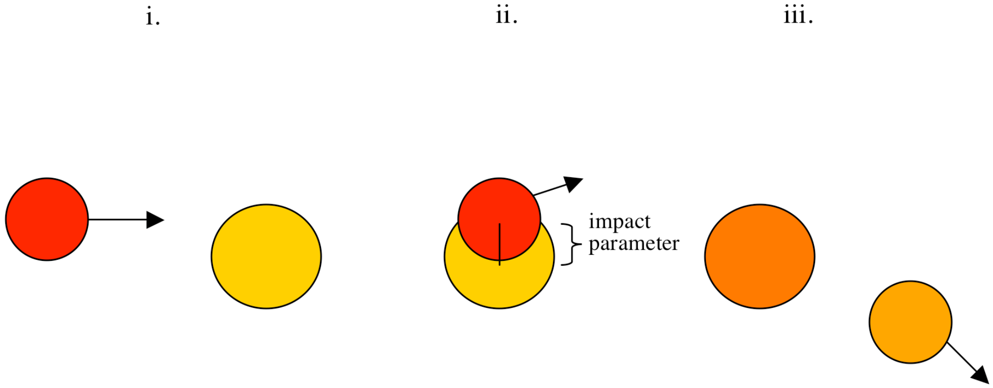

Fig. 3. A schematic of a deep inelastic nuclear collision.

At the smallest impact parameters, when the projectile and target are most overlapping, a compound or composite nucleus may be formed. The fusion of projectile and target cannot occur if there is too much angular momentum produced in the collision. The limiting angular momentum for compound nucleus formation is called the critical angular momentum. Compound nucleus forming nuclear collisions have given rise to new elements and allow for study of nuclear reactions far from the valley of stability.

Small impact parameter, compound nucleus forming nuclear collisions are one way to study of nuclear fragmentation. The compound nuclei formed in these energetic collisions can be highly excited and, after progressing toward and perhaps reaching thermodynamic and chemical equilibrium, break up to form complex fragments. The fragments formed from small impact parameter heavy-ion nuclear collisions are the type of fragments studied in the current NIMROD work. The journey from collision to fragment formation and the evolution toward equilibrium of the chemical degree of freedom within the compound nucleus before the fragments are formed and during the cooling and expansion phases is presently of interest.

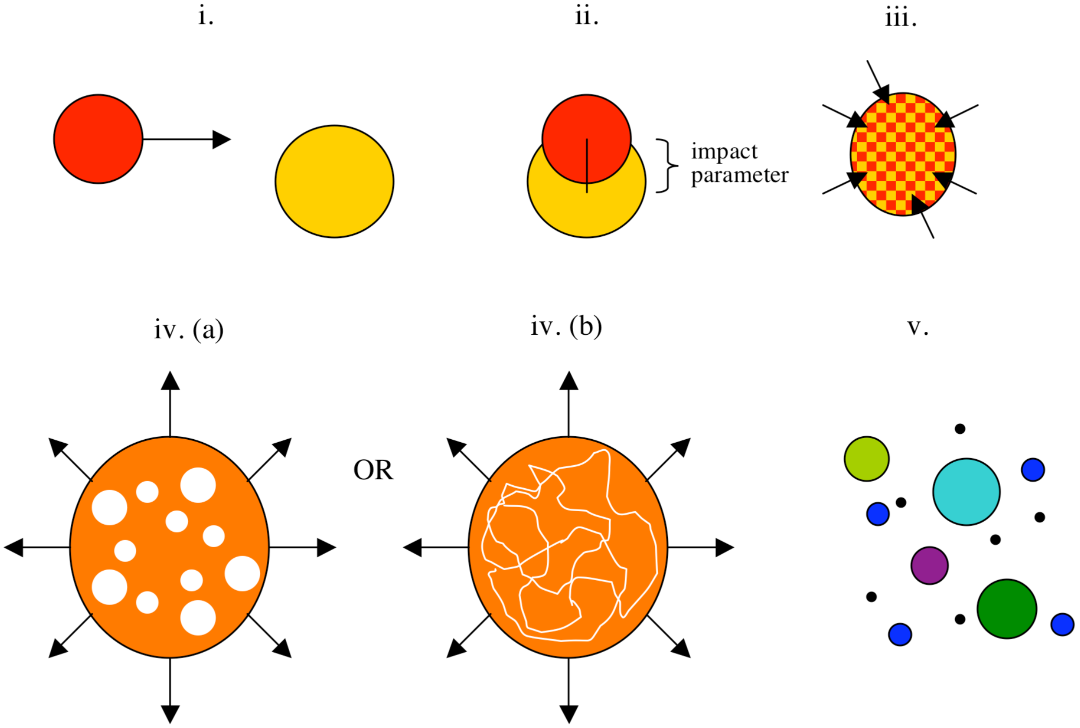

Fig. 4. A schematic of central intermediate energy nuclear collision.

In very simple terms, during a central, or small impact parameter, heavy-ion nuclear collision, a composite system is formed in which there is an initial compression stage where nucleon exchange and kinetic energy transfer can all occur. Following the heating stage is an cooling and expansion stage in which the compound system becomes unstable and forms bubbles or cracks which lead to fragment formation. N/Z and thermodynamic equilibrium may continue through the cooling and expansion phases. In Fig. 4 is shown a general schematic drawing of an intermediate energy heavy-ion central collision which leads to fragmentation. The five basic steps in Fig. 4 are as follows. i.) The projectile (red) approaches the target (yellow) at a small impact parameter. ii. and iii.) The collision occurs and a heated and possibly compressed composite system is created. iv.) The composite system isentropically expands while cooling, forming bubbles or cracks. v.) The composite system becomes unstable and fragments.

Computer simulations

Computer codes are used to simulate experimental results from nuclear collision studies [23,24]. By using computer simulation, the physics incorporated in the simulation may be tested for sensitivity. Also, computer simulations help correctly correlate experimental data and the physics in the nuclear equation of state. The nucleons interacting in the nuclear collision are controlled by many different forces which can include the mean field and nucleon-nucleon collisions, which are governed by the Pauli exclusion principle. The fragments shown in part v. of Fig. 4 are representative of the physics which occurs during the equilibration of the excited nuclear material which participated in the nuclear collision. Fragments formed at freeze out, when interaction between the nucleons in the composite system stops, carry physics information from the nuclear collision interaction. However, the fragments which are formed at freeze out are not the fragments which are seen in detectors during experiments. These fragments, called primary fragments, go through a deexcitation process by giving off secondary fragments, protons, neutrons and gammas. The secondary fragments may even go through a deexcitation process. The final fragments which remain after the deexcitation process are the fragments which are seen by detectors.

The temperature or excitation energy per nucleon of fragments seen from intermediate energy heavy-ion nuclear collisions is directly related to the amount of kinetic energy transferred from the projectile to the composite system. In the simplest case, one may assume that the projectile kinetic energy is completely given to the composite system and so the resulting excitation per nucleon indicates the temperature of the fragments emitting system and therefore of the fragments. Aspects of nuclear collisions prevent complete kinetic energy transfer from the projectile to the target. One such aspect involves pre-equilibrium emission. Pre-equilibrium emission occurs prior to equilibration of the composite system and serves to carry away kinetic energy from the composite system. This lowers the temperature of the equilibrated system. It also lowers the observed excitation energy per nucleon of fragments detected from the collision. In addition, during the collision kinetic energy may be lost due to irreversible nucleon friction which causes the heating of nucleons, angular momentum, and collective and radial flow. These processes also result in a lowering of the temperature from the temperature assumed from complete kinetic energy transfer.

There are more complications after the freeze out occurs. The fragments formed at the end of nucleon interaction during the expansion phase of the reaction are themselves excited and often decay into other fragments in a statistical decay mechanism. This decay of fragments formed at freeze out, which will now be called pre-fragments since they are not the fragments which are detected but are the fragments which exist prior to the fragment redistribution due to statistical decay, will change the distribution in two ways. It will lower the yields of excited and unstable fragments as they decay and it will raise the yield of the fragments into which the pre-fragments are decaying. The redistribution of pre-fragments due to secondary decay (the former) and side-feeding (the latter) obscures the original fragment distribution occurring in freeze out.

Another effect altering the character of the pre-fragments is the Coulomb repulsion felt by the fragments while they are being formed and are decaying which can accelerate them slightly in directions not associated with the angular distribution of the pre-fragments. Computer simulations are very useful as they can be used to track the evolution from pre-fragments and observed fragments, thus connecting the observable to the physics of interest.

There are two main types of simulations codes, statistical and dynamical [25]. Dynamical codes track the nuclear collision through the interaction phase, employing the nuclear equation of state in various forms to predict in a chronologically stepwise fashion the outcome of each event. The nuclear equation of state explicitly allows for terms including mean field forces, nucleon-nucleon collisions and Pauli blocking, and neutron and proton or chemical asymmetry. Dynamical codes are very computer processing time intensive and can take many months to complete with enough statistics to make a confident comparison to experimental data. Statistical codes begin with a set of initial parameters which identify the collision and assume the composite system decays statistically into complex fragments and nucleus according to weighted distributions. Statistical codes are much less computer processing time intensive and can give results with good statistics in no more than days.

Statistical codes

SMM, or Simultaneous Multifragmentation Model [26,27,28], is a statistical code that starts with the inputs of A, Z, initial volume and excitation energy, E*, at the time of step iv in Fig. 4. In the SMM model interaction among fragments stops after break up. Then, the deexcitation of excited primary fragments happens in the final stage.

In SMM, thermodynamic equilibrium is assumed just before break up volume is reached. All heavy fragments (A>=5) are treated as compressible liquid drops and lighter (A<=4) ones are part of a gas mixed with liquid drops. There are three stages of fragmentation which are of importance (in the view ref. 26 authors), (1) composite system creation and onset of instability, (2) primary fragment creation during the expansion phase (3) secondary fragment creation from the deexcitation of the primary fragments. Excitation energy is channeled both into transverse flow and thermal motion. SMM assumes thermal and chemical equilibration occurs before fragment emission begins. In other words, temperature and composition are assumed to be homogeneous prior to primary fragment emission. Droplets correspond to nuclear fragments and their size depends on thermal, surface and Coulomb energies and entropy. The liquid drop equation contains bulk, surface, asymmetry, Coulomb and translational motion terms that contribute to the energy and entropy characteristics of the compound system. These are all taken together to develop the most probable partitions that lead to final fragment distributions.

GEMINI [29] is a statistical simulation code that uses sequential binary decays to describe the fragments seen in products of nuclear reactions. Each possible division of the compound nucleus, or CN, formed in the nuclear collision is taken into account. Each step of the decay chain is chosen using Monte Carlo techniques until the resulting fragments are stable against further decay.

The input for GEMINI is given as some combination of the projectile and target and E* is given by the Q value for fusion. The maximum spin of the CN is a parameter used to fit the model to experimental cross section data. Agreement between code and experimental data is found by comparing shape and size of charge distributions and appropriately adjusting until a match is achieved.

Dynamical codes

BUU [30] (named for Boltzmann-Uheling-Uhlenbeck) is a dynamical code in which both the projectile and target nuclei are cold prior to touching in the nuclear collision. When nucleons collide, temperature and entropy go up. Temperature goes back down as pieces come out of the interaction. Entropy changes only slightly after break up happens. Then, density falls until nucleons stop interacting (freeze out).

The cascade model, upon which BUU is built, is a microscopic model in which all nucleons are initially treated as points in a sphere without assigning Fermi momenta. If Fermi momenta are assigned to initial nucleons, the nuclei would not be stable prior to collision. Monte-Carloing is used to get each nucleon’s starting position. The model’s purpose is to predict where and at what time nucleons collide. To collide, nucleons must be within a set distance from each other within a set division of time.

BUU improves on the cascade model by folding in the mean field. The inclusion of the mean field allows for Fermi momenta to be considered while keeping the initial states stable. Also, BUU checks for spin-isospin degeneracy and enforces the Pauli principle. In practice, allowing Pauli blocking means that when two nucleons come into collision distance in the needed time interval and have a surrounding density that will allow scattering, a collision is permitted. If they are surrounded by high density of nucleons, the collision is not allowed.

BUU has some limitations. BUU does not produce fragments and so cannot be directly compared to experimental results without passing through some kind of coalescence model. Fluctuations are introduced to enhance reproducibility of experimental data. Monte-Carloing of initial position of nucleons gives fluctuations. The scattering angle of collisions is Monte-Carloed, too, giving more fluctuations. BUU ishes out fluctuations by showing average behavior of many interactions of test particles.

Extended BUU explains spectator/participant type reactions and their velocity distributions well. The inclusion of momentum dependence of nuclear interaction serves to make it more repulsive. With a more repulsive nuclear interaction, data that is previously thought to agree with a harder equation of state can be better described by a softer equation of state [30].

AMD, or Antisymmeterized Molecular Dynamics, is another dynamical type of computer simulation code, which is developed from QMD, or Quantum Molecular Dynamics [31,32]. A comprehensive review of QMD may be found in ref. 33. In QMD, distinguishable Gaussian wave packets in phase space are used to represent nucleons in a collision. The Thomas-Fermi model is used to imitate the initial phase space, or ground state, distribution. In this way, the Pauli principle is observed such that only one nucleon can occupy each h^3 volume in phase space. As the collision progresses, the classical equation of motion and the stochastic nucleon-nucleon collisions dictate the movement of the center of the Gaussian wave packets in phase space. At the final state, the Pauli principle is enforced as stated earlier.

Fermionic Molecular Dynamics [34], or FMD, is an antisymmeterized version of QMD in which the wave function of a nucleons involved in a nuclear collision is depicted as a Slater determinant of Gaussian wave packets of nucleons. The propagation through time of the collision is dictated by a time-dependent variational principle. The Pauli principle is explicitly dealt with in an antisymmeterized form of molecular dynamics due to the fact that when two nucleons occupy the same position, the Slater determinant goes to zero and is therefore not allowed.

AMD takes Fermionic Molecular Dynamics and adds in the nucleon-nucleon collision process. AMD does a good job of reproducing ground state binding energies and shell effects [35], but does not include any description of the secondary statistical decay, which is usually quite important when trying to reproduce experimental results from nuclear collisions. The larger the masses of the target and projectile in the nuclear collision, the longer the calculation takes to complete, as the number of terms in the calculation goes as $A^4/16$, where A is the number of nucleons involved in the collision. For an AMD calculation of a collision between ^{58}Fe and ^{58}Fe, the number of terms included in the calculation of one collision is $(58+58)^4/16$ or 11,316,496 terms.

A modification to AMD is found with AMD-V [32], in which the Slater determinant describing the collision is broken up into several Slater determinants so that, for example, hot fragments, which may have a diffuse tail to their wave function, can separate that part of their wave function and emit a particle to de-excite. AMD-V gives a description for a fluctuating mean field that is a result of the diffusion or breaking up of a single-particle wave function as well as the branching into exit channels of a single collision, both processes of which are important in simulating intermediate energy heavy-ion nuclear collisions.

CHAPTER III

EXPERIMENTAL AND ANALYSIS DETAILS

Beams and targets

The experimental data are taken at Texas A&M University using beams produced by the Cyclotron Institute's K500 Superconducting Cyclotron. The beams used are 35 and 45 MeV/nucleon ^{58}Fe and ^{58}Ni and 35 MeV/nucleon ^{54}Fe and ^{64}Ni. The targets used are ^{58}Fe, ^{58}Ni, ^{54}Fe and ^{64}Ni. See Table 1 and Table 2 for details about beam and target materials. All beam material is obtained from Trace Sciences International [36]. ^{58}Ni, ^{54}Fe and ^{64}Ni Target materials are obtained from Micromatter, Inc. [37]. ^{58}Fe targets are obtained from Targetlabor [38].

Table 1. Beam materials, energies, charge states and purities.

Beam	Energy	Charge State	Purity
^{58}Fe	35 MeV/u	18+	93.13% [*]
^{58}Fe	45 MeV/u	20+	" "
^{58}Ni	45 MeV/u	20+	>99%
^{58}Ni	35 MeV/u	18+	" "
^{64}Ni	35 MeV/u	20+	96.48%, 98.02%
^{54}Fe	35 MeV/u	17+	99.92%

---

[*] The remaining 6.87% material in the ^{58}Fe beam material included 6.7% ^{57}Fe, 0.16% ^{56}Fe, and 0.01% ^{55}Fe. The difference in the charge state to mass ratio of ^{57}Fe and ^{58}Fe is 1.7% in the charge states from both beam energies. The K500 Cyclotron can pick out a difference in charge of mass ratio of 1 in 5000, or 0.02%, according to a private communication with Dr. Don May.

Table 2. Target materials, thicknesses and purities.

Target	Thickness	Purity
^{58}Fe	1 mg/cm^2	91.19%
^{58}Ni	1.7 mg/cm^2	>99%
^{64}Ni	1.14 mg/cm^2	97.92%
^{54}Fe	1 mg/cm^2	99.92%, 97.61%

Beam current intensities vary between about 30 and 60 pA. The chronological order of the beam and target combinations is seen in Table 3. In order to ensure purity of delivered beams to the detector, a 0.25 millimeter thick aluminum foil is placed at Faraday Cup #2 (FC02), which strips almost all electrons from the beam material, differentiating Fe from Ni by their different charge to mass ratios. The energy lost in the foil is less than one percent, according to the energy loss code SRIM, (Stopping Range of Ions in Matter) (version 2000.40) [39].

Table 3. Chronologic order of beam and target combinations.

Chronologic Order	Energy and Beam + Target
1	35 MeV/u ^{58}Fe + ^{58}Fe
2	35 MeV/u ^{58}Fe + ^{58}Ni
3	35 MeV/u ^{58}Fe + ^{54}Fe
4	45 MeV/u ^{58}Fe + ^{58}Fe
5	45 MeV/u ^{58}Fe + ^{58}Ni
6	45 MeV/u ^{58}Ni + ^{58}Fe
7	45 MeV/u ^{58}Ni + ^{58}Ni
8	35 MeV/u ^{58}Ni + ^{58}Fe
9	35 MeV/u ^{58}Ni + ^{58}Ni
10	35 MeV/u ^{58}Ni + ^{64}Ni
11	35 MeV/u ^{64}Ni + ^{64}Ni
12	35 MeV/u ^{54}Fe + ^{54}Fe
13	35 MeV/u ^{54}Fe + ^{58}Ni

NIMROD

Nimrod in the proper noun form is defined [40] as “a descendant of Ham represented in Genesis as a mighty hunter and a king of Shinar.” The experimental apparatus used for this study is named NIMROD or Neutron Ion Multidetector for Reaction Oriented Dynamics. NIMROD is an combination of more than one different apparatus including the second generation of the Neutron Ball and the modified CsI(Tl) Ball.

Neutron Ball

The design for the original Neutron Ball (NBL) is first reported on in 1985 [41]. The purpose of the NBL is to detect neutron multiplicity in an effort to understand excitation energy dissipation in intermediate energy heavy ion collisions. It is a spherically shaped, 1.5 m diameter, 4 pi detector filled with about 1700 liters of Gadolinium (Gd) doped (0.3% wt) pseudocumene liquid scintillator. The NBL is equipped with sixteen 5 inch photomultiplier tubes evenly spaced around the sphere. It have three major components: a center ring and two hemispheres one each on the top and bottom. A reaction chamber in the shape of a cylinder 45 cm tall with a 40 cm diameter is placed in the center of the NBL for small detectors and trigger devices. See Fig. 5 for a schematic drawing of the NBL. The center ring is split into six removable modules that gave opportunities to use big external counters without losing a great deal of neutron detection efficiency. See Fig. 6 for a top view of the center ring of the NBL.

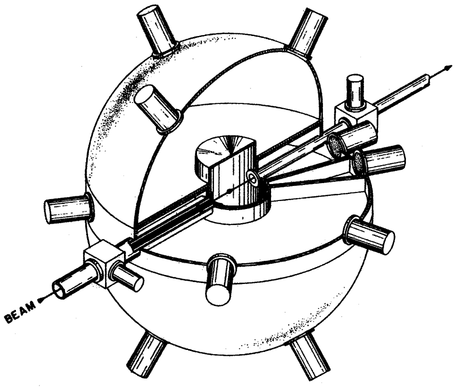

Fig. 5. A schematic drawing of the original Neutron Ball.

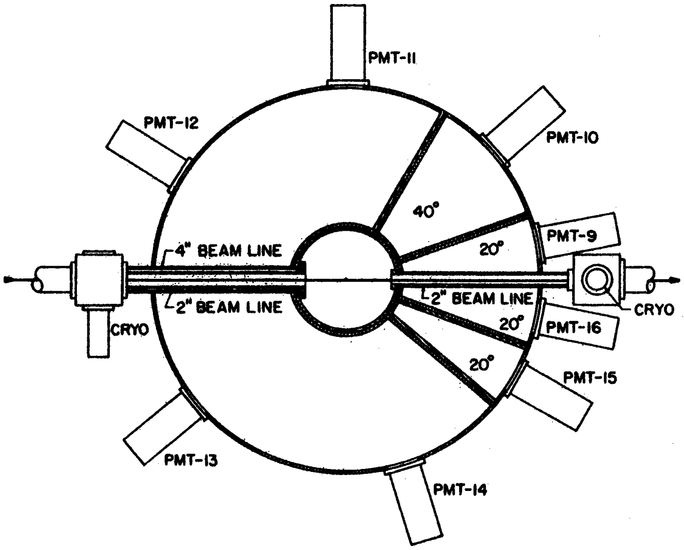

Fig. 6. A schematic of the top view of the center ring of original Neutron Ball.

During a nuclear collision in the NBL, a gamma ray flash is given off in the scintillator by colliding neutrons and protons. Next, the neutrons are thermalized, and after about a microsecond, are mostly captured by Gd nuclei. The Gd capture of a neutron raises the Gd nucleus into an excited state. Then, the Gd nucleus emits an average of three gamma rays totaling in energy to about 8 MeV. A raw neutron multiplicity comes from the number of delayed flashes associated with the Gd nucleus' neutron capture. A more accurate neutron multiplicity comes after correcting for efficiency (which is about 85% with ^{252}Cf), background and pileup.

Neutrons interacting with the Gd doped organic scintillator yield two groups of signals. The first is called a prompt signal, which comes from the recoil of the protons occurring in the thermalization of the neutrons. The prompt gamma ray signal gives information about the sum of the kinetic energy of all neutrons in the event plus the gammas from the event and the energetic charged products from neutron-induced reactions in the scintillator. The second type of signal is the delayed signal. The delayed signal is generated by the neutron capture of the Gd nuclei. The total number of delayed signals represents the number of neutrons emitted in the event after correction for detection efficiency is taken into account [42].

Because of the long time scale of the neutron capture process, the gate on a neutron capture event can be from 50 to 100 microseconds wide. The long time gate allows enough time to count the number of flashes from the Gd nuclei neutron capture deexcitations [43]. In an experiment, this can mean reaction rates on the order of 1000 events per second. In 1993, tests on the NBL are run to see if it would be useful for faster data collection [44]. It is found that the neutron detection time might be brought down from the original time on the order of microseconds to the order of nanoseconds by setting a higher threshold on the gamma fast flash energy, which is linearly dependent on the number of neutrons detected. Triggering on the fast flash eliminates the need to wait for all Gd neutron captures before proceeding with subsequent trigger logic. This greatly reduces the signal processing and dead time and allows for faster data acquisition rates.

CsI Ball

The design of the almost 4π CsI(Tl) crystal array is reported as finished in 1991 [45]. It is comprised of seven rings of 96 CsI(Tl) crystals, each with a light guide and a PMT. The angular coverage of each of the seven rings are 20-27 degrees (ring 1), 27-38 degrees (ring 2), 38-52 degrees (ring 3), 52-75 degrees (ring 4), 75-105 degrees (ring 5), 105-135 degrees (ring 6) and 135-170 degrees (ring 7). See Fig. 7 for a schematic drawing of the CsI(Tl) Ball in the described configuration. In 1995, ionization chambers are placed in front of the CsI(Tl) crystals, replacing what are thin plastic scintillator foils, in the effort to make better heavy ion identification and also to bring down energy thresholds [46]. The anode of the ionization chamber is the Mylar coating on the CsI(Tl) crystals and the cathode is made of a Nickel-coated Copper housing. Initial tests of the ionization chamber using 100 torr of CF_4 gas and a 30 MeV/nucleon ^{40}Ar beam on a target of ^{197}Au showed good mass separation [46]. In 1996, one ionization chamber in each ring is augmented by a Silicon detector to help with energy calibration [47].

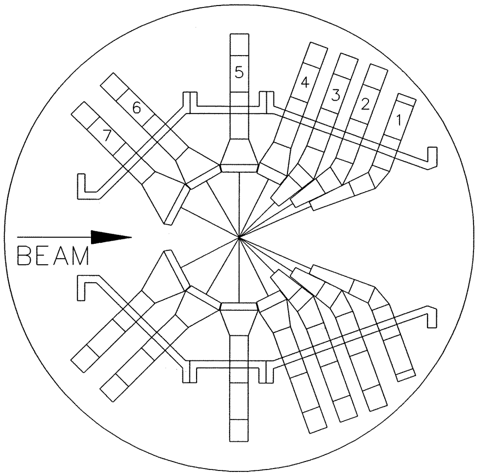

Fig. 7. A schematic of a cross section of the CsI(Tl) Ball.

Reports of plans for coupling the NBL and the CsI(Tl) Ball began in 1994 [48]. To accommodate the size of the CsI(Tl) Ball, the NBL is modified by taking the two hemispheres from the top and bottom, pulling them apart, rotating them 90 degrees and placing them on the left and right of a new central, cylindrically shaped section, which holds a cavity for the CsI(Tl) Ball that measures 125 cm in length and 60 cm in diameter [49]. The additional detection chamber space would also allow for expansion of the inner detector by the addition of a forward array or large vacuum chamber. The new cylindrical section to the NBL increased the total volume of liquid scintillator from about 1700 liters to about 2400 liters. In 1998, upgrades to the NBL are reported as being complete and its integration into the detector known as NIMROD is finalized [50].

NIMROD (2000)

In 1997, an upgrade to the CsI(Tl) Ball is undertaken which added an array of Silicon detectors between 3.6 and 45 degrees, replacing the detectors in the CsI(Tl) Ball between 20 and 45 degrees [51, 52, 53]. See Table 4 for the thicknesses of all of the NIMROD CsI(Tl) crystals and the angular range of each ring. Two telescopes in each ring are expanded to include a 100 micron and 500 micron Silicon detector between the Gas Ionization chamber and the CsI(Tl) crystals.

Table 4. NIMROD ring angles and CsI(Tl) crystal thicknesses.

Ring no.	CsI(Tl) thickness (mm)	Phi at center (degrees)	Range in Phi (degrees)
2	100	4.31	3.61 - 5.01
3	100	6.41	5.11 - 7.71
4	100	9.43	8.0 - 10.86
5	100	12.93	10.99 - 14.87
6	65	18.15	15.34 - 20.96
7	65	24.45	21.14 - 27.76
8	60	32.08	28.65 - 35.51
9	60	40.39	35.78 - 45.0
10	30	61.17	48.17 – 74.17
11	10	90	75 – 105
12	10	121	105 – 137
13	10	152.5	137 – 168

See Table 5 for the detector numbers of the double Silicon telescopes and the Silicon thicknesses.

Table 5. Double Silicon telescope detector numbers.

Ring no.	First Silicon (150 micron)	Second Silicon (500 micron)	CsI(Tl)	Phi at center (degrees)
2	2	4	0	120
2	8	11	12	300
3	1	5	1	112.5
3	3	6	1	127.5
3	7	10	13	292.5
3	9	12	13	307.5
4	20	24	25	112.5
4	21	25	25	127.5
4	28	32	37	292.5
4	29	33	37	307.5
5	19	23	26	112.5
5	22	26	26	127.5
5	27	31	38	292.5
5	30	34	38	307.5
6	42	46	51	112.5
6	43	47	51	127.5
6	50	54	69	292.5
6	51	55	69	307.5
7	44	48	50	112.5
7	41	45	52	127.5
7	52	56	68	292.5
7	49	53	70	307.5
8	64	68	76	112.5
8	65	69	76	127.5
8	72	76	94	292.5
8	73	77	94	307.5
9	66	70	75	112.5
9	63	67	77	127.5
9	74	78	93	292.5
9	71	75	95	307.5
10	85	86	130	270
11	87	88	138	135
12	89	90	154	270
13	91	92	162	270

Two more telescopes in each ring are expanded by one 300 micron Silicon detector and one telescope in each ring is expanded to have one 150 micron Silicon detector. See Table 6 for the list of single Silicon telescopes with 300 micron Silicon detectors. See Table 7 for the list of single Silicon telescopes with 150 micron Silicon detectors.

Table 6. 300 micron single Silicon telescope detector numbers.

Ring no.	Silicon ID (300 micron)	CsI(Tl) ID	Phi at center (degrees)
2	16	6	210
2	18	18	30
3	15	7	210
3	17	19	30
4	38	24	210
4	40	32	30
5	37	43	210
5	39	44	30
6	60	60	210
6	62	100	30
7	59	59	202.5
7	59	61	217.5
7	61	99	22.5
7	61	101	37.5
8	82	85	210
8	84	112	30
9	81	84	202.5
9	81	86	217.5
9	83	111	22.5
9	83	113	37.5

Table 7. 150 micron single Silicon telescope detector numbers.

Ring no.	Silicon ID (150 micron)	CsI(Tl) ID	Phi at center (degrees)
2	14	4	180
3	13	5	180
4	36	29	180
5	35	30	180
6	58	57	180
7	57	56	172.5
7	57	58	187.5
8	80	82	180
9	79	81	172.5
9	79	83	187.5

See the Appendix for detector maps which include all theta and phi angle values, detector types, numbering, and thickness for each ring in NIMROD.

Fig. 8 shows NIMROD with the outer second generation Neutron Ball and the inner modified CsI(Tl) Ball.

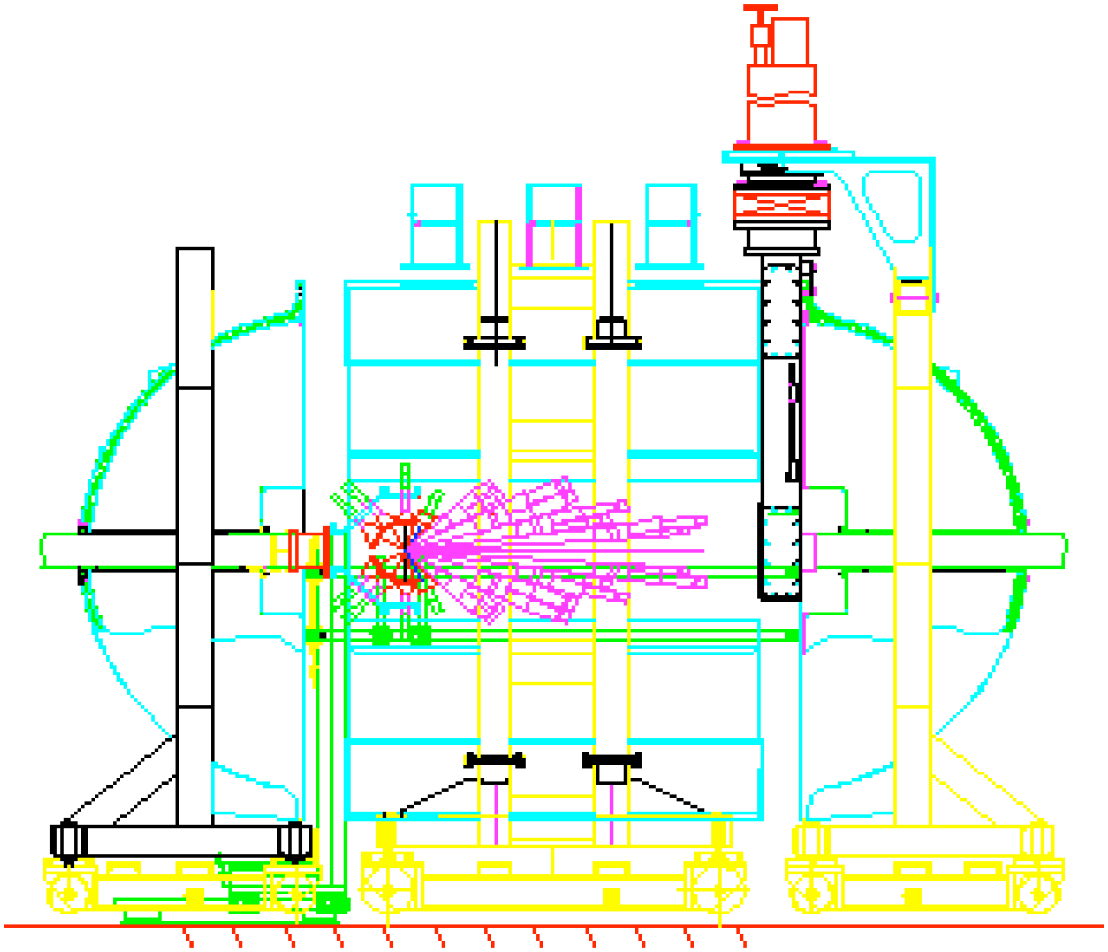

Fig. 8. A NIMROD 2000 AutoCAD rendering.

Fig. 9 shows an expanded view of the inner charged particle array that is the CsI(Tl) Ball. Fig. 10 shows an enlarged cross section of the charged particle array with ring number labeling. The pink detectors are from the newest CsI(Tl) Ball modification and the red detectors are rings from the original CsI(Tl) Ball. Ring 10, shown in red next to the pink detectors in rings 8 and 9, is made to couple the new part of the CsI(Tl) Ball to the original part.

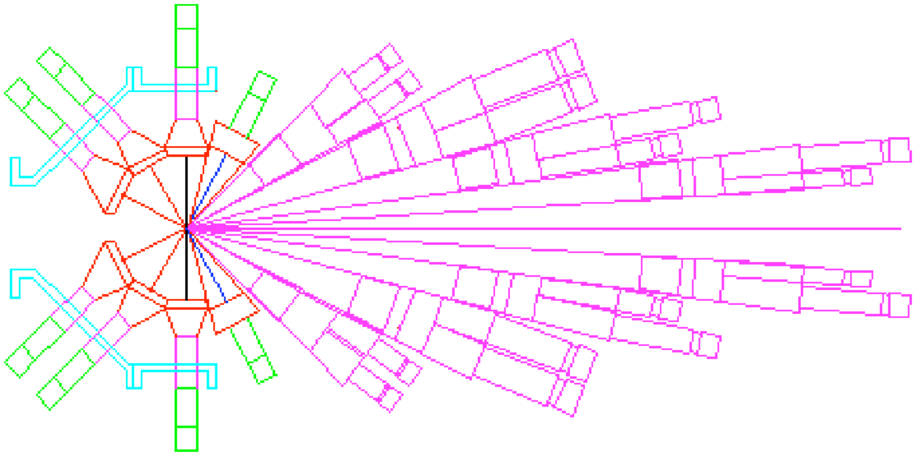

Fig. 9. The NIMROD inner charged particle array expanded.

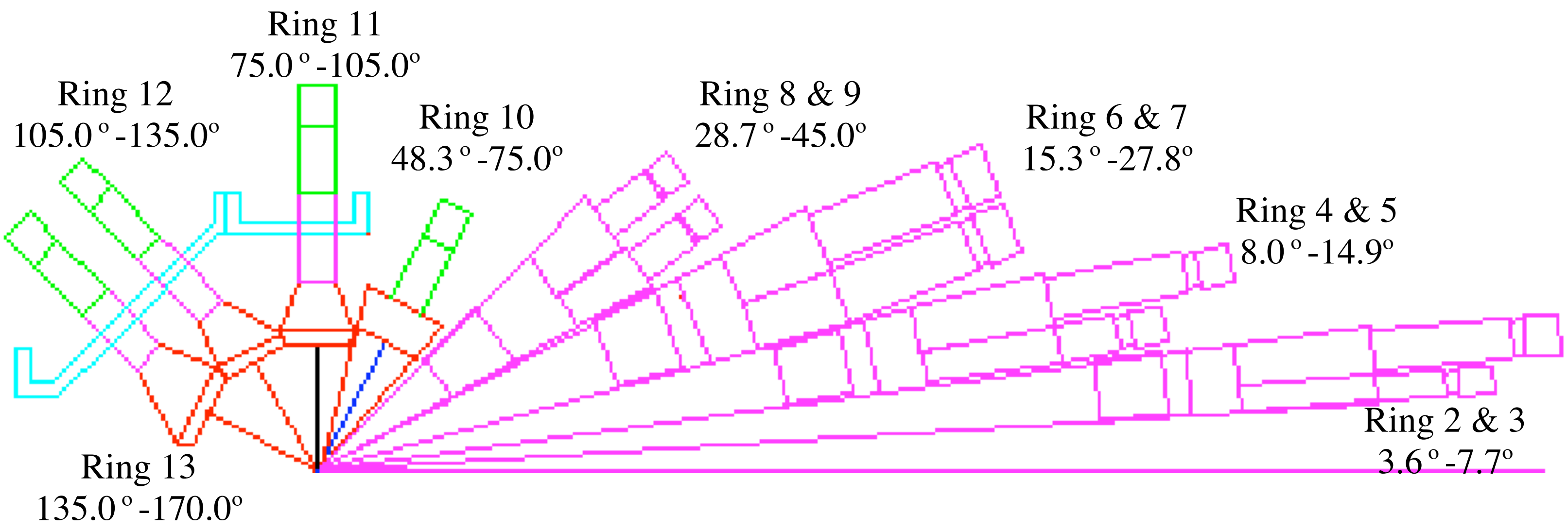

Fig. 10. The NIMROD charged particle array with ring labeling.

The photomultiplier tubes (PMTs) used in NIMROD 2000 are Hamamatsu R1924 and R1355 [52]. The PMTs are glued with BC-610 epoxy directly onto the crystals. The CsI(Tl) crystals are wrapped in three layers of 4000ths of an inch thick teflon tape and one layer of 10 micron thick double sided aluminized Mylar to stop light leaks and crosstalk between CsI(Tl) crystals [53]. The gas ion chambers gave two dead layers of 1.4 micron single sided aluminized Mylar. The Mylar of the gas ion chambers is glued to the G-10 frame with Clear RTV Silicone Adhesive Sealant. Punch through energies given by SRIM (version 2000.40) [39] for Silicon and Cesium Iodide detectors of all thicknesses are shown in Table 8. The amount of energy loss of $^{18}\mathrm{O}$ in CF_4 gas is 0.12%.

Table 8. Punch through energies in MeV.

Isotope	Silicon 150mm	Silicon 300mm	Silicon 500mm	CsI(Tl) 10mm	CsI(Tl) 30mm	CsI(Tl) 60mm	CsI(Tl) 65mm	CsI(Tl) 100mm
p	4.0	6.1	8.2	52.1	98.3	147.4	154.5	199.4
d	5.3	8.0	10.8	69.2	130.8	195.3	204.5	262.9
t	6.1	9.4	12.8	81.7	154.9	231.2	242.2	311.0
He^{3}	14.3	21.5	28.9	183.3	346.5	520.2	545.8	706.3
He^{4}	16.0	24.2	32.6	206.8	390.7	585.4	613.6	792.2
Li^{6}	30.4	45.9	61.8	392.7	741.6	1116.4	1170.8	1517.3
Li^{7}	32.4	49.0	66.0	419.2	792.3	1189.8	1247.2	1613.8
Be^{7}	46.1	69.2	92.2	574.5	1087.4	1640.8	1722.1	2241.0
Be^{9}	50.9	76.9	103.0	639.6	1207.6	1815.4	1903.2	2469.5
Be^{10}	52.9	80.5	107.8	668.3	1260.4	1892.5	1986.0	2571.5
B^{10}	67.9	102.6	137.6	865.5	1640.8	2480.5	2602.7	3392.6
B^{11}	70.4	106.7	143.4	902.0	1707.2	2575.8	2703.9	3519.3
C^{11}	85.9	130.4	175.2	1117.1	2123.5	3229.5	3391.6	4440.7
C^{12}	88.8	135.1	181.8	1158.1	2201.0	3339.3	3508.1	4584.3
C^{13}	91.5	139.7	187.9	1198.6	2274.9	3445.5	3617.5	4720.9
C^{14}	93.9	143.9	194.0	1236.2	2343.4	3547.1	3724.2	4854.0
N^{14}	112.3	171.9	231.9	1492.9	2843.3	4324.8	4546.7	5962.4
N^{15}	115.2	176.7	238.7	1536.3	2923.7	4442.7	4665.6	6112.0
O^{16}	135.2	208.4	283.3	1841.1	3520.8	5373.0	5648.3	7424.1
O^{17}	138.2	213.4	290.4	1887.9	3607.0	5500.6	5778.6	7586.2

Offline and online analysis

The analysis of NIMROD data follows four general steps. First, the data are taken in lmd file form. Second, the data are reduced into *.root files for further analysis. Third, the reduced *.root files are filtered down into physics tape files called trees. And lastly, the physics tree files are analyzed to produce plots of physical observables. See Fig. 11 for a flowchart of the four major steps of NIMROD data analysis.

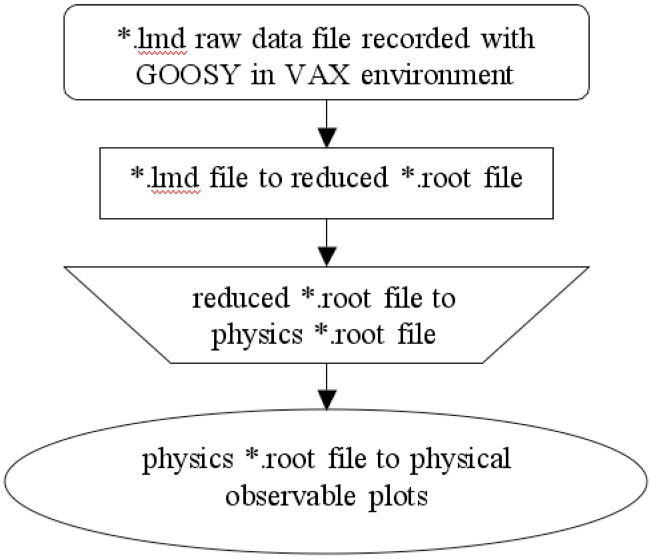

Fig. 11. A flowchart of the steps in NIMROD data analysis.

Raw data acquisition

The data are taken with a VMS computer named DAQ (short for Data AcQuisition) as *lmd files with an acquisition program name GOOSY (Gsi Online Offline SYstem), which is gained from GSI by the Cyclotron Institute in 1989 [54]. These NIMROD data are among the last data to be taken by GOOSY on the VMS computer, as an Institute-wide movement from VMS to UNIX computer systems is begun in 1999 [55]. The UNIX based analysis (both online and offline) adopted is based on ROOT [56], which is a code used in experiment NA49 at CERN. The ROOT analysis package is mixed with the code used at the BRAHMS experiment to make CycAps, the analysis suite that is used for this study. The ROOT version used prior to April 2004 is 3.03/09, released on November 13, 2002. As of April 2004, the ROOT version in use is 4.00/03, released on April 15, 2004.

Raw lmd file reduction

Using CycAps, the raw *.lmd files are reduced to *.root files for analysis including calibration and physics tape production. The *.lmd file nomenclature system is described by lxxxxxxyyyzzz.lmd, where xxxxxx is month, day and year of the beginning of the experiment, yyy is the run number and zzz is the file number within each run (with leading zeros for single and double digit run and file numbers). An example of an *.lmd filename holding data taken in the fifth file of the first run of an experiment beginning on March 16, 2000, is l031600001005.lmd. The *.lmd files are grouped by run number so that the filename structure for the reduced *.root files is given by Rxxxxxxyyy_z.root, where xxxxxx is the beginning date of the experiment and yyy is the run number and now z is the reduced file number of that run. An example of a reduced filename is R031600001_1.root. In some cases, memory constraints in ROOT dictate that more than one reduced file be created to encompass all of the *.lmd files in a single run. The data are split into two chronological pieces, March and April. The March data are reduced using the event structure file T031600Event.cxx and the April data are reduced by T040300Event.cxx.

Calibration and gates for three gains

The gains of the Silicon detectors are changed multiple times during data acquisition; therefore, all calibration and gating procedures are completed three times. The calibration of the double Silicon detectors begins by using ROOT to pick off channels of isotope punch through points on raw Silicon versus Silicon spectra. SRIM [39] is used to get the punch through energies and then Microsoft Excel (version X for Mac) is used to get the best three parameters in Equation 4 which yields the Silicon energy as a function of channel.

$$Silicon\_Energy\_Loss = par[0] + par[1] * channel + par[2] * \sqrt{channel} \qquad (4)$$

The Excel solver function is used to minimize the sum of the squares of the differences between the SRIM punch through energy values and values calculated using Equation 4. The minimization is achieved by varying an initial set of calibration parameters, par[0], par[1] and par[2]. The least square linear fits to channel versus energy plots using the calibration parameters obtained by this Excel minimization technique are good, giving R values that vary between .99 and 1. An R value equal to 1 represents a perfectly linear fit. There is a nonlinear term in the Silicon energy equation, which is inherited from a 3-line calibration code written by Martin Veselsky. The nonlinear term is meant to address the function of a Silicon which has some nonlinear response. The amount of non-linearity present in the calibration constants is trivial as most fits of the punch through energies versus the corresponding channels have an R value very close to one, which would imply perfect linearity.

Next, ROOT is used to pick off various channels from isotope lines on slow CsI(Tl) versus Silicon raw spectra. The Silicon calibration parameters obtained in the first step are used to convert the Silicon channels into energy. Then, an energy loss code [57] is used to match energy loss in the Silicon detector with energy loss in the CsI(Tl) detector. Given the set of channel and energy data for the CsI(Tl), the Excel minimization technique is used again to find the best parameters for Equation 5, which gives light output from a CsI(Tl) detector as a function of the energy (*E*) of the particle [58].

$$CsI\_Light\_Output = E - \rho \ln\left(1 + \frac{E}{\rho}\right) \text{ where } \rho = \eta Z^2 A \qquad (5)$$

The factor of η is a multiplicative factor relating to the energy and light deposited in the crystal. The CsI(Tl) energy spectra produced using the Tassan-Got energy calibration parameters are compared to literature values as a check for reproducibility. CsI(Tl) energy spectra are found to be in agreement with energy spectra from similar systems in the literature. Energy spectra from single Silicon detectors are scaled to match the double Silicon detector energy spectra on a ring by ring basis.

Gates are drawn by hand around all visibly separated isotope lines for each Silicon and CsI(Tl) detector. For those detectors with poor resolution, lines are drawn around visibly separated charge lines and for detectors with even poorer resolution, lines are drawn around charged particles only, giving at least some useful information to be used in global event characterization.

Table 9. Double Silicon telescope detector statuses.

Ring	ID	Works	Z	A	Integrate?
2	2_4_0	•	•	•	
2	8_11_12	•	•	•	
3	1_5_1				
3	3_6_1	•	•	•	•
3	7_10_13	•	•	•	•
3	9_12_13	•	•	•	•
4	20_24_25				
4	21_25_25	•	•	•	
4	28_32_37	•	•	•	
4	29_33_37	•	•	•	
5	19_23_26	•	•	•	•
5	22_26_26	•	•	•	
5	27_31_38	•	•	•	•
5	30_34_38				
6	42_46_51	•	•	•	•
6	43_47_51	•	•	•	•
6	50_54_69	•	•	•	•
6	51_55_69	•	•	•	
7	44_48_50	•	•	•	
7	41_45_52	•	•	•	
7	52_56_68	•	•	•	•
7	49_53_70				
8	64_68_76	•	•	•	•
8	65_69_76				
8	72_76_94	•	•		
8	73_77_94	•	•		
9	66_70_75	•	•	•	•
9	63_67_77	•	•	•	•
9	74_78_93	•	•		
9	71_75_95	•	•		
10	85_86_130				
11	87_88_138				
12	89_90_154				
13	91_92_162				

The double Silicon telescopes yield the majority of the isotopically resolved data included in this study. The single and no Silicon telescopes are important for mass identification and charged particle multiplicity. Table 9 and Table 10 show lists of all silicon detectors, their working status, what type of resolution they show, and which are integrated for analysis. Dots appear beside telescopes that are working, have resolution in Z and A, and are used to integrate yields for further analysis. Many detectors are working, but gave energy spectra which in the end are deems not integratable due to several reasons. The primary reason detectors are not integrated is that their raw spectra shapes are back bending or non-linear and therefore gave unbelievable particle energy distributions. All detectors in ring 2 are omitted from integration for this reason. Another common reason detectors are not included in the final integration is that the gains are set so high that a large fraction of the data is cut off from analysis.

All CsI(Tl) crystal detector statuses are shown in Table 11. Dots appear beside telescopes that are working, have resolution in Z and A, and are used to integrate yields for further analysis.

Table 10. All single Silicon telescope detector statuses.

Ring	ID	Works	Z	A	Integrate
2	14_4	•	•		
2	16_6	•	•		
2	18_18	•	•		
3	13_5	•	•		
3	15_7	•	•		
3	17_19	•	•		
4	36_29	•	•		
4	38_24	•	•	•	
4	40_32	•	•	•	•
5	35_30	•	•		
5	37_43	•	•	•	•
5	39_44	•			
6	58_57	•	•		
6	60_60				
6	62_100	•	•		
7	57_56	•	•		
7	57_58	•	•		
7	59_59	•	•		
7	59_61				
7	61_101				
7	61_99	•	•		
8	80_82				
8	82_85	•	•		
8	84_112				
9	79_81	•	•		
9	79_83	•	•		
9	81_84	•	•		
9	81_86	•	•		
9	83_11	•	•		
9	83_113	•	•		

Table 11. All CsI(Tl) detector statuses.

Ring	ID	Works?	Z	A	Integrate?	Ring	ID	Works?	Z	A	Integrate?
2	0					3	1	•	•	•	
2	2	•	•	•		3	3	•	•	•	•
2	4	•	•	•		3	5	•	•	•	
2	6	•	•	•		3	7	•	•	•	
2	8	•	•	•		3	9	•	•	•	•
2	10	•	•	•		3	11	•	•	•	
2	12					3	13				
2	14	•	•	•		3	15	•	•	•	
2	16	•	•	•		3	17	•	•	•	•
2	18	•	•	•		3	19	•	•	•	
2	20					3	21				
2	22	•	•	•		3	23	•	•	•	
4	24					5	26	•	•	•	
4	25					5	28	•	•	•	
4	27	•	•	•		5	30	•	•	•	
4	29	•	•	•		5	32	•	•	•	•
4	33	•	•	•		5	34				
4	35	•	•	•		5	36				
4	37	•	•	•		5	38	•	•	•	
4	39	•	•	•		5	40	•	•	•	
4	41	•	•	•	•	5	42	•	•	•	
4	43	•	•	•		5	44	•	•	•	•
4	45	•	•	•		5	46	•	•	•	
4	47	•	•	•		5	48				
6	51	•	•	•		8	76	•	•	•	•
6	54	•	•	•	•	8	79	•	•	•	•
6	57	•	•	•		8	82	•	•	•	•
6	60	•	•	•		8	85	•	•	•	
6	63	•	•	•		8	88	•	•	•	
6	66					8	91	•	•	•	
6	69	•	•	•		8	94	•	•	•	
6	72	•	•	•		8	109	•	•	•	
6	97	•	•	•		8	112				
6	100					8	115				
6	103	•	•	•		8	118	•	•	•	
6	106	•	•	•		8	169				

Table 11 (continued).

Ring	ID	Works?	Z	A	Integrate?	Ring	ID	Works?	Z	A	Integrate?
7	50	•	•	•		9	75	•	•	•	
7	52	•	•	•		9	77	•	•	•	
7	53	•	•	•		9	78	•	•	•	•
7	55	•	•	•		9	80	•	•	•	•
7	56	•	•	•		9	81	•	•	•	•
7	58	•	•	•		9	83	•	•	•	•
7	59	•	•	•	•	9	84	•	•	•	•
7	61					9	86	•	•	•	•
7	62	•	•	•		9	87	•	•	•	•
7	64	•	•	•	•	9	89	•	•	•	
7	65	•	•	•	•	9	90	•	•	•	•
7	67	•	•	•		9	92	•	•	•	•
7	68	•	•	•	•	9	93	•	•	•	•
7	70	•	•	•	•	9	95	•	•	•	•
7	71	•	•	•		9	108	•	•	•	
7	73	•	•	•	•	9	110				
7	96	•	•	•		9	111	•	•	•	
7	98					9	113	•	•	•	
7	99					9	114				
7	101					9	116				
7	102					9	117	•	•	•	
7	104	•	•	•		9	119	•	•	•	
7	105	•	•	•		9	168				
7	107	•	•	•		9	170				
10	120	•	•	•		11	136	•	•	•	
10	121	•	•	•		11	137	•	•	•	
10	122	•	•	•		11	138	•	•	•	
10	123					11	139	•	•	•	•
10	124	•	•	•		11	140	•	•	•	
10	125	•	•	•		11	141	•	•	•	
10	126	•	•	•		11	142	•	•	•	
10	127					11	143				
10	128	•	•	•	•	11	144	•	•	•	•
10	129					11	145				
10	130	•	•	•		11	146	•	•	•	
10	131	•	•	•		11	147	•	•	•	
10	132					11	148	•	•	•	
10	133	•	•	•	•	11	149	•	•	•	•
10	134										
10	135										

Table 11 (continued).

Ring	ID	Works?	Z	A	Integrate?	Ring	ID	Works?	Z	A	Integrate?
12	150	•	•	•	•	13	158	•	•	•	•
12	151	•	•	•	•	13	159	•	•	•	
12	152	•	•	•		13	160				
12	153					13	161				
12	154					13	162				
12	155	•	•	•	•	13	163				
12	156	•	•	•	•	13	164				
12	157					13	165				

*note: #s 31, 49, 74, 166 and 167 are not associated with CsI(Tl) detectors.

Due to Silicon detector threshold issues, light charged particle integrated yields come only from CsI(Tl) detector energy spectra. Intermediate mass fragment integrated yields are taken from detectors in double Silicon detector telescopes. Integration limits for all ratios in 2 rings are shown in Table 12. In Table 12, there are seven columns of integration limits. The second, third and fourth columns represent integration limits on the low, high and total energy spectrum for each ratio in ring 3 (theta$_{\text{lab}}$=6°). The last column holds limits for the low energy part of each ratio in ring 9, (theta$_{\text{lab}}$=40°). There is only one integration limit range for ring 9 due to the fact that the majority of the data exists in the low energy range.

Table 12. Integration limits for each ratio in two rings in NIMROD.

Ratio	Low (6º)	High (6º)	Total (6º)	(40º)
p/d	25,70	150,240	25,240	20,70
p/t	25,70	100,240	25,240	15,70
d/t	25,70	100,240	25,240	15,70
$^{3/4}$He	80,150	200,300	80,300	50,150
$^{6/7}$Li	120,220	280,360	120,360	105,200
$^{9/10}$Be	170,350	375,500	170,500	126,138
$^{10/11}$B	260,400	425,600	260,600	169,179
$^{12/13}$C	290,450	475,700	290,700	222,238
$^{14/15}$N	360,450	515,700	360,700	280,295
$^{16/17}$O	440,520	565,750	440,750	340,362
t/^{3}He	60,110	200,340	60,340	45,110
^{7}Li/Be	140,245	300,500	140,500	109,115
^{10}Be/B	210,350	405,550	210,550	167,180
^{11}B/C	270,400	450,650	270,650	205,215
^{14}C/N	350,450	505,650	350,650	270,290

Reduced file to physics file

After the reduced *.root files are created, physics tape data can be produced with the inclusion of calibration constants and gates using the CycAps programs. The source file which takes the reduced file and makes physics trees is CreatePhysicsTreeModule.cxx. CreatePhysicsTreeModule.cxx consists of about 3000 lines of C++ and ROOT code and is broken up into sections called methods or functions. The sequence of the program is as follows.

The relevant libraries are loaded and the program's constructor is called. CreatePhysicsTreeModule() is a constructor. The constructor is a class member function that has the same name as the class, i.e., CreatePhysicsTreeModule. The constructor is automatically called every time an object that belongs to the class is created. In other words, when an object is created, its members are initialized by a constructor function [59].

~CreatePhysicsTreeModule() is a destructor. A function with the same name as the class but with a ~ before it is called a destructor. It is a special member of the class and is automatically called when an object is destroyed, like when the program exits the scope in which the constructor is called. The destructor releases the memory held by each object in the class [60].

Next, DefineHistograms() is called. Inside DefineHistograms, The histogram root file is created and all histograms are defined for raw and energy spectra. Also, a table that will match up Silicon and CsI(Tl) detector numbers that are in front of one another is defined. Then, the input file (a reduced file) is added and its configuration is verified. Then, the event structure constructor, CycEvent(), is called, followed by the calling of the NimrodEvent() constructor.

After all pertinent constructors are called, the Init() method is called. Inside Init, the gain is set for the data being read to 2, 3, or 4, by calling SetGain(). When SetGain() is called, the gain is set to the index of 3 unless it is a data file in runs 16-28 (gain 2) or begins with R042000 (gain 4). Also inside Init(), all gate files are read into memory by calling methods ReadCsISiGateFile(), ReadSiSiGateFile(), and ReadCsIGateFile(). Arrays that identify (a) the type of telescope each module in NIMROD holds (0, 1, or 2), (b) the ring that each CsI(Tl) crystal sits in, (c) all calibration constants, (d) the set of raw Silicon channel scale factors, (e) 15 sets of scaling factors for all CsI(Tl) slow and fast channel data are created and defined. And finally, the Silicon threshold is set to 25 and the method SetupTree() is called inside Init().

Inside SetupTree(), the physics tree is defined and created. Then, the method Begin() is called. Inside Begin(), several global parameters are initialized, like EventNumber and other counting variables. Next, EventStatisticsStart() is called and begins to keep track of how long the analysis is taking. EventStatisticsStart() is responsible for the output one sees while running that reads how many events have been analyzed and how much time is remaining in the analysis.

Next, the Event() method is called. Event() is where the meat of the program lies. In summary, Event() parses through each event's particles, gets their channel information, decides whether or not the particle hit a gate, calibrates the particle's energy, and fills raw and energy spectra. Many methods are called from inside Event() to accomplish all these tasks.

GetTimeStepofSlowFastShift() is one method called from Event(). Inside GetTimeStepofSlowFastShift, the data file being read in is matched to the slice of time the data fell in so that the correct scaling factors can be used to move the slow and fast CsI(Tl) channel data in the gates. To explain, due to a wandering shift in the gain of all CsI(Tl) detectors through time (that is not uniform across all detectors in one time step), the data must shifted by a factor ranging from plus or minus 1% - 7% so the gates will lay correctly over the isotope lines in the slow versus fast spectra. The greatest shift factor needed is 7% by channel, which translates to 10.4% (^{4}He), 9.6% (^{7}Li) and 8.3% (^{11}B) by energy. The scale factors are read in during the Init() method.

At the end of each event, EventStatisticsEnd() is called. At the end of the analysis of all the events, End() is called. Inside End, the histogram and tree files are written and closed. Then, Finish() is called. Inside Finish(), final event counts are printed out and the method SetState() is called, passing a value of kFinish.

Physics trees to observables

Once the physics *.root files are created, CycAps is then again used to filter the data and fill different types of plots used in the final analysis. The source file which takes physics tree files and makes global event characteristic and energy histograms for analysis is StudyPhysicsTreeModule.cxx. StudyPhysicsTreeModule.cxx consists of about 1000 lines of C++ and ROOT code and is broken up (just like CreatePhysicsTreeModule.cxx) into sections called methods or functions. The sequence of this program is as follows.

The relevant libraries are loaded and the program's constructor is called. StudyPhysicsTreeModule() is the constructor and ~StudyPhysicsTreeModule() is the deconstructor. Their purposes are identical to those discussed for

CreatePhysicsTreeModule.cxx above. DefineHistograms() is called first. Inside DefineHistograms(), the histogram root file is created and all histograms are defined for global event characteristic and energy spectra. Tables that will define which detectors are working, cut values for multiplicity function, and a table that will match up Silicon and CsI detector numbers that are in front of one another are all defined inside DefineHistograms(). There are three inputs requested inside DefineHistograms() consisting of the centrality cut, event trigger and system number being analyzed. The choices of centrality are 10%, 10 to 20%, 20 to 30%, 30 to 40%, 40 to 50% most central.

Next, inside DefineHistograms(), the type of trigger is selected. The types of trigger can be minimum bias (multiplicity CsI(Tl) >= 1), high multiplicity (multiplicity CsI(Tl) >= 5), and the pulser trigger. Then, the system number is inputted to give the titles of the histograms the name and energy of each beam and target combination.

After DefineHistograms, the Init() method is called. Inside Init, the method GetSystemParameters() is called. Inside GetSystemParameters(), the beam energy and the beam and target's masses are used to calculate the beam rapidity and velocity in the lab and center of mass frame, which are used to determine mean rapidity charge.

Begin() and EventStatisticsStart() are called and perform the same function as in CreatePhysicsTreeModule.cxx. Next, the Event() method is called. Inside the Event() method is, again, where the meat of this program lies. In summary, Event() parses through each event, and calculates the Mfunction value, which is equal to the sum of the number of neutrons detected by the Neutron Ball plus the slope of the line fit to the ridge on the plot of Mcp vs. Mnb multiplied times the number of charged particles detected in the event (see Equation 3). If the Mfunction falls within the boundaries of the centrality cut requested in DefineHistograms(), then the event's particles are sifted through and their energy information is filled into energy spectra. Also, global event characteristic spectra are filled inside the Event() method.

Just as in CreatePhysicsTreeModule.cxx, at the end of each event, the method named EventStatisticsEnd() is called. At the end of the analysis of all the events, End() is called. Inside End(), the histogram file is written and closed. Then, Finish() is called.

Inside Finish(), final event counts are printed out and the method SetState() is called, passing a value of kFinish.

Electronics diagrams

Schematic electronics diagrams for the NIMROD 2000 setup are seen in the figures on pages 49, 50, 54, 57, and 58. Some modules found on more than one page (or more than once on the same page) are indicated in the case where a module is colored. The electronics diagrams for the NIMROD 2000 experiment are broken into seven sections and include diagrams for signals from the CsI detectors and Silicon detectors, master trigger logic, Neutron Ball, Pulser, and the radio frequency or RF of the Cyclotron.

In Fig. 12 are shown the signal electronics for the CsI detectors. The CsI detector electronics form the bulk of the electronics for NIMROD. They also set the Master Trigger, with the Silicon detectors acting as slaves to the Master Trigger. The signals from the CsI detectors come through the ceiling in the experimental cave and up through the floor to the high bay electronics area. The CsI signals are split and attenuated into three pieces, one each for the fast and slow signal which go into a Lecroy 1995F ADC and one which goes into a LeCroy 612A amplifier. The gate for the ADCs is set later on and will be mentioned in the text which follows.

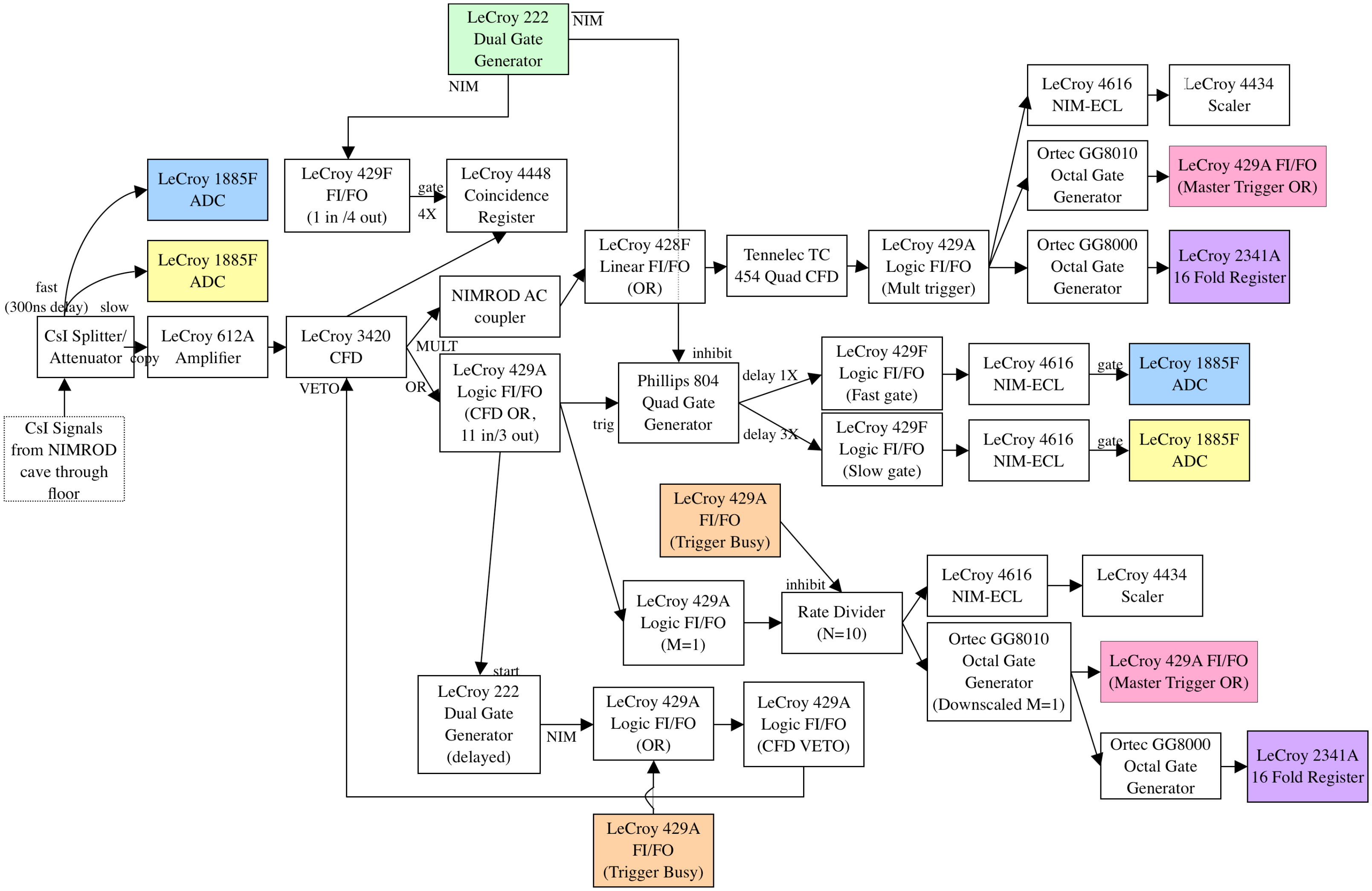

Fig. 12. Electronics diagram for CsI signal from detector to trigger.

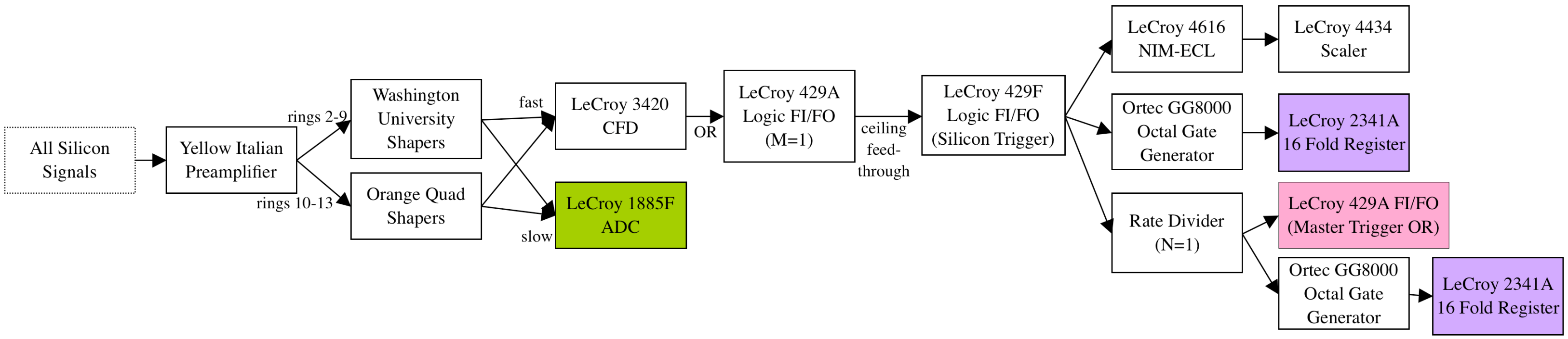

Fig. 13. Electronics diagram for Si signal from detector to trigger.

After amplification in the LeCroy 612A amplifier, the CsI signal's has three outputs from the LeCroy 3420 CFD, 1) a signal terminates in a LeCroy 4448 Coincidence Register, 2) a MULT output which goes to a NIMROD AC coupler and 3) an OR output which goes to a LeCroy 429A Logic FI/FO. The LeCroy 449 Coincidence Register has a GATE input which is fed by a LeCroy 429F FI/FO which is fed by the $\overline{\text{NIM}}$ output of a LeCroy 222 Dual Gate Generator which can be seen later in the master trigger electronics and is light green in color. The same LeCroy 222 Dual Gate Generator which is light green in color has an NIM output which serves as an INHIBIT to a Phillips 804 Quad Gate Generator, which will be mentioned later and inhibits the setting of the ADC gates for the CsI detectors.

The CsI detector signal coming from the MULT output of the Lecroy 3420 CFD then is sent to the NIMROD AC coupler. The AC coupler removes any DC offset to the CsI signal. Then this CsI signal goes on to a LeCroy 428F Linear FI/FO, which is set to OR for all CsI signals, and then on to a Tennelec TC 454 Quad CFD. From the Tennelec TC 454 Quad CFD, the CsI signal is sent to a Lecroy 429A Logic FI/FO and is split into three signals, one which hits a LeCroy 4434 Scaler module via a LeCroy 4616 NIM-ECL converter, one which goes through an Ortec GG8010 Octal Gate Generator and then on to the master trigger LeCroy 429A FI/FO module, which is set to OR. The last of the three signals from the LeCroy 429 A Logic FI/FO is sent through an Ortec GG8000 Octal Gate Generator and terminates in a LeCroy 2341A 16 Fold Register.

The CsI detector signal coming from the OR output of the LeCroy 3420 CFD is sent through a LeCroy 429A Logic FI/FO that is set to OR is copied three times. The three copies from the FI/FO are sent to 1) the trigger input of a Phillips 804 Quad Gate Generator which eventually sets the gate for the CsI ADCs, 2) a Lecroy 429A Logic FI/FO (designated M=1) which goes on to set the master trigger logic, and also 3) a LeCroy 222 Dual Gate Generator which goes on to VETO the CsI CFDs.

The Philips 804 Quad Gate Generator has an INHIBIT input which is fed by the light green LeCroy 222 Dual Gate Generator's anti NIM output which is mentioned earlier. The first of the three signals listed which goes to a Phillips 804 Quad Gate Generator has two outputs, one which is delayed through one channel and sent to a LeCroy 429F Logic FI/FO for the fast signal logic and one which is delayed through three channels and sent to a LeCroy 429F Logic FI/FO for the slow signal logic. Both the fast and slow logic signals go from the LeCroy 419F Logic FI/FOs go through a LeCroy 4616 NIM-ECL and into the GATE input of the LeCroy 1885F ADCs which are mentioned three paragraphs earlier.

The second of the CsI signals coming from LeCroy 429A Logic FI/FO that is set to OR (fed by the LeCroy 3420 CFD) is sent to a LeCroy 429A Logic FI/FO designated with M=1. This signal is sent on to a Rate Divider and divided by a factor of 10. The INHBIT input of the Rate Divider is fed by a LeCroy 429A FI/FO, which is designated master trigger busy. From the Rate Divider, the CsI signal is sent to be terminated in a LeCroy 4434 Scaler via a Lecroy 4616 NIM-ECL module. It is also sent from the Rate Divider to an Ortec GG8010 Octal Gate Generator designated as the downscaled M=1 module. From the Ortec GG8010 Octal Gate Generator, this signal is sent both onto the master trigger OR LeCroy 429A FI/FO module and a Lecroy 2341A 16 Fold Register via an Ortec GG8000 Octal Gate Generator.

The second of the CsI signals coming from LeCroy 429A Logic FI/FO that is set to OR (fed by the LeCroy 3420 CFD) is sent to the START input of a LeCroy 222 Dual Gate Generator. The NIM output of that LeCroy 222 Dual Gate Generator is sent to a LeCroy 429A Logic FI/FO, which is ORed by the trigger busy signal sent by a LeCroy 429A FI/FO seen later in the master trigger logic electronics diagram. The output of the LeCroy 429A Logic FI/FO OR is sent on to a LeCroy 429A Logic FI/FO designated as the CFD VETO module. The signal from the CFD VETO LeCroy 429A Logic FI/FO module is sent back to the LeCroy 3420 CFD VETO input.

In Fig. 13 are shown the signal electronics for the Silicon detectors. The Silicon electronics are shaped by a preamplifier, amplified and then ORed into a signal which is sent on to the master trigger logic and ORed to the CsI signals. This means that a CsI or a Silicon must have been hit in order to get an event. In the NIMROD 200 experimental cave, the Silicon signals come from the detectors and then go into the Yellow Italian

Preamplifiers. Signals from rings two through nine are then sent to Ishington University Shapers and signals from rings ten through thirteen are sent to Orange Quad Shapers. From both types of shapers, the fast signal is sent to a LeCroy 3420 CFD. The OR output of the LeCroy 3420 CFD is sent to a LeCroy 429A Logic FI/FO designated by M=1. From the M=1 FI/FO module, the fast Silicon signals are sent from the experimental cave through the ceiling and up through the floor of the high bay electronics area. The fast signals are then put into a LeCroy 429F Logic FI/FO designated as the Silicon trigger module. From the Silicon trigger FI/FO module, the fast Silicon signal is sent to three places. One signal terminates in a LeCroy 4434 Scaler via a LeCroy 4616 NIM-ECl converter module. Another signal goes through an Ortec GG8000 Octal Gate Generator and then onto a LeCroy 2341A 16 Fold Register. The third signal goes through a Rate Divider which is set to divide by one and then on to the master trigger OR LeCroy 429A FI/FO as well as another LeCroy 2341A 16 Fold Register via an Ortec GG8000 Octal Gate Generator.

The slow component of the Silicon signals are sent from the shapers to a LeCroy 1885F ADC which has a GATE signal set by the master trigger electronics.

In Fig. 14 are shown the master trigger electronics. The master trigger electronics have two main functions, 1) to tigger gates for the ADCs for the CsI and Silicon detectors and 2) to tell the computer when the electronics are busy to give the electronics time to process the data. The master trigger electronics begin with a LeCroy 429A FI/FO which is an OR for the CsI and Silicon signals. From the LeCroy 429A FI/FO, the master trigger signal is sent to both an Ortec 661 Log/Linear Ratemeter and a LeCroy 365AL 4 Fold Logic Unit.

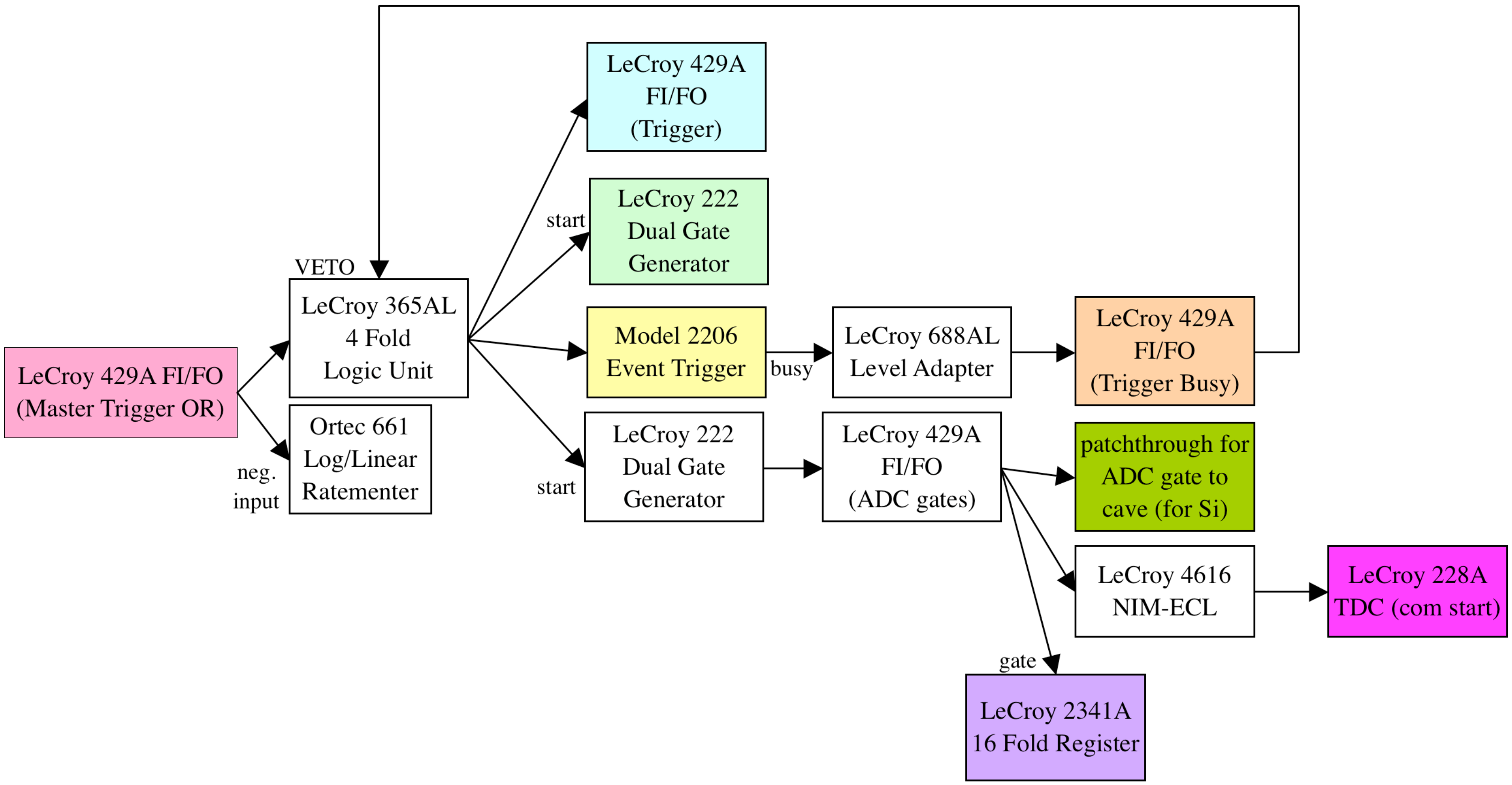

Fig. 14. Master trigger electronics diagram.

The LeCroy 365AL 4 Fold Logic Unit has four outputs. The first output is another LeCroy 429A FI/FO module labeled as Trigger which will serve as a trigger for the Neutron Ball electronics which will be discussed below. The second output from the LeCroy 365Al 4 Fold Logic Unit leads to the start input of a LeCroy 222 Dual Gate Generator which is seen in the top part of Fig. 12. The third output from the LeCroy 365AL 4 Fold Logic Unit leads to a Model 2206 Event Trigger which has a BUSY output leading to a LeCroy 688AL Level Adapter and then to a LeCroy 429A FI/FO labeled Trigger Busy. This LeCroy 429A FI/FO labeled Trigger Busy has a signal which goes back to the VETO input of the LeCroy 365AL 4 Fold Logic Unit.

The fourth output from the LeCroy 365Al 4 Fold Logic Unit goes to the START input of a LeCroy 222 Dual Gate Generator and then on to a LeCroy 429A FI/FO module labeled ADC gates. These are the ADC gates for the Silicon detectors, which are downstairs. The LeCroy 429A FI/FO module labeled ADC gates has three outputs. The first output of the LeCroy 429A FI/FO module goes back down to the experimental cave to set the gate for the Silicon detectors in the LeCroy 1885F ADC seen in Fig. 13. The second output of the LeCroy 429A FI/FO module goes to the START input of a LeCroy 228A TDC via a LeCroy 4616 NIM-ECl level adapter. The signal going to the TDC sets the common start for the TDC in the electronics of the RF. This TDC will be seen later in the figure detailing the RF electronics. The third output from the LeCroy 429A FI/FO module labeled ADC gates goes to the GATE input of a LeCroy 2341A 16 Fold Register. The 16 fold register will be seen again in the diagram for the pulser electronics.

In Fig. 15 are shown the signal electronics for the Neutron Ball detector. The Neutron Ball signals are triggered by the master trigger electronics, which are triggered by an OR between the CsI and Silicon signals. The LeCroy 429A FI/FO from the master trigger electronics in Fig. 14 labeled Trigger begins the Neutron Ball electronics diagram and has two outputs. The first output of the LeCroy 429A FI/FO labeled Trigger leads to an Ortec GG8010 Octal Gate Generator labeled NBL energy. This Ortec GG8010 Octal Gate Generator has a signal which leads to the GATE input of a Phillips 7166 QDC which has 20 signal inputs from feedthroughs from the Neutron Ball in the experimental cave.

The second output of the LeCroy 429A FI/FO labeled Trigger goes to the START input of a LeCroy 222 Dual Gate Generator which leads to another LeCroy 222 Dual Gate Generator whose delayed output goes to another LeCroy 222 Dual Gate Generator and whose NIM output goes to a Phillips 756 Quad 4 Fold Logic Unit. The last LeCroy 222 Dual Gate Generator has a NIM output which also goes to a Phillips 756 Quad 4 Fold Logic Unit.

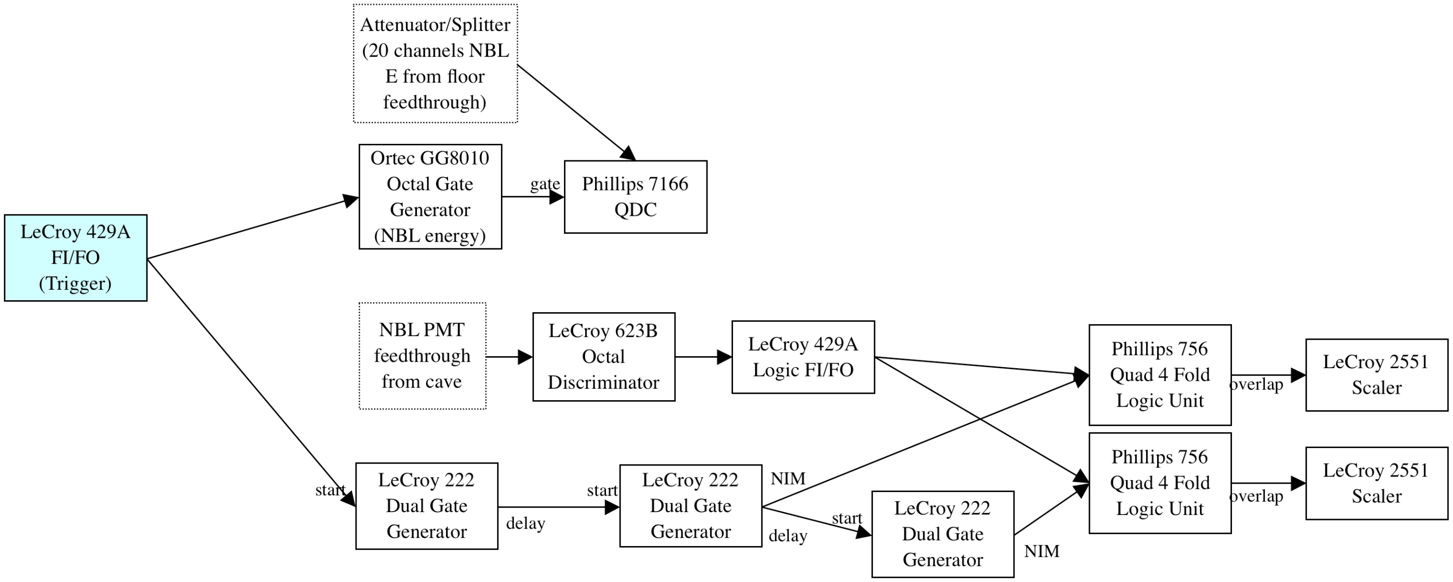

Fig. 15. Electronics diagram from NBL signal to QDC and scalers.

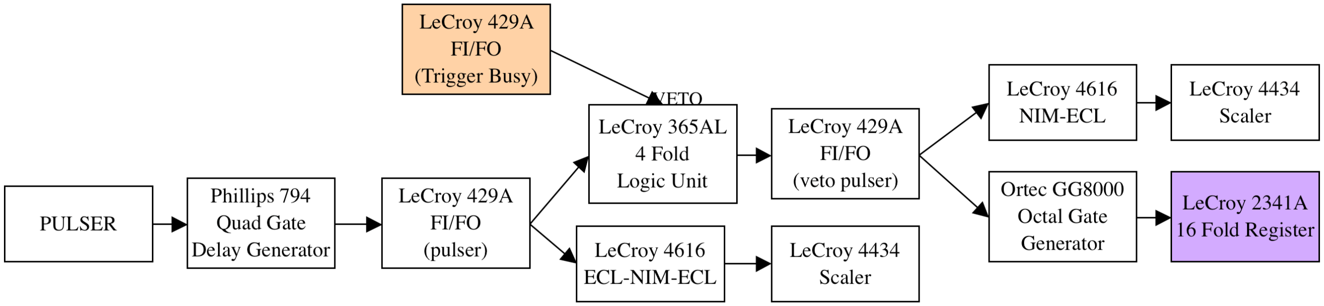

Fig. 16. Electronics diagram from Pulser signal to bit register and scalers.

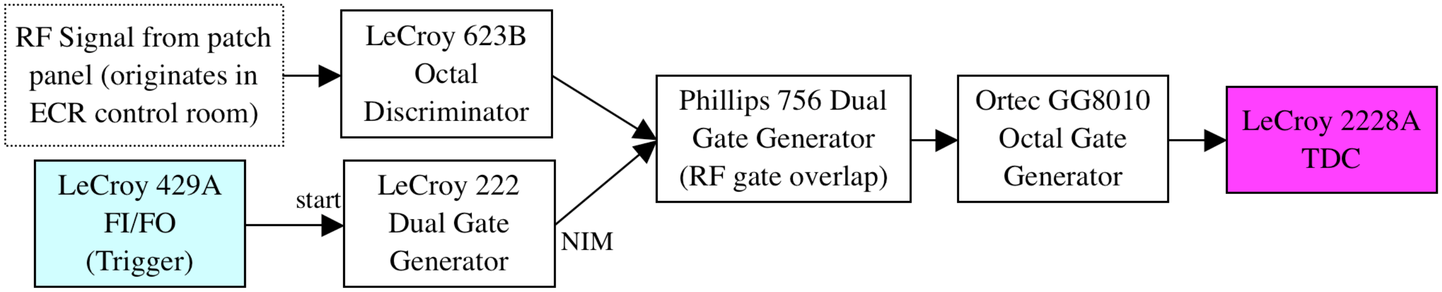

Fig. 17. Electronics diagram from RF signal and trigger to TDC.

The Neutron Ball's photomultiplier tube signals lead from the experimental cave into a LeCroy 623B Octal Discriminator and then into a LeCroy 429A Logic FI/FO that has two outputs. Each of the two outputs go to each of the two Phillips 756 Quad 4 Fold Logic Units. The overlap of the two signals in each of the two Phillips 756 Quad 4 Fold Logic Units lead to a LeCroy 2251 Scaler.

In Fig. 16 are shown the pulser electronics. The pulser event is VETOed by the master trigger electronics BUSY signal. A pulser is put into a Phillips 794 Quad Gate Delay Generator which leads to a LeCroy 429A FI/FO labeled pulser. The LeCroy 429A FI/FO labeled pulser has two outputs. One output of the LeCroy 429A FI/FO labeled pulser leads to a LeCroy 365AL 4 Fold Logic Unit whose VETO input is fed by the LeCroy 429A FI/FO labeled Trigger Busy, as seen in Fig. 14. From the LeCroy 365AL 4 Fold Logic Unit, the signal is sent to a LeCroy 429A FI/FO labeled veto pulser and then on to two places, one is a LeCroy 4434 Scaler (via a LeCroy 4616 NIM-ECL level adapter) and the other is a LeCroy 2341A 16 Fold Register (via an Ortec GG8000 Octal Gate Generator). The second output from the LeCroy 429A FI/FO labeled pulser terminates in a LeCroy 4434 Scaler via a LeCroy 4616 NIM-ECl level adapter.

In Fig. 17 are shown the electronics diagram for signals from the RF of the Cyclotron. The signal for the RF comes from a patch panel and originates in the ECR control room. The RF signal leads to a LeCroy 623B Octal Discriminator and then to a Phillips 756 Dual Gate Generator labeled RF gate overlap. The LeCroy 429A FI/FO labeled Trigger seen in Fig. 14 and Fig. 15 has an output which leads to the START input of a LeCroy 222 Dual Gate Generator. The LeCroy 22 Dual Gate Generator has a NIM output which leads to the Phillips 756 Dual Gate Generator labeled RF gate overlap. The Phillips 756 Dual Gate Generator labeled RF gate overlap leads to an Ortec GG8010 Octal Gate Generator and then to the LeCroy 2228A TDC seen in Fig. 14.

Table 13 lists all modules used in the NIMROD 2000 experiment and their descriptions.

Table 13. Alphabetical list of electronics components used by NIMROD.

Electronics Module	Description
BNC (Berkeley Nucleonics Corporation) Model BH-1 Tail Pulse Generator	The BNC Model BH-1 Tail Pulse Generator [61] is a double-wide NIM module with settings for frequency, delay, rise and fall time, amplitude, single or double pulse, external or internal reference, polarity and attenuator.
BiRa Model 2206 Event Trigger	The Bi Ra Model 2206 Event Trigger [62] is a double-wide CAMAC module 16 channel 32 bit register which stores one bit of event data in each channel from trigger logic sources. The Bi Ra Model 2206 gives a 5 bit binary output representing the highest bit number. There is a double buffer which provides assurance that output data does not change during readout.
GSI CF4000 Quad CFD	GSI CF4000 Quad CFD is a single-wide 4 independent channel NIM module constant fraction discriminator with settings for threshold, width, and delay with one input and two outputs.
LeCroy 1885F ADC	The LeCroy 1885F ADC (Analog to Digital Converter) is 96 channel a fastbus charge analog to digital converter offering a low and high range output [63].
LeCroy 222 Dual Gate Generator	The LeCroy 222 Dual Gate Generator [64] is a single-wide NIM modules which gives a adjustable width prompt or delayed gate for either a TTL or fast NIM input and TTL or NIM (Normal and NIM-bar) outputs. Each of the two channels in the LeCroy 222 Dual Gate Generator has an OR input which can extend the gate and delay interval with external input.
LeCroy 2341A 16 Fold Register	The LeCroy 2341A Coincidence Register [65] is a 16 channel single-wide CAMAC module with standard NIM logic level inputs. The 16 logic Lemo connector input channels which are in coincidence with a common fast gate input are added into an output current proportional to the amount of input signal coming in during the coincidence that can be readout with CAMAC commands. The LeCroy 2341A Coincidence Register has a front panel Lemo connector for CLEAR which answers a negative logic level input.

Table 13. (continued.)

Electronics Module	Description
LeCroy 3420 CFD	The LeCroy 3420 CFD [66] is a single-wide CAMAC module that gives logic pulses when the input signal surpasses the threshold. CFDs take a constant fraction of the input pulse and use it to extract the timing of the output pulse in relation to the input pulse. By taking the constant percentage of the input pulse, jitter due to input signals' differing rise times and amplitudes is avoided.
LeCroy 365AL 4 Fold Logic Unit	The LeCroy 365AL 4 Fold Logic Unit [67] is a single-side NIM module with NIM logic level inputs that give output pulses when inputs meet some preset logical condition such as AND and OR.
LeCroy 428F FI/FO	The LeCroy 428F Linear FI/FO [68] is a single-side NIM module with 4 channels, each of which have 4 bipolar inputs and 4 linear direct-coupled outputs.
LeCroy 429A FI/FO	The LeCroy 429A Logic FI/FO [68] is a single-side NIM module with 4 logic inputs accepting NIM and TTL level signals, 4 normal logic outputs and 2 complementary logic outputs. The LeCroy 429A Logic FI/FO 4 channels can be coupled in groups of two or four to give up to 16 inputs and 24 outputs with the use of a switch on the front panel.
LeCroy 4434 Scaler	The LeCroy 4434 Scaler [69] is a single-wide CAMAC module with 32 channels of 24 bit scalers that expects ECL level inputs. Front panel Lemo connector input commands include LOAD, CLEAR and VETO or INHIBIT. These can also be accessed through the CAMAC DATAWAY. LOAD stops the scalers while transferring the channels' contents to the internal buffers, or latches. CLEAR resets the scaler channels (usually after a LOAD command has been sent.) VETO or INHIBIT rejects scaler data for the duration of the VETO or INHIBIT input signal (usually during data acquisition.)

Table 13. (continued.)

Electronics Module	Description
LeCroy 4448 Coincidence Register	The LeCroy 4448 Coincidence Register [69] is a single-wide CAMAC module with 48 inputs that, when in coincidence with a common fast gate input, give a logical "1" data level which are kept in three 16 bit buffer register groups. The stored data in the buffer is readout with CAMAC commands. The Lemo connector on the front panel labeled CLEAR provides an input which erases all three register memories. One can also send a clear through the CAMAC.
LeCroy 4616 ECL-NIM-ECL	The LeCroy 4616 ECL-NIM-ECL [70] is a single-wide 16 channel NIM module which can both convert ECL to NIM and NIM to ECL. In the first case, three NIM outputs and one ECL output are given for one ECL input. In the second case, one NIM input gives one ECL output. The inputs are direct-coupled.
LeCroy 612A Amplifier	The LeCroy 612A Amplifier [71] is a single-wide 12 channel NIM module with a fixed gain of 10X. Each channel gives a fan out of 2 outputs.
LeCroy 623B Octal Discriminator	The LeCroy 623B Octal Discriminator [72] is a single-wide 8 channel NIM module that delivers a logic pulse when given analog input which exceeds some set threshold. Each channel has 3 NIM level outputs whose widths are adjustable. There is also a common VETO or INHIBIT Lemo connector on the front panel of the LeCroy 623B Octal Discriminator.
LeCroy 688AL Level Adapter	The LeCroy 688AL Level Adapter [73] is a single-wide 8 channel NIM module of both direct-coupled NIM-TTL and TTL-NIM conversions. The NIM-TTL conversion accepts normal or complementary NIM logic level signals. The TTL-NIM conversion accepts standard negative TTL logic level inputs.
Orange Quad Shaper	The Orange Quad Shaper is single-wide 4 independent channel NIM module with pole zero, fine, and coarse gain adjustment, positive or negative signal input and fast and slow signal outputs.

Table 13. (continued.)

Electronics Module	Description
Ortec 661 Log/Linear Ratemeter	The Ortec Model 661 Log/Linear Rate Meter [74] is a single-wide NIM module which give the counting rate of random input pulses. The input signals can be unipolar or bipolar and are accepted if they fall in the range of +150mV to +10V. An adjustable threshold exists for positive inputs and a fixed threshold of -250mV exists for negative inputs.
Ortec AD811 Octal ADC	The Ortec AD811 Octal ADC [75] is a single-wide 8 channel CAMAC module. Given positive unipolar or bipolar signals, the Ortec AD811 Octal ADC measures the peaks when the strobe Lemo connector input on the front panel delivers the start. All 8 channels begin peak conversion upon delivery of the strobe input signal. The width of the conversion gate is adjustable. Upon completion of the conversion gate, a LAM (Look-At-Me) is given and the collected data is held until reset from CAMAC controls. The module can be blocked by the internal busy latch or by a CAMAC INHIBIT signal.
Ortec GG8000/GG8010 Octal Gate Generator	The Ortec GG8000 Octal Gate Generator [76] and the Ortec GG8010 Octal Gate Generator [77] are single-wide 8 channel NIM modules which accept fast negative NIM signals and give an output pulse with an adjustable delay and width. All channels are independent from each other.
Ortec Model RD 2000 Rate Divider	The Ortec Model RD 2000 Dual Fast Rate Divider [78] is a single-wide 2 independent channel NIM module which accepts only fast NIM input signals. The rate of division can be set between 1 and 1000. There is an INHIBIT input on the Ortec Model RD 2000 Dual Fast Rate Divider. Also, there is 1/n output signal whose rate corresponds to the input signal rate divided by the set division factor “n”.
Phillips Model 7164 ADC	The Phillips Model 7164 ADC [79] is a 16 Lemo connector channel CAMAC module with individual pedestal corrections and upper and lower thresholds for each channel. Conversion of analog peak signals to digital signals starts with the Common GATE input. Data is cleared by a front panel CLEAR signal or a CAMAC CLEAR command.

Table 13 (continued.)

Electronics Module	Description
Phillips Model 7164H ADC	The Phillips Model 7164H ADC [79] is similar to the Phillips 7164 ADC except it has ribbon cable header input connections as compared to Lemo input connections.
Phillips Model 7166 QDC	The Phillips Model 7166 QDC (Q/charge to Digital Converter) [80] is a single-wide 16 channel CAMAC module with a common GATE input which begins conversion. The CLEAR front panel input or a CAMAC CLEAR command releases all data in each channel.
Phillips Model 7186 ADC	The Phillips Model 7186 TDC (Time to Digital/amplitude Converter) [81] is a single-wide 16 channel CAMAC module which starts conversion upon receipt of a COMMON input. Data is cleared from the Phillips 7186 TDC via front panel CLEAR signal or through the CAMAC clear command.
Phillips Model 748 Octal Linear FI/FO	The Phillips Model 748 Octal Linear FI/FO [82] is a single-wide 8 channel NIM module with four 1X gain outputs from one input.
Phillips Model 756 Dual Gate Generator	The Phillips Model 756 Dual Gate Generator [83] is a single-wide 4 channel NIM module with direct-coupled AND, OR, FI/FO and anti-coincidence functions with VETO.
Phillips Model 794 Quad Gate Generator	The Phillips Model 794 Quad Gate Generator [84] is a single-wide 4 channel NIM module with NIM and TTL inputs and NIM, TTL and ECL outputs. The module may be trigger by the TRIGGER or OR inputs.
Phillips Model 804 Quad Rotary Attenuator	The Phillips Model 804 Quad Rotary Attenuator [85] is a single-wide 4 channel NIM module attenuator.
Tennelec TC 248 Amplifier	The Tennelec TC 248 Amplifier [86] is a single-wide NIM module signal amplifier with positive or negative input selection, unipolar and bipolar outputs, coarse and fine gain and pole-zero adjustments.

Table 13 (continued.)

Electronics Module	Description
Tennelec TC 454 Quad CFD	The Tennelec TC 454 Quad CFD (Constant Fraction Discriminator) [87] is a single-wide, 4 channel NIM module which receives fast negative input (NIM) signals. Every channel can be adjusted for the fraction used in the discrimination. Delay for the timing signal is to be supplied by using an appropriately long cable across the delay connectors. Also, every channel has its own threshold setting and three separate fast negative (NIM) outputs. One can adjust the width of the output to help prevent false triggering coming from trailing edge noise from pile-up. Inputs on the rear panel give each channel a separate gate from an external signal. The Tennelec TC 454 four channels can be combined in any combination by use of internal switches and controlled by the master BIN gate, which is available on select NIM bins.
Ishington University Shapers	The Ishington University shapers are single-wide 16 channel CAMAC modules with a header input, out put and attenuated output.
Yellow Italian Preamplifier	The yellow Italian preamplifiers are one-half inch wide and half as tall as normal NIM modules with two independent channels per module. Each channel has a HV, input and an output connection. The gain of this preamp is 2 mV/MeV. It is charge sensing. It does not invert the signal.

CHAPTER IV
IMPACT PARAMETER CHARACTERIZATION

The current study is interested in collisions with small impact parameters leading to formation of a compound nucleus. Impact parameter cannot be directly experimentally measured; therefore, experimenters must use the available physical observables which are known to depend on impact parameter to distinguish centrality of collisions. Many studies of impact parameter selection have been conducted [88-97].

It is thought that centrality cuts on two or more observables (multidimensional) are more sensitive to impact parameter than cuts on only one observable (one dimensional) [88]. Care must be taken when choosing observables to include in a two dimensional cut to avoid autocorrelation between the observables. A study [89] details observables strongly correlated with impact parameter that are scrutinized for autocorrelation effects. Autocorrelations may arise from conservation laws of mass, charge and energy and can falsely enhance or suppress observable values obtained from selecting events by centrality. The two variables which are the best choice for centrality selection should closely depend on centrality and should not be autocorrelated. For a basic example of autocorrelation, take the case of centrality cuts in two dimensions of charged particle multiplicity and light charged particle multiplicity. Although the emission of charged particles and light charged particles both strongly depend on impact parameter, light charged particles are a subset of charged. Therefore, these two observables autocorrelate and are not a good choice for two dimensional centrality cuts.

NIMROD data have been two dimensionally cut for centrality in other studies on light charged particle multiplicity and transverse energy of light charged particles [90] and multiplicity of charged particle and neutrons [91]. Neutron and charged particle emission may be good choices for a two dimensional centrality cut because they have both been shown to strongly correlated with impact parameter [92, 93, 94, 95]. A study of joint neutron and charged particle multiplicity discusses the two part distribution seen in charged particle multiplicity versus neutron multiplicity plots [96]. The first part of the ridge changes very little with charged particle multiplicity but increases quickly with neutron multiplicity until a point is reached when the charged particle multiplicity begins to vary along with the neutron multiplicity. Each observable then increases linearly along the second part of the distribution. The first part of the distribution is dominated by neutron emission in lower energy collisions where the Coulomb barrier helps to block charged particle emission. At higher energies, charged particles overcome their Coulomb barrier and are emitted along with neutrons in the collision.

A different study asserts centrality cuts on only charged particles do a better job of selecting for impact parameter than cuts on neutron multiplicity [97]. They show flatter 2 alpha azimuthal correlation functions of the data selected with cuts on multiplicity of charged particles, indicating a more central event selection than do the same functions with data cut on neutron multiplicity.

A way to discern which experimental observable is best used to cut on centrality is to compare experimental results to a model calculation. One could then verify impact parameter distributions in each cut as given by the model calculation output; the cuts leading to the best separation in impact parameter will indicate the better choice. AMD-V [32] is used to simulate the same mass systems of 35 and 45 MeV/nucleon ^{58}Fe on ^{58}Fe, ^{58}Fe on ^{58}Ni, ^{58}Ni on ^{58}Fe and ^{58}Ni on ^{58}Ni. Each AMD-V event is passed through the GEMINI [29] code 100 times to give 100 final de-excited distributions of particles for each AMD-V/GEMINI event calculation. This multiplication of statistics maximizes computational effort while still yielding a stochastic distribution of final event fragment distributions.

A two dimensional cut on centrality using charged particles and neutron multiplicities will be compared to one dimensional centrality cuts on charged particles in both experimental and AMD-V/GEMINI data. The corresponding impact parameter distributions will be shown as a function of centrality cut. The mean value of each impact parameter distribution and its resolution will be charted. The cut leading to the impact parameter distributions with the best resolution will indicate which observable choice is better for the centrality cut.

Seven NIMROD observables related to collision centrality are chosen for their dependence on centrality. They are (1) the multiplicity of charged particles (Mcp), (2) multiplicity of light charged particles (Mlcp), (3) multiplicity of intermediate mass fragments (Mimf), (4) multiplicity of neutrons (Mnb), (5) the midrapidity charge (MRC), (6) the transverse energy (Etrans), and (7) the midrapidity transverse energy (MREtrans). The multiplicity of charged particles is the total number of charged particles detected in all gates during offline analysis. The multiplicity of light charged particles include charged particles with Z<3 and the multiplicity of intermediate charged particles include charged particles with Z>2. The multiplicity of neutrons is given by the neutron ball signal in NIMROD. The midrapidity charge is tallied from the total charge of particles having rapidity values within a gate set around the beam velocity. The gate minimum is 0.5 to 1.5 times the beam rapidity. The transverse energy is obtained from adding up the energy perpendicular to the beam axis of each particle in an event. The midrapidity transverse energy is calculated by adding the energy perpendicular to the beam axis of particles falling inside the midrapidity gate. Each observable listed is dependent on collision centrality; the more central or violent the collision, the higher the value of each observable. The maximum values of each observable correspond to the collisions which have the smallest impact parameter.

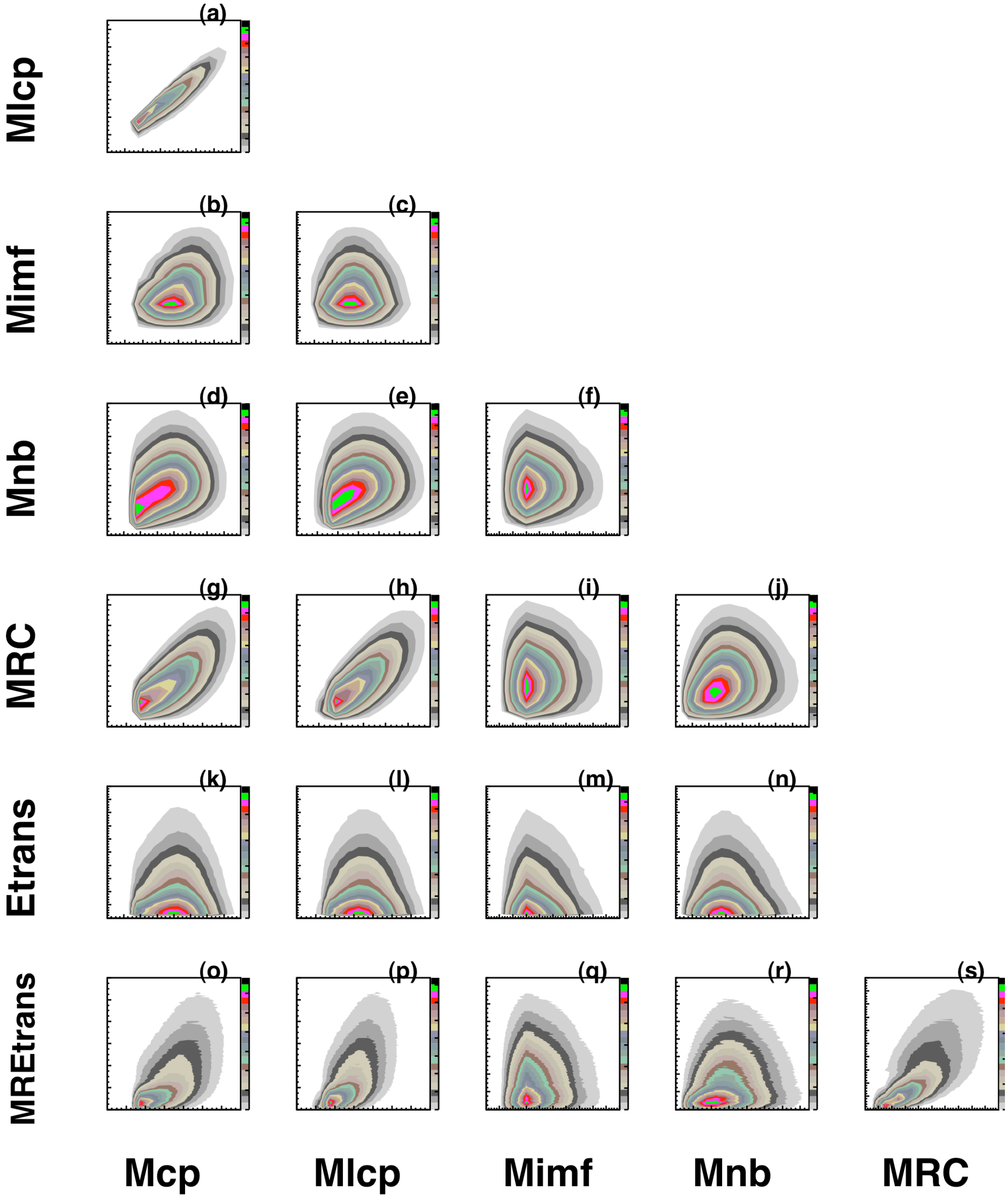

Fig. 18. Correlated two dimensional observables related to centrality in NIMROD data, including the multiplicity of charged particles (Mcp), multiplicity of light charged particles (Mlcp), multiplicity of intermediate mass fragments (Mimf), multiplicity of neutrons (Mnb), the midrapidity charge (MRC), the transverse energy (Etrans), and the midrapidity transverse energy (MREtrans).

Fig. 18 shows seven NIMROD observables for 35 MeV/nucleon ^{58}Fe on ^{58}Fe plotted as functions of one another. The columns, respectively from left to right, show along the x axis the multiplicity of charged particles (Mcp), the multiplicity of light charged particles (Mlcp), multiplicity of intermediate mass fragments (Mimf), the multiplicity of neutrons (Mnb), and the midrapidity charge (MRC). The rows, respectively from top to bottom, show along the y axis Mlcp, Mimf, Mnb, MRC, the transverse energy (Etrans) and the midrapidity transverse energy (MREtrans). The contour colors indicate the z axis and the scales are set arbitrarily. In all plots in Fig. 18, the data shown are taken with a minimum bias trigger (multiplicity CsI detectors hit greater than or equal one.) Observables correlated to centrality in Fig. 18 have increasing trends in both the x and y directions. Of the panels in Fig. 18, the five that show the strongest centrality correlation include the multiplicity of charged particles (Mcp), the multiplicity of light charged particles (Mlcp), multiplicity of neutrons (Mnb), and the mid-rapidity charge (MRC).

Of the two dimensional plots seen in Fig. 18, the plots with good centrality correlation in both x and y throughout the entire range of the data distributions are Mcp vs. Mlcp (a), Mcp vs. Mnb (d), Mlpc vs. Mnb (e), Mcp vs. MRC (g), and Mlcp vs. MRC (h). Of these five panels, now shown in Fig. 19, the first panel is an excellent example of autocorrelation between Mlcp and Mcp and is therefore a poor choice for centrality cut observable. The same is true for the two right-most panels in Fig. 19, although the effect is somewhat diminished. The least autocorrelation is seen in panels labeled (d) and (e). Either choice would be a good choice for the least autocorrelated centrality dependent pair of observables; however Mcp and Mnb, has a slight advantage over Mlcp and Mnb because the range of Mcp is greater than Mlcp. Because there are more combinations of Mcp and Mnb than Mlcp and Mnb, Mcp and Mnb give more flexibility with the placement of the centrality cut.

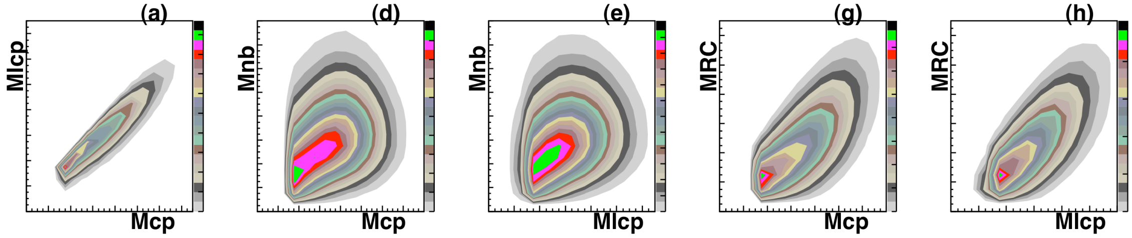

Fig. 19. Correlated two dimensional NIMROD centrality cut observables, including Mcp vs. Mlcp (a), Mcp vs. Mnb (d), Mlcp vs. Mnb (e), Mcp vs. MRC (g), and Mlcp vs. MRC (h).

The two observables used to make two dimensional centrality cuts in the current NIMROD data are Mcp and Mnb. These cuts are made by fitting a line to the ridge of the minimum bias charged particle multiplicity versus multiplicity neutron plots. An example using 35 MeV/nucleon ^{58}Ni on ^{58}Ni data is shown in Fig. 20. The slope of the ridge line is extracted. Then, a value named Mfunction (see Equation 6) is calculated for each event. Mfunction is used to fill a plot of Mfunction versus number of events, shown in Fig. 21.

$$Mfunction = 1.0 * Mnb + slope * Mcp \qquad (6)$$

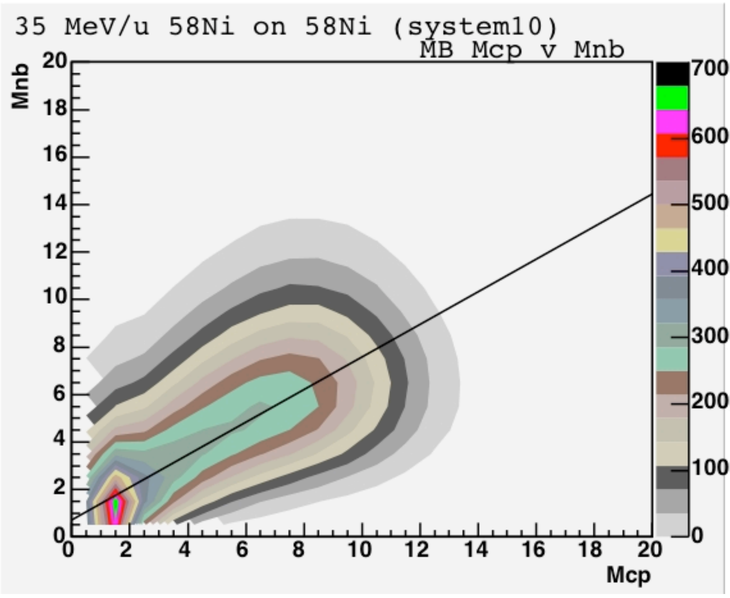

Fig. 20. Mcp versus Mnb for 35 MeV/u ^{58}Ni on ^{58}Ni minimum bias trigger data.

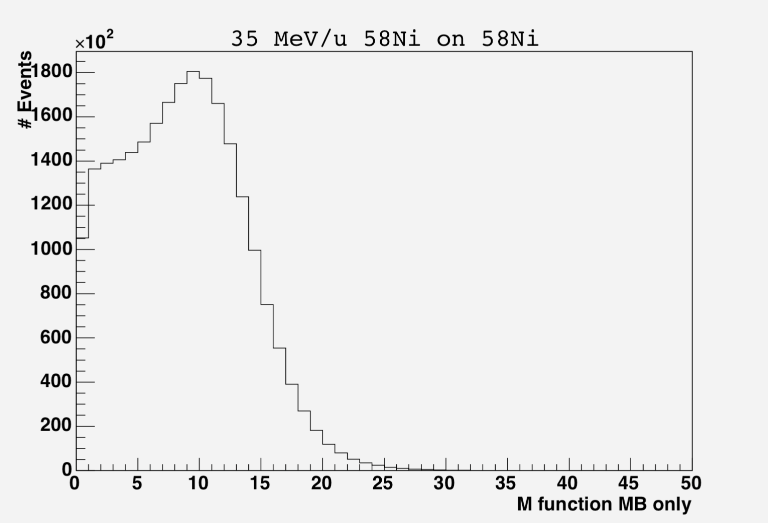

Fig. 21. Mfunction values for 35 MeV/u ^{58}Ni on ^{58}Ni minimum bias trigger data.

A new plot of Mfunction versus percent of events (see Fig. 22) is created in which the first bin is given the value of the first Mfunction bin from Fig. 21. The second bin in the new plot is the sum of the first and second bin of the Mfunction bin. The third bin in the new plot is the sum of the first, second, and third Mfunction bins and so on throughout all Mfunction values. All bins in Fig. 22 are divided by the total number of events to normalize the plot to 1 or 100%.

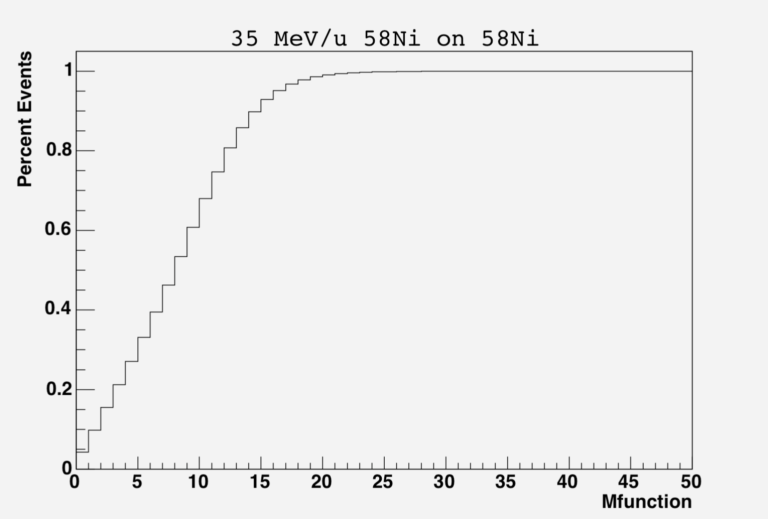

Fig. 22. Mfunction values plotted as a function of percent events for 35 MeV/u ^{58}Ni on ^{58}Ni minimum bias trigger data.

Horizontal lines are drawn on Fig. 22 at 0.9, 0.8, 0.7, 0.6 and 0.5 and the corresponding Mfunction values at the intersection with the distribution line are extracted. See Fig. 23 for an example of the Mfunction cut lines. These Mfunction values represent the centrality cut limits used in StudyPhysicsTreeModule.cxx. One dimensional cuts on charged particle multiplicity are found in an analogous manner as cuts on both charged particle and neutron multiplicities.

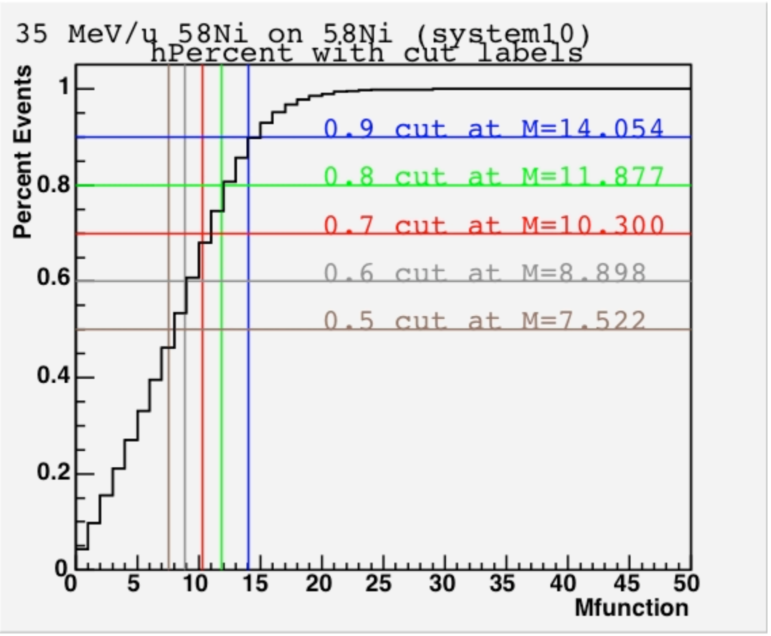

Fig. 23. Mfunction values versus percent events with cut lines overlaid for 35 MeV/u ^{58}Ni on ^{58}Ni minimum bias trigger data.

Experimental data from three systems did not include a minimum bias trigger. The systems missing minimum bias data are ^{58}Fe on ^{58}Fe, ^{58}Fe on ^{58}Ni and ^{58}Fe on ^{54}Fe, all at 35 MeV/nucleon. To make the two dimensional centrality cut, one needs the slope of the ridge of the charged particle versus neutron multiplicities' minimum bias distribution. To make the one dimensional cut, minimum bias charged particle multiplicity distribution is needed. Cut values which correspond to five 10% most central increments (10%, 20%, 30%, 40% and 50% most central) are needed for each type of cut, as well. Therefore, estimates for the slope of the ridge on the Mnb versus Mcp and Mfunction cut values for two dimensional cuts and Mcp cut values for one dimensional cuts must be made using the data from systems at the same projectile energy having minimum bias data.

Seen in Fig. 24 is the slope of the ridge on Mnb versus Mcp distribution plotted as a function of the composite system's N/Z ratio for measured and extrapolated data. The systems used to estimate cut values for data lacking a minimum bias trigger are ^{58}Fe on

^{58}Fe, ^{58}Ni on ^{58}Fe, ^{58}Ni on ^{58}Ni and ^{58}Ni on ^{64}Ni, all at 35 MeV/nucleon. These systems are shown as closed triangles in Fig. 24. The systems lacking minimum bias data are ^{58}Fe on ^{54}Fe, ^{58}Fe on ^{58}Ni and ^{58}Fe on ^{58}Fe, all at 35 MeV/nucleon. These systems are shown as open squares in Fig. 24. A linear fit is used to interpolate the ridge of the Mnb vs. Mcp slope for the systems of 35 MeV/nucleon ^{58}Fe on ^{58}Ni and 35 MeV/nucleon ^{58}Fe on ^{54}Fe. A polynomial fit is used to extrapolate the ridge slope values for the system of 35 MeV/nucleon ^{58}Fe on ^{58}Fe because a slight curve is seen in the Mcp vs. Mnb ridge slope vales for the three systems of 35 MeV/nucleon ^{58}Ni on ^{58}Ni, 35 MeV/nucleon ^{58}Ni on ^{58}Fe, and 35 MeV/nucleon ^{58}Ni on ^{64}Ni. The polynomial fit is shown in Fig. 24 as a dotted line. The differences between the interpolated slopes from the linear fit and the interpolated slopes from the polynomial fit for the systems of 35 MeV/nucleon ^{58}Fe on ^{58}Ni and 35 MeV/nucleon ^{58}Fe on ^{54}Fe are 0.6 and 0.4 %, respectively.

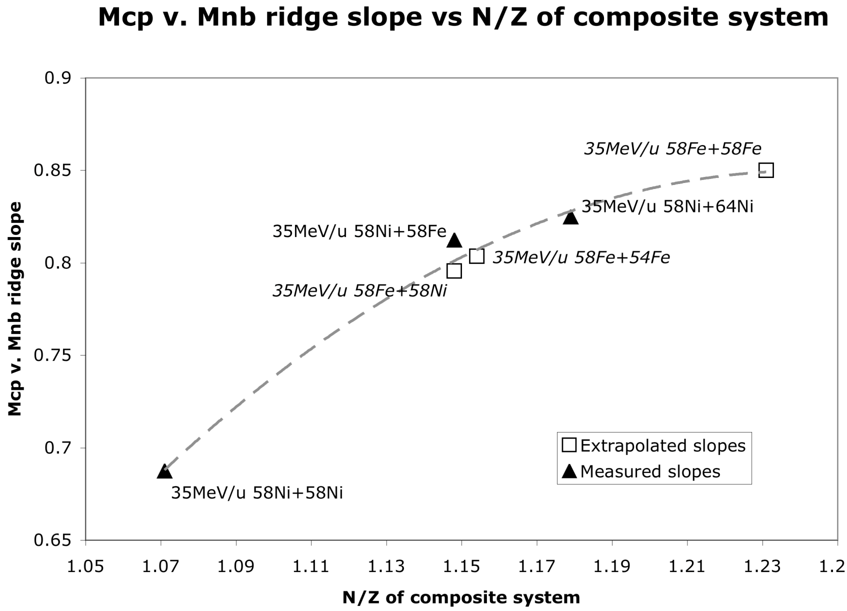

Fig. 24. Slope of ridge on Mnb versus Mcp distribution plotted as a function of the N/Z of the composite system for the experimental data points of systems 35 MeV/u ^{58}Ni on ^{58}Ni, ^{58}Ni on ^{58}Fe, and ^{58}Ni on ^{64}Ni, for the interpolated data points of systems 35MeV/u ^{58}Fe on ^{58}Ni and ^{58}Fe on ^{54}Fe, and for the extrapolated data point of system 35 MeV/u ^{58}Fe on ^{58}Fe.

In Fig. 25 is seen Mfunction values plotted as a function of the composite system N/Z ratio for measured and extrapolated data. Measured data are filled in symbols and extrapolated data are empty symbols. The Mfunction values from the same three systems with minimum bias data listed as seen in Fig. 24 are linearly fit. Then, that linear fit is extrapolated to obtain Mfunction values for the three systems without minimum bias data.

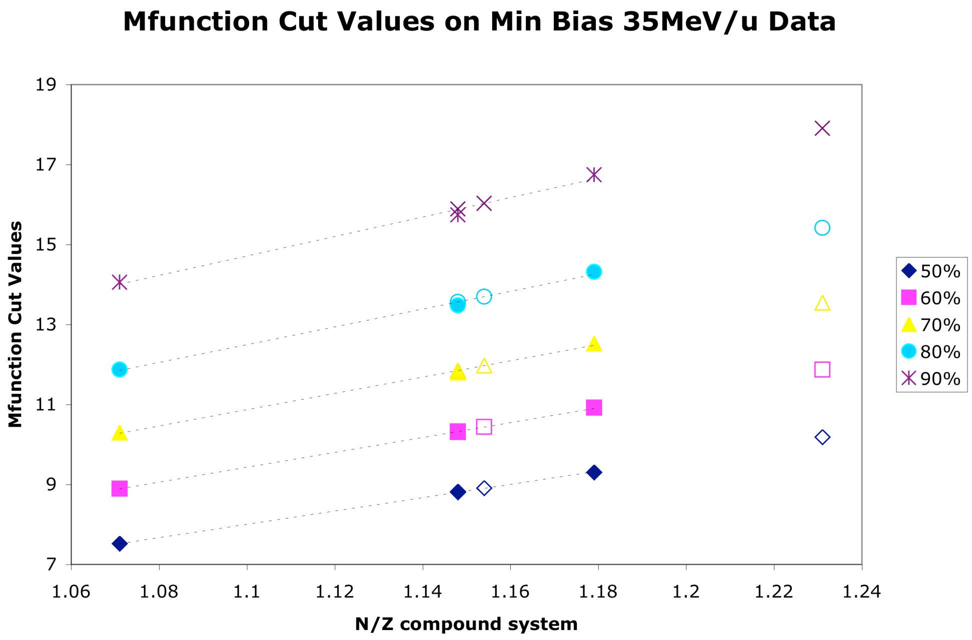

Fig. 25. Mfunction measured (solid), interpolated and extrapolated (empty) values plotted as a function of the N/Z of the combined system.

Shown in Fig. 26 are values for cuts on Mcp plotted as function of the N/Z ratio of the composite system for measured and extrapolated data. Values for Mcp cuts are extrapolated in the same fashion as values for Mcp versus Mnb cuts.

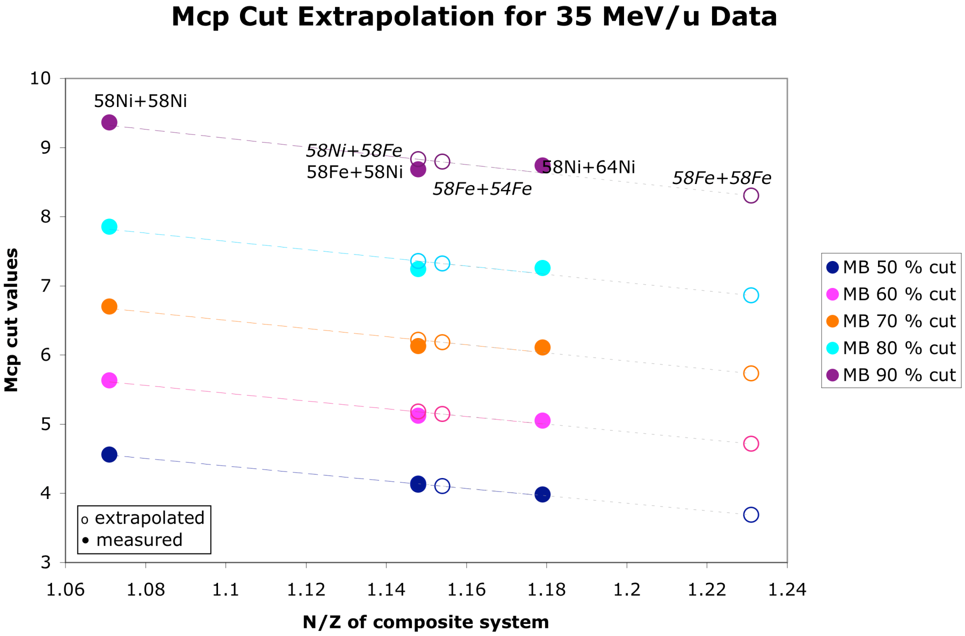

Fig. 26. Mcp measured (solid), interpolated and extrapolated (empty) values plotted as a function of the N/Z of the combined system.

The AMD-V/GEMINI data needs to be normalized and filtered before being directly compared to experimental data. All AMD-V/GEMINI data shown are passed through a filter which takes into account detector efficiency, angular coverage and detector thresholds. The number of AMD-V/GEMINI events simulated for each impact parameter value when plotted as a function of impact parameter has a sharp discontinuity at b = 3 fm that is explained as follows. The events with impact parameter of 3 or less are of the most interest in this study, therefore the most computational time and effort are put into events in that range. Fig. 27 shows all systems' events simulated by AMD-V/GEMINI plotted as a function of impact parameter.

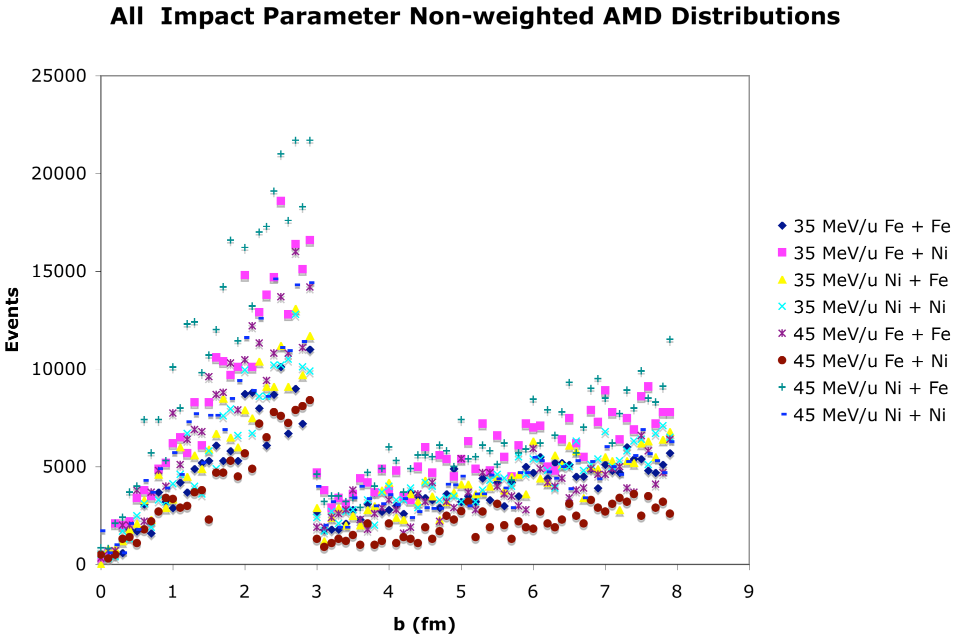

Fig. 27. Number of AMD-V/GEMINI events actually computed versus the impact parameter distributions.

To mimic a geometric impact parameter distribution which reproduces a minimum bias trigger experimental data distribution in centrality, the discontinuous data is scaled to become a continuous distribution. The slope of both segments of the impact parameter distribution are calculated as $m_{0\text{-}3}$ and $m_{3\text{-}8}$. Each event in the range of 3 fm to 8 fm is entered the number of times matching the ratio of the two slopes, $m_{0\text{-}3}/m_{3\text{-}8}$, to remove the discontinuity. The discontinuity may also be removed by taking the inverse ratio of the slopes and diving the events in the lower range by that ratio. See Fig. 28 for each system's events simulated by AMD-V/GEMINI plotted as a function of impact parameter. The discontinuity at b = 3 fm in Fig. 27 is no longer seen because the events from b = 3 fm to b = 8 fm have been weighted (scaled up).

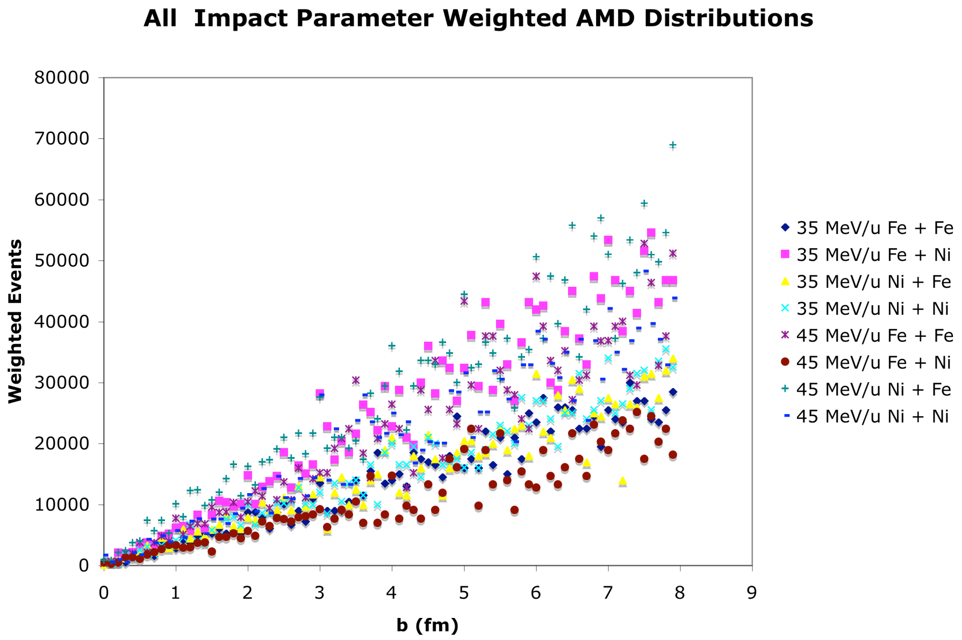

Fig. 28. Scaled number of AMD-V/GEMINI events versus the impact parameter distributions.

In Fig. 29, from top to bottom, experimental and AMD-V/GEMINI data are shown from 35 MeV/nucleon ^{58}Fe on ^{58}Fe, ^{58}Fe on ^{58}Ni, ^{58}Ni on ^{58}Fe and ^{58}Ni on ^{58}Ni systems. From left to right are shown the experimental minimum bias Mcp versus Mnb with ridge slope line and the five centrality cuts overlaid in the first column. In the second column, the AMD-V/GEMINI filtered and weighted data is shown with its ridge slope line coupled with cut lines corresponding to experimental cut values. Lastly, in the rightmost column is shown the total weighted impact parameter distribution for the AMD-V/GEMINI data along with impact parameter distribution for each centrality cut. The color key for the cut lines is seen in the first column panels in Fig. 29. The two top rows are systems missing minimum bias experimental data (35 MeV/nucleon ^{58}Fe on ^{58}Fe, ^{58}Fe on ^{58}Ni) and have cut lines assigned from extrapolated values.

In Fig. 30, from top to bottom, data are shown from 45 MeV/nucleon ^{58}Fe on ^{58}Fe, ^{58}Fe on ^{58}Ni, ^{58}Ni on ^{58}Fe and ^{58}Ni on ^{58}Ni. From left to right are shown the experimental minimum bias Mcp versus Mnb with ridge slope line and the five centrality cuts overlaid in the first column. In the second column, the AMD-V/GEMINI filtered and weighted data with its ridge slope line coupled with cut lines corresponding to experimental cut values. Lastly, in the rightmost column is shown the total weighted impact parameter distribution for the AMD-V/GEMINI data along with impact parameter distribution for each centrality cut. The color key for the cut lines is seen in the first column panels.

In Fig. 31, from top to bottom, data are shown from 35 MeV/nucleon ^{58}Fe on ^{58}Fe, ^{58}Fe on ^{58}Ni, ^{58}Ni on ^{58}Fe and ^{58}Ni on ^{58}Ni. From left to right are shown the experimental minimum bias Mcp distributions with the five centrality cuts overlaid in the first column. In the second column, the AMD-V/GEMINI filtered and weighted data with cut lines corresponding to experimental Mcp cut values. Lastly, in the rightmost column is shown the total weighted impact parameter distribution for the AMD-V/GEMINI data along with impact parameter distribution for each centrality cut. The color key for the cut lines is seen in the first column panels. The two top rows are systems missing minimum bias experimental data (35 MeV/nucleon ^{58}Fe on ^{58}Fe, ^{58}Fe on ^{58}Ni) and have cut lines assigned from extrapolated values. The Mcp from the AMD-V/GEMINI have shifted to higher values relative to the data due to the focus of computational time on events with $b<=3$ fm.

In Fig. 32, from top to bottom, data are shown from 45 MeV/nucleon ^{58}Fe on ^{58}Fe, ^{58}Fe on ^{58}Ni, ^{58}Ni on ^{58}Fe and ^{58}Ni on ^{58}Ni. From left to right are shown the experimental minimum bias Mcp distributions with the five centrality cuts overlaid in the first column. In the second column, the AMD-V/GEMINI filtered and weighted data with cut lines corresponding to experimental Mcp cut values. Lastly, in the rightmost column is shown the total weighted impact parameter distribution for the AMD-V/GEMINI data along with impact parameter distribution for each centrality cut. The color key for the cut lines is seen in the first column panels. Again, the Mcp from the AMD-V/GEMINI have shifted to higher values relative to the data due to the focus of computational time on events with $b<=3$ fm.

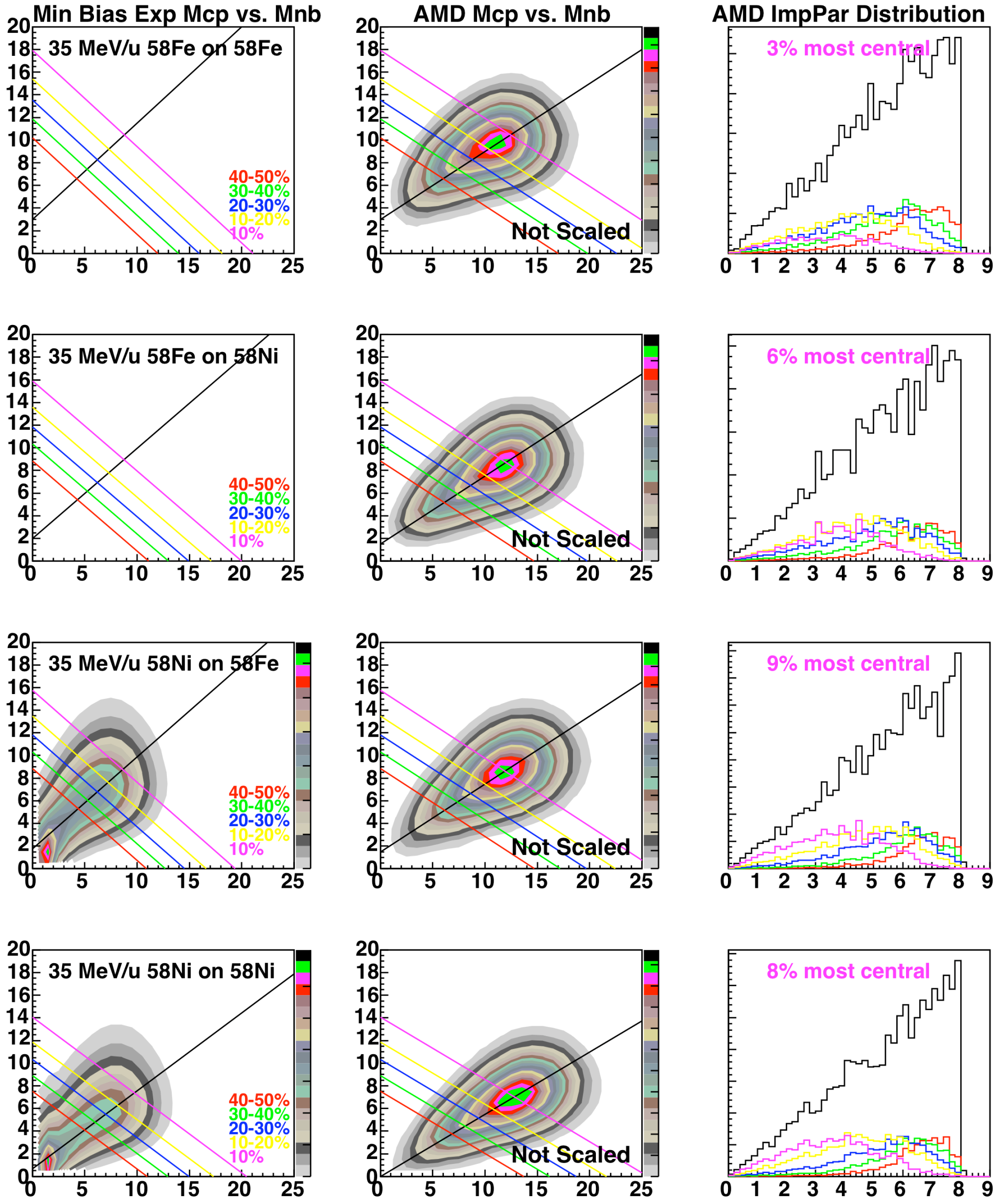

Fig. 29. Unscaled Mcp vs. Mnb plots for experimental data with centrality cuts overlaid (first column), AMD-V/GEMINI Mcp vs. Mnb plots with centrality cuts overlaid (second column) and AMD-V/GEMINI impact parameter distributions (third column) broken up by centrality cut for 35 MeV/nucleon ^{58}Fe on ^{58}Fe (first row), ^{58}Fe on ^{58}Ni (second row), ^{58}Ni on ^{58}Fe (third row), and ^{58}Ni on ^{58}Ni (bottom row).

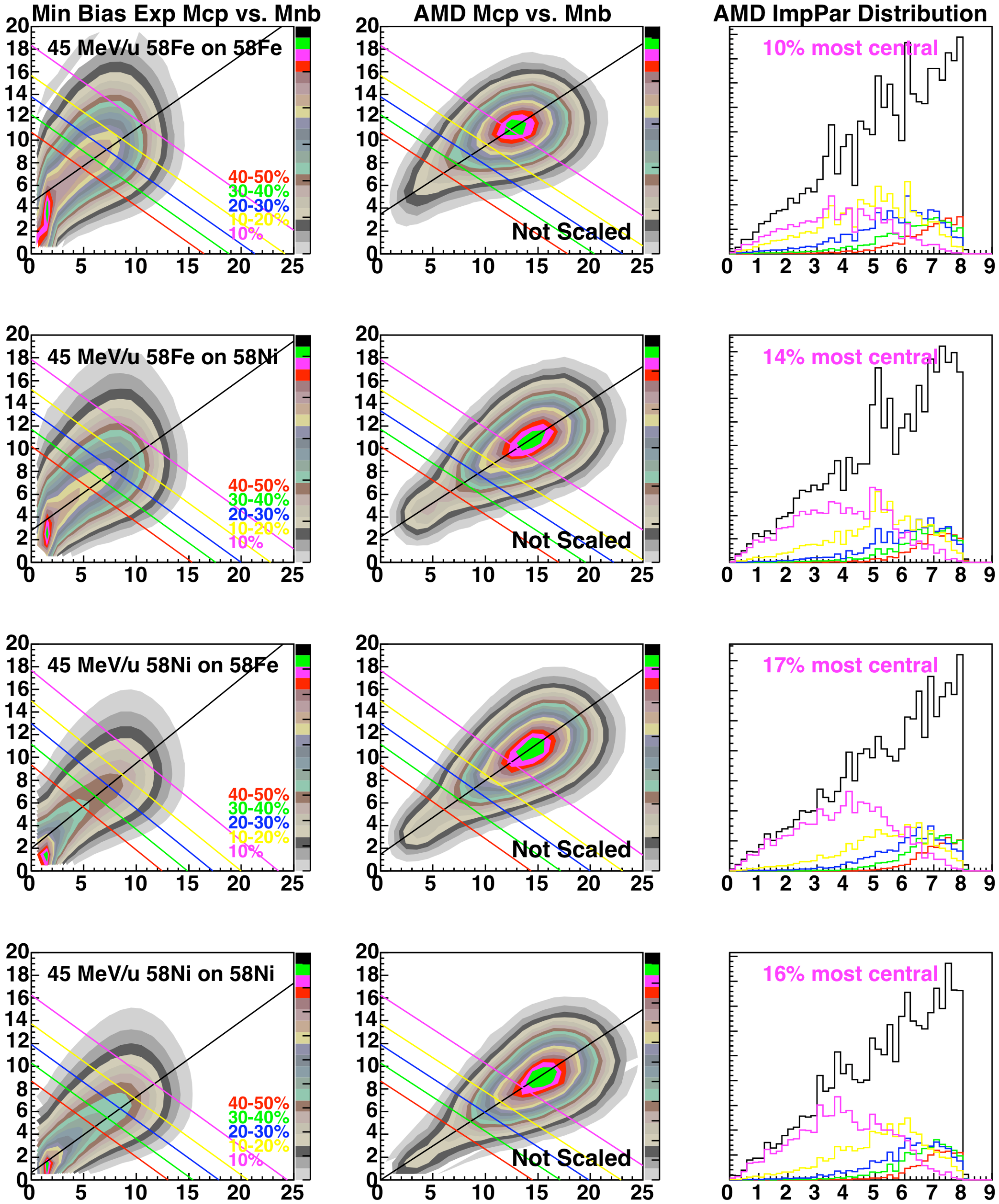

Fig. 30. Unscaled Mcp vs. Mnb plots for experimental data with centrality cuts overlaid (first column), AMD-V/GEMINI Mcp vs. Mnb plots with centrality cuts overlaid (second column) and AMD-V/GEMINI impact parameter distributions (third column) broken up by centrality cut for 45 MeV/nucleon ^{58}Fe on ^{58}Fe (first row), ^{58}Fe on ^{58}Ni (second row), ^{58}Ni on ^{58}Fe (third row), and ^{58}Ni on ^{58}Ni (bottom row).

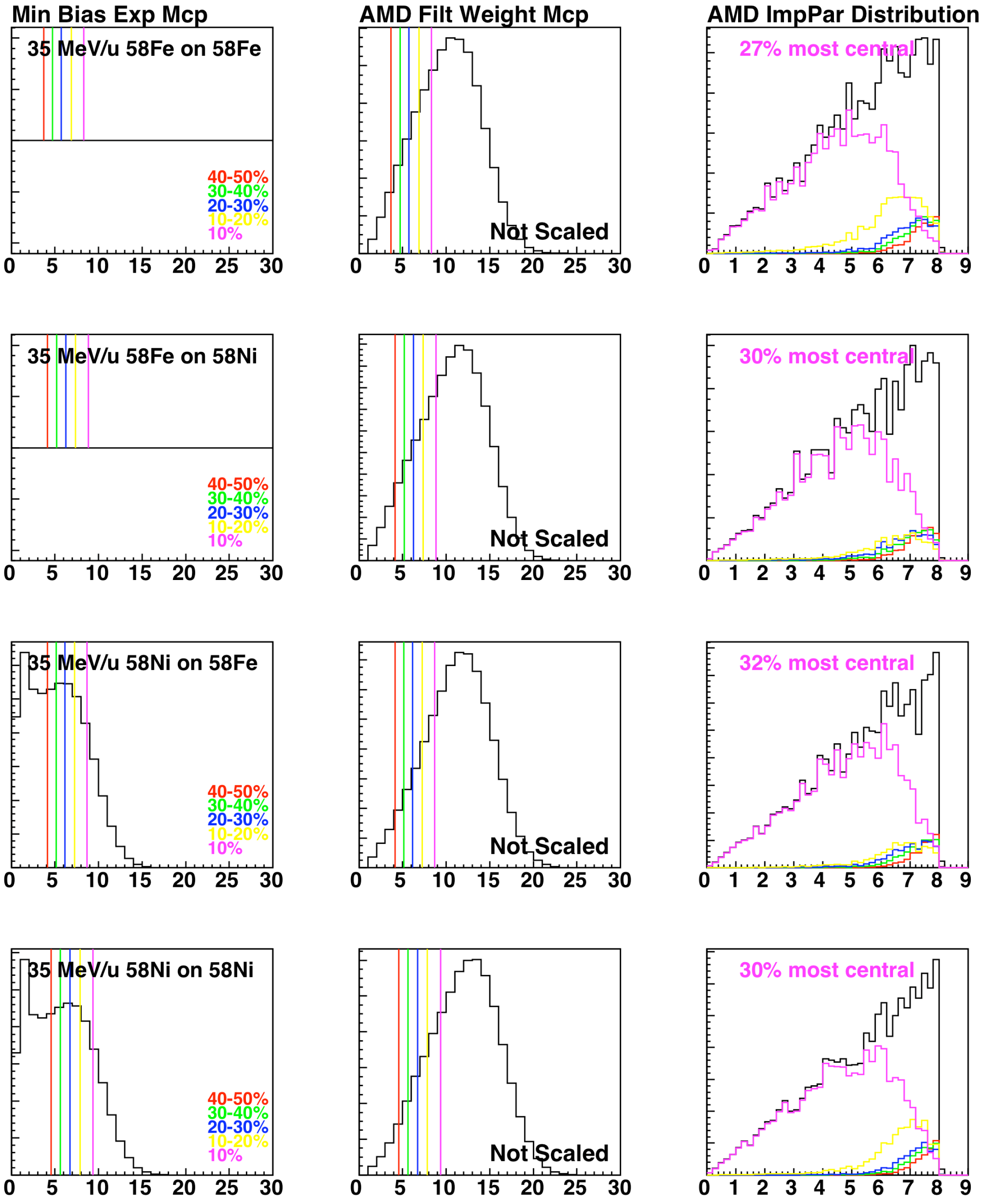

Fig. 31. Unscaled Mcp plots for experimental data with centrality cuts overlaid (first column), AMD-V/GEMINI Mcp plots with centrality cuts overlaid (second column) and AMD-V/GEMINI impact parameter distributions (third column) broken up by centrality cut for 35 MeV/nucleon ^{58}Fe on ^{58}Fe (first row), ^{58}Fe on ^{58}Ni (second row), ^{58}Ni on ^{58}Fe (third row), and ^{58}Ni on ^{58}Ni (bottom row).

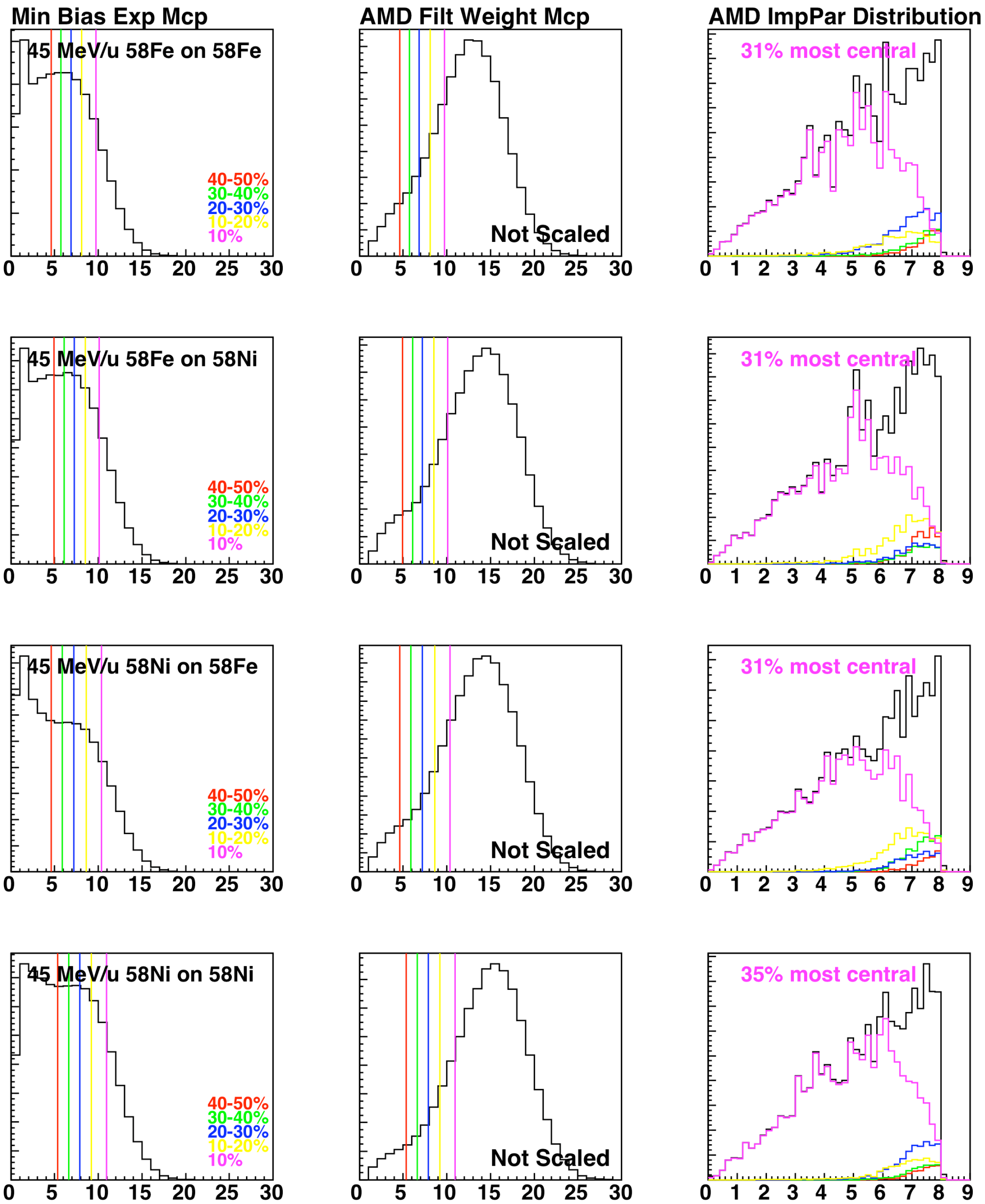

Fig. 32. Unscaled Mcp plots for experimental data with centrality cuts overlaid (first column), AMD-V/GEMINI Mcp plots with centrality cuts overlaid (second column) and AMD-V/GEMINI impact parameter distributions (third column) broken up by centrality cut for 45 MeV/nucleon ^{58}Fe on ^{58}Fe (first row), ^{58}Fe on ^{58}Ni (second row), ^{58}Ni on ^{58}Fe (third row), and ^{58}Ni on ^{58}Ni (bottom row).

In Fig. 30 is shown the same type of data as Fig. 29, but for the 45 MeV/nucleon systems. Fig. 31 and Fig. 32 are analogous to Fig. 29 and Fig. 30 , but with one dimensional centrality cuts on charged particles. In all four figures, the number of events in the most central cut of the AMD-V/GEMINI data are used to calculate the percent centrality of that cut. Before the percentage of total AMD-V/GEMINI geometrically distributed events could be calculated, the total number of events in an impact parameter distribution which reached the touching sphere radius of the projectile and target must be calculated. The touching sphere radius for two A=58 nuclei is given by Equation 7.

$$r = r_o * A^{1/3} \approx 1.5\,fm * 58^{1/3} \approx 11.6\,fm \tag{7}$$

The AMD-V/GEMINI data are run for events up to an impact parameter of 8 fm because peripheral events are of little interest. By calculating the area of a triangle with height equal to the number of events in the weighted impact parameter distribution and a base of 8 fm and a triangle of height equal to a linear projection of the first triangle to 12 fm and a base of 12 fm and dividing the two, one finds that the number of events in each systems' AMD-V/GEMINI impact parameter distribution to 8 fm is equal to about 44.45% of the total events if the AMD-V/GEMINI data are calculated to 12 fm. See Fig. 33 for an example of how the percentage is calculated. In Fig. 33, AMD-V/GEMINI data for 35 MeV/nucleon 58Fe on 58Fe are shown by the diamond points. The hypotenuse of the triangle is a linear fit to the data points which extends out to 12 fm. The area of triangle (a) is 44.45% the size of areas (a) and (b) together.

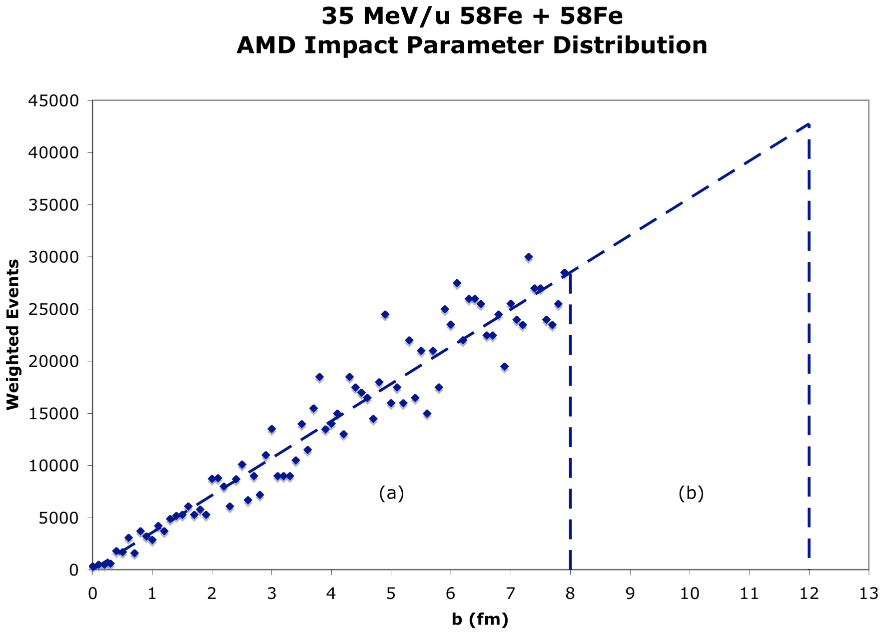

Fig. 33. 35 MeV/nucleon ^{58}Fe on ^{58}Fe AMD-V/GEMINI impact parameter distribution extrapolated from a range of 8 fm to a range of 12 fm.

The number of AMD-V/GEMINI events as a percentage of total AMD-V/GEMINI events extrapolated to 12 fm in the most central cut in Fig. 29 through Fig. 32 are not equal to 10%, which would match the experimental percentage of events for the same centrality cut. In Table 14 are shown the percentage events of the number of AMD-V/GEMINI events in the most central cut of the total number of events in a 12 fm distribution. The desired value is 10% in all cases. The Mcp and Mnb two dimensional centrality cuts on the AMD-V/GEMINI data are much closer to the desired value than are the one dimensionally Mcp cut data.

Table 14. The percentage of AMD-V/GEMINI events in the most central cut, unshifted.

System	% events in most central AMD-V Mcp v. Mnb cut	% events in most central AMD-V Mcp cut
35 MeV/u 58Fe on 58Fe	3	27
35 MeV/u 58Fe on 58Ni	6	30
35 MeV/u 58Ni on 58Fe	9	32
35 MeV/u 58Ni on 58Ni	8	30
45 MeV/u 58Fe on 58Fe	10	31
45 MeV/u 58Fe on 58Ni	14	31
45 MeV/u 58Ni on 58Fe	17	31
45 MeV/u 58Ni on 58Ni	16	35

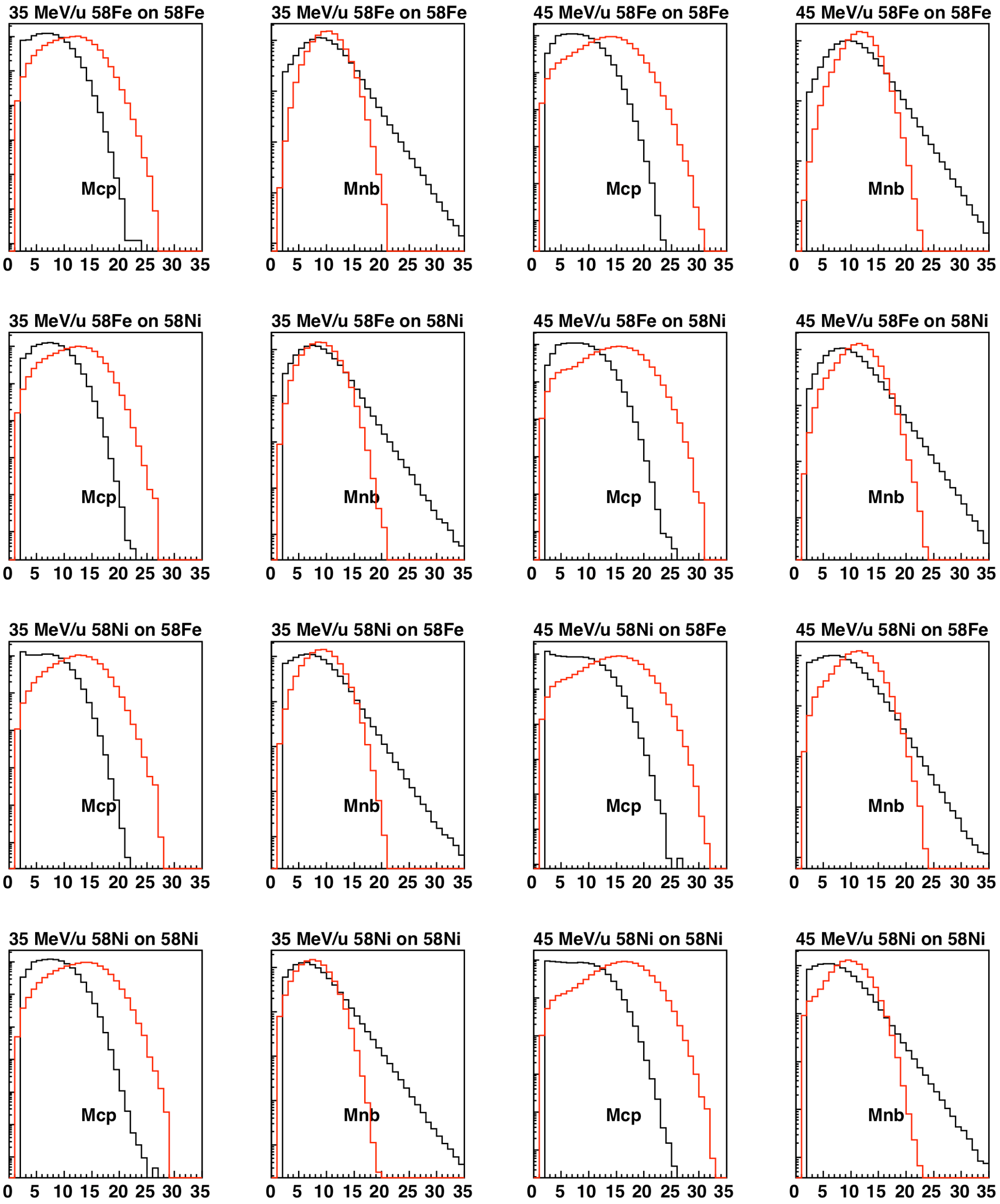

Fig. 34. Experimental (black) and AMD-V/GEMINI (red) Mcp and Mnb one dimensional distributions for 35 (first and second columns) and 45 (third and fourth columns) MeV/nucleon ^{58}Fe on ^{58}Fe (first row), ^{58}Fe on ^{58}Ni (second row), ^{58}Ni on ^{58}Fe (third row), and ^{58}Ni on ^{58}Ni (fourth row).

AMD-V/GEMINI under-predicts neutron emission and over-predicts charged particle production. Therefore, the percent centrality for AMD-V/GEMINI data cut with experimental cut values (Mfunction or Mcp) is not equal to percent centrality for experimental data cut with experimental cut values. See Fig. 34 for overlaid experimental and AMD-V/GEMINI Mcp and Mnb distributions. In Fig. 34, from top to bottom, data shown are from the following systems: ^{58}Fe on ^{58}Fe, ^{58}Fe on ^{58}Ni, ^{58}Ni on ^{58}Fe and ^{58}Ni on ^{58}Ni. In the first and second columns are 35 MeV/nucleon systems experimental (black) and AMD-V/GEMINI (red) Mcp (first column) and Mnb (second column) distributions. In the third and fourth columns are 45 MeV/nucleon systems experimental (black) and AMD-V/GEMINI (red) Mcp (third column) and Mnb (fourth column) distributions. To allow for the discrepancy in neutron and charged particle emission between AMD-V/GEMINI and experimental data, the AMD-V/GEMINI centrality cuts are scaled so that the number of events included in the most central cut is a close as possible to 10%. All of the simulation data's Mfunction values are scaled by the same multiplication factor until the 10% most central cut included 10% of the simulation data. The exact value of 10% is achieved for the two dimensionally cut data, but not for the Mcp cut data due to the fact that the Mfunction cuts are non-integer cuts and the Mcp cuts are integer value cuts (one cannot cut on a fraction of a charged particle, but one can cut on a fraction of a mixture of neutrons and charged particles).

In each system, the AMD-V/GEMINI data cuts are scaled to come as close as possible to matching the 10% value achieved in the experimental data cuts, by adjusting the Mfunction cut values accordingly. See Table 15 for the list of scale factors and scaled percentages for the most central cut for AMD-V/GEMINI systems. In Table 15, are shown scale factors and scaled percentage of events of the number of AMD-V/GEMINI events in the most central cut of the total number of events in a 12 fm distribution. The desired value is 10% in all cases. In order to achieve the desired 10% value in the two dimensionally cut data, scaling of a factor of up to 11% is needed. The scaling factor necessary to put the one dimensionally cut data varied between 50% and 60%.

Table 15. The percentage of scaled AMD-V/GEMINI events in the most central cut, shifted.

System	Mcp v. Mnb cut scale factor	Mcp v. Mnb cut %	Mcp cut scale factor	Mcp cut %
35 MeV/u 58Fe on 58Fe	.89	10	1.5	10
35 MeV/u 58Fe on 58Ni	.94	10	1.5	9
35 MeV/u 58Ni on 58Fe	.98	10	1.5	11
35 MeV/u 58Ni on 58Ni	.98	10	1.5	10
45 MeV/u 58Fe on 58Fe	1	10	1.5	11
45 MeV/u 58Fe on 58Ni	1.06	10	1.6	9
45 MeV/u 58Ni on 58Fe	.92	10	1.6	9
45 MeV/u 58Ni on 58Ni	1.09	10	1.6	10

The data cut on Mcp only does not allow a range of cut values which exactly correspond to 10% of the data. Each unit of charged particle multiplicity added into the most central cut does not correspond to the same % events added for all systems. Only in the application of a two dimensional cut can one tune in the exact percentage of 10% most central in cutting all of the data. A much larger mass system may give an event distribution which allows for more precise one dimensional cuts on Mcp that are identical in % centrality across all systems. However, for these systems of A=58, the two dimensional cut on Mcp and Mnb allows for comparison of equal centrality among all systems and one dimensional cuts on Mcp do not. Fig. 35 through Fig. 38 show the same data as Fig. 29 through Fig. 32, but now the AMD-V/GEMINI cut values are scaled to yield as close as possible to 10% of the total events in the most central cut.

In Fig. 35, from top to bottom, data are shown from 35 MeV/nucleon ^{58}Fe on ^{58}Fe, ^{58}Fe on ^{58}Ni, ^{58}Ni on ^{58}Fe and ^{58}Ni on ^{58}Ni. From left to right are shown the experimental minimum bias Mcp versus Mnb with ridge slope line and the five centrality cuts overlaid in the first column. In the second column, the AMD-V/GEMINI filtered and weighted data with its ridge slope line coupled with cut lines corresponding to experimental cut values scaled to contain the 10% most central events in the most central cut. Lastly, in the rightmost column is shown the total weighted impact parameter distribution for the AMD-V/GEMINI data along with impact parameter distribution for each centrality cut. The color key for the cut lines is seen in the first column panels. The two top rows are systems missing minimum bias experimental data (35 MeV/nucleon ^{58}Fe on ^{58}Fe, ^{58}Fe on ^{58}Ni) and have cut lines assigned from extrapolated values.

In Fig. 36, from top to bottom, data are shown from 45 MeV/nucleon ^{58}Fe on ^{58}Fe, ^{58}Fe on ^{58}Ni, ^{58}Ni on ^{58}Fe and ^{58}Ni on ^{58}Ni. From left to right are shown the experimental minimum bias Mcp versus Mnb with ridge slope line and the five centrality cuts overlaid in the first column. In the second column, the AMD-V/GEMINI filtered and weighted data with its ridge slope line coupled with cut lines corresponding to experimental cut values scaled to contain the 10% most central events in the most central cut. Lastly, in the rightmost column is shown the total weighted impact parameter distribution for the AMD-V/GEMINI data along with impact parameter distribution for each centrality cut. The color key for the cut lines is seen in the first column panels.

In Fig. 37, from top to bottom, data are shown from 35 MeV/nucleon ^{58}Fe on ^{58}Fe, ^{58}Fe on ^{58}Ni, ^{58}Ni on ^{58}Fe and ^{58}Ni on ^{58}Ni. From left to right are shown the experimental minimum bias Mcp distributions with the five centrality cuts overlaid in the first column. In the second column, the AMD-V/GEMINI filtered and weighted data with cut lines corresponding to experimental cut values scaled to contain as close as possible to the 10% most central events in the most central cut. Lastly, in the rightmost column is shown the total weighted impact parameter distribution for the AMD-V/GEMINI data along with impact parameter distribution for each centrality cut. The color key for the cut lines is seen in the first column panels. The two top rows are systems missing minimum bias experimental data (35 MeV/nucleon ^{58}Fe on ^{58}Fe, ^{58}Fe on ^{58}Ni) and have cut lines assigned from extrapolated values.

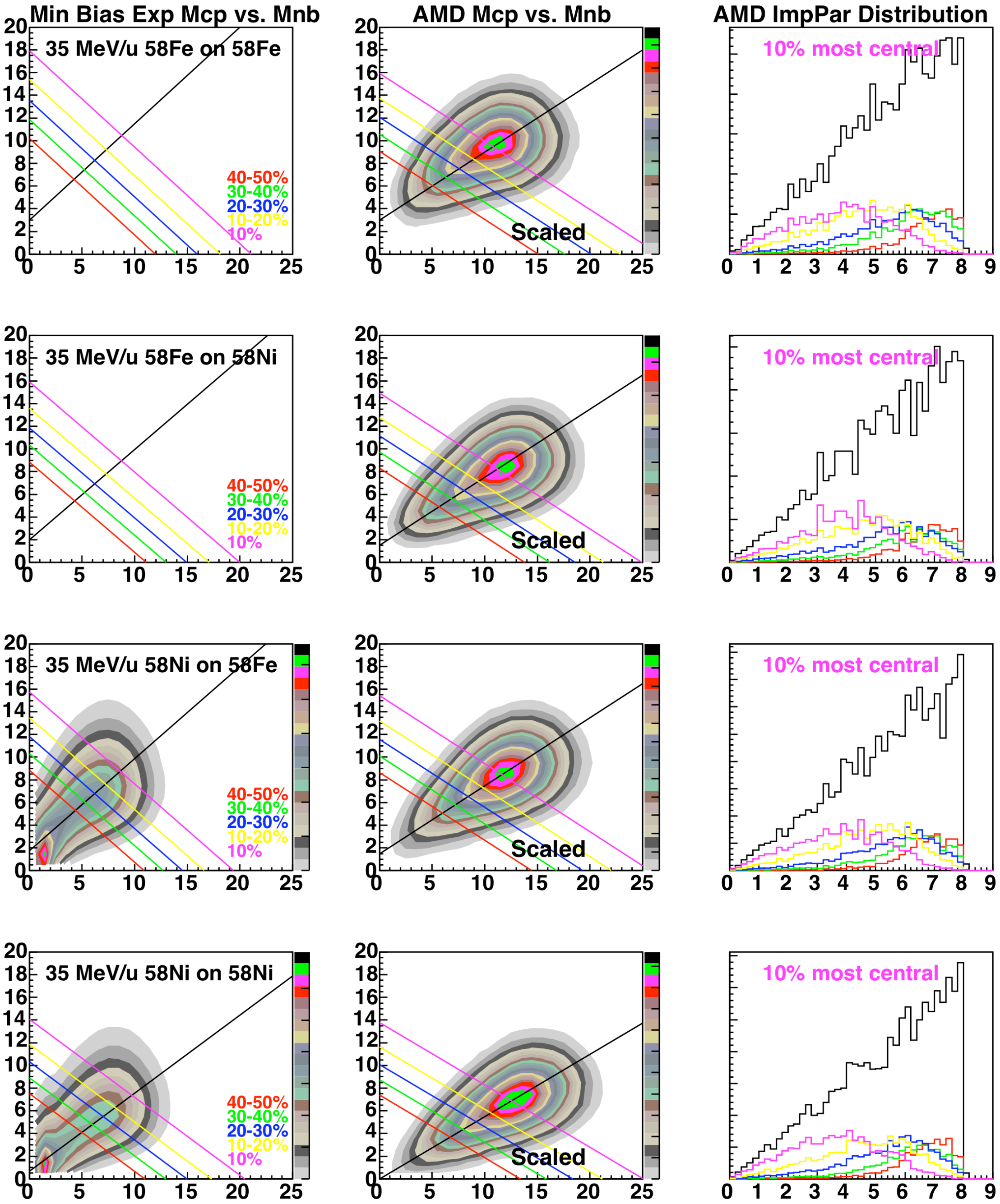

Fig. 35. Scaled Mcp vs. Mnb plots for experimental data with centrality cuts overlaid (first column), AMD-V/GEMINI Mcp vs. Mnb plots with centrality cuts overlaid (second column) and AMD-V/GEMINI impact parameter distributions (third column) broken up by centrality cut for 35 MeV/nucleon ^{58}Fe on ^{58}Fe (first row), ^{58}Fe on ^{58}Ni (second row), ^{58}Ni on ^{58}Fe (third row), and ^{58}Ni on ^{58}Ni (bottom row).

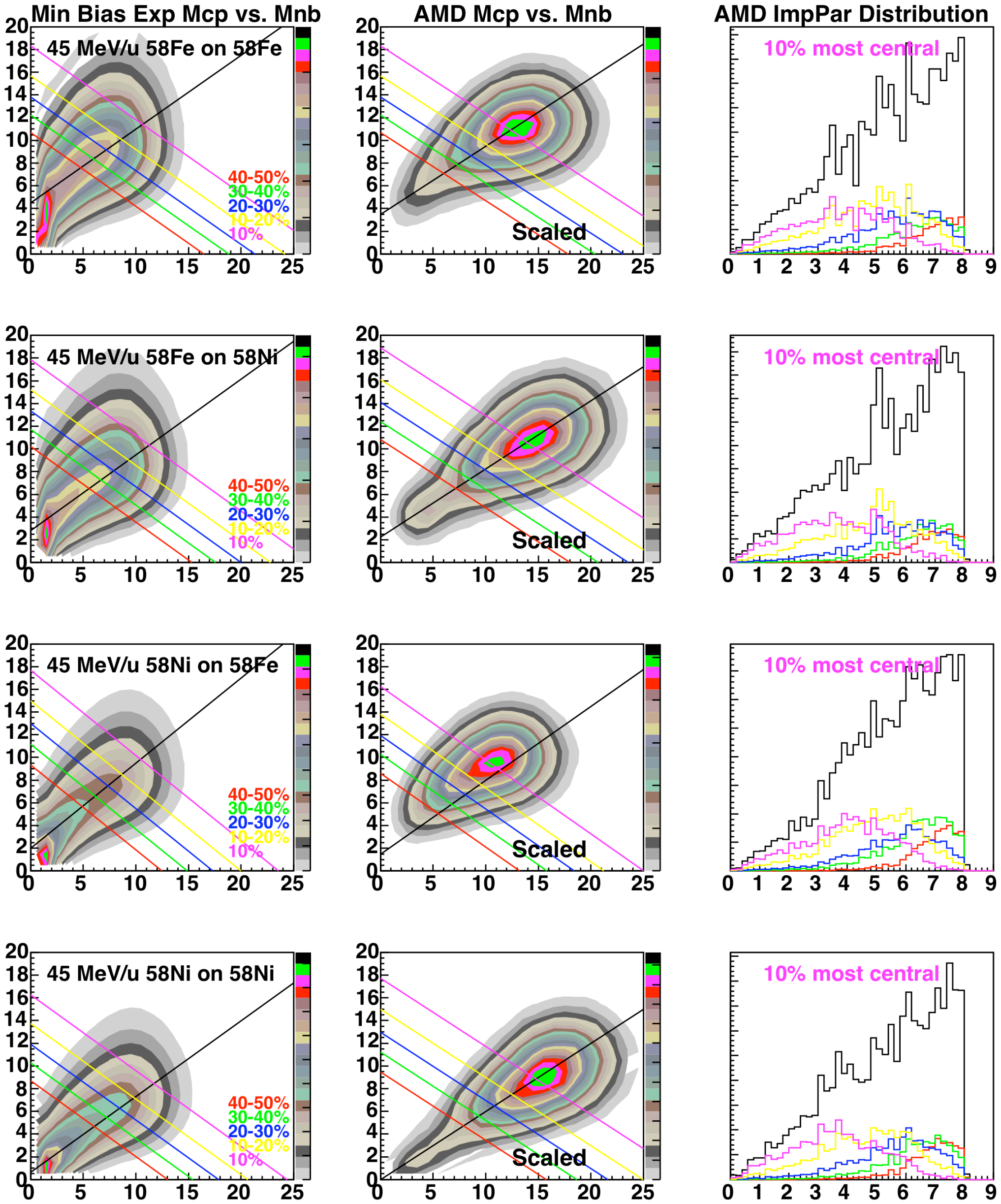

Fig. 36. Scaled Mcp vs. Mnb plots for experimental data with centrality cuts overlaid (first column), AMD-V/GEMINI Mcp vs. Mnb plots with centrality cuts overlaid (second column) and AMD-V/GEMINI impact parameter distributions (third column) broken up by centrality cut for 45 MeV/nucleon ^{58}Fe on ^{58}Fe (first row), ^{58}Fe on ^{58}Ni (second row), ^{58}Ni on ^{58}Fe (third row), and ^{58}Ni on ^{58}Ni (bottom row).

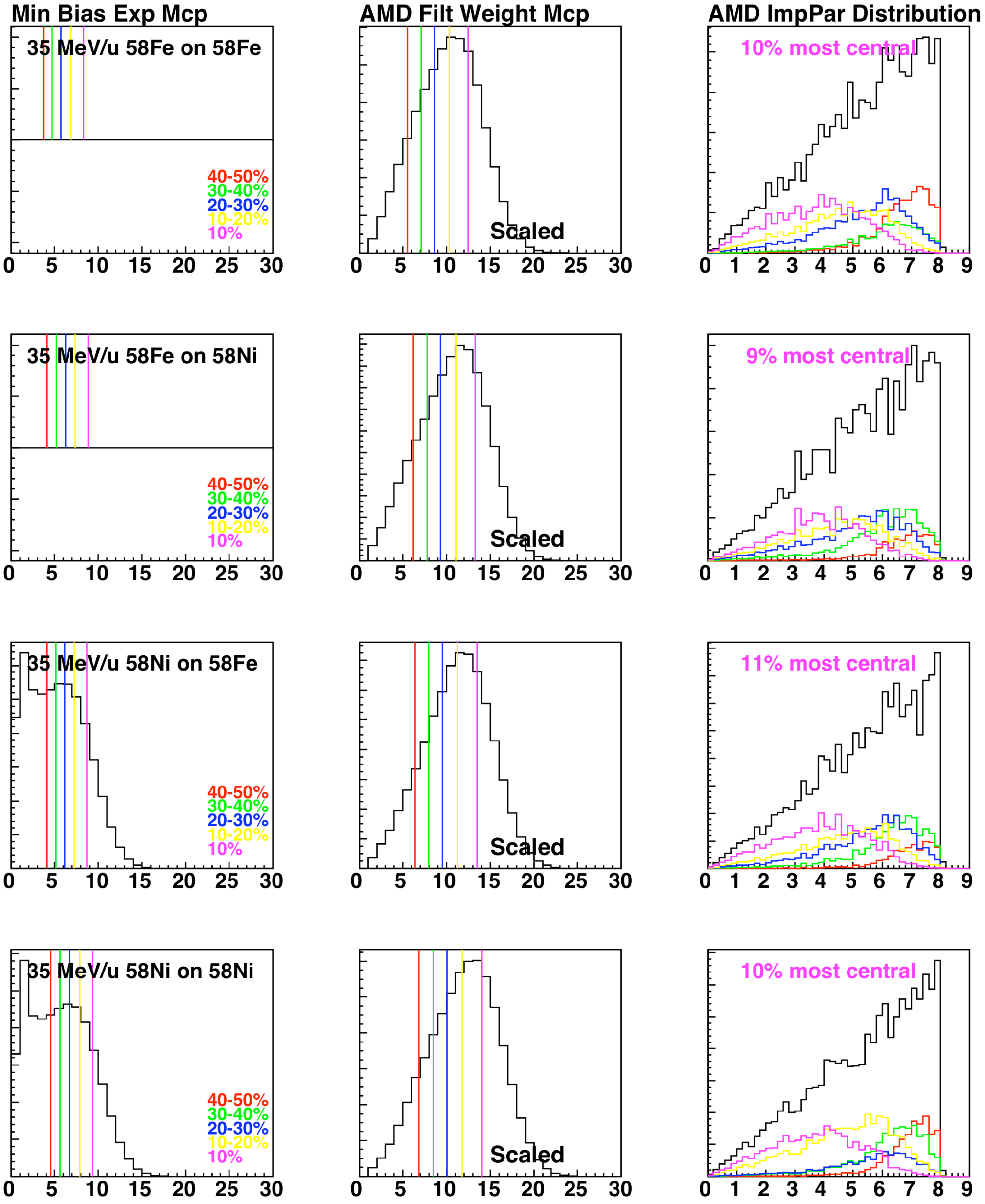

Fig. 37. Scaled Mcp plots for experimental data with centrality cuts overlaid (first column), AMD-V/GEMINI Mcp plots with centrality cuts overlaid (second column) and AMD-V/GEMINI impact parameter distributions (third column) broken up by centrality cut for 35 MeV/nucleon ^{58}Fe on ^{58}Fe (first row), ^{58}Fe on ^{58}Ni (second row), ^{58}Ni on ^{58}Fe (third row), and ^{58}Ni on ^{58}Ni (bottom row).

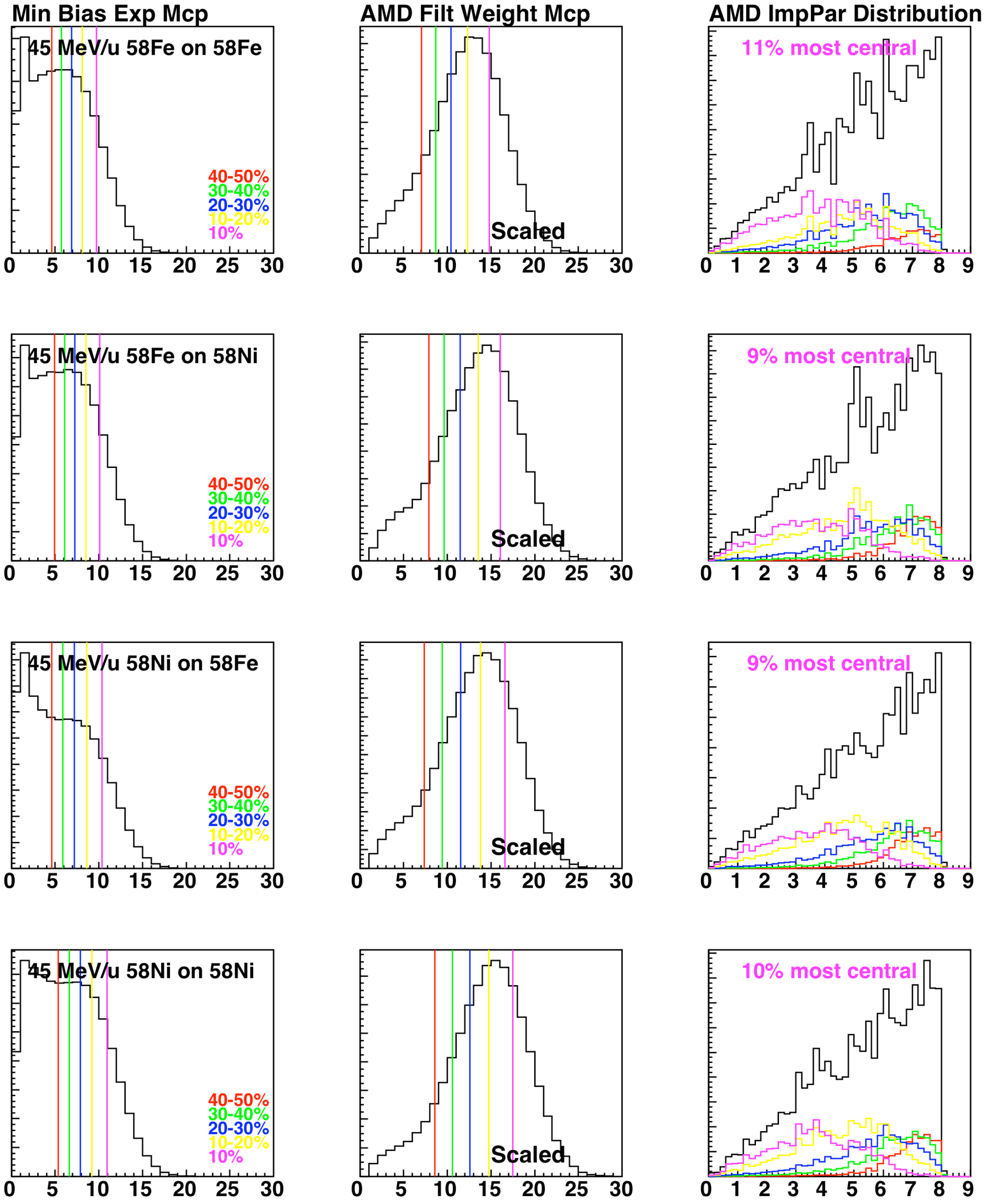

Fig. 38. Scaled Mcp plots for experimental data with centrality cuts overlaid (first column), AMD-V/GEMINI Mcp plots with centrality cuts overlaid (second column) and AMD-V/GEMINI impact parameter distributions (third column) broken up by centrality cut for 45 MeV/nucleon ^{58}Fe on ^{58}Fe (first row), ^{58}Fe on ^{58}Ni (second row), ^{58}Ni on ^{58}Fe (third row), and ^{58}Ni on ^{58}Ni (bottom row).

In Fig. 38, from top to bottom, data are shown from 45 MeV/nucleon ^{58}Fe on ^{58}Fe, ^{58}Fe on ^{58}Ni, ^{58}Ni on ^{58}Fe and ^{58}Ni on ^{58}Ni. From left to right are shown the experimental minimum bias Mcp distributions with the five centrality cuts overlaid in the first column. In the second column, the AMD-V/GEMINI filtered and weighted data with cut lines corresponding to experimental cut values scaled to contain as close as possible to the 10% most central events in the most central cut. Lastly, in the rightmost column is shown the total weighted impact parameter distribution for the AMD-V/GEMINI data along with impact parameter distribution for each centrality cut. The color key for the cut lines is seen in the first column panels.

Fig. 39 shows the mean impact parameter value from Gaussian fit to impact parameter distribution of events falling in the 10% most central cut for both one dimensional Mcp cuts and two dimensionally Mcp and Mnb cuts on centrality. The mean value of the impact parameter varies from 3 fm to 4 fm for the eight systems simulated by AMD-V/GEMINI.

Seen in Fig. 40 are the sigma values from Gaussian fit to impact parameter distribution of events falling in the 10% most central cut for both one dimensional Mcp cuts and two dimensionally Mcp and Mnb cuts on centrality.

See Table 16 for lists of the sigma values and the percent difference for each system (expressed as a percentage of the one dimensional Mcp cut sigma value). Sigma values of a Gaussian fit to the most central cut impact parameter distribution are shown for two and one dimensional cuts. The percent difference of the two sigma values are shown as a percentage of the Mcp sigma value.

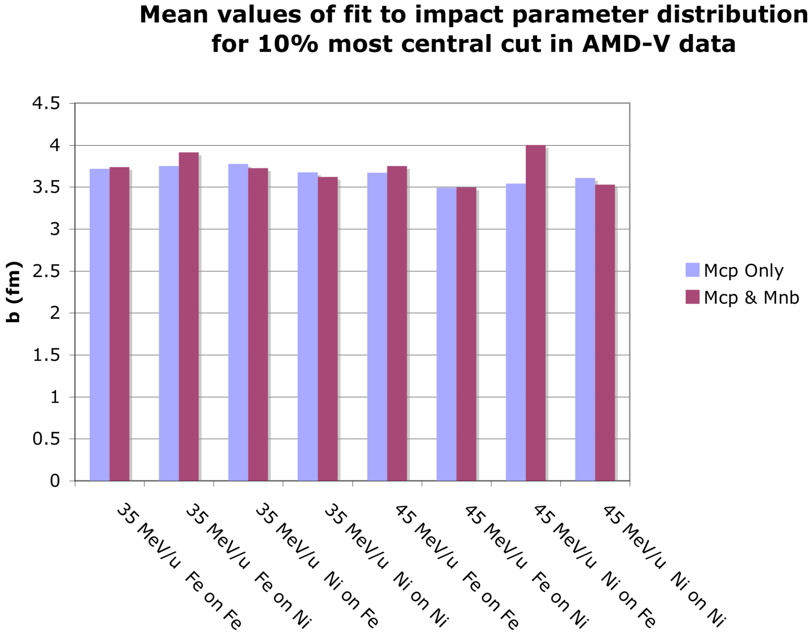

Fig. 39. Mean impact parameter values for 10% most central cuts for the one dimensional centrality cut of Mcp (blue) and the two dimensional centrality cut of Mcp and Mnb (pink) for AMD-V/GEMINI systems 35 and 45 MeV/nucleon ^{58}Fe on ^{58}Fe, ^{58}Fe on ^{58}Ni, ^{58}Ni on ^{58}Fe, and ^{58}Ni on ^{58}Ni.

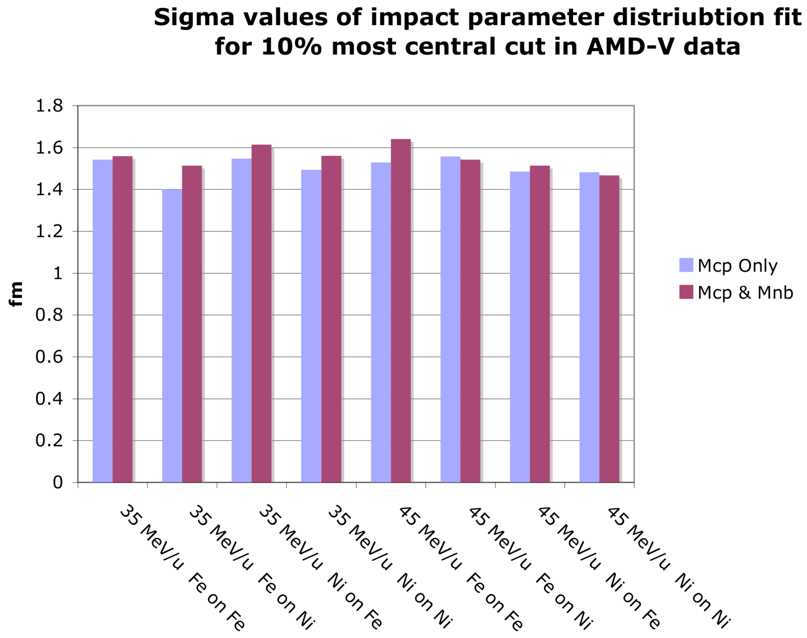

Fig. 40. Sigma values of impact distributions for 10% most central cuts for the one dimensional centrality cut in Mcp (blue) and two dimensional centrality cut in Mnb and Mcp (pink) for AMD-V/GEMINI systems 35 and 45 MeV/nucleon ^{58}Fe on ^{58}Fe, ^{58}Fe on ^{58}Ni, ^{58}Ni on ^{58}Fe, and ^{58}Ni on ^{58}Ni.

Table 16. Sigma values of Gaussian fits of the one dimensional centrality cut in Mcp and two dimensional centrality cut in Mnb and Mcp for AMD-V/GEMINI systems 35 and 45 MeV/nucleon ^{58}Fe on ^{58}Fe, ^{58}Fe on ^{58}Ni, ^{58}Ni on ^{58}Fe, and ^{58}Ni on ^{58}Ni.

System	Mcp v. Mnb sigma	Mcp sigma	% difference
35 MeV/u 58Fe on 58Fe	1.6	1.5	1.0%
35 MeV/u 58Fe on 58Ni	1.5	1.4	8.2%
35 MeV/u 58Ni on 58Fe	1.6	1.5	4.3%
35 MeV/u 58Ni on 58Ni	1.6	1.5	4.5%
45 MeV/u 58Fe on 58Fe	1.6	1.5	7.3%
45 MeV/u 58Fe on 58Ni	1.5	1.6	-1.0%
45 MeV/u 58Ni on 58Fe	1.5	1.5	2.0%
45 MeV/u 58Ni on 58Ni	1.5	1.5	-1.1%

The one dimensional cuts on Mcp and the two dimensional cuts on Mcp and Mnb give distributions which are the similar in percent centrality across all systems. The main difference between the two different types of centrality cuts is that the two dimensional cut allows for better dialing in of the exact percentage of events which are desired. Therefore, two dimensional cuts on Mcp and Mnb will be used to cut on centrality for these NIMROD data sets.

Looking to Fig. 41, one sees the impact parameter distribution for events in the five different Mcp versus Mnb centrality cut bins for 35 MeV/nucleon ^{58}Ni on ^{58}Ni AMD-V/GEMINI data. The pink line represents the most central cut (10%). The yellow, blue, green and red lines represent the next four 10% most central cut slices in decreasing order. There is a range of impact parameters for each centrality cut and the peak of that range increases in impact parameter as centrality decreases.

From this page on in the current study, whenever centrality cuts are referred to, they refer to the two dimensional centrality cut on Mcp and Mnb via the Mfunction method described here in Chapter 4.

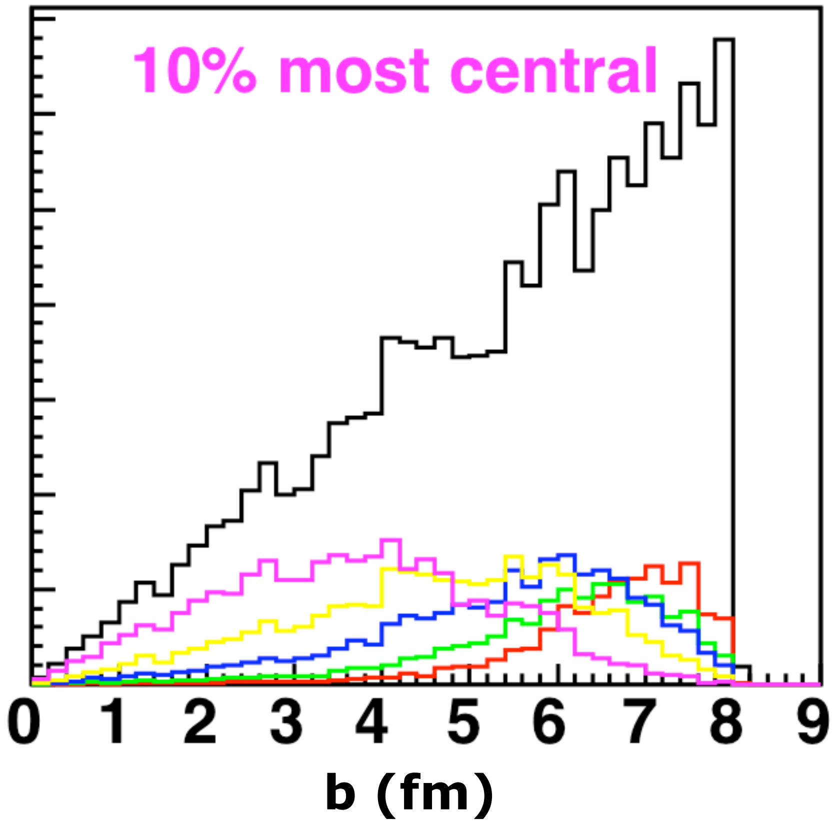

Fig. 41. AMD-V/GEMINI impact parameter distribution for all centrality cuts from 10% most central (pink) to 40 to 50% most central (red) for 35 MeV/nucleon ^{58}Ni on ^{58}Ni.

CHAPTER V

EXPERIMENTAL RESULTS

Data are taken in two time segments, one in March and one in April. In March, the high multiplicity trigger is set to CsI hit multiplicity greater than or equal five and the minimum bias trigger is set to CsI hit multiplicity greater than or equal one and is downscaled by a factor of 100. In April, the minimum bias trigger is changed to CsI hit multiplicity greater than or equal to three. Also, the minimum bias trigger downscale and the high multiplicity trigger are mistakenly taken out in the April run.

See Fig. 42 and Fig. 43, which show data taken in April and March, respectively. These two figures show the distribution of Mcp, Mnb, Mfunction and hPercent plots described in Chapter V. In both Fig. 42 and Fig. 43, the top row of panels show charged particle multiplicity distributions. The second row shows neutron multiplicity distributions. The third row shows the Mfunction values as a function of Mcp and Mnb multiplicities and the fourth and bottom row shows the fraction of events that each bin constitutes as a function of multiplicity bin. In Fig. 42, the first column shows data from 35 MeV/nucleon ^{64}Ni on ^{64}Ni, the second column shows data from 35 MeV/nucleon ^{54}Fe on ^{54}Fe and the third column shows data from 35 MeV/nucleon ^{54}Fe on ^{58}Ni, all of which are taken in April. In Fig. 43, the first column shows data from 35 MeV/nucleon ^{58}Ni on ^{58}Fe, the second column shows data from 35 MeV/nucleon ^{58}Ni on ^{58}Ni and the third column shows data from 35 MeV/nucleon ^{58}Ni on ^{64}Ni, all of which are taken in March.

In Fig. 42, notice the row of data showing Mcp distribution plots and how they are sharply peaked toward three and are very shallow as Mcp increases. Events with charged particle multiplicity greater than or equal to ten are virtually nonexistent for these data, whereas for the earlier data, these exit channels are well populated. (See Fig. 43 for well-populated greater than ten charged particle multiplicity March data.) The bias of the April data is simply too different to be compared directly to the data sets taken in March for this central impact parameter study. Therefore, only data from the mass symmetric systems of 35 and 45 MeV/nucleon ^{58}Fe and ^{58}Ni on ^{58}Fe and ^{58}Ni will be presented further in the current study.

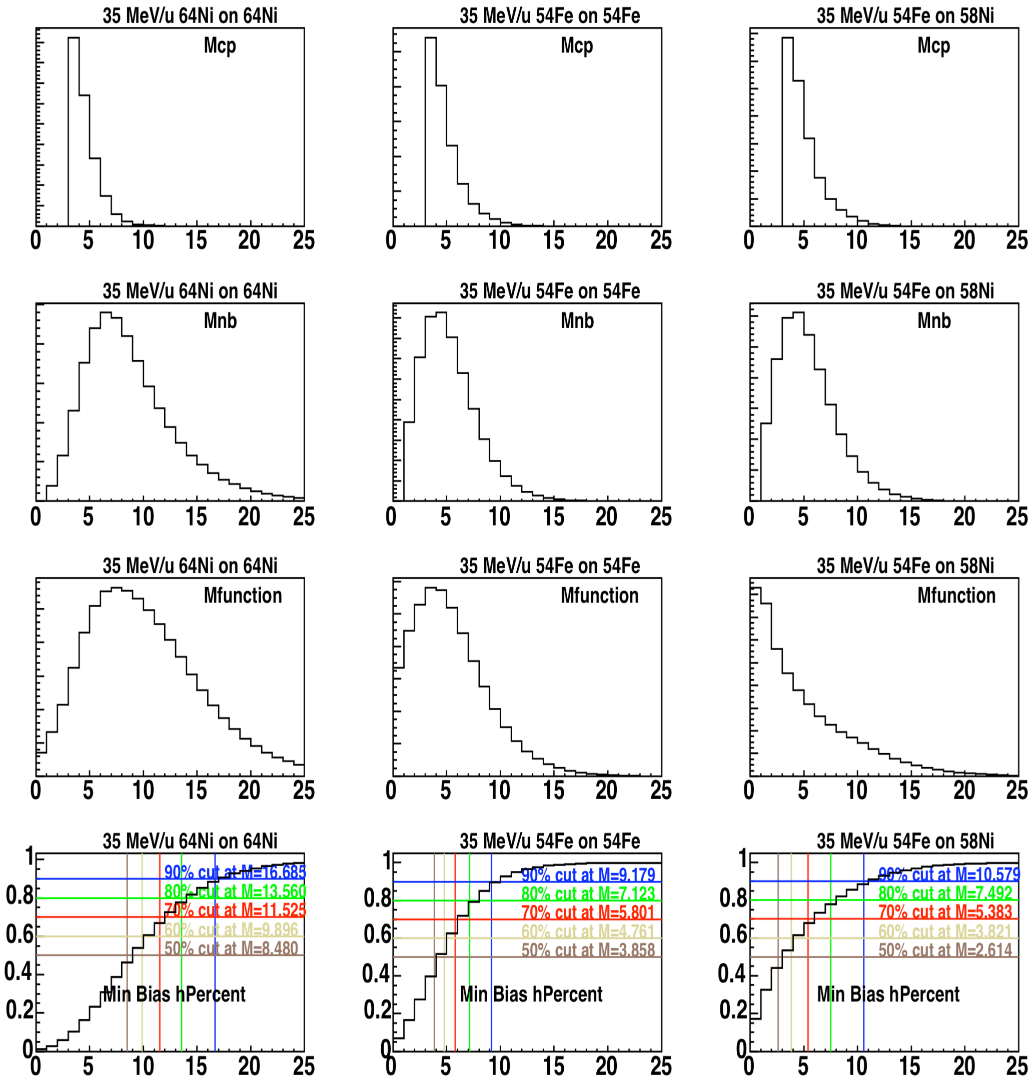

Fig. 42. Mcp, Mnb, Mfunction and hPercent plots from the systems of 35 MeV/nucleon ^{64}Ni on ^{64}Ni, ^{54}Fe on ^{54}Fe and ^{54}Fe on ^{58}Ni (April data).

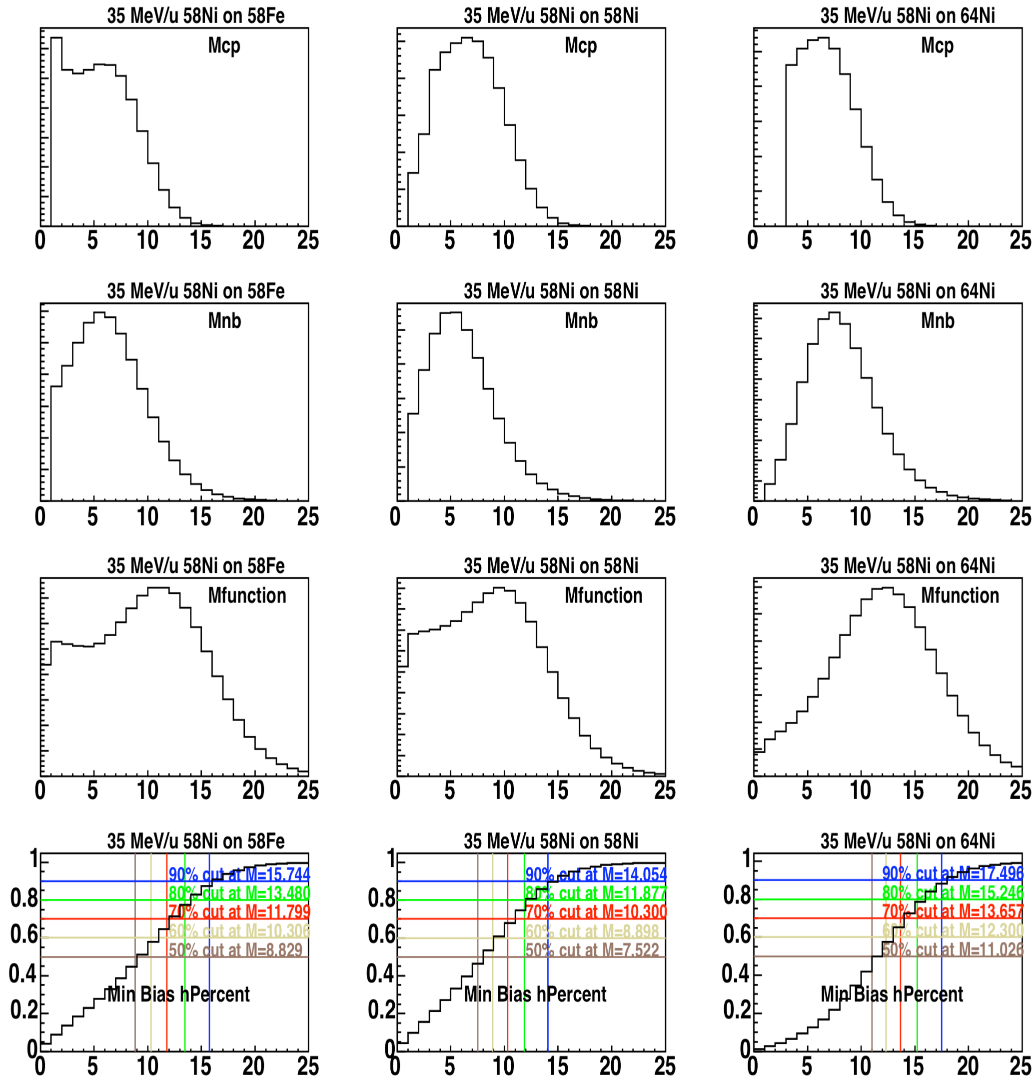

Fig. 43. Mcp, Mnb, Mfunction and hPercent plots from the systems of 35 MeV/nucleon ^{58}Ni on ^{58}Fe, ^{58}Ni on ^{58}Ni, and ^{58}Ni on ^{64}Ni (March data).

Isotope and isobar ratios are extracted for 19 isotopes in eight rings in order to study N/Z equilibration. The isotopes included in the analysis are p, d, t, ^{3}He, ^{4}He, ^{6}Li, ^{7}Li, ^{7}Be, ^{9}Be, ^{10}Be, ^{10}B, ^{11}B, ^{11}C, ^{12}C, ^{13}C, ^{14}C, ^{14}N, ^{15}N, ^{16}O, and ^{17}O. The isotope ratios studied are p/d, p/t, $^{3/4}$He,$^{6/7}$Li, $^{7/9}$Be, $^{7/10}$Be, $^{10/11}$B, $^{12/11}$C, $^{12/13}$C, $^{12/14}$C, $^{14/15}$N, $^{16/17}$O. The isobar ratios studied are t/^{3}He, ^{7}Li/Be, ^{10}Be/B, ^{11}B/C, and ^{14}C/N. (N/Z) tracer terms are extracted for all isotope and isobar ratios.

The lab angles of isotopically resolved fragments are 4.3 to 40.4 degrees and are from NIMROD rings 2 through 9. As one goes back in lab angle, statistics of all isotopes decrease. As the mass of the isotope increases, statistics also decrease. As a result, only the lightest isotopes have robust statistics in the backward most angles. In order to increase statistics, the isobar and isotope ratio results include data from the two most central cuts or the 20% most central data. N/Z tracer terms, however, are shown as a function of 10% most central increments of data as explained in the previous chapter.

It could be expected that an evolving type of source is seen as the lab angle increases from a forward focused preequilibrium emission [98] source at forward angles to a more equilibrated compound nuclear source at backward angles. If so, angular data which can be verified to be from the same source could be binned at the most central cut in order to increase statistics.

A moving source fit applied to NIMROD data could help deconvolve the emission sources and describe how many of each isotope came from each source. A moving source fit assumes three sources of emission: a target-like, projectile-like and an intermediate velocity source. Data taken at a later time with NIMROD, which have different electronics' gain setting, etc., are fit with a moving source fit and show little contamination from the target-like velocity source and very little from the projectile-like velocity source at 40 degrees in the lab [99]. Therefore, data from 40 degrees in the lab frame will be studied for their N/Z equilibration observables.

In Fig. 44 are shown energy spectra for ^{7}Li for rings 3 through 9 in NIMROD. In Fig. 45, Fig. 46, and Fig. 47 are shown energy spectra for isotopes at theta$_{lab}$=6^{o} (ring 3) for the isotope ratios p/d, $^{3/4}$He, $^{6/7}$Li, and $^{9/10}$Be (Fig. 45), $^{10/11}$B, $^{12/13}$C, $^{14/15}$N, and $^{16/17}$O (Fig. 46), and t/^{3}He, ^{7}Li/Be, ^{10}Be/B, ^{11}B/C, and ^{14}C/N (Fig. 47.) Overlaid on the energy spectra are integration limits with three ranges, low (between two blue lines), high (between two pink lines), and total (between first blue line and second pink line.)

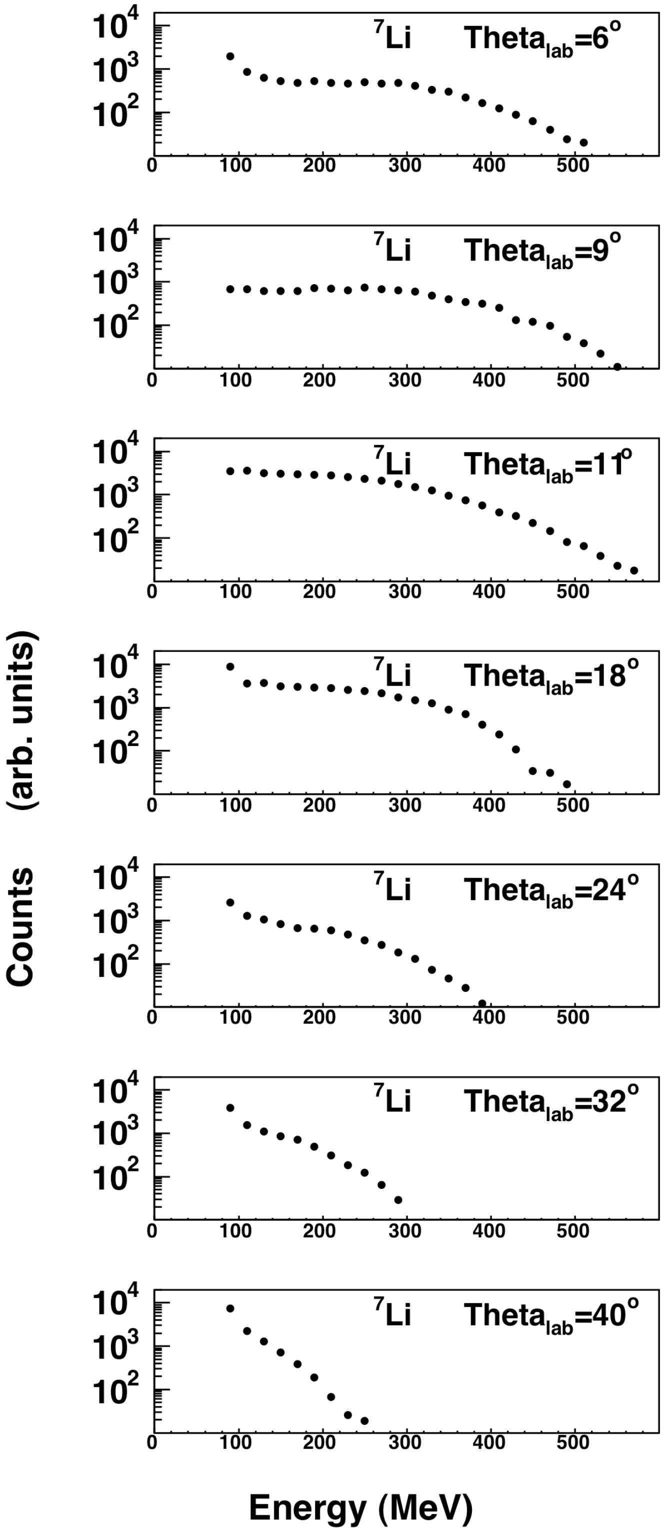

Fig. 44. Inclusive energy spectra of ^{7}Li in rings 3 through 9 of NIMROD.

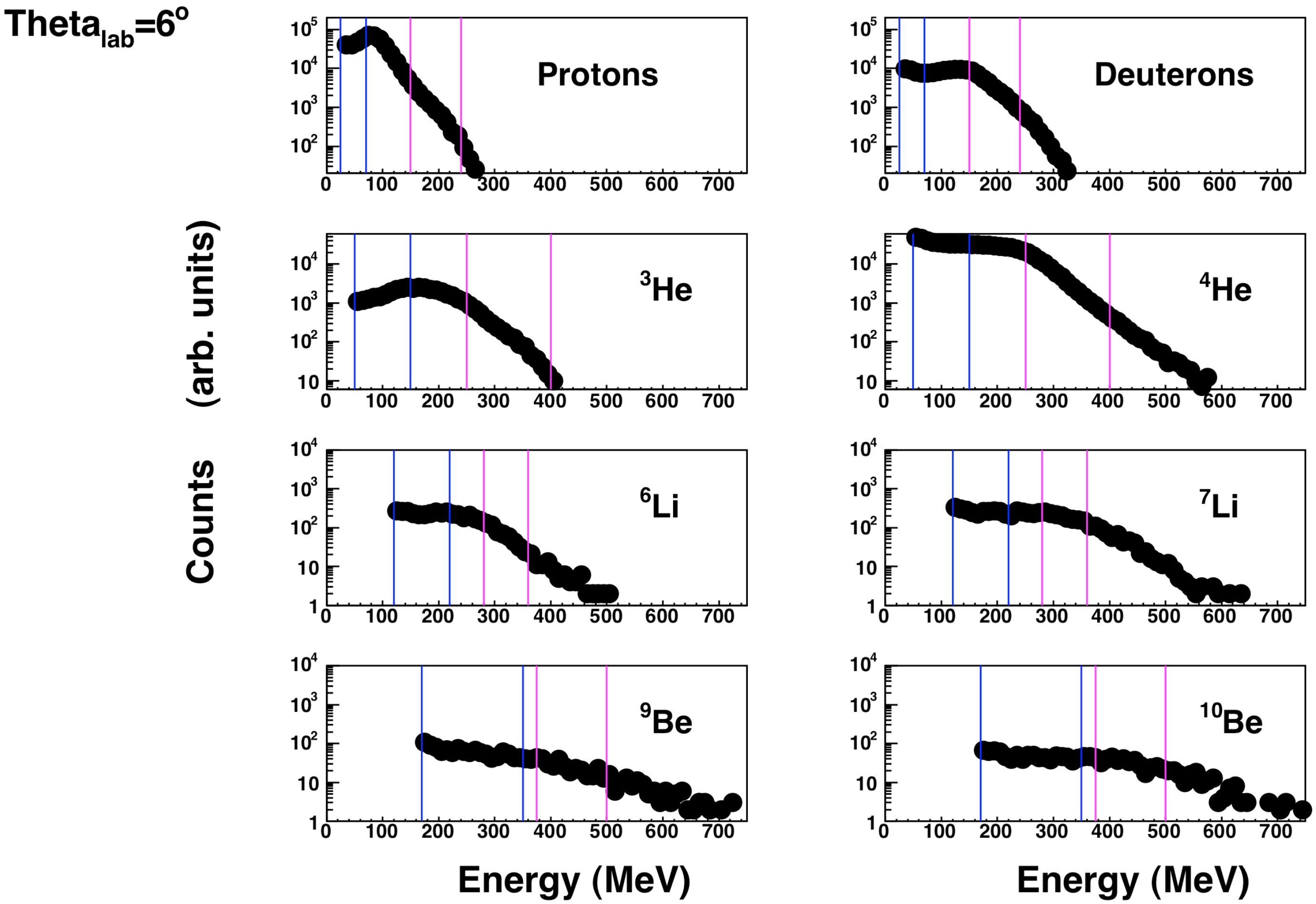

Fig. 45. Inclusive energy spectra from NIMROD ring 3, lab theta of 6 degrees, for protons, deutrons, ^{3}He, ^{4}He, ^{6}Li, ^{7}Li, ^{9}Be, and ^{10}Be with lower integration limits in blue and higher intergration limits in pink.

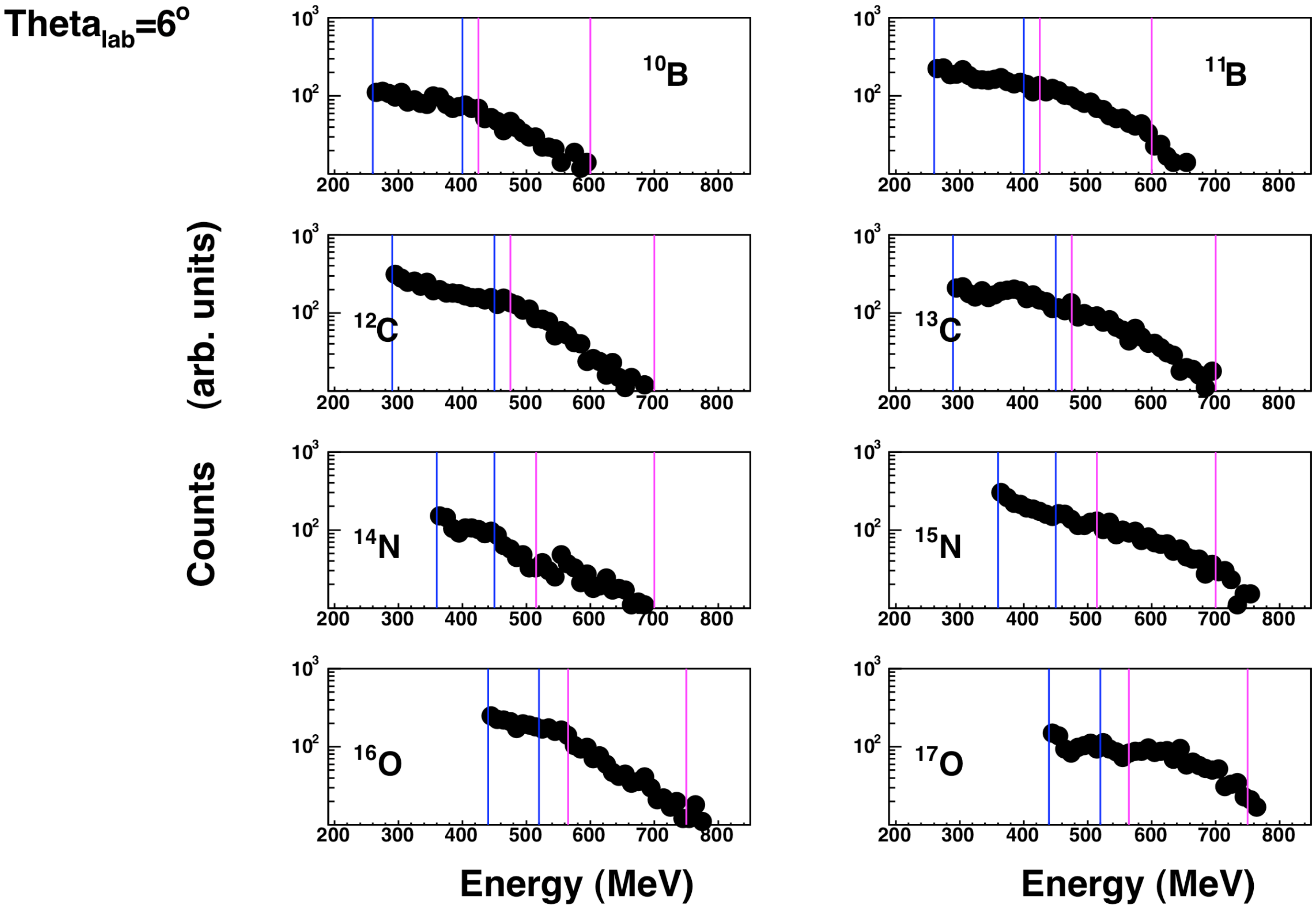

Fig. 46. Inclusive energy spectra from NIMROD ring 3. lab theta of 6 degrees, for ^{10}B, ^{11}B, ^{12}C, ^{13}C, ^{14}N, ^{15}N, ^{16}O, and ^{17}O with lower integration limits in blue and higher intergration limits in pink.

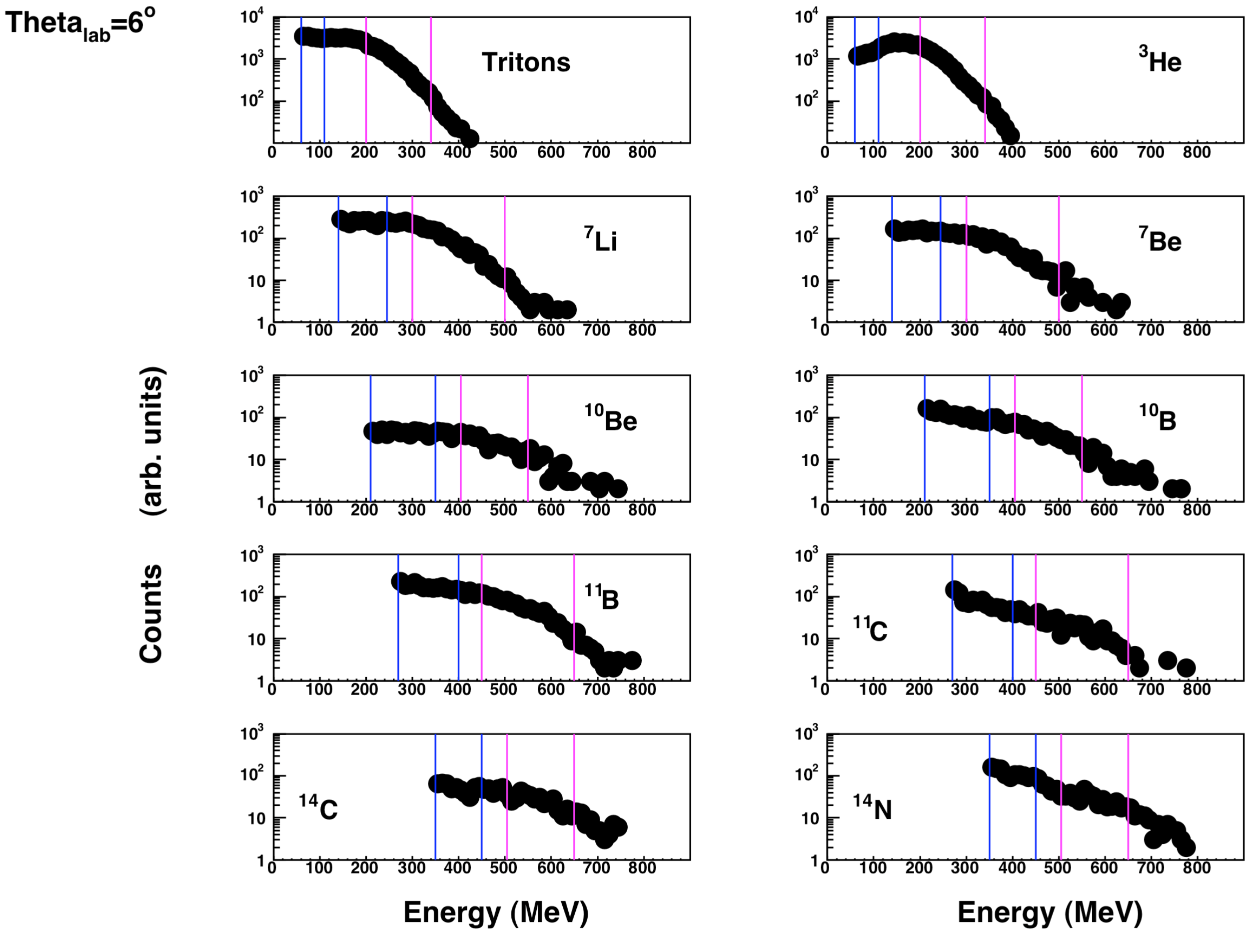

Fig. 47. Inclusive energy spectra from NIMROD ring 3, lab theta of 6 degrees, for tritons, ^{3}He, ^{7}Li, ^{7}Be, ^{10}Be, ^{10}B, ^{11}B, ^{11}C, ^{14}C, and ^{14}N with lower integration limits in blue and higher intergration limits in pink.

In Fig. 48, Fig. 49, and Fig. 50 are shown inclusive NIMROD energy spectra for isotopes at $\text{theta}_{\text{lab}}$=40° (ring 9) for the isotope ratios p/d, $^{3/4}$He, $^{6/7}$Li, and $^{9/10}$Be (Fig. 48), $^{10/11}$B, $^{12/13}$C, $^{14/15}$N, and $^{16/17}$O (Fig. 49), and t/^{3}He, ^{7}Li/Be, ^{10}Be/B, ^{11}B/C, and ^{14}C/N (Fig. 50.) Overlaid on the energy spectra are integration limits with one range (between two blue lines).

In Fig. 45 through Fig. 50, the energy scales along the x axis are in MeV and are constant for all energy spectra appearing in the same figure, but change from figure to figure in order to expand the pertinent sections of the spectra. In the energy spectra from ring 9, $\text{theta}_{\text{lab}}$=40°, there is only one integration limit range as compared to three in energy spectra from ring 3, $\text{theta}_{\text{lab}}$=6°, because at the backward angle, there is little or no high energy tail on which to cut for integration. The integration limits take into account threshold effects and the varying level of statistics between systems. The energy spectra shown in Fig. 45 through Fig. 50 are from the most statistically robust system, ^{58}Ni on ^{58}Ni at 35 MeV/nucleon. Upper limits of integration are set bearing in mind the endpoint of spectra from the systems with less statistics and are therefore sometimes placed short of the endpoint of the system shown.

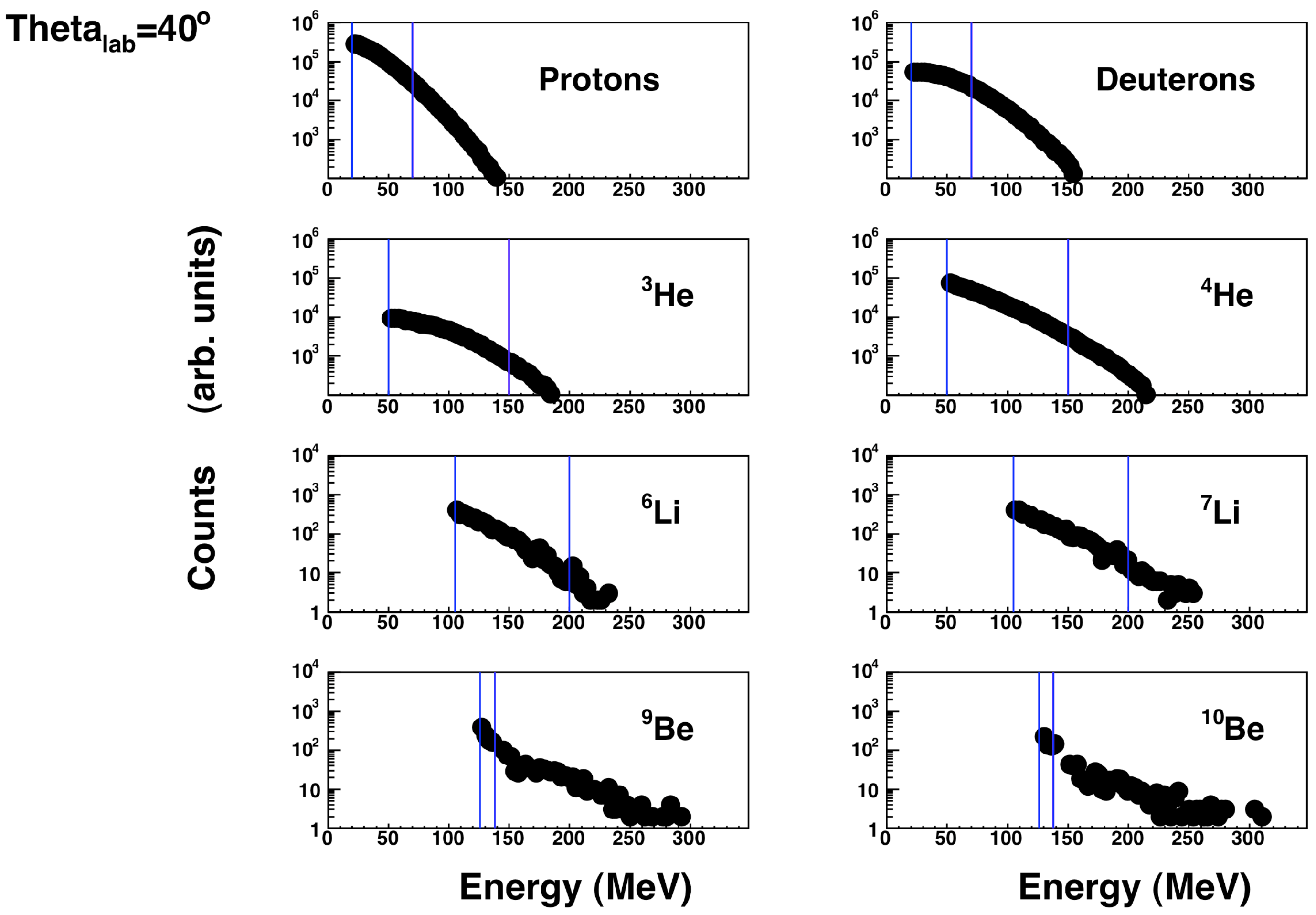

Fig. 48. Inclusive energy spectra from NIMROD ring 9. lab theta of 40 degrees, for ^{10}B, ^{11}B, ^{12}C, ^{13}C, ^{14}N, ^{15}N, ^{16}O, and ^{17}O with lower integration limits in blue and higher intergration limits in pink.

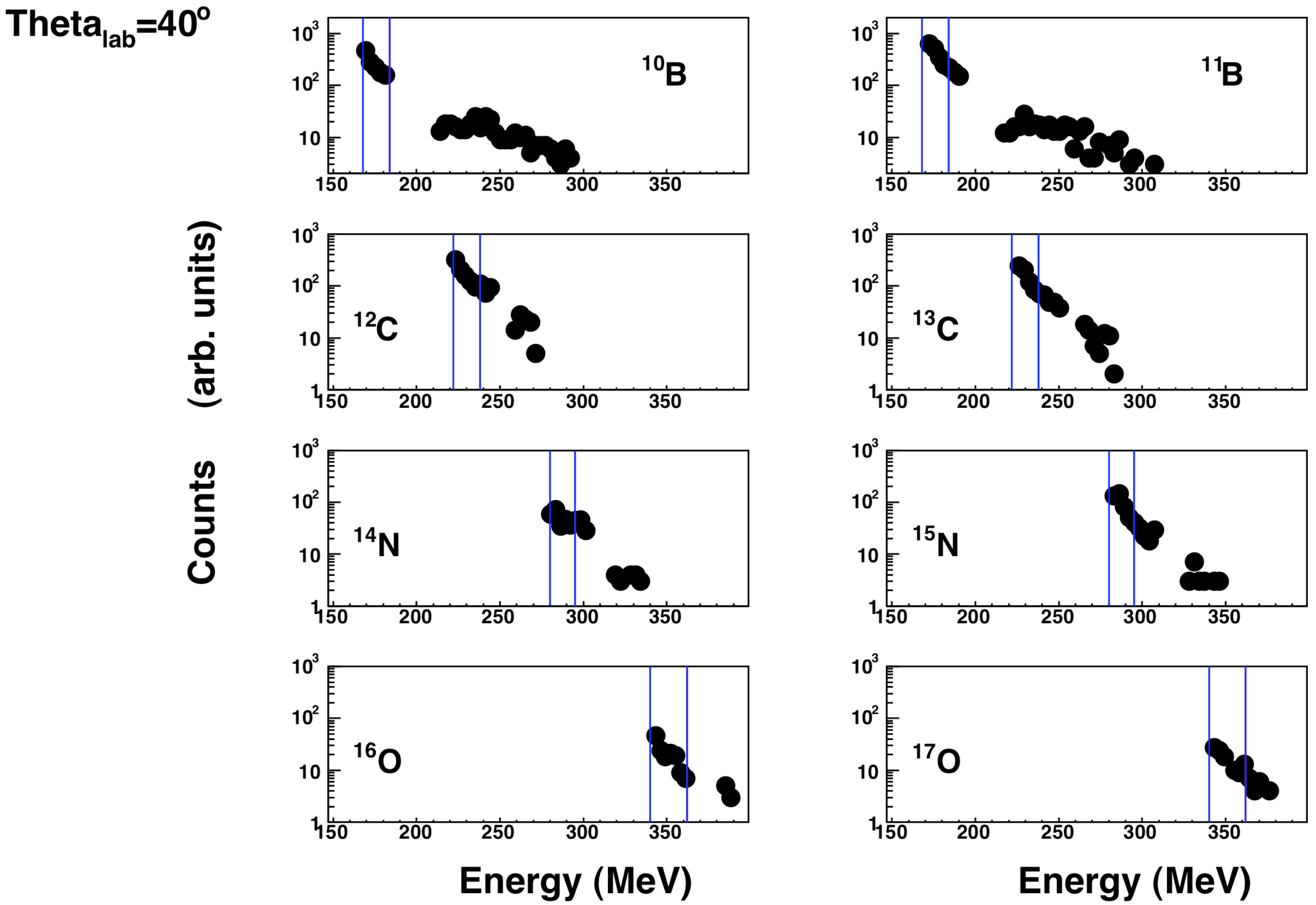

Fig. 49. Inclusive energy spectra from NIMROD ring 9. lab theta of 40 degrees, for ^{10}B, ^{11}B, ^{12}C, ^{13}C, ^{14}N, ^{15}N, ^{16}O, and ^{17}O with lower integration limits in blue and higher intergration limits in pink.

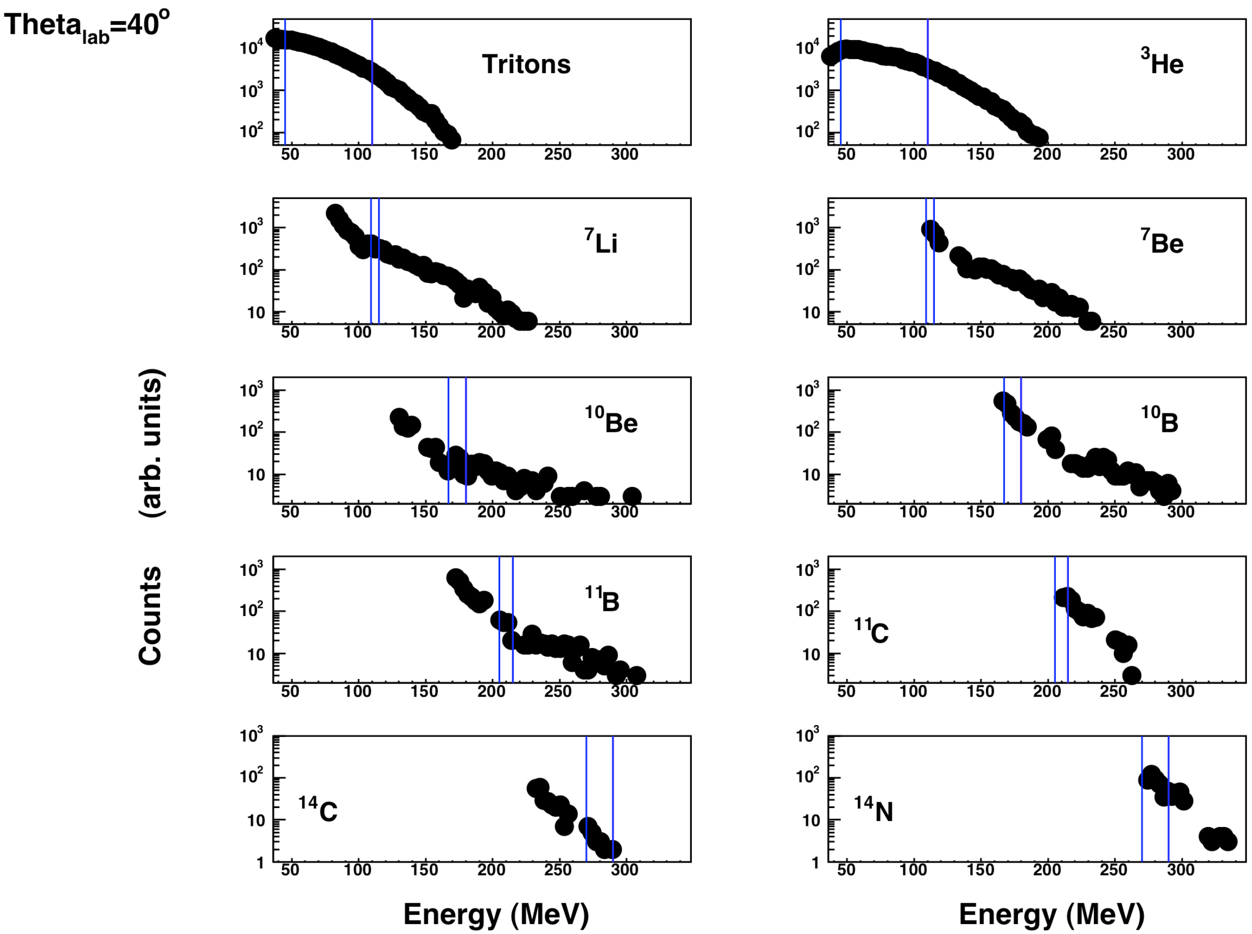

Fig. 50. Inclusive energy spectra from NIMROD ring 9, lab theta of 40 degrees, for tritons, ^{3}He, ^{7}Li, ^{7}Be, ^{10}Be, ^{10}B, ^{11}B, ^{11}C, ^{14}C, and ^{14}N with lower integration limits in blue and higher intergration limits in pink.

Experimental isobar and isotope ratios

Isotope and isobar ratios are used to investigate N/Z equilibration by plotting them as a function of the combined system N/Z, $(N/Z)_{CS}$. Equation 8 shows how $(N/Z)_{CS}$ is calculated for the system of ^{58}Fe on ^{58}Ni.

$$\left(\frac{N}{Z}\right)_{cs} = \left(\frac{N}{Z}\right)_{FeNi} = \frac{N_{Fe}+N_{Ni}}{Z_{Fe}+Z_{Ni}} = \frac{32+30}{26+28} = 1.148 \qquad (8)$$

If hot nuclear matter has become equilibrated before emitting fragments, then the isobaric ratios plotted for two different systems having identical (N/Z) content, such as the case in the 35 and 45 MeV/nucleon ^{58}Fe on ^{58}Ni and ^{58}Ni on ^{58}Fe systems, will be equal to one another. Further, if the ratios of the four systems of ^{58}Fe and ^{58}Ni on ^{58}Ni and ^{58}Fe fall along a line as a function of the $(N/Z)_{CS}$, then the fragments are emitted from a composite, N/Z equilibrated system. If the ratios of the systems with the same targets (projectiles) are more similar in value, then the emitted system is said to be more target-like (projectile-like).

Seen in Fig. 51 are isobaric ratio yields of ^{7}Li/Be of data taken at $\text{theta}_{lab}=40^{o}$ as a function of $(N/Z)_{CS}$ of systems with combined A=58 cut on the 10% most central events. From right to left in each panel, ratio values from data of the systems Ni and Fe on Ni are shown in circles and Fe and Ni on Fe are shown in triangles. The black symbols represent 35 MeV/nucleon data while the red symbols represent 45 MeV/nucleon data. In Fig. 51, the dependence of the ratio value on the choice of integration limit is studied. In the top half of Fig. 51 are shown ratio values for integration limits chosen to fall before the energy threshold of the CsI (109MeV to 115MeV) and on the bottom half of Fig. 51 are shown ratio values with integration limits chosen to fall higher than the energy threshold of the CsI (165MeV to 200MeV). The magnitude of the ratios do change with the choice of integration limits from about 0.4 for data from 35 MeV/nucleon Ni + Ni in the top integration choice to about 0.7 for data from the same system in the bottom integration choice. Notice that the two mixed systems show similar equilibration behavior in all cases of both energy of beam and integration limits within error bars. In other words, the two mixed systems in the center of each panel are all overlying within error bars. It is the equilibration behavior in the ratio values which are of most interest in the current study, not the magnitude of the ratio values. The statistics decrease dramatically in the high energy range of the second set of integration limits, 165MeV to 200 MeV, as is seen by the large error bars of the 35MeV/nucleon Fe on Fe ratio value. Therefore, the conclusion of Fig. 51 is that the lower integration limit is chosen for its more robust statistics across all systems for data from ring 9, theta$_{\text{lab}}$=40°. For a review of tabulated integration limits seen in these energy spectra, look to Table 12.

The error bars shown in Fig. 51 are purely statistical. Statistical error bars are calculated via the standard propagation of random error analysis, an example of which may be found in Equation 9 [100].

$$[\varepsilon(F)]^2 = \left(\frac{\partial F}{\partial x}\right)^2 [\varepsilon(x)]^2 + \left(\frac{\partial F}{\partial y}\right)^2 [\varepsilon(y)]^2 + \left(\frac{\partial F}{\partial z}\right)^2 [\varepsilon(z)]^2 + \ldots \qquad (9)$$

where $\varepsilon(F)$, $\varepsilon(x)$, $\varepsilon(y)$, and $\varepsilon(z)$, are the error of the function F and the errors in the variables contained in function $F\ (x, y, z, \ldots)$. The error in isotope yield, which are obtained from the integration of energy spectra, are assumed to be equal to the square root of that yield.

The error bars in Fig. 51 do not include systematic errors which originate from gain drift, which have a maximum (but individually varying through time) shift of 7% in energy. The statistical error bars in Fig. 51 also do not include error originating from gate placement, i.e., the approximate amount of missing isotope yield of the desired isotope and the approximate amount of undesired isotope yield which erroneously falls into each gate.

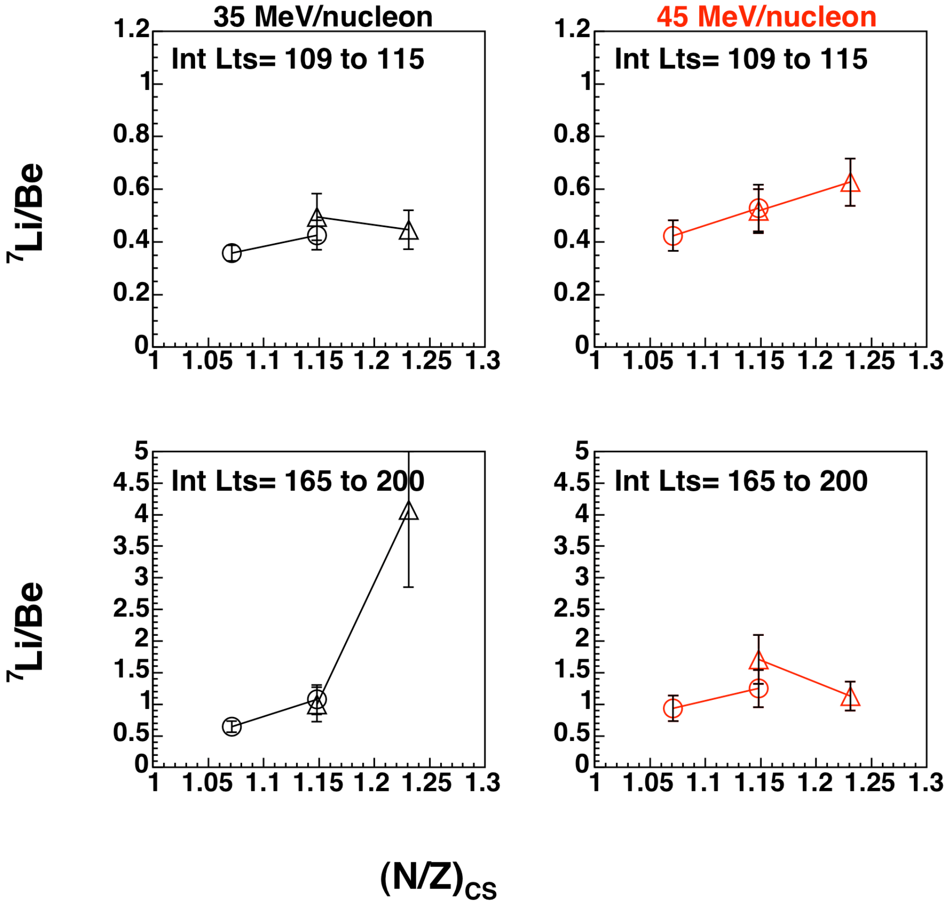

Fig. 51. Dependence of isobaric ratio ^{7}Li/Be values on integration limit for data from ring 9, theta$_{lab}$=40°, cut on the 10% most central events for 35 (black) and 45 (red) MeV/nucleon ^{58}Ni, ^{58}Fe on ^{58}Ni (circles) and ^{58}Ni, ^{58}Fe on ^{58}Fe (triangles).

Seen in Fig. 52 is an example of gates drawn around elements and isotopes in raw spectra from two super telescopes in ring 3 (theta$_{lab}$=6°) in NIMROD. The distributions of isotopes inside the gates do not break off sharply, but instead have some diffuse character at their boundaries. This diffuseness may cause a gate to include a small number of undesired isotopes and exclude a small number of desired isotopes. The statistical error bars in Fig. 51 do not include the error associated with the calibration process, as well. The calibrations from the current NIMROD study can be said to be good to about 15% in energy. The gates drawn in the current NIMROD study have a very approximate uncertainty of about 5%.

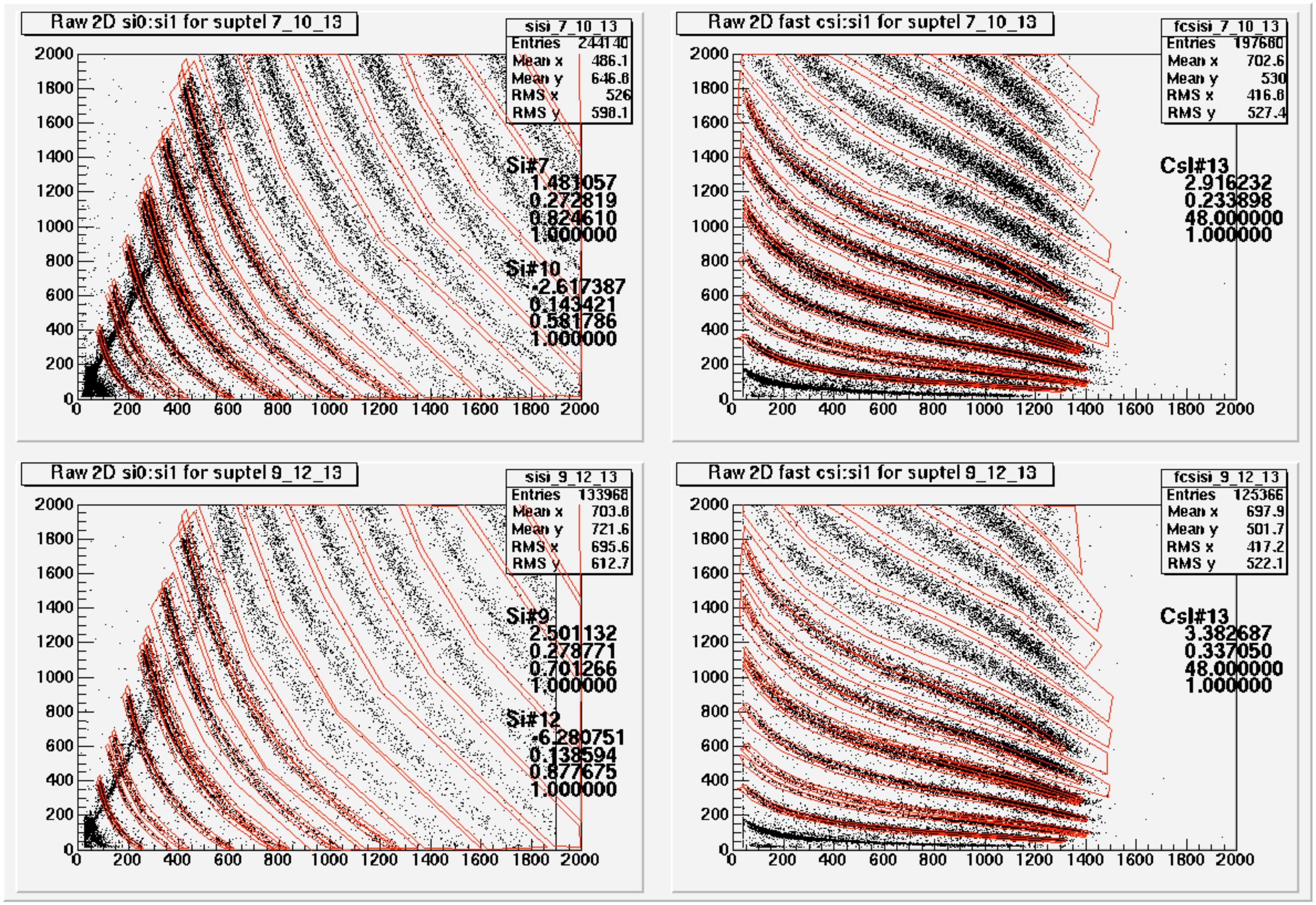

Fig. 52. An example of gated super telescope raw spectra from ring 3 in NIMROD, lab theta of 6 degrees with 150 and 300 micron thick Silicon detectors and a 100mm thick CsI detectors.

There is larger difference in magnitude for data taken from different integration limit ranges in the more forward ring at theta$_{lab}$=6^o. In the more forward data, the cut on integration is likely cutting on different sources, such as an intermediate and or target velocity source at low energies compared to a fast preequilibrium and projectile velocity source at higher energies. Look to Fig. 53 for an example of this difference in the comparison of p/d yield ratio using the three different integration limits in NIMROD ring 3 (theta$_{lab}$=6^o) at 35 MeV/nucleon beam energy.

In Fig. 53, the top row shows data which are cut for the 40 to 50% most central events and the bottom row shows data which are cut for the 10% most central events. The left two panels are data from the low energy range integration limits. The middle two panels are from data with the high energy range integrations limits. The right panels show data from the integration limits that include the low and high range and the gap in between. There is a plain difference in the magnitude across the top row as the data show values around 3 and 4 for the low integration limit range ratios and values between 0 and 1 for the high integration limit range ratios. The combined integration limit range ratios have intermediate values. The difference in the equilibrium behavior is not so clear. The distance between the two mixed entrance channel systems' ratio values is similar if taken as a percent of their relative magnitude. However, in the first column of Fig. 53, one can clearly see a movement toward N/Z equilibration from the 40 to 50% central cut data to the 10% most central data.

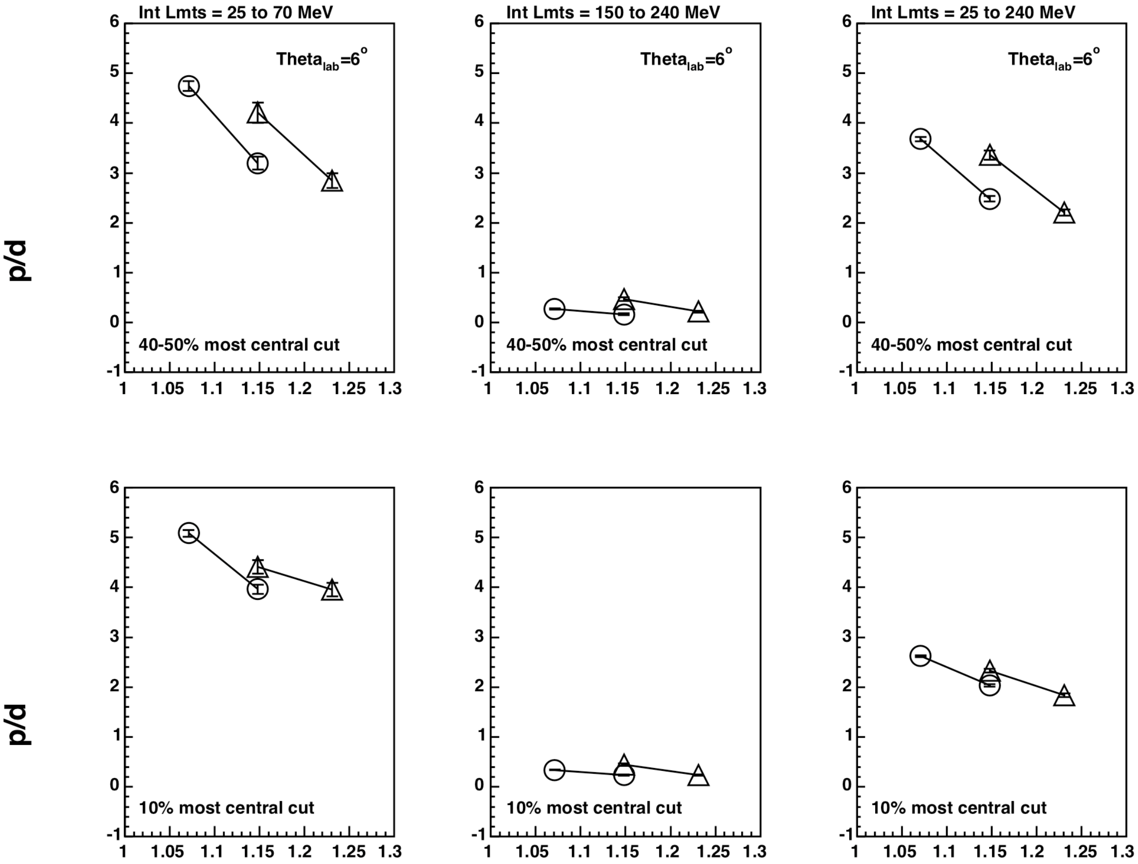

Fig. 53. p/d ratio value dependence on integration limit range at theta$_{lab}$=6° for data cut on the 10% most central events on the bottom and 40 to 50% most central on the top for 35 MeV/nucleon ^{58}Ni, ^{58}Fe on ^{58}Ni (circles) and ^{58}Ni, ^{58}Fe on ^{58}Fe (triangles).

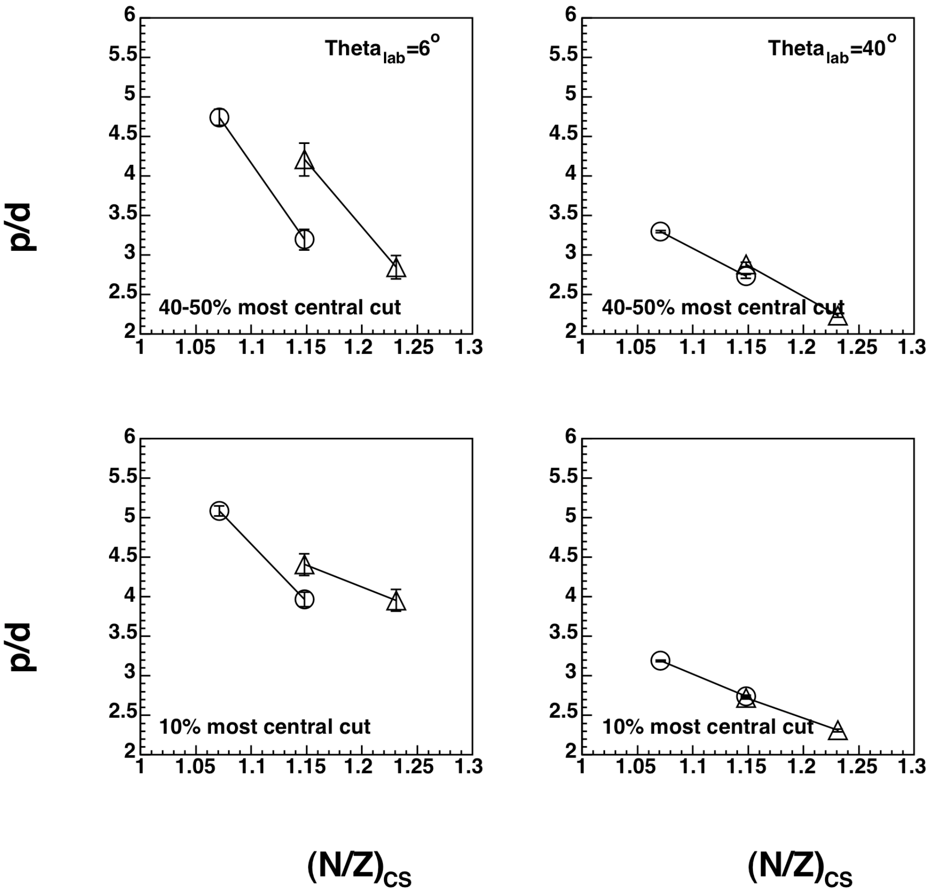

Fig. 54. p/d ratio equilibration behavior difference between theta$_{lab}$=6° on the left and 40° on the right for data cut on the 10% most central events on the bottom and 40 to 50% most central on the top for 35 MeV/nucleon ^{58}Ni, ^{58}Fe on ^{58}Ni (circles) and ^{58}Ni, ^{58}Fe on ^{58}Fe (triangles).

In Fig. 54 are shown 35 MeV/nucleon p/d ratio values again at 40 to 50% most central (top row) and 10% most central (bottom row), but this time with data from theta$_{lab}$=6° on the left two panels and data from theta$_{lab}$=40° on the right two panels. Whereas data from both angles shows movement toward greater N/Z equilibration (i.e., the mixed entrance channel systems ratio values become more similar), the data at the more forward angle shows more difference with centrality cut than the more backward angle. The more backward angle begins much closer to complete N/Z equilibration at a 40-50% most central cut and becomes completely N/Z equilibrated at the 10% most central cut. The data in Fig. 54 further supports the justification for assuming a sole intermediate velocity source at $\text{theta}_{\text{lab}}$=40°, as discussed in Chapter 4.

In Fig. 55 and Fig. 56 are shown isotope and isobar ratios from NIMROD at $\text{theta}_{\text{lab}}$= 40^0 (ring 9) with a centrality cut for the 10% most central events for the isotopes and 20% most central events for the isobars. The red data are at 45 MeV/nucleon beam energy and the black data are at 35 MeV/nucleon beam energy. From left to right, the circles represent ratio values from the systems ^{58}Ni on ^{58}Ni and ^{58}Fe on ^{58}Ni and the triangles represent ratio values from the systems ^{58}Ni on ^{58}Fe and ^{58}Fe on ^{58}Fe. The solid lines connect the two systems' ratios sharing the same target. The error bars shown are purely statistical.

The same $(N/Z)_{CS}$ but different target and projectile combination data points in Fig. 55 show equilibrated behavior in all isotope ratios, with the exception of $^{3/4}$He. The same $(N/Z)_{CS}$ but different target and projectile combination data points in Fig. 56 show equilibrated behavior in all isobar ratios, with the exception of t/^{3}He. It has been previously shown [13] that light charged particles at intermediate beam energies and at $\text{theta}_{\text{lab}}$=40° are not emitted from a fully combined target and projectile system, but from a smaller subset of the target and projectile which has not yet fully combined. For instance, if the ratio values of the light charged particles are plotted not as a function of the combined systems' N/Z, but as a function of an unequal mixture of target and projectile nucleons, a linear trend can be seen in the ratio values.

Shown again in Fig. 57 are the isotopic and isobaric ratio values for all ratios which include LCPs, p/d, d/t, p/t, $^{3/4}$He and t/^{3}He with a cut of 10% most central for the isotopes and 20% most central for the isobars. In the case of p/d, in the top row of Fig. 57, the data appear to be equilibrated and linearly dependent to fully combined target and projectile systems' N/Z. In the case of d/t and p/t yield ratio data, in the second and third rows of Fig. 57, the data appear to be equilibrated at 45 MeV/nucleon beam energy and not at 35 MeV/nucleon beam energy. In last two rows of data, the $^{3/4}$He and t/^{3}He ratios do not show N/Z equilibration at either beam energy.

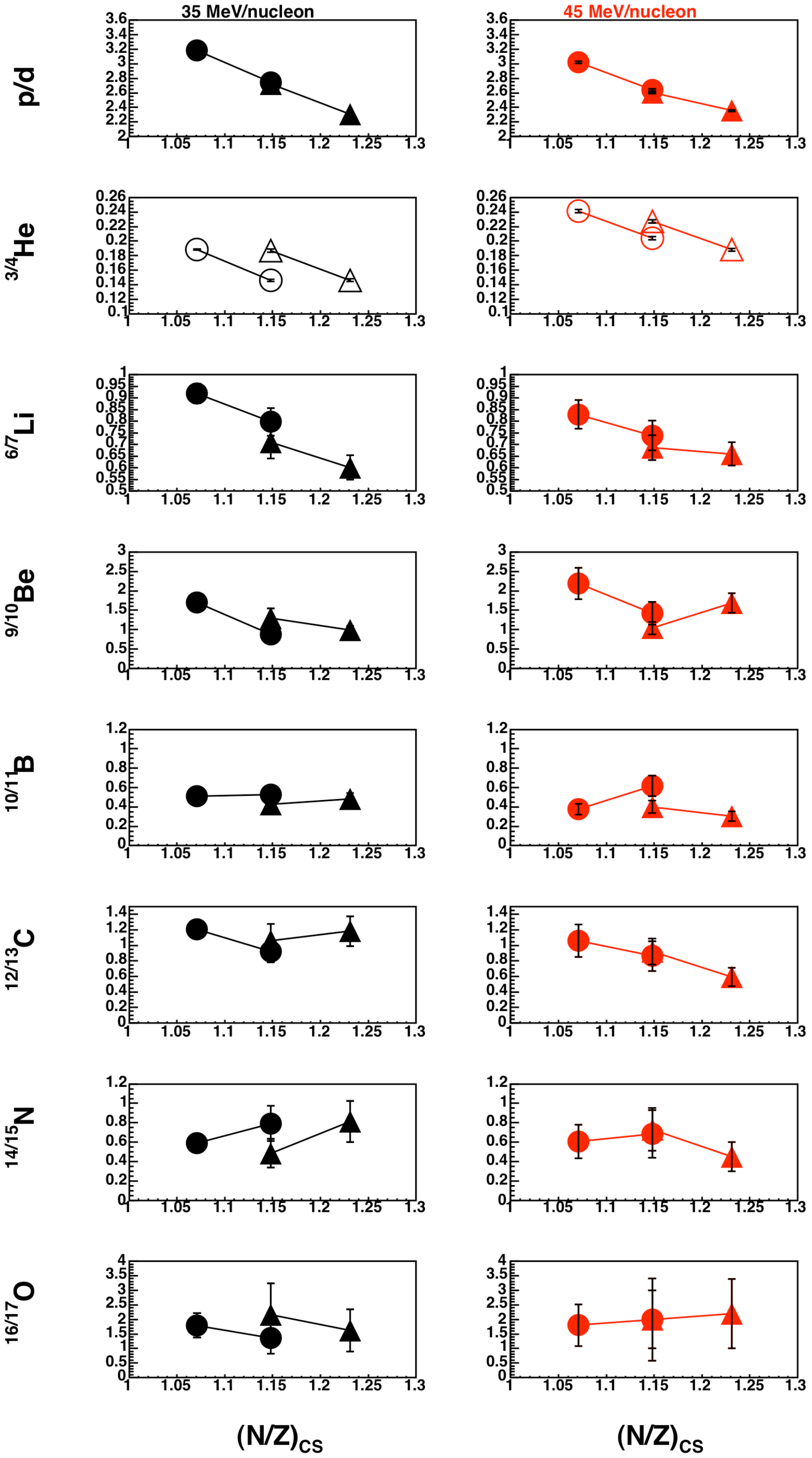

Fig. 55. Isotope yield ratios from NIMROD for data from theta$_{lab}$= 40^0 (ring 9) with a centrality cut for the 10% most central events for 35 (black) and 45 (red) MeV/nucleon ^{58}Ni, ^{58}Fe on ^{58}Ni (circles) and ^{58}Ni, ^{58}Fe on ^{58}Fe (triangles).

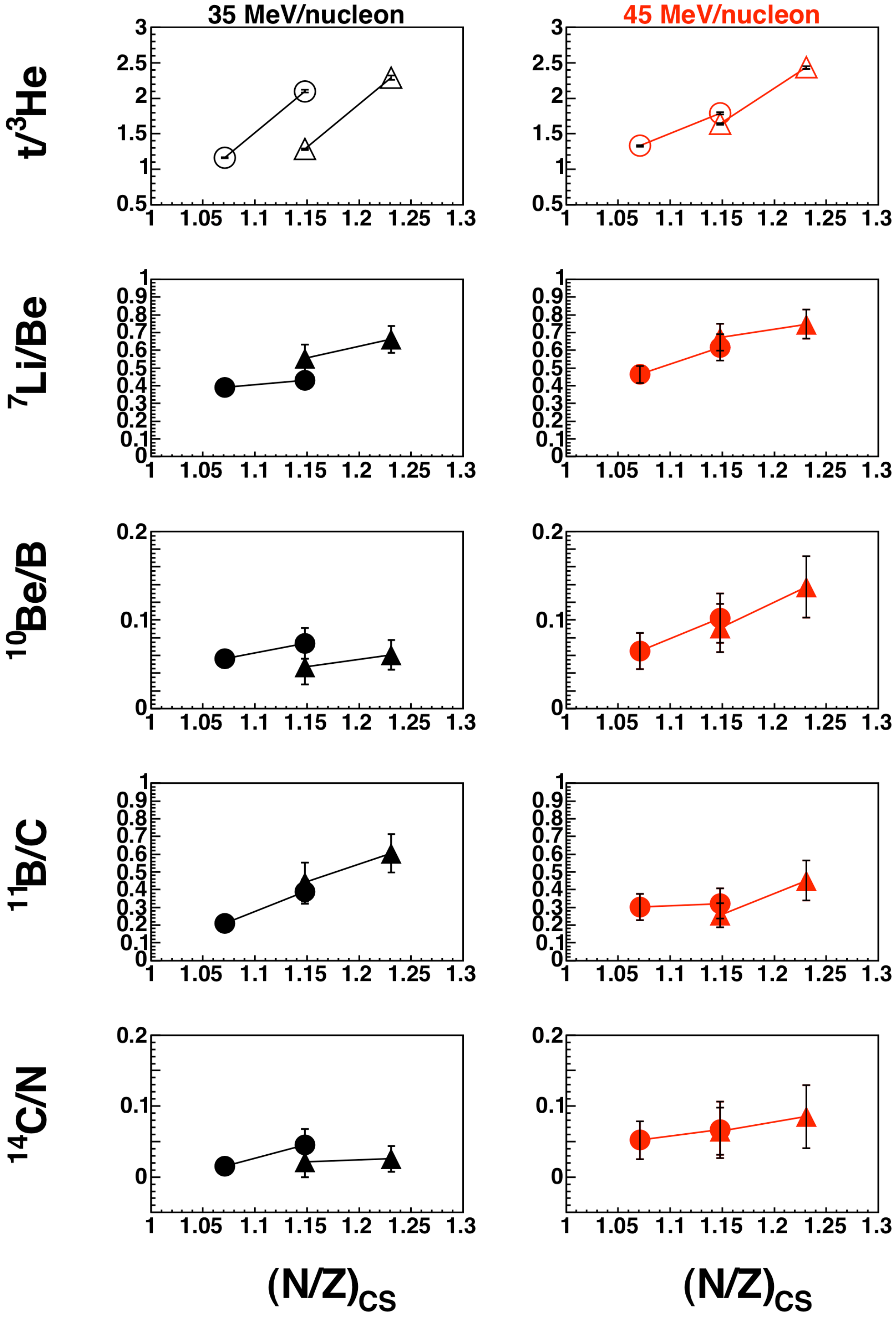

Fig. 56. Isobar yield ratios from NIMROD for data from theta$_{lab}$= 40^0 (ring 9) with a centrality cut for the 20% most central events for 35 (black) and 45 (red) MeV/nucleon ^{58}Ni, ^{58}Fe on ^{58}Ni (circles) and ^{58}Ni, ^{58}Fe on ^{58}Fe (triangles).

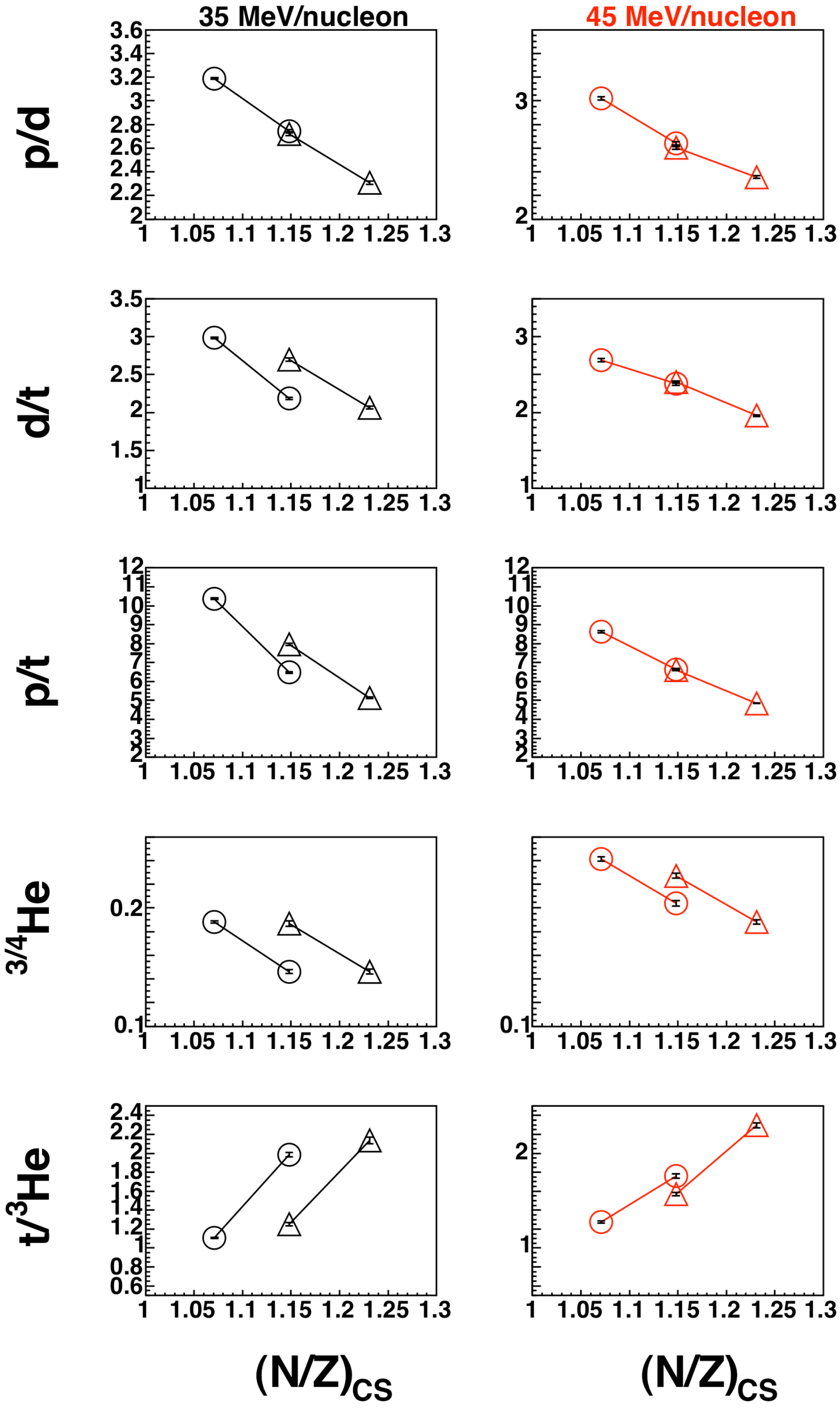

Fig. 57. LCP yield ratios from NIMROD for data from theta$_{lab}$= 40^0 (ring 9) with a centrality cut for the 10% most central events for isotopes and 20% most central events for isobars for 35 (black) and 45 (red) MeV/nucleon ^{58}Ni, ^{58}Fe on ^{58}Ni (circles) and ^{58}Ni, ^{58}Fe on ^{58}Fe (triangles).

In the case where N/Z equilibration is not seen, the process by which one may discern the approximate contribution of target and projectile nucleons in the emission source (described in ref. [13]) is utilized in the current study. In Fig. 58 are shown 35 MeV/nucleon beam energy d/t ratio values. In Fig. 59 are shown 35 MeV/nucleon beam energy p/t ratio values. In Fig. 60 and Fig. 61 are shown $^{3/4}$He ratio values at 35 and 45 MeV/nucleon beam energies. In Fig. 62 and Fig. 63 are shown t/^{3}He ratio values at 35 and 45 MeV/nucleon beam energies.

In Fig. 58 through Fig. 63 are shown each ratio in Fig. 57 which showed nonequilibrated N/Z behavior replotted as a function of a various mixtures of target and projectile nucleons. These data are cut for the 10% most central events for the isotopes and 20% most central for the isobars. The unscaled data are shown in red squared symbols and the scaled data are shown in triangles, circles, squares, etc. The error bars shown are purely statistical and the dotted lines are a least squares linear fit to the set of scaled data. In each of these figures, the legends note the value of X, where X is the ratio of target to projectile nucleons in the parameter along the x axis. The best linear fit closely describes the N/Z of the emitting source.

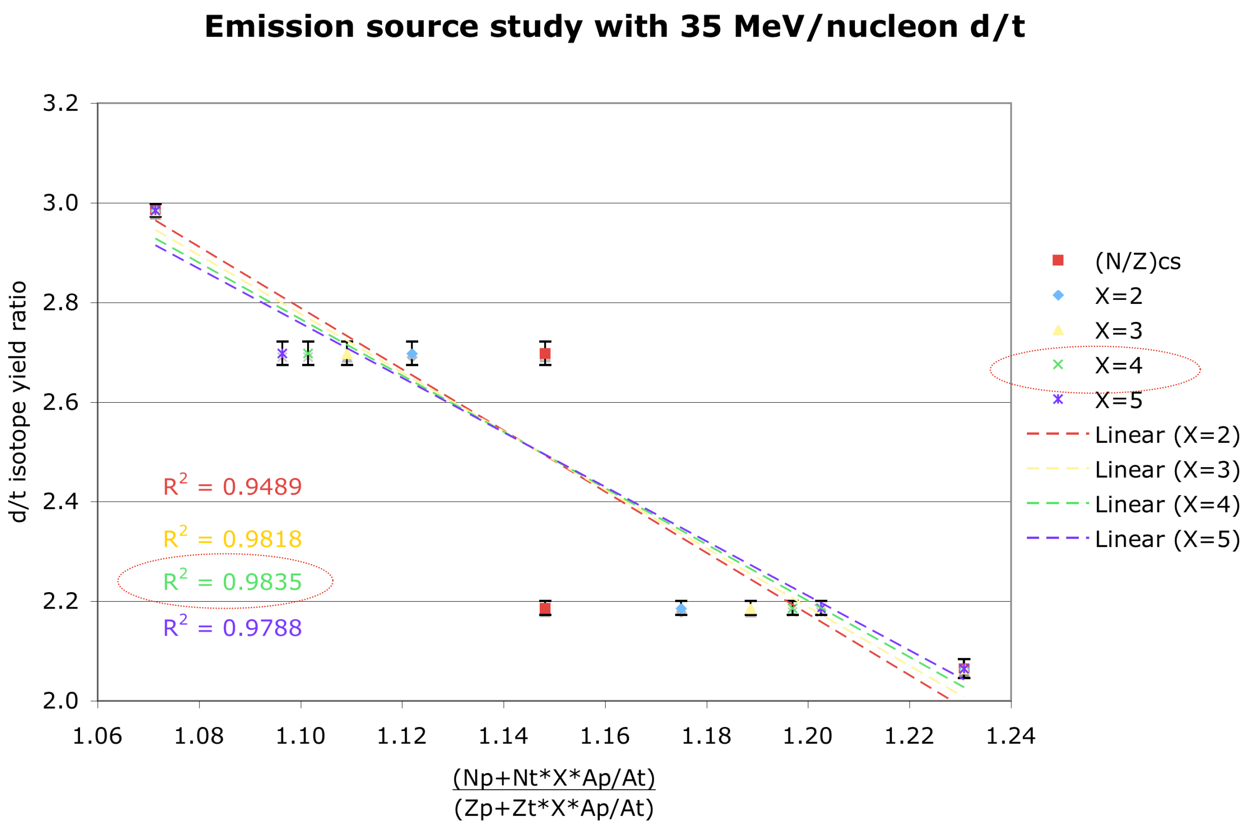

Fig. 58. d/t isotope ratios at 35 MeV/nucleon for data from theta$_{lab}$= 40^0 (ring 9) with a centrality cut for the 10% most central events plotted as a function of a combined system with varying contribution from target and projectile.

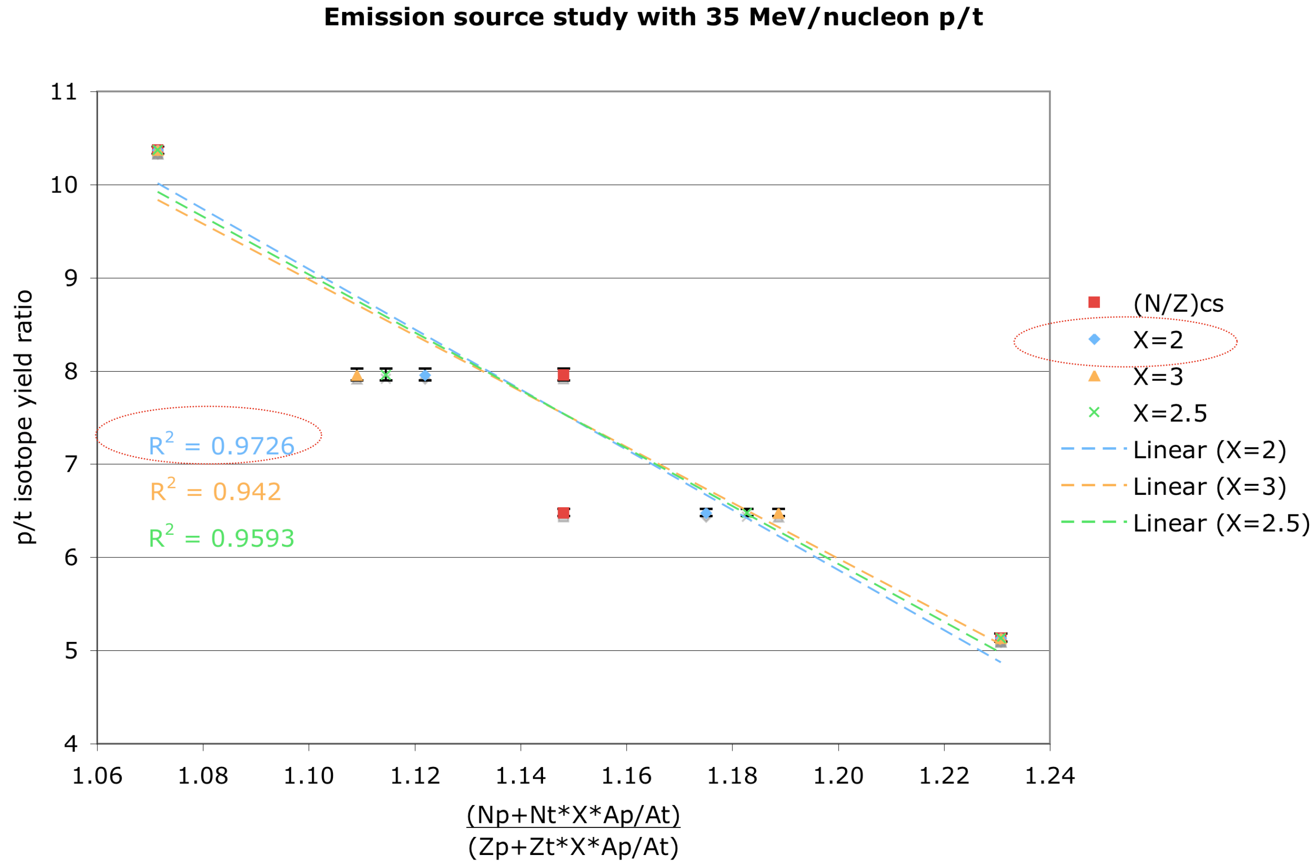

Fig. 59. p/t isotope ratios at 35 MeV/nucleon for data from $\text{theta}_{\text{lab}} = 40^0$ (ring 9) with a centrality cut for the 10% most central events plotted as a function of a combined system with varying contribution from target and projectile.

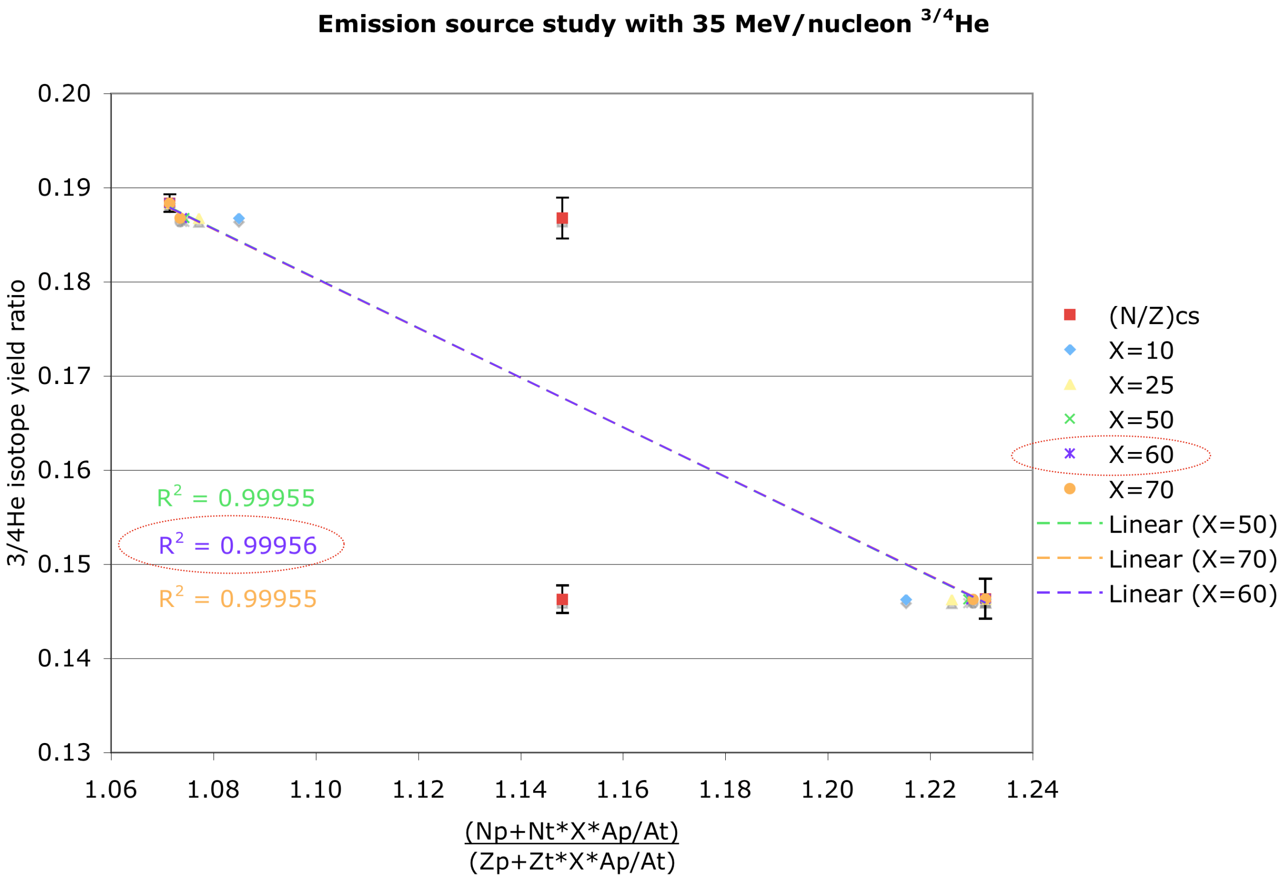

Fig. 60. $^{3/4}$He isotope ratios at 35 MeV/nucleon for data from theta$_{lab}$= 40^0 (ring 9) with a centrality cut for the 10% most central events plotted as a function of a combined system with varying contribution from target and projectile.

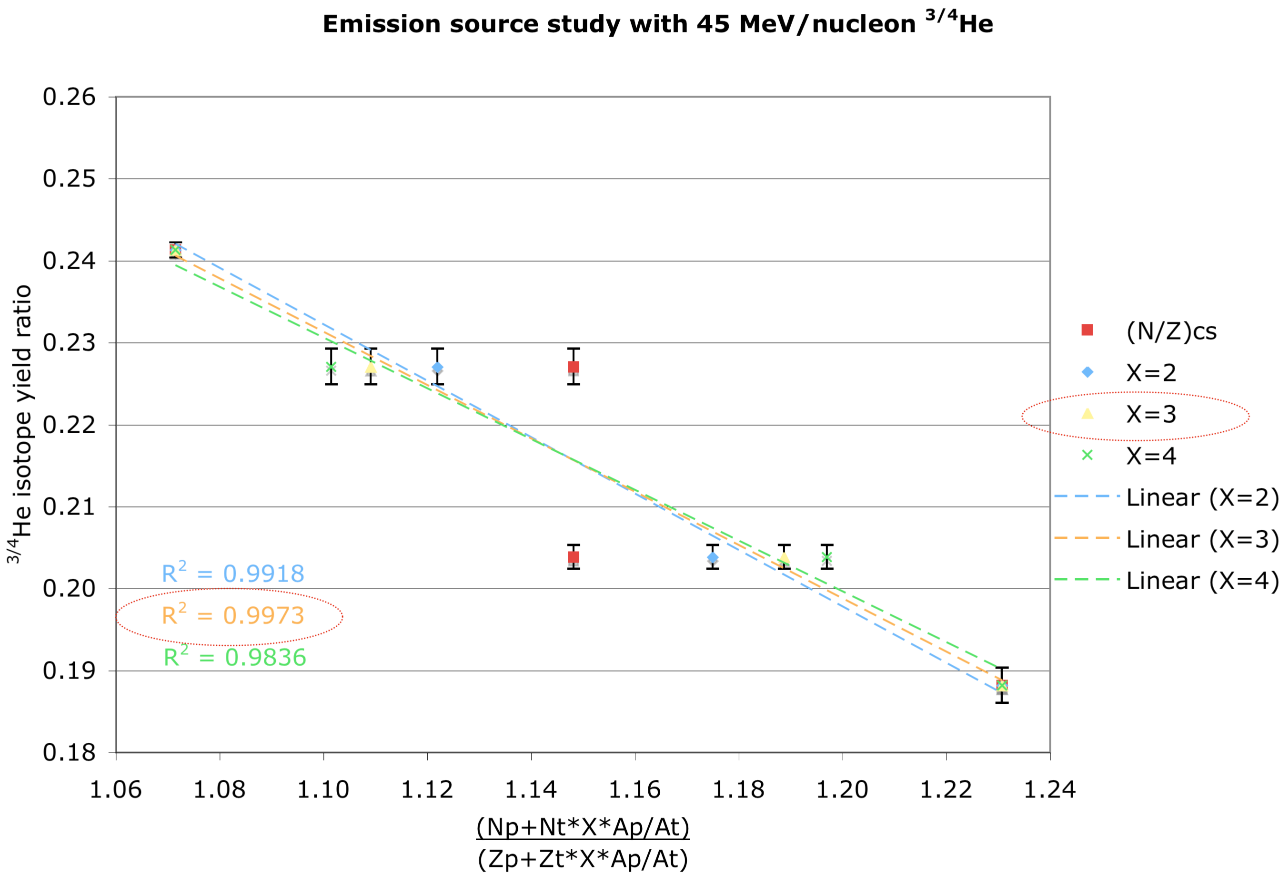

Fig. 61. $^{3/4}$He isotope ratios at 45 MeV/nucleon for data from theta$_{lab}$= 40^0 (ring 9) with a centrality cut for the 10% most central events plotted as a function of a combined system with varying contribution from target and projectile.

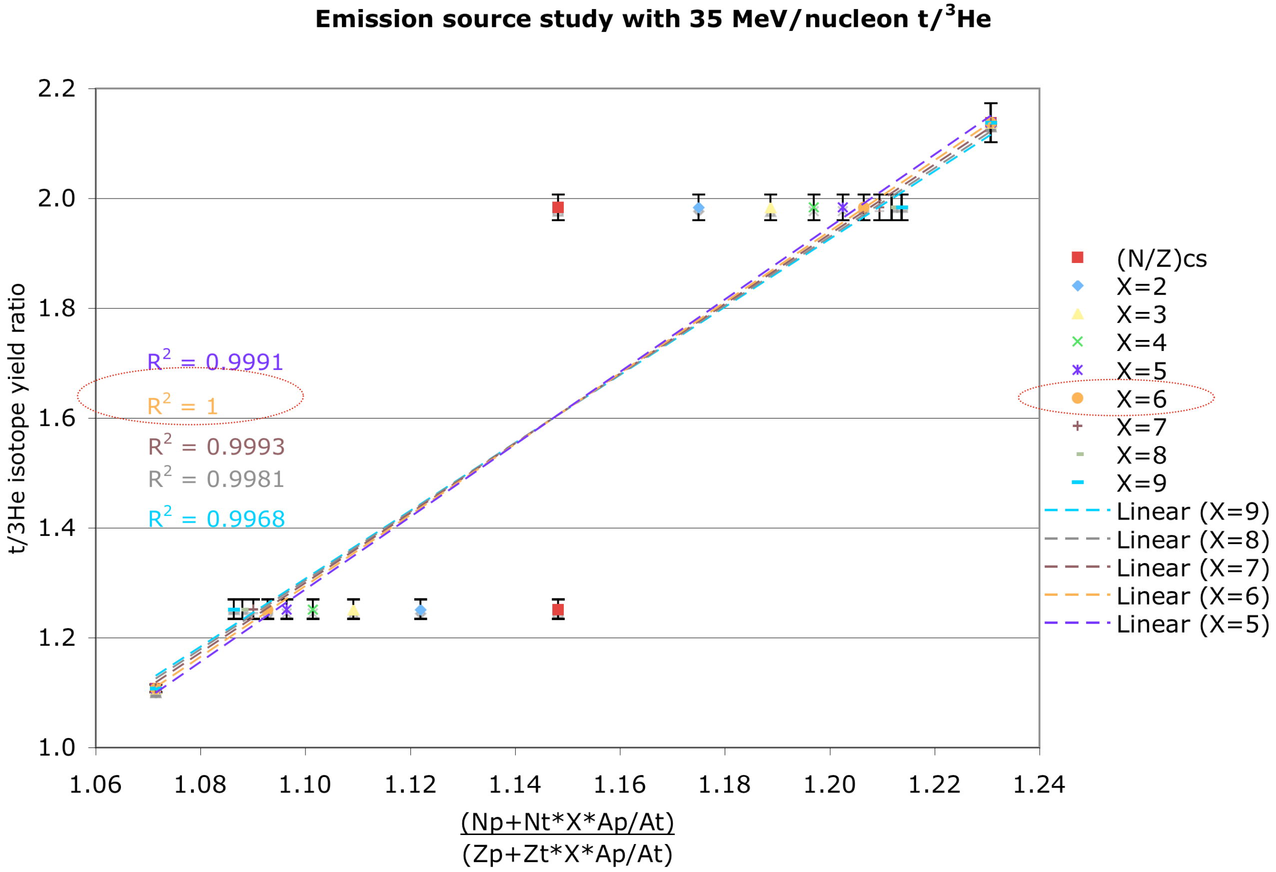

Fig. 62. t/^{3}He isotope ratios at 35 MeV/nucleon for data from theta$_{lab}$= 40^0 (ring 9) with a centrality cut for the 20% most central events plotted as a function of a combined system with varying contribution from target and projectile.

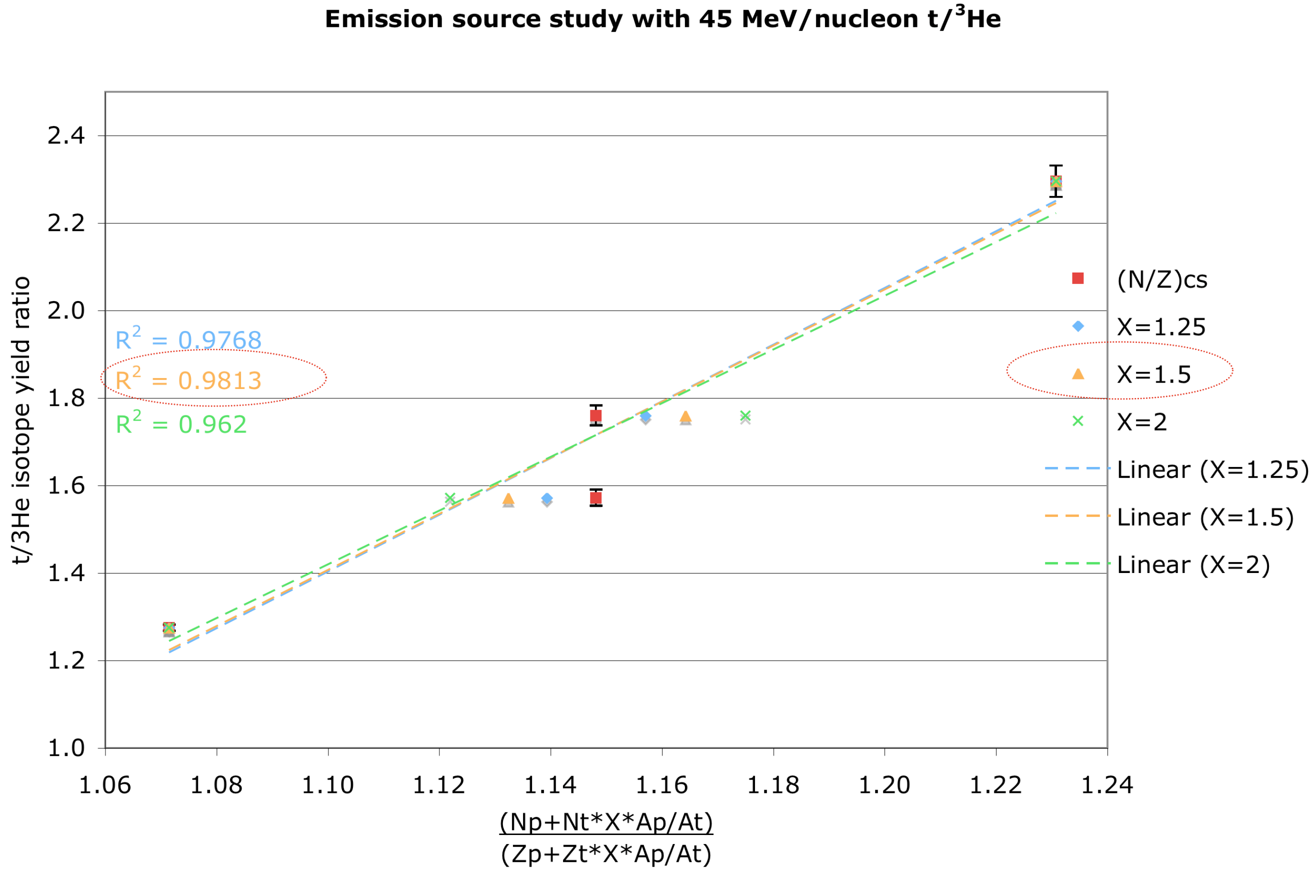

Fig. 63. t/^{3}He isotope ratios at 45 MeV/nucleon for data from theta$_{lab}$= 40^0 (ring 9) with a centrality cut for the 20% most central events plotted as a function of a combined system with varying contribution from target and projectile.

Beginning with the lighter fragments, in Fig. 58, the admixture of target and projectile nucleons comes close to a linear approximation when plotted with the experimental d/t ratio values with 35 MeV/nucleon beam energy when the mixture is 1 part target and 4 parts projectile nucleons. This suggests deuterons and tritons (at 35 MeV/nucleon beam energy) are emitted at a point when the target and projectile have only partially combined.

In Fig. 59, the ratio of target to projectile nucleons which can be plotted most linearly with the experimental p/t ratio values at 35 MeV/nucleon is 1 part target nucleons to 2 parts projectile nucleons. This suggests that protons are emitted from a source which is slightly less mixed than deuterons.

In Fig. 60 and Fig. 61 are shown $^{3.4}$He ratio values at 35 and 45 MeV/nucleon plotted again as a function of the unequal projectile and target nucleon source. These data are cut for the 10% most central data. At 35 MeV/nucleon (Fig. 60), the amount of mixing suggested by the most linear fit implies a ratio of 1:60 target to projectile nucleons. This means that $^{3/4}$He ratio fragments are emitted from a source that is mostly projectle like with very little target mixed in. One could say the $^{3/4}$He ratio reflects only the N/Z of the projectile. In direct large contrast to that, however, in Fig. 61, the $^{3/4}$He ratio data with 45 MeV/nucleon beam energy are best described by an emitting source made up of 1 part target and 3 parts projectile.

In Fig. 62 and Fig. 63 are shown ratio values for t/^{3}He ratios plotted in the same fashion as the last few figures. For data at 35 MeV/nucleon beam energy, the mixing of target and projectile which gives the most linear fit is 1:6 target to projectile. For data at 45 MeV/nucleon, the mixing of target and projectile which gives the most linear fit is 1:1.5 target to projectile nucleons.

At theta$_{lab}$=40° with 10% most central cut, the ratios which include A=3 fragments stand out as coming from the most nonequilibrated N/Z emitting source at both beam energies. On the whole, the Z=1 fragments with the same bias, seem to come from a much more N/Z equilibrated source than the A=3 and Z=2 fragments at both beam energies. The fragments seen at $\text{theta}_{\text{lab}}=40^{\circ}$ with 10% most central cut with Z>2 (IMFs) show equilibration in both beam energies.

In summary, by using the isotopic and isobaric ratios to study N/Z equilibration of 35 and 45 MeV/nucleon data, one can see that, within error bars, ratios involving IMFs are fully N/Z equilibrated at both energies and that ratios involving LCPs have mixed results at $\text{theta}_{\text{lab}}=40^{\circ}$. Any ratio at $\text{theta}_{\text{lab}}=40^{\circ}$ which includes an A=3 fragment shows N/Z nonequilibration at one or both energies. The next step is to compare these results to the N/Z tracer method [18] data results.

Experimental N/Z tracer terms

One way to use the N/Z tracer method is to use ratios of isotopes and isobars instead of the collected charge in a given cell of momentum space. Equation 10 shows how an example of an N/Z tracer term for the isotopic yield ratio of p/d is calculated for the two symmetric and two asymmetric reactions ^{58}Fe and ^{58}Ni on ^{58}Fe and ^{58}Ni.

$$N/Z\_tracer\_term = \frac{2*(p/d)_X - (p/d)_{NiNi} - (p/d)_{FeFe}}{(p/d)_{NiNi} - (p/d)_{FeFe}}, \qquad (10)$$

where $(p/d)_X$ is the isotopic yield ratio of protons to deuterons from one of the four systems, $(p/d)_{\text{NiNi}}$ is the ratio of protons to deuterons from ^{58}Ni on ^{58}Ni and $(p/d)_{\text{FeFe}}$ is the proton to deuteron yield ratio from ^{58}Fe on ^{58}Fe. If X equals NiNi, the value of the N/Z tracer term is positive one. If X equals FeFe, then the value of N/Z tracer term equals negative one. If X equals NiFe or FeNi, then N/Z tracer term takes on an intermediate value between positive and negative one. As an example, take the (p/d) ratio values for each system and substitute the $(N/Z)_{\text{CS}}$ for each system, one gets the value of 1 for the NiNi = X, 0.0375 for FeNi = NiFe = X, and -1 for FeFe = X. The isotopic and isobaric ratios with sufficient statistics for N/Z tracer term study are relegated to the LCPs. Therefore, N/Z tracer terms using p/d, d/t, p/t, $^{3/4}$He, and t/^{3}He will be studied.

In Fig. 64 through Fig. 68 are N/Z tracer terms calculated using data from theta$_{lab}$=40°. The top panels show 35 MeV/nucleon beam energy data in black symbols. The bottom panels show 45 MeV/nucleon beam energy data in red symbols. The x and cross symbols represent the mirror systems of ^{58}Ni on ^{58}Ni and ^{58}Fe on ^{58}Fe. The triangles represent the mixed system of ^{58}Ni on ^{58}Fe and the circles represent the mixed system of ^{58}Fe on ^{58}Ni. As one looks from right to left in Fig. 64 through Fig. 68, the centrality cut of the data is increasing in 10% increments from 40 to 50% most central at the right to 10% most central at the left. If the two mixed system data trends come together at the left, then mixing is said to be complete and N/Z equilibration has occurred prior to emission of the fragments in the ratio used for the N/Z tracer term. If not, then N/Z equilibration is not complete before fragment emission.

From the data using isobaric and isotopic ratios, one can expect that the N/Z tracer term using the p/d ratio at both beam energies to show a source which is characteristic of a combined target and projectile system. And, the N/Z tracer term using d/t and p/t at 45 MeV/nucleon should also show an emission source which is characteristic of a combined target and projectile system. One can also expect that the ratios d/t and p/t at 35 MeV/nucleon as well as the $^{3/4}$He and t/^{3}He ratios at both beam energies will show an emission source which is projectile-like when used to calculate and plot N/Z tracer term trends.

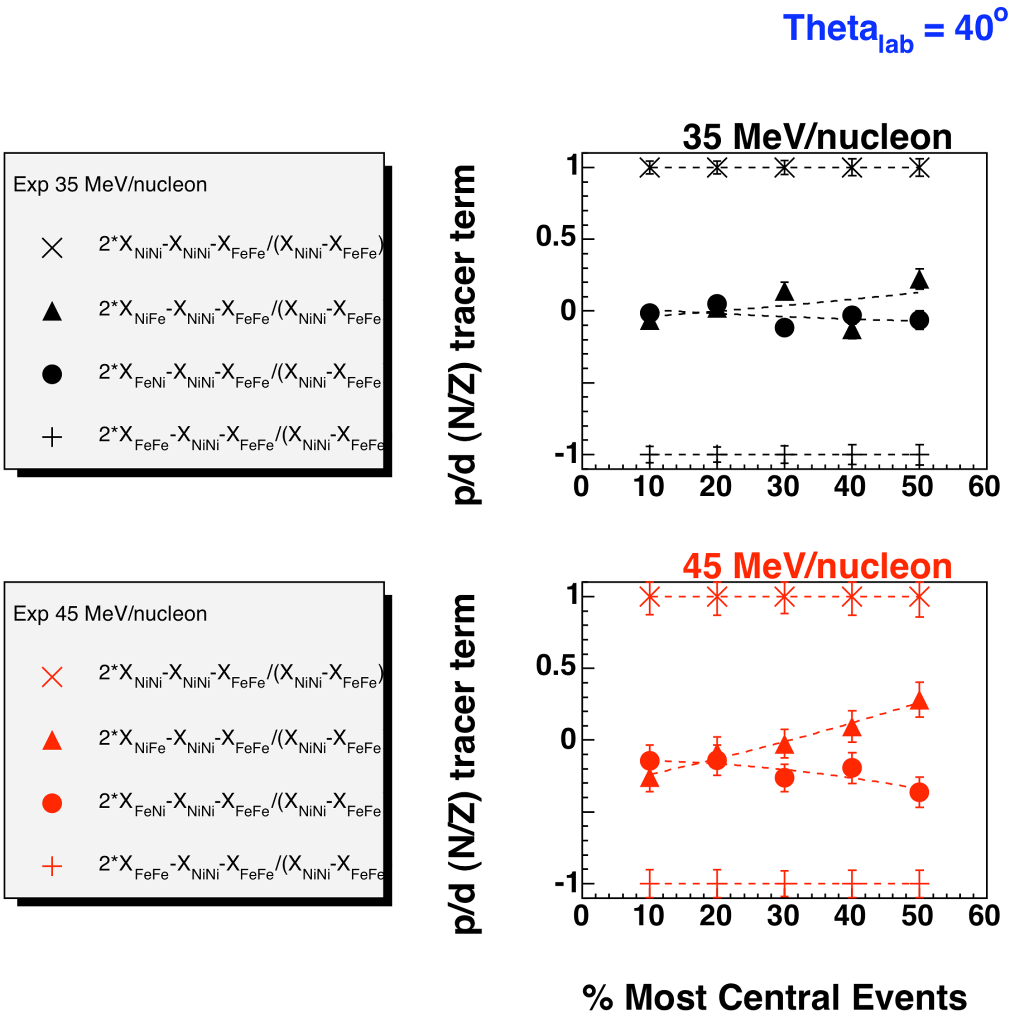

Fig. 64. N/Z tracer term using p/d ratio from theta$_{lab}$=40° plotted as a function of centrality.

The N/Z tracer term calculated using p/d, as seen in Fig. 64, shows emission from a combined target and projectile system at both energies of 35 and 45 MeV/nucleon. This result agrees well with the result from the isotope ratio trend in Fig. 55 and in Fig. 57.

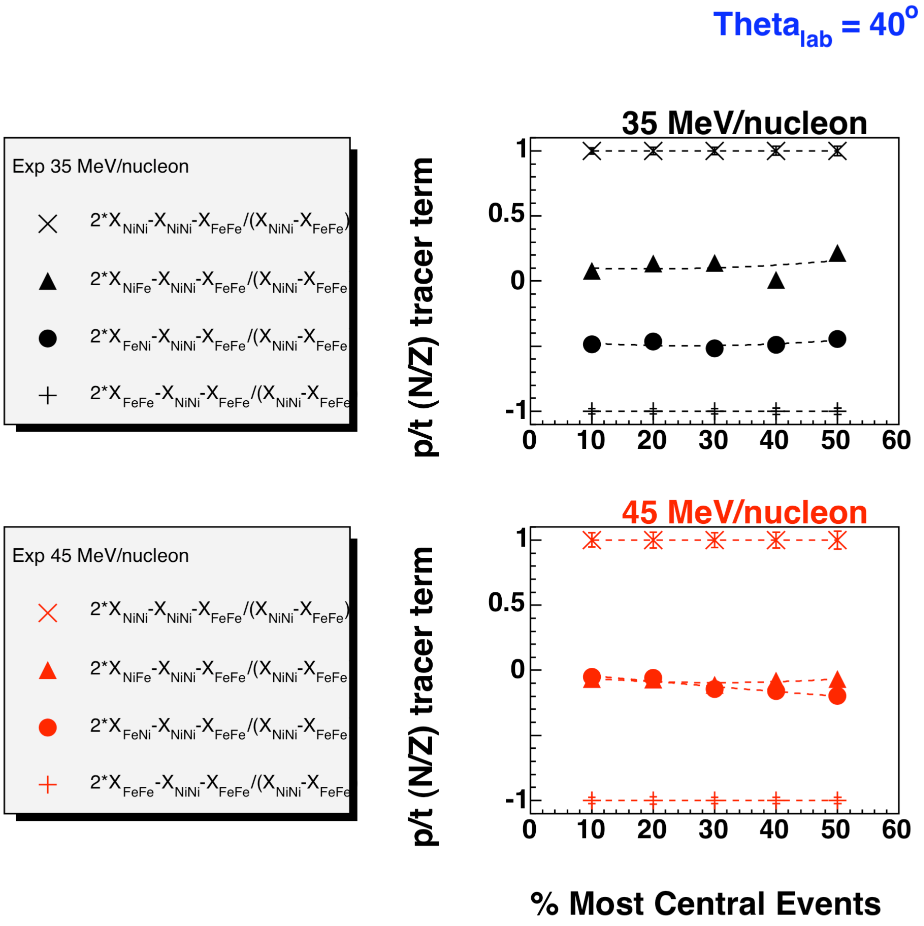

Fig. 65. N/Z tracer term using p/t ratio from theta$_{lab}$=40° plotted as a function of centrality.

In Fig. 65 are seen N/Z tracer terms calculated using p/t yield ratios from theta$_{lab}$=40°. Unlike the N/Z tracer term calculated using p/d (Fig. 64), the 35 MeV/nucleon N/Z tracer terms trend for p/t show an emitting source which is projectile-like. The 45 MeV/nucleon N/Z tracer term trend with the p/t ratio looks to be emitted from a well-combined target and projectile system. This suggests that deuterons and tritons emitted at theta$_{lab}$=40° at 35 and 45 MeV/nucleon are emitted from sources with differing N/Zs.

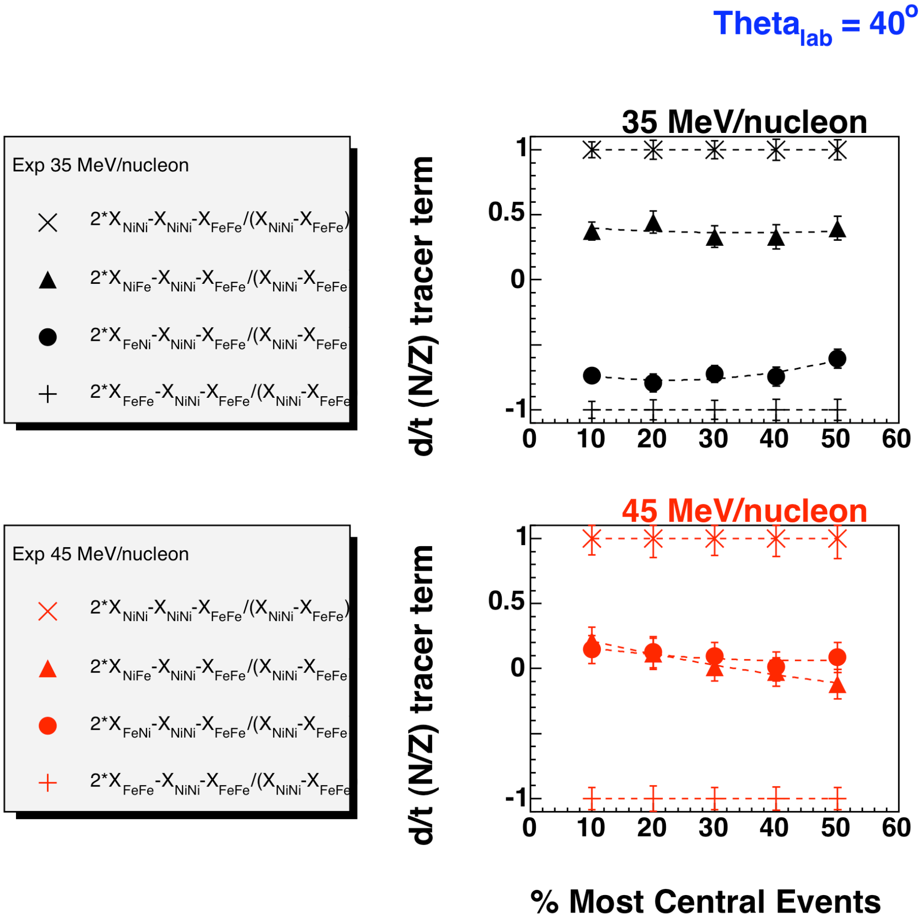

Fig. 66. N/Z tracer term using d/t ratio from theta$_{lab}$=40° plotted as a function of centrality.

In Fig. 66 are seen N/Z tracer terms calculated using d/t yield ratios from theta$_{lab}$=40°. Again, the 35 MeV/nucleon N/Z tracer terms trend for d/t show little progress toward N/Z equilibrium. The 45 MeV/nucleon N/Z tracer term trend with d/t looks to be fully N/Z equilibrated within error bars at all centrality cuts. This supports the conclusion that deuterons and tritons are emitted from source with characteristics of the projectile at 35 MeV/nucleon and of the combined system at 45 MeV/nucleon.

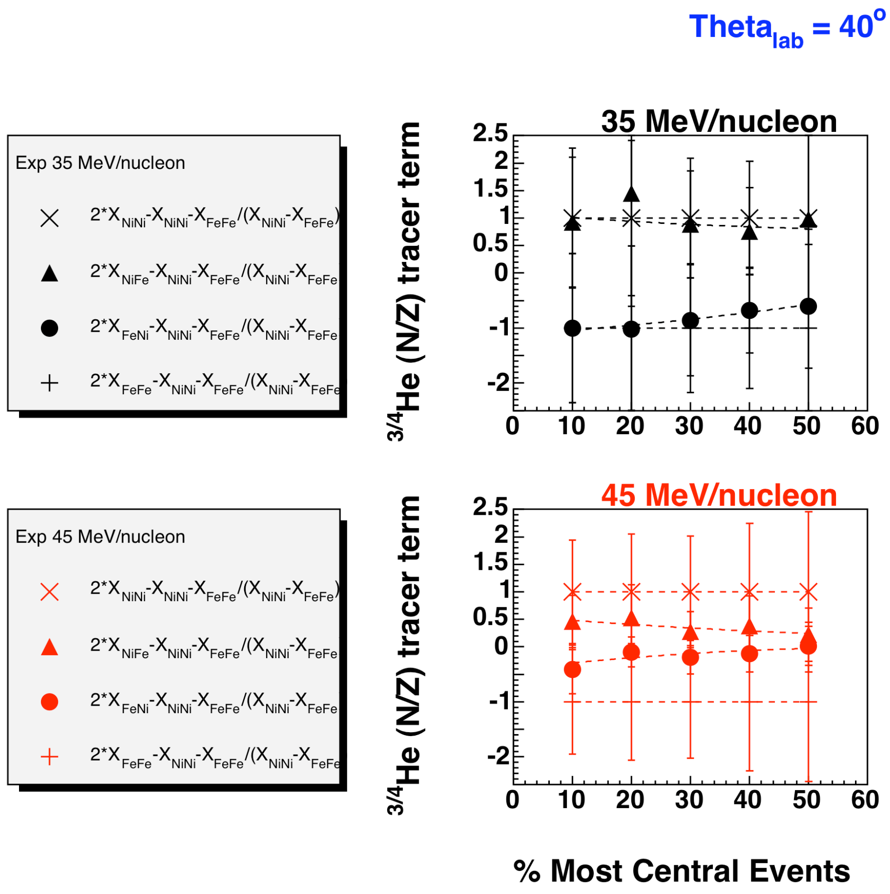

Fig. 67. N/Z tracer term using $^{3/4}$He ratio from theta$_{lab}$=40° plotted as a function of centrality.

In Fig. 67 are shown the N/Z tracer terms calculated with $^{3/4}$He isotopic ratio values. The error bars on these data are quite large, however the N/Z trend seen progresses in a mostly non-random fashion. Within the context of the large error bars, the trend of the N/Z $^{3/4}$He tracer term shows that ^{3}He and ^{4}He fragments are emitted from a source which is characteristic of the projectile. In Fig. 55 and Fig. 57 (and later in Fig. 60 and Fig. 61), one certainly sees evidence of an emitting source which is predominantly projectile-like (combined system-like) when considering the $^{3/4}$He ratio values at 35 MeV/nucleon (45 MeV/nucleon). These N/Z $^{3/4}$He tracer term results are consistent with the picture shown using isotope ratios.

In Fig. 68 are shown the N/Z tracer terms calculated using the t/^{3}He isobaric ratio values. As before, in Fig. 62 and Fig. 63, one again sees evidence of projectile-like emitting source, which is previously shown to have ratio of target to projectile nucleons of 1:6 (1:1.5) when using the t/^{3}He ratio values at 35 MeV/nucleon (45 MeV/nucleon) in the emission source study from ref. [13]. These N/Z t/^{3}He tracer term results are also consistent with the conclusion that A=3 fragments (as well as alphas) are emitted from a source which is characteristic of the projectile at both beam energies. Also, the t/^{3}He results show that the emitting source more projectile-like at 35 MeV/nucleon beam energy and more combined system-like at 45 MeV/nucleon beam energy.

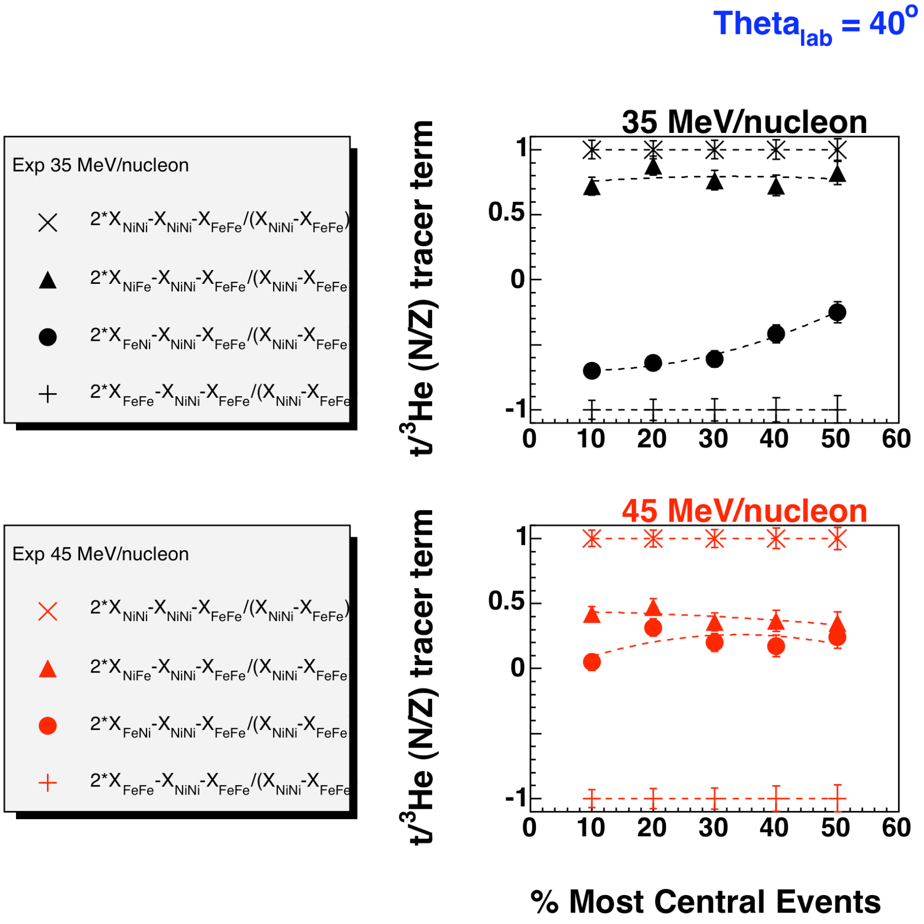

Fig. 68. N/Z tracer term using t/^{3}He ratio from theta$_{lab}$=40° plotted as a function of centrality.

CHAPTER VI
SIMULATION RESULTS

AMD-V is run to simulate the reactions of 35 and 45 MeV/nucleon ^{58}Ni, Fe on ^{58}Ni, Fe on computers at the VPP700E supercomputer facility in RIKEN, Japan [101]. The hard equation of state equation of state, EOS, (K=360 MeV) is employed by AMD-V during calculations. The dynamic calculations are stopped at a time of 280 fm/c, adequately allowing for the excitation of the nucleons involved in the collision [102]. The excited fragments are then fed to GEMINI 100 times for each event. These events are filtered for NIMROD angular acceptance and energy thresholds and analyzed in the same manner as the experimental data with one exception. Due to the low number of statistics available of AMD-V/GEMINI data and since AMD-V/GEMINI does not contain experimental detector threshold issues, the integration limits for the following theta$_{lab}$=40° data are opened to include the full range of the energy spectra. The effect of comparing experimental and simulation data with differing integration limits may make some change in the magnitude of the ratio values, but should have little effect on the equilibration behavior, as is shown earlier in Chapter 5.

Integration limits for the AMD-V/GEMINI data are tabulated in Table 17 below as a function of the ratio. The ratios listed are those retaining sufficient statistics after the detector filter with the more inclusive integration limits.

Table 17. AMD-V/GEMINI integration limits.

Ratio	Limits (MeV)
p/d	20,70
3/4He	50,150
6/7Li	100,200
t/3He	40,110
7Li/Be	80,230

In Fig. 69 are shown isotopic ratios p/d, $^{3/4}$He, and $^{6/7}$Li from theta$_{lab}$=40^{o} with a cut for the 10% most central events plotted as a function of the combined projectile and target N/Z with AMD-V/GEMINI results overlaid. The red (blue) experimental (simulation) data are at 45 MeV/nucleon beam energy and the black (green) experimental (simulation) data are at 35 MeV/nucleon beam energy. From left to right, the circles represent ratio values from the systems ^{58}Ni on ^{58}Ni and ^{58}Fe on ^{58}Ni and the triangles represent ratio values from the systems ^{58}Ni on ^{58}Fe and ^{58}Fe on ^{58}Fe. The solid lines connect the two systems' ratios sharing the same target. The error bars shown are purely statistical.

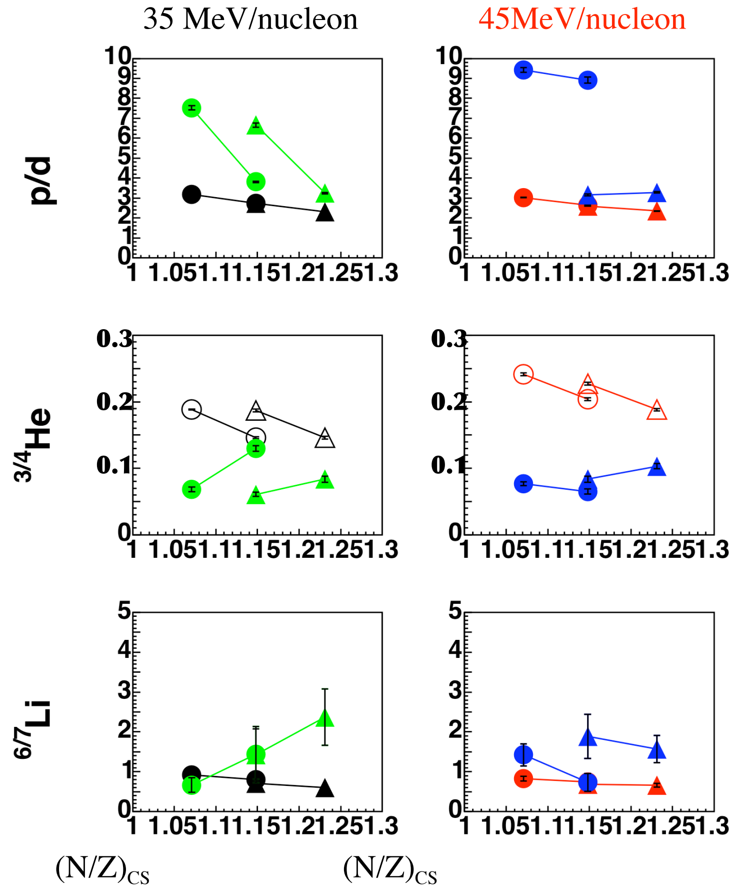

Fig. 69. Isotope ratios for AMD-V/GEMINI data from theta$_{lab}$= 40^0 (ring 9) with a centrality cut for the 10% most central events. Circles are ^{58}Fe on ^{58}Fe and ^{58}Ni on ^{58}Fe. Triangles are ^{58}Fe on ^{58}Ni and ^{58}Ni on ^{58}Ni. Red and black are experimental 35 and 35 MeV/nucleon data, respectively. Green and blue are AMD-V/GEMINI 35 and 45 MeV/nucleon data, respectively.

Ignoring the differences in magnitude (which may be due to the difference in integration limit ranges), the simulation data in Fig. 69 still does a poor job of matching the experimental result of the amount of N/Z equilibration in the cases of 35 and 45 MeV/nucleon p/d ratio data, 35 MeV/nucleon $^{3/4}$He ratio data and 45 MeV/nucleon $^{6/7}$Li ratio data. The N/Z equilibration behavior of the 45 MeV/nucleon $^{3/4}$He ratio data and the 35 MeV/nucleon $^{6/7}$Li ratio is reproduced by the simulation data, but the N/Z dependence of these observables is not well matched. The simulation data fail to reproduce the experimental results in all but two of the observables in Fig. 69.

In Fig. 70 are shown isobaric ratios t/^{3}He and ^{7}Li/Be with AMD-V/GEMINI and experimental results. These data are at 40 degrees in the lab frame and are cut for the 20% most central events. For these experimental results, the AMD does a fair job of reproducing the equilibration and trend behavior for the A=7 but not the A=3 observables. The N/Z equilibration experimental behavior in the ^{7}Li/Be ratio at both 35 and 45 MeV/nucleon is reproduced by the simulation results. The N/Z nonequilibration experimental behavior in the t/^{3}He ratio is not reproduced by the simulation results, which show N/Z equilibrated behavior for the t/^{3}He ratios at both energies.

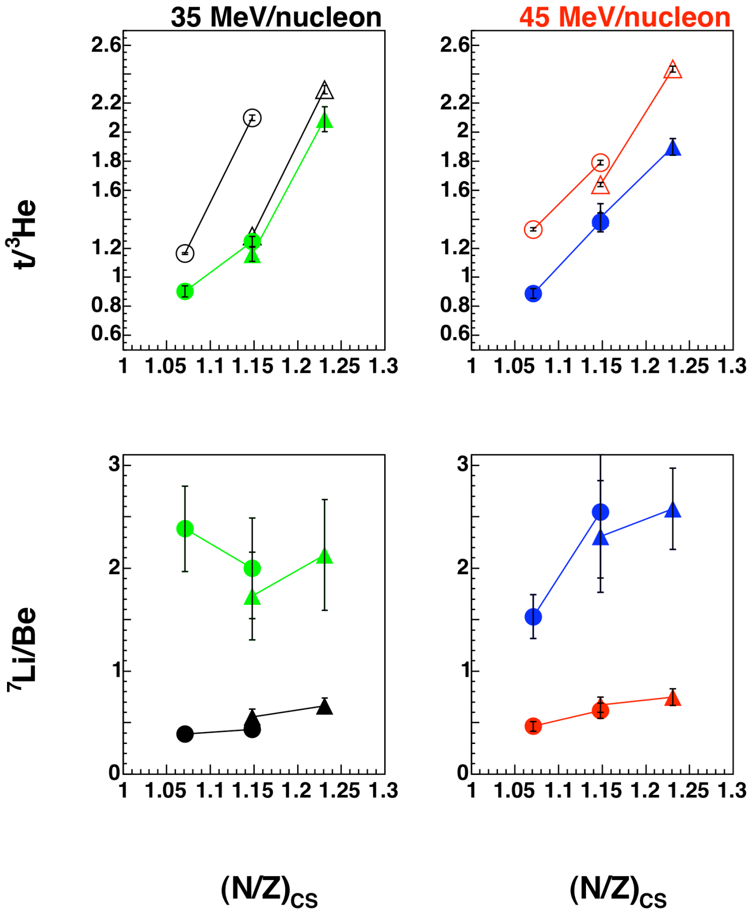

Fig. 70. Isobar ratios for AMD-V/GEMINI data from theta$_{lab}$= 40^0 (ring 9) with a centrality cut for the 20% most central events. Circles are ^{58}Fe on ^{58}Fe and ^{58}Ni on ^{58}Fe. Triangles are ^{58}Fe on ^{58}Ni and ^{58}Ni on ^{58}Ni. Red and black are experimental 35 and 35 MeV/nucleon data, respectively. Green and blue are AMD-V/GEMINI 35 and 45 MeV/nucleon data, respectively.

In Fig. 71 and Fig. 72 are shown p/d and p/t N/Z tracer term results with experimental and simulation results. The top panels show 35 MeV/nucleon beam energy experimental (simulation) data in black (green) symbols. The bottom panels show 45 MeV/nucleon beam energy experimental (simulation) data in red (blue) symbols. The x and cross symbols represent the mirror systems of ^{58}Ni on ^{58}Ni and ^{58}Fe on ^{58}Fe. The triangles represent the mixed system of ^{58}Ni on ^{58}Fe and the circles represent the mixed system of 58Fe on 58Ni. As one looks from right to left in Fig. 71 and Fig. 72, the centrality cut of the data is increasing in 10% increments from 40 to 50% most central at the right to 10% most central at the left. If the two mixed system data trends come together at the left, then mixing is said to be complete and N/Z equilibration has occurred prior to emission of the fragments in the ratio used for the N/Z tracer term. If not, then N/Z equilibration is not complete before fragment emission began.

AMD-V/GEMINI indicates a projectile-like source at 35 MeV/nucleon and a combined target and projectile system source at 45 MeV/nucleon. If one looks closely at the bottom panel of Fig. 71, one notices that the N/Z tracer lines for the two mixed systems have completely passed through each other and are on opposite sides of the x axis. This implies a large deficit in the amount of stopping AMD-V/GEMINI has produced when considering the 45 MeV/nucleon proton and deuteron fragment emissions and a little too much mixing which occurs at 35 MeV/nucleon in comparison to experimental results.

Again, in Fig. 72, are shown N/Z tracer term experimental and AMD-V/GEMINI results, but now using the p/t isotope ratio observable. AMD-V/GEMINI does a much better job reproducing the 35 MeV/nucleon experimental results with nearly overlapping trends in the two data sets. However, once more, in the 45 MeV/nucleon results, the AMD-V/GEMINI show much less stopping than appears in the experimental data. These results suggest that more stopping is need to adequately describe experimental results at 45 MeV/nucleon.

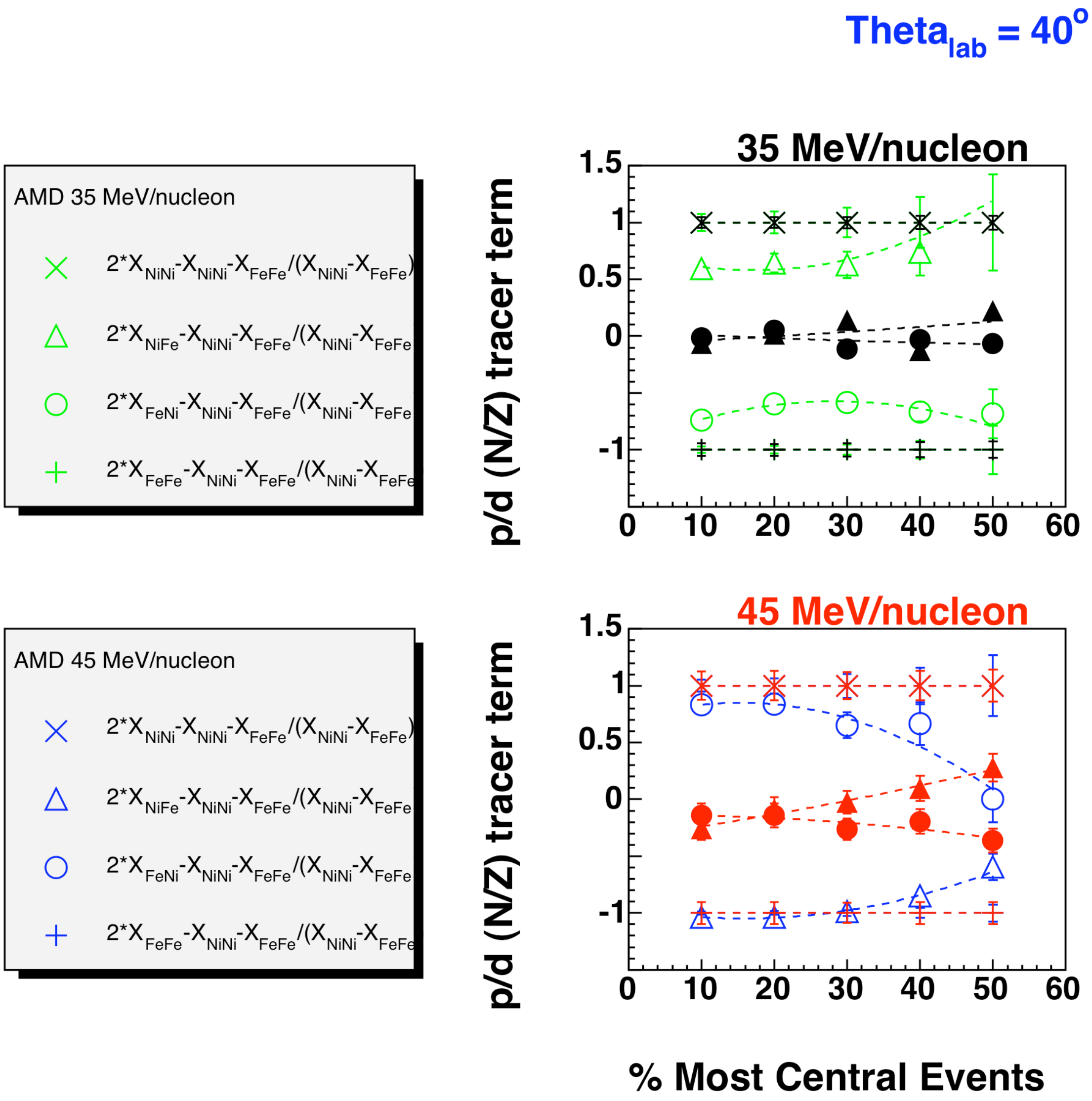

Fig. 71. p/d N/Z tracer term AMD-V/GEMINI results for data from $\text{theta}_{\text{lab}}= 40^0$ (ring 9) plotted as a function of centrality.

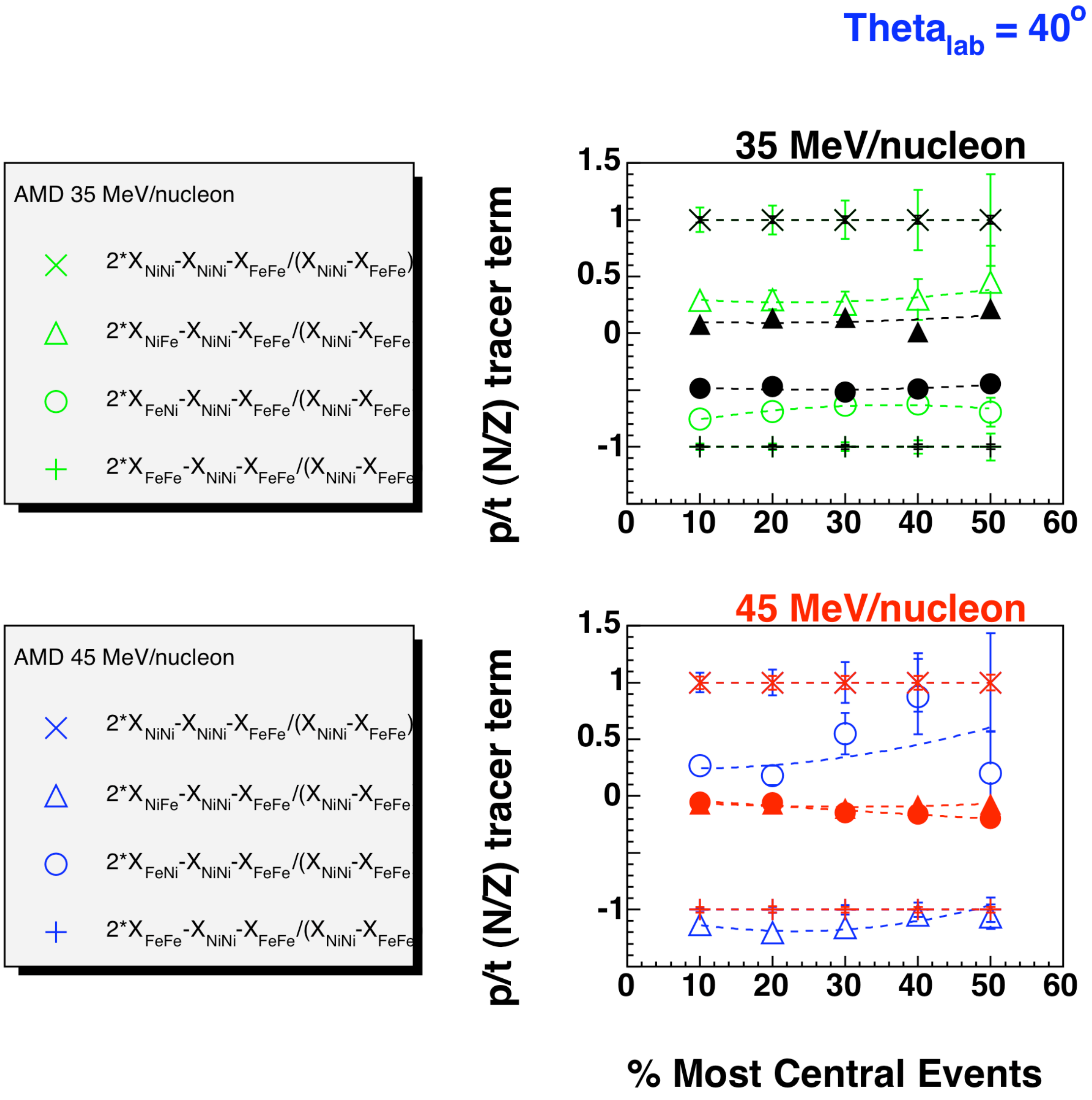

Fig. 72. p/t N/Z tracer term AMD-V/GEMINI results for data from $\mathrm{theta}_{\mathrm{lab}} = 40^0$ (ring 9) plotted as a function of centrality.

AMD-V/GEMINI data available at this time for the ^{58}Fe, Ni on ^{58}Fe, Ni are only of the hard EOS type (K=360). There are, however, data available with both hard and soft EOS parameters for a system similar in mass and energy. AMD-V/GEMINI has been run successfully on the cluster machines here at the Cyclotron for one system at two different K values [103]. These calculations are of the same type described earlier, with the addition of a soft EOS calculation. In Fig. 73 are shown a comparison of AMD-V/GEMINI simulations on a similar mass and energy system, 35 MeV/nucleon ^{64}Ni on ^{64}Ni run with both the soft and hard EOS values of K=228 and 360, respectively.

The data shown in Fig. 73 on the left side are the parallel versus perpendicular velocity of all fragments from unfiltered events at b<=3fm in units of c in the lab frame. On the right side of Fig. 73 are shown the projections of the x axis. In the top panels of Fig. 73 are shown data calculated using the hard EOS K value of 360 and on the right are the data calculated using the soft EOS K value of 228. In the past [18], plots like these have been used to test sensitivity of the EOS to stopping and or mixing of target and projectile nucleons. The top right panel in Fig. 73 shows a single peaked structure while the bottom right panel of Fig. 73 shows a slightly double peaked structure. This difference indicates a difference in the amount of stopping occurring in the reaction between the hard and soft EOS. The data in Fig. 73 is replotted in Fig. 74 with the addition of the system 35 MeV/nucleon ^{58}Ni on ^{58}Ni, which is run with the hard EOS. As in the A=64 system hard EOS AMD-V/GEMINI data, the A=58 hard EOS AMD-V/GEMINI data show a single peaked distribution in parallel velocity, but with much better statistics. There are better statistics for these data are because they are run much more time efficiently by a supercomputer. The data in the top two rows of panels in Fig. 74 were run on Linux boxes at the Cyclotron Institute at a much slower rate.

The signal of a difference in stopping between the hard and soft EOS using AMD-V is expected to be much larger and easier to see if one are to compare the soft EOS data to the hard EOS N/Z tracer term results shown in the current study because the N/Z tracer term is a much more sensitive observable when considering stopping which occurs in nuclear collisions than are velocity peak widths and separation.

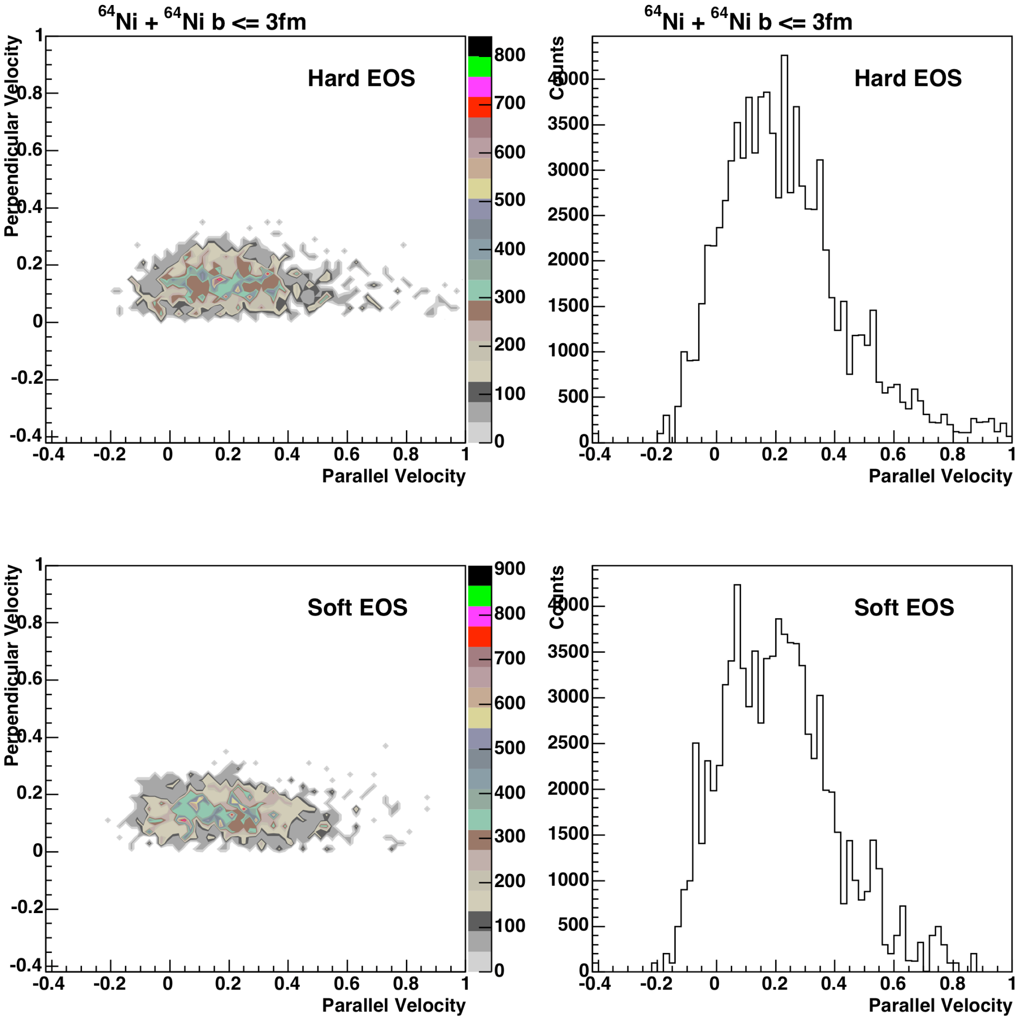

Fig. 73. AMD-V/GEMINI parallel velocity versus perpendicular velocity two dimensional plots (left) and parallel velocity one dimensional plots (right) for the hard (top) and soft (bottom) EOS for the systems of 35 MeV/nucleon ^{64}Ni on ^{64}Ni at an impact parameter of 3 or less.

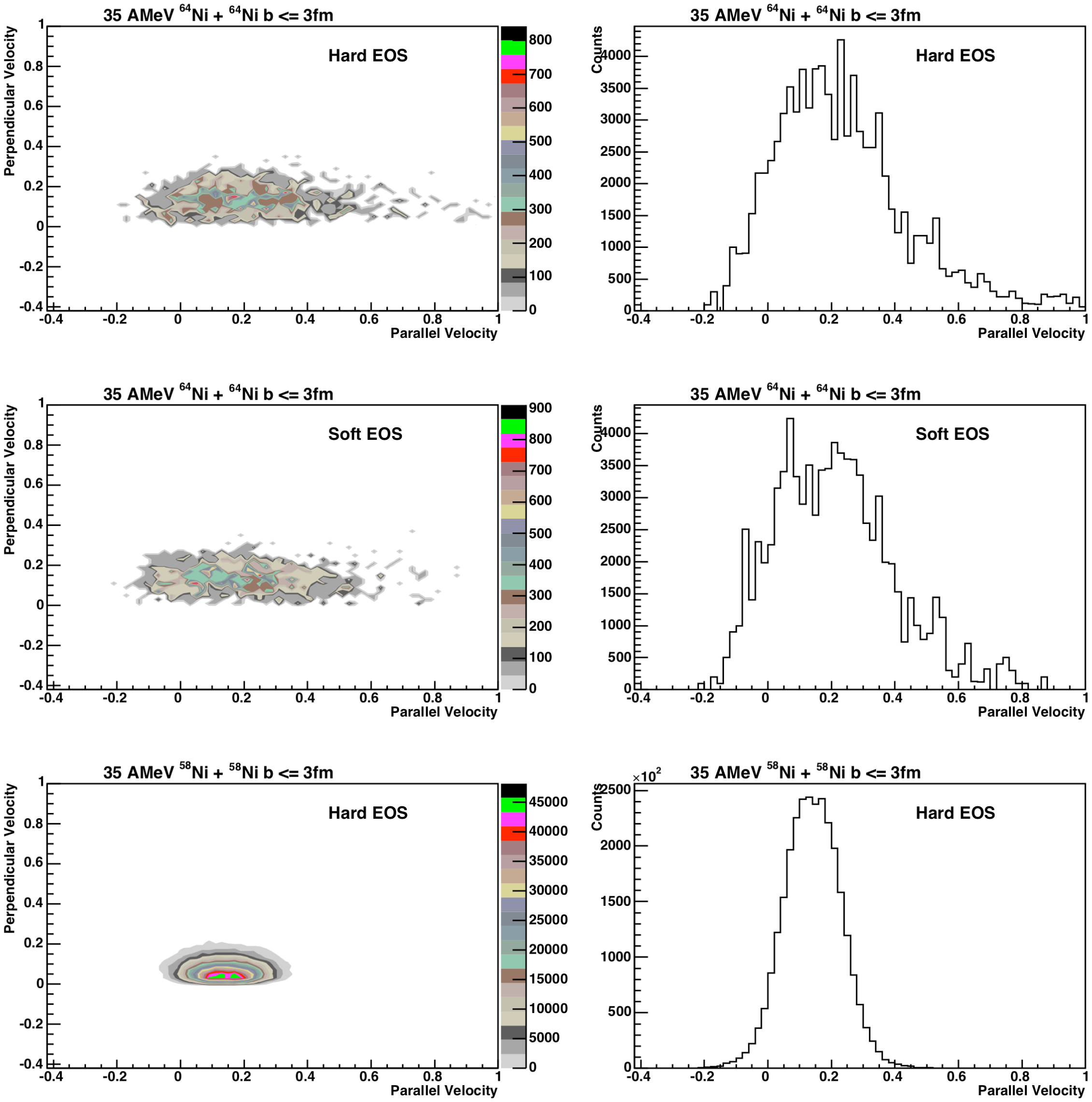

Fig. 74. AMD-V/GEMINI parallel velocity versus perpendicular velocity two dimensional plots (left) and parallel velocity one dimensional plots (right) using the hard EOS (bottom) and the soft EOS (top) for the systems of 35 MeV/nucleon ^{64}Ni on ^{64}Ni (top) and35 MeV/nucleon ^{58}Ni on ^{58}Ni (bottom) at an impact parameter of 3 or less.

CHAPTER VII
SUMMARY

The study of the N/Z dependent part of the nuclear equation of state is becoming more and more important due to the planned building of the Rare Isotope Accelerator, or RIA [1]. Nuclei far from the valley of stability may be produced by RIA and accelerated to conduct nuclear collision experiments that reach N/Z asymmetries which have not been seen before. Another reason the study of the N/Z dependence of the nuclear equation of state is interesting is that it relates to the cooling rates of neutron stars and to supernovae mechanisms [2, 3, 4, 5].

The current study of N/Z equilibration uses the ratios of isotopically resolved yields from the nuclear collisions of 35 and 45 MeV/nucleon ^{58}Fe, Ni on ^{58}Fe, Ni. Also, the N/Z tracer term is calculated using the isotopically resolved yield ratios to study N/Z equilibration. If the fragments emitted from the two asymmetric collisions of Fe on Ni and Ni on Fe have isotope yield ratios which are the same, then the emitting system is N/Z equilibrated prior to the emission of those fragments. If not, then the emitting system is not equally represented by target and projectile nucleons. If the same ratios give an N/Z tracer term not equal to zero, then they too are not fully N/Z equilibrated before fragment emission.

Intermediate energy, heavy-ion nuclear collisions can be broken into four main types which vary by decreasing impact parameter, elastic scattering collisions, grazing collisions, damped collisions and compound nucleus forming collisions [19, 20]. The last type of collision, compound nucleus forming collisions, is the type of collision used to study nuclear multifragmentation. It is also the type of collision in which the current study is interested. Basically, during a central or small impact parameter intermediate energy heavy-ion nuclear collision, a composite nucleus is formed made up of nucleons from both the target and the projectile. There is an initial stage where the compound nucleus becomes compressed and heated. Then there is a stage in which the compressed region expands and cools. At some point during the expansion phase, fragments are formed which are detected by the experimental apparatus. The compound nucleus may or may not show N/Z equilibration depending on how much mixing occurred in the compound nucleus between the projectile and the target before fragments are emitted.

Computer codes are used to simulate nuclear collisions. If the results from experimental data align with results from computer simulations, we may be able to fully understand the underlying physics in the nuclear equation of state. There are two main types of computer simulation codes, dynamic and statistical [25]. Dynamic computer simulations follow the collision through the interaction phase and use the nuclear equation of state to predict in a stepwise manner the outcome of each event. Statistical codes, on the other hand, start of with a given set of initial parameters which assume the collision has already occurred and that the nucleons are already excited. Then, statistical codes take the excited system of nucleons and decay them statistically into complex fragments and nucleons according to weighted distributions. Dynamic codes take up much more computing time than statistical codes, but they also allow for a more thorough treatment of the nuclear collision.

NIMROD is used to conduct the experiment in the current study. NIMROD has 12 concentric rings which vary in lab angle theta from 3.6 degrees to 170 degrees. Each of the 12 rings of NIMROD contains 2 super telescopes and 3 single telescopes. Each super telescope contains two Silicon detectors and one Cesium Iodide detector. Each single telescope holds one Silicon detector and one Cesium Iodide detector. The rings of NIMROD used in the 2000 experiment are numbered from two to thirteen. There are 12 Cesium Iodide detectors in rings two, three, four, five, six, and eight. There are 24 Cesium Iodides in rings seven and nine. There are 16 Cesium Iodide detectors in ring ten, 14 in ring eleven and eight in rings twelve and thirteen. Multiplicity and LCP information come mainly from the Cesium Iodide detectors while IMF isotope yield are obtained solely from the super and single telescopes.

Various cuts of centrality are considered when choosing the method of selecting central events in these NIMROD data. To best select the most central events, one can either use one physical observable which is correlated to impact parameter or a combination of two or more observables which are not autocorrelated to each other and which are both correlated to impact parameter. Many different combinations of physical observables are investigated for their correlation to impact parameter including (1) the multiplicity of charged particles (Mcp), (2) multiplicity of light charged particles (Mlcp), (3) multiplicity of intermediate mass fragments (Mimf), (4) multiplicity of neutrons (Mnb), (5) the midrapidity charge (MRC), (6) the transverse energy (Etrans), and (7) the midrapidity transverse energy (MREtrans).

AMD-V/GEMINI impact parameter distribution results are used to compare the precision of centrality selection between a one dimensional centrality cut in Mcp and a two dimensional centrality cut in Mcp and Mnb. A two dimensional centrality cut is chosen over a one dimensional centrality cut because it gives a more sensitive means of dialing in the desired centrality of the events. The five physical observables that show the strongest centrality correlation include the multiplicity of charged particles (Mcp), the multiplicity of light charged particles (Mlcp), multiplicity of neutrons (Mnb), and the mid-rapidity charge (MRC). The two of these five physical observables which are the least autocorellated are Mcp and Mnb. Therefore, the impact parameter characterization for events taken with NIMROD is made using the multiplicities of both neutrons from the Neutron Ball and charged particles from the inner charged particle array of NIMROD.

There are five cuts on centrality used for these NIMROD data which vary in ten percent increments from the 50 to 60 percent most central events to the 10 percent most central events. Most data shown in this study are from the 10 percent most central events as this is the centrality bin most likely to contain compound nucleus forming types of nuclear collisions.

Plotting the isotope yield ratios as a function of the N/Z ratio of the combined system of the target and projectile, the values for two ratios that have different targets and projectiles but identical N/Z combined content will be equal if the emitting system included the complete N/Z equilibrated target and projectile combined nucleons before fragment emission. In the example where the two systems with matching N/Z of the combined target and projectile have isotope yield ratios that do not match, the ratio of target and projectile nucleons in the combined emitting system are adjusted by a scaling factor and the ratio values are replotted as a function of the scaled N/Z values. The scaling factor which gives matching ratio values that vary linearly indicates the extent of mixing which the target and projectile underwent before fragment emission.

Previous work using isobar and isotope ratios to study N/Z equilibration [17] shows results of isotope yield ratios detected at a lab angle of 40 degrees ^{7}Li/Be, ^{10}Be/B, and ^{11}B/C for the systems ^{40}Ar, ^{40}Ca + ^{58}Fe, ^{58}Ni at the energies of 33 and 45 MeV/nucleon. The ^{7}Li/Be and ^{10}Be/B data are cut for the 10% most central events and ^{11}B/C data are cut for the 20% most central events. These data show N/Z equilibration at 35 MeV/nucleon and N/Z nonequilibrium at 45 MeV/nucleon. The current study, for the systems of ^{58}Fe, ^{58}Ni on ^{58}Fe, ^{58}Ni, sees N/Z equilibrium with IMF ratios at both 35 and 45 MeV/nucleon for the same systems. One reason for the discrepancy between the two results may be that the previous study [17] used an angular cut at 40 degrees to select for centrality with the argument that at 40 degrees, there is little contamination from pre-equilibrium fragments or non-central type events. In Fig. 54 in the current study, one can see that there a difference in the N/Z equilibration between two different centrality cuts at 40 degrees in the lab. Another difference between the two studies is the masses of the systems investiagated; one is mass 40 on mass 58 and the other is mass 58 on mass 58. An earlier study [104] concludes that equilibration occurs if the system is large enough to overcome finite size effects.

An investigation of fragment emission source character [13] is used for the current study in the case where the isotopic and isobaric ratios (at $\text{theta}_{\text{lab}}=40^{\circ}$ and with cuts of 10% and 20% most central events, respectively) did not display N/Z equilibration. The process involves plotting the yield ratio values as a function of a system with N/Z that varies in amounts of target and projectile nucleons. The N/Z mixture of target and projectile nucleons which has the most linear trend of isotope or isobar yield ratio values comes closest to describing the N/Z of the emitting system.

The observables in the previous study [13] were the isotope yield ratios of t/p, t/d, $^{7/6}$Li, $^{9\text{-}11}$Be/^{7}Be, and $^{11/10}$B at 40 degrees in the lab. In the case of the IMF ratios, the previous study found the emitting system to be a fully combined projectile and target. This is also the case for the current study, which includes IMF isotope yield ratios of $^{6/7}$Li, $^{9/10}$Be, $^{10/11}$B, $^{12/13}$C, $^{14/15}$N, and $^{16/17}$O. In the previous study [13], the LCP yield ratios of t/p and t/d are found to be not fully target and projectile N/Z combined. The t/p ratio is found to be a mixture of 1:1 target to projectile nucleons while the t/d ratio is found to be a mixture of 1:2 target to projectile nucleons in the previous study [13].

The observables in the current NIMROD study which did not show N/Z equilibration are 35 MeV/nucleon d/t, p/t, $^{3/4}$He, t/^{3}He and 45 MeV/nucleon $^{3/4}$He and t/^{3}He. In the case of 35 MeV/nucleon d/t, the admixture of target and projectile nucleons comes close to a linear approximation when plotted against a system whose N/Z mixture is 1 part target and 4 parts projectile nucleons. This suggests deuterons and/or tritons at 35 MeV/nucleon beam energy are emitted at a point when the target and projectile have only partially combined. In the case of 35 MeV/nucleon p/t, the mix of target and projectile nucleons comes close to a linear approximation when plotted against a system whose N/Z mixture is 2 parts target and 3 parts projectile nucleons. This suggests protons and/or tritons at 35 MeV/nucleon beam energy are emitted at a point when the target and projectile have also only partially combined.

In the case of 35 MeV/nucleon $^{3/4}$He, the amount of N/Z mixing suggested by the most linear fit implies a ratio of 1:60 target to projectile nucleons. This means that He fragments are emitted from a source that is mostly projectle like with very little target mixed in. One could say the $^{3/4}$He ratio reflects only the N/Z of the projectile. In the case of 35 MeV/nucleon t/^{3}He, the mixing of target and projectile which gives the most linear fit is 1:6 target to projectile. In the case of 45 MeV/nucleon $^{3/4}$He the $^{3/4}$He ratio data with 45 MeV/nucleon beam energy are best described by an emitting source made up of 1 part target and 3 parts projectile. In the case of 45 MeV/nucleon t/^{3}He, the mixing of target and projectile which gives the most linear fit is 2:3 target to projectile nucleons.

The N/Z tracer method [18] is used with ratios of isotopes and isobars to see how the amount of nuclear stopping or N/Z mixing changes as a function of the centrality of the event. The N/Z tracer term calculated using the yield ratio p/d shows emission from a combined target and projectile system at both energies of 35 and 45 MeV/nucleon. The trend of the 35 MeV/nucleon N/Z tracer terms for yield ratio p/t shows an emitting source which is projectile-like. The trend of the 45 MeV/nucleon N/Z tracer term with the p/t ratio appears to be emitted from a well-combined target and projectile system. This suggests that deuterons and tritons emitted at $\mathrm{theta}_{\mathrm{lab}}=40^{\circ}$ at 35 and 45 MeV/nucleon are emitted from sources with differing N/Zs.

The trend of the 35 MeV/nucleon N/Z tracer terms for d/t shows little progress toward N/Z equilibrium across the five centrality cuts. The trend of the 45 MeV/nucleon N/Z tracer term with d/t appears to be fully N/Z equilibrated within error bars at all centrality cuts. This supports the conclusion that deuterons and tritons are emitted from a source with characteristics of the projectile at 35 MeV/nucleon and of the combined system at 45 MeV/nucleon. Within large error bars, the trend of the N/Z $^{3/4}$He tracer term shows that ^{3}He and ^{4}He fragments are emitted from a source which is characteristic of the projectile. This result is also found in the emission source study [13] previously conducted.

In the case of the N/Z tracer term for the isobar yield ratio of t/^{3}He, one sees evidence of a projectile-like emitting source, which previously has been shown to have a ratio of target to projectile nucleons of 1:6 (1:1.5) when using the t/^{3}He ratio values at 35 MeV/nucleon (45 MeV/nucleon) in the emission source study [13]. The 35 MeV/nucleon N/Z t/^{3}He tracer term results are consistent with the conclusion that A=3 fragments are emitted from a source which is characteristic of the projectile. Also, the t/^{3}He results show that the emitting source is more projectile-like at 35 MeV/nucleon beam energy and more combined system-like at 45 MeV/nucleon beam energy.

In general, LCPs are found to be emitted from systems which have not yet fully combined. The fragments with A=3 are emitted from the least target and projectile combined systems. This finding is consistent with an earlier study [105] which concluded that ^{3}He are emitted earlier than ^{4}He. IMFs in the current study are seen to be emitted by N/Z equilibrated sources, within statistical error bars. The earlier study [105] finds similar results for IMFs; they are seen to have temperatures which indicate formation late in the cooling process.

AMD-V [32] has been run with GEMINI [29] as the afterburner to simulate the reactions of 35 and 45 MeV/nucleon ^{58}Ni, Fe on ^{58}Ni, Fe on computers at the VPP700E supercomputer facility in RIKEN, Japan [106]. The hard equation of state, EOS, (K=360 MeV) is employed by AMD-V during calculations. The dynamic calculations are stopped at a time of 280 fm/c, adequately allowing for the excitation of the nucleons involved in the collision [102]. The excited fragments are then fed to the afterburner code GEMINI 100 times for each event.

The simulation data show much less stopping than the experimental N/Z equilibration data in the cases of 35 and 45 MeV/nucleon p/d, 35 MeV/nucleon $^{3/4}$He, and 45 MeV/nucleon $^{6/7}$Li. The behavior of the N/Z equilibration ratio of the 45 MeV/nucleon $^{3/4}$He and 35 MeV/nucleon $^{6/7}$Li is reproduced by the simulation data, but the N/Z dependence of these observables is not well matched. In other words, the ^{58}Fe on ^{58}Ni and ^{58}Ni on ^{58}Fe ratio data points for the experimental are close in value and the AMD-V/GEMINI ^{58}Fe on ^{58}Ni and ^{58}Ni on ^{58}Fe ratio data points are close in value, but the experimental and AMD-V/GEMINI data points are not close in value. The simulation data fail to reproduce the experimental results in all but two of the observables in Fig. 69.

The experimental isobaric ratios t/^{3}He and ^{7}Li/Be are compared with AMD-V/GEMINI results. These data are at 40 degrees in the lab frame and are cut for the 20% most central events. For these experimental results, the AMD does a fair job of reproducing the equilibration and trend behavior for the A=7 but not the A=3 observables. The experimental behavior of the N/Z equilibration ratio in the ^{7}Li/Be ratio at both 35 and 45 MeV/nucleon is reproduced by the simulation results. The N/Z nonequilibration behavior in the experimental t/^{3}He ratio is not reproduced by the simulation results, which show N/Z equilibrated behavior for the t/^{3}He ratios at both energies.

With the p/d ratio N/Z tracer term observable, AMD-V/GEMINI indicates a projectile-like source at 35 MeV/nucleon and a combined target and projectile system source at 45 MeV/nucleon. At 45 MeV/nucleon, the N/Z tracer lines for the two mixed systems have completely passed through each other and are on opposite sides of the x axis for the p/d ratio N/Z tracer term observable. This implies a large deficit in the amount of stopping AMD-V/GEMINI has produced when considering the 45 MeV/nucleon proton and deuteron fragment emissions and a little too much mixing which occurs at 35 MeV/nucleon in comparison to experimental results.

For the p/t isotope ratio observable, AMD-V/GEMINI does a much better job reproducing the 35 MeV/nucleon experimental results with nearly overlapping trends in the two data sets. However, once more, in the 45 MeV/nucleon results, the AMD-V/GEMINI show much less stopping than appears in the experimental data. These results suggest that more stopping is need to adequately describe experimental results at 45 MeV/nucleon

AMD-V/GEMINI data available for the current study are only of the hard EOS type (K=360) at this time. There are, however, data available with both hard and soft EOS parameters for a system similar in mass and energy. AMD-V/GEMINI has been run successfully on the Linux cluster machines here at the Cyclotron for one system at two different K values [107]. These calculations are of the same type described earlier, with the addition of a soft EOS calculation. A comparison of AMD-V/GEMINI simulations on a similar mass and energy system, 35 MeV/nucleon ^{64}Ni on ^{64}Ni run with both the soft and hard EOS values of K=228 and 360, respectively, has been performed. These data are the parallel versus perpendicular velocity of all fragments from unfiltered events at b<=3fm in units of c in the lab frame. These data are calculated using the hard EOS K value of 360 and the soft EOS K value of 228.

In the past [18], data like these have been used to test sensitivity of the EOS to stopping and or mixing of target and projectile nucleons. The hard EOS data show a single peaked structure while the soft EOS data show a slightly double peaked structure. This difference indicates a change in the amount of stopping occurring in the reaction between the hard and soft EOS. The signal of a difference in stopping between the hard and soft EOS using AMD-V is expected to be much larger and easier to see if one is to compare the soft EOS data to the hard EOS N/Z tracer term results shown in the current study because the N/Z tracer term is a much more sensitive observable when considering stopping which occurs in nuclear collisions than are velocity peak widths and separation

The N/Z tracer term observable has proven to be a clear and sensitive tool to use when considering the differences in N/Z mixing between the data at two energies. In the future, it should also be a sensitive tool for seeing the differences in N/Z mixing between the hard and soft EOS. Simulation codes which are run to help understand nuclear collision experimental results and the nuclear equation of state can be fine tuned toward accuracy by reconciling them to carefully chosen and appropriately sensitive experimental observables. Pinpointing the onset or failure of N/Z equilibration will improve simulation code predictions and understanding of the physics involved in N/Z asymmetric nuclear collisions, as well as supernovae and neutron star behaviors. In summary, the N/Z tracer term coupled with the ratios of isotopic and isobaric yields from well characterized central events of nuclear collisions between varying N/Z target and projectiles is one such sensitive tool which has been shown to illuminate the dependence of fragment emission on N/Z equilibration.

REFERENCES

[1] "Scientific Opportunities with an Advanced ISOL Facility", DOE report, 1997, http://www.er.doe.gov/henp/isolopaper.pdf.

[2] David Arnett and Grant Bazan, Science **276**, 1359 (1997).

[3] P. Danielewicz, R., and W. G. Lynch, Science **298**, 1592 (2002).

[4] Bao-An Li, Phys. Rev. C **69**, 034614 (2004).

[5] Bao-An Li, Nucl. Phys. A **734**, 593 (2004).

[6] J. Brzychczyk, D. S. Brakcen, K. Kwiatowski, K. B. Morley, E. Renshaw, and V. E. Viola, Phys. Rev. C **47**, 1553 (1993).

[7] R. Pak, Bao-An Li, W. Benenson, O. Bjarki, J. A. Brown, S. A. Hannuschke, R. A. Lacey, D. J. Magestro, A. Nadasen, E. Norbeck, D. E. Russ, M. Steiner, N. T. B. Stone, A. M. Vander Molen, G. D. Westfall, L. B. Yang, and S. J. Yennello, Phys. Rev. Lett. **78**, 1026 (1997).

[8] R. Pak, W. Benenson, O. Bjarki, J. A. Brown, S. A. Hannuschke, R. A. Lacey, Bao-An Li, A. Nadasen, E. Norbeck, P. Pogodin, D. E. Russ, M. Steiner, N. T. B. Stone, A. M. Vander Molen, G. D. Westfall, L. B. Yang, and S. J. Yennello, Phys. Rev. Lett. **78**, 1022 (1997).

[9] Lie-Wen Chen, Feng-Shou Zhang, and Zhi-Yuan Zhu, Phys. Rev. C **61**, 067601 (2000).

[10] Bao-An Li, Zhongzhou Ren, C. M. Ko and Sherry J. Yennello, Phys. Rev. Lett. **76**, 4492 (1996).

[11] Chen Liewen, Zhang Fengshou, and Jin Genming, Phys. Rev. C **58,** 2283 (1998).

[12] R. Planeta, S. H. Zhou, K. Kwiatkowski, W. G. Wilson, V. E. Viola, H. Breuer, D. Benton, F. Khazaie, R. J. McDonald, A. C. Mignerey, A. Weston-Dawkes, R. T. de Souza, J. R. Huizenga and W. U Schroder, Phys. Rev. C **38**, 195 (1988).

[13] R. Wada, K. D. Hildebrand, U. Lynen, W. F. J. Müller, H. J. Rabe, H. Sann, H. Stelzer, W. Trautmann, R. Trockel, N. Brummun, R. Glasow, K. H. Kampert, and R. Santo, E. Eckert, J. Pochodzalla, I. Bock and D. Pelte, Phys. Rev. Lett. **58,** 1829 (1987).

[14] S. J. Yennello, B. Young, J. Yee, J. A. Winger, J. S. Winfield, G. D. Westfall, A. Vander Molen, B. M. Sherrill, J. Shea, E. Norbeck, D. J. Morrissey, T. Li, E. Gualtieri, D. Craig, W. Benenson, and D. Bazin, Phys. Lett. B **321**, 15 (1994).

[15] Bao-An Li and C. M. Ko, Phys. Rev. C **57**, 2065 (1998).

[16] Bao-An Li and Sherry J. Yennello, Phys. Rev. C **52**, R1746 (1995).

[17] H. Johnston. T. White, B. A. Li, E. Ramakrishnan, J. Winger, D. J. Rowland, B. Hurst, F. Gimeno-Nogues, D. O'Kelly, Y.-W. Lui, and S. J. Yennello, Phys. Rev. C **56**, 1972 (1997).

[18] F. Rami, Y. Leifels, B. de Schauenburg, A. Gobbi, B. Hong, J. P. Alard, A. Andronic, R. Averbeck, V. Barret, Z. Basrak, N. Bastid, I. Belyaev, A. Bendarag, G. Berek, R. Čaplar, N. Cindro, P. Crochet, A. Devismes, P. Dupieux, M. Dzelalija, M. Eskef, C. Finck, Z. Fodor, H. Folger, L. Fraysse, A. Genoux-Lubain, Y. Grigorian, Y. Grishkin, N. Herrmann, K. D. Hildenbrand, J. Kecskemeti, Y. J. Kim, P. Koczon, M. Kirejczyk, M. Korolija, R. Kotte, M. Kowalczyk, T. Kress, R. Kutsche, A. Lebedev, K. S. Lee, V. Manko, H. Merlitz, S. Mohren, D. Moisa, J. Mösner, W. Neubert, A. Nianine, D. Pelte, M. Petrovici, C. Pinkenburg, C. Plettner, W. Reisdorf, J. Ritman, D. Schüll, Z. Seres, B. Sikora, K. S. Sim, V. Simion, K. Siwek-Wilczynska, A. Somov, M. R. Stockmeier, G. Stoicea, M. Vasiliev, P. Wagner, K. Wisniewski, D. Wohlfarth, J. T. Yang, I. Yushmanov, and A. Zhilin, Phys. Rev. Lett. **84**, 1120 (2000).

[19] J. Tõke and W. U. Schröder, Ann. Rev. Nucl. Part. Sci. **42**, 401 (1992).

[20] G. Friedlander, J. W. Kennedy, E. S. Macias and J. M. Miller, *Nuclear and Radiochemistry*, (John Wiley & Sons, New York, 1981), Third Edition, p. 179-186.

[21] S. Karataglidis, K. Amos, B. A. Brown, and P. K. Deb, Phys. Rev. C **65**, 044306 (2002).

[22] E. Gross, J. de Boer, R. M. Diamond, F. S. Stephens, and P. Tjøm, Phys. Rev. Lett. 35, 565-568 (1975).

[23] C. Gelbke and D. Boal, Prog. Part. Nucl. Phys. **19**, 33 (1987).

[24] D. Boal, Ann. Rev. Nucl. Part. Sci., **37**, 1 (1987).

[25] L. G. Moretto and G. J. Wozniak, Ann. Rev. Nucl. Part. Sci., **43**, 379 (1993).

[26] J. P. Bondorf, R. Donangelo, I. N. Mishustin, C. J. Pethick, H. Schulz, K. Sneppen, Nuc. Phys. A **443**, 321 (1985).

[27] J. Bondorf, R. Donangelo, I. N. Mishustin and H. Schulz, Nucl. Phys. **A444**, 460, (1985).

[28] J. P. Bondorf, A. S. Botvina, A. S. Iljinov, I. N. Mishustin, K. Sneppen, Phys. Rep. **257**, 133 (1995).

[29] R. J. Charity, M. A. McMahan, G. J. Wozniak, R. J. McDonald, L. G. Moretto, *et al*. Nucl. Phys. **A483**, 371 (1988).

[30] G. F. Bertsch and S. Das Gupta, Phys. Rep. **160**, 189 (1988).

[31] A. Ono, H. Horiuchi, T. Maruyama and A. Ohnishi, Prog. Theo. Phys. **87**, 1185 (1992).

[32] A. Ono and H. Horiuchi, Phys. Rev. C **53**, 2958 (1996).

[33] J. Aichelin, Phys. Rep. **202**, 233 (1991).

[34] H. Feldmeier, Nucl. Phys. **A515**, 147 (1990).

[35] A. Ono, H. Horiuchi, T. Maruyama, and A. Ohnishi, Phys. Rev. Lett. **68**, 2898 (1992).

[36] Trace Sciences International, Ontario, Canada.

[37] Micromatter, Inc., Deer Harbor, WA.

[38] Targetlabor, Darmstadt, Germany.

[39] J. F. Ziegler, J. P, Biersack, U. Littmark, *Stopping and Ranges of Ions in Matter*, Pergamon Press, New York (1984).

[40] http://www.m-w.com/, Merriam-Webster, Inc., 2005.

[41] R. P. Schmitt, G. Nebbia, D. Fabris, K. Hagel, J. B. Natowitz, *et al.*, Progress in Research Cyclotron Institute Texas A&M University 1985-1986, p. 106.; Progress in Research Cyclotron Institute Texas A&M University 1986-1987, p. 101.; Progress in Research Cyclotron Institute Texas A&M University 1987-1988, p. 88.; Progress in Research Cyclotron Institute Texas A&M University 1988-1989, p. 119.; Progress in Research Cyclotron Institute Texas A&M University 1989-1990, p. 87.; Progress in Research Cyclotron Institute Texas A&M University 1990-1991, p. 104.

[42] B. Djerroud, D. K. Agnihotri, S. P. Baldwin, W. Skulski, J. Tõke, W. U. Schröder, R. J. Charity, J. F. Dempsey, D. G. Sarantites, L. G. Sobotka, B. Lott, W. Loveland, and K. Aleklett, Phys. Rev. C **64**, 034603 (2001).

[43] R. P. Schmitt, L. Cooke, G. Derrig, D. Fabris, B. Hurst, *et al.*, Nucl. Instrum. and Meth. A354 487 (1995).

[44] F. Haddad, K. Hagel, J. Li, N Mdeiwayeh, J. B. Natowitz, *et al.*, Progress in Research Cyclotron Institute Texas A&M University 1993-1994, p. V-151.

[45] B. Xiao, G. Derrig, K. Hagel, R. Wada, J. B. Natowitz, *et al.*, Progress in Research Cyclotron Institute Texas A&M University 1991-1992, p. 126.; Progress in Research Cyclotron Institute Texas A&M University 1992-1993, p. V-144.; Progress in Research Cyclotron Institute Texas A&M University 1993-1994, p. V-156.

[46] R. Wada, K. Hagel, J. B. Natowitz, B. Xiao, Y. Zhao, *et al.*, Progress in Research Cyclotron Institute Texas A&M University 1995-1996, p. 138.

[47] R. Wada, K. Hagel, B. Xiao, J. Cibor, J. Li, *et al.*, Progress in Research Cyclotron Institute Texas A&M University 1996-1997, p. V-12.

[48] B. Xiao, G. Derrig, F. Haddad, K. Hagel, J. Li, *et al.*, Progress in Research Cyclotron Institute Texas A&M University 1994-1995, p. 205.

[49] R. P. Schmitt, B. Hurst, G. Derrig, J. B. Natowitz, J. Shumbera, *et al.*, Progress in Research Cyclotron Institute Texas A&M University 1997-1998, p. V-17.

[50] R. P. Schmitt, G. J. Derrig, J. Shumbera, D. Utley, R. Wada, *et al.*, Progress in Research Cyclotron Institute Texas A&M University 1998-1999, p. V-13.

[51] N. Marie, R. LaForest, K. Hagel, E. Ramakrishnan, R. Wada, *et al.*, Progress in Research Cyclotron Institute Texas A&M University 1997-1998, p. V-19.

[52] R. Wada, N. Marie, M. Murray, R. LaForest, K. Hagel, *et al.*, Progress in Research Cyclotron Institute Texas A&M University 1998-1999, p. V-15.

[53] T. Keutgen, R. Wada, M. Murray, K. Hagel, E. Martin, *et al.*, Progress in Research Cyclotron Institute Texas A&M University 1999-2000, p. V-11.

[54] K. Hagel, R. Wada, J. B. Natowitz, M. Gonin, Y. Lou, *et al.*, Progress in Research Cyclotron Institute Texas A&M University 1989-1990, p. 121.

[55] K. Hagel, R. Burch, R. Wada, K. Ko, D. Rosenfeld, Progress in Research Cyclotron Institute Texas A&M University 1999-2000, p. V-9.

[56] http://root.cern.ch/, Rene Brun and Fons Rademakers, 2005.

[57] DONNA code, W. G. Meyer (unpublished).

[58] L. Tassan-Got, Nucl. Instrum. Meth. B **194** 503 (2002).

[59] H. M. Dietel and P. J. Deitel, *C++ How To Program*, Prentice Hall, New York, (1994), p. 365-388.

[60] H. M. Dietel and P. J. Deitel, *C++ How To Program*, Prentice Hall, New York, (1994), p. 355, 371-2.

[61] *Instruction Manual Tail Pulse Generator Model BH-1*, Berkeley Nucleonics Corporation, Berkeley, CA.

[62] *Bi Ra Model 2206A Event Trigger Module Technical Description Manual* (Bi Ra System, Inc., Albuquerque, NM.

[63] http://www.lecroy.com/lrs/dsheets/1885f.htm, Lecroy Corporation, 2005.

[64] http://www.lecroy.com/lrs/dsheets/222.htm, Lecroy Corporation, 2005.

[65] http://www-esd.fnal.gov/esd/catalog/main/lcrynim/2341a-spec.htm, EG&G Ortec, 2005.

[66] http://www.lecroy.com/lrs/dsheets/3420.htm, Lecroy Corporation, 2005.

[67] http://www.lecroy.com/lrs/dsheets/365al.htm, Lecroy Corporation, 2005.

[68] http://www.lecroy.com/lrs/dsheets/428.htm, Lecroy Corporation, 2005.

[69] http://www.lecroy.com/lrs/dsheets/2551.htm, Lecroy Corporation, 2005.

[70] http://www.lecroy.com/lrs/dsheets/688.htm, Lecroy Corporation, 2005.

[71] http://www.lecroy.com/lrs/dsheets/612.htm, Lecroy Corporation, 2005.

[72] http://www.lecroy.com/lrs/dsheets/623.htm, Lecroy Corporation, 2005.

[73] http://www.lecroy.com/lrs/dsheets/688.htm, Lecroy Corporation, 2005.

[74] http://www.ortec-online.com/electronics/ctr/661.htm, EG&G Ortec, 2005.

[75] http://www-esd.fnal.gov/esd/catalog/main/egg/ad811.htm, EG&G Ortec, 2005.

[76] *GG8000 Octal Gate Generator Data Sheet* (EG&G Ortec, 100 Midland Rd, Oak ridge, TN, 37830, 615-482-4411). More current contact information may be found at http://www.ortec-online.com.

[77] www.ortec-online.com/pdf/delaytut.pdf, EG&G Ortec, 2005.

[78] *EG&G Ortec RD 2000 Dual Fast Rate Divider Manual* ((EG&G Ortec, 100 Midland Rd, Oak ridge, TN, 37830, 615-482-4411). More current contact information may be found at http://www.ortec-online.com.

[79] http://www.phillipsscientific.com/pdf/7164ds.pdf, Phillips Scientific, 2005.

[80] http://www.phillipsscientific.com/pdf/7166ds.pdf, Phillips Scientific, 2005.

[81] http://www.phillipsscientific.com/pdf/7186ds.pdf, Phillips Scientific, 2005.

[82] http://www.phillipsscientific.com/preview/748pre.htm, Phillips Scientific, 2005.

[83] http://www.phillipsscientific.com/pdf/756ds.pdf, Phillips Scientific, 2005.

[84] http://www.phillipsscientific.com/pdf/794ds.pdf, Phillips Scientific, 2005.

[85] http://www.phillipsscientific.com/pdf/804ds.pdf, Phillips Scientific, 2005.

[86] http://www.canberra.com/products/1101.asp, Canberra Industries, Inc., 2005.

[87] http://www.canberra.com/products/694.asp, Canberra Industries, Inc., 2005.

[88] Christophe David, Marc Freslier, and Jörg Aichelin, Phys. Rev. C **51**, 1453 (1995).

[89] W. J. Llope, J. A. Conrad, C. M. Mader, G. Peilert, W. Bauer, D. Craig, E. Gualtieri, S. Hannuschke, R. A. Lacey, J. Lauret, T. Li, A. Nadasen, E. Norbeck, R. Pak, N. T. B. Stone, A. M. Vander Molen, G. D. Westfall, J. Yee, and S. J. Yennello, Phys. Rev. C **51**, 1325 (1995).

[90] R. Wada, T. Keutgen, K. Hagel, Y. G. Ma, J. Wang, M. Murray, L. Qin, P. Smith, J. B. Natowitz, R. Alfarro, J. Cibor, M. Cinausero, Y. El Masri, D. Fabris, E. Fioretto, A. Keksis, S. Kowalski, M. Lunardon, A. Makeev, N. Marie, E. Martin, Z. Majka, A. Martinez-Davalos, A. Menchaca-Rocha, G. Nebbia, G. Prete, V. Rizzi, A. Ruangma, D. V. Shetty, G. Souliotis, P. Staszel, M. Veselsky, G. Viesti, E. M. Winchester, S. J. Yennello, W. Zipper, and A. Ono, Phys. Rev. C **69**, 044610 (2004).

[91] Y. G. Ma, R. Wada, K. Hagel, J. Wang, T. Keutgen, Z. Majka, M. Murray, L. Qin, P. Smith, J. B. Natowitz, R. Alfaro, J. Cibor, M. Cinausero, Y. El Masri, D. Fabris, E. Fioretto, A. Keksis, M. Lunardon, A. Makeev, N. Marie, E. Martin, A. Martinez-Davalos, A. Menchaca-Rocha, G. Nebbia, G. Prete, V. Rizzi, A.

Ruangma, D. V. Shetty, G. Souliotis, P. Staszel, M. Veselsky, G. Viesti, E. M. Winchester, and S. J. Yennello, Phys. Rev. C **69**, 031604 (2004).

[92] A. Del Zoppo, R. Alba, C. Agodi, G. Bellia, R. Coniglione, P. Finocchiaro, V. Latora, K. Loukachine, C. Maiolino, E. Migneco, A. Peghaire, P. Piattelli, D. Santonocito, and P. Sapienza, Phys. Rev. C **50**, 2930 (1994).

[93] T. Ethvignot, A. Elmaani, N. N. Ajitanand, J. M. Alexander, E. Bauge, P. Bier, L. Kowalski, M. T. Magda, P. Désesquelles, H. Elhage, A. Giorni, D. Heuer, S. Kox, A. Lleres, F. Merchez, C. Morand, D. Rebreyend, P. Stassi, J. B. Viano, S. Benrachi, B. Chambon, B. Cheynis, D. Drain, and C. Pastor, Phys. Rev. C **43**, R2035 (1991).

[94] E. Piasecki, S. Bresson, B. Lott, R. Bougault, J. Colin, E. Crema, J. Galin, B. Gatty, A. Genoux–Lubain, D. Guerreau, D. Horn, D. Jacquet, U. Jahnke, J. Jastrzebski, A. Kordyasz, C. Le Brun, J. F. Lecolley, M. Louvel, M. Morjean, C. Paulot, L. Pienkowski, J. Pouthas, B. Quednau, W. U. Schröder, E. Schwinn, W. Skulski, and J. Töke, Phys. Rev. Lett. **66**, 1291 (1991).

[95] M. Morjean, J. Frehaut, D. Guerreau, J. L. Charvet, G. Duchêne, H. Doubre, J. Galin, G. Ingold, D. Jacquet, U. Jahnke, D. X. Jiang, B. Lott, C. Magnago, Y. Patin, J. Pouthas, Y. Pranal and J. L. Uzureau, Phys. Lett. B **203**, 215 (1988).

[96] J. Tõke, D. K. Agnihotri, W. Skulski and W. U. Schröder, Phys. Rev. C **63**, 024604 (2001).

[97] G. J. Kunde, S. Gaff, C. K. Gelbke, T. Glasmacher, M. J. Huang, R. Lemmon, W. G. Lynch, L. Manduci, L. Martin, R. Popescu, and M. B. Tsang, Phys. Rev. C **55**, R990 (1997).

[98] D. Prindle, R. Vandenbosch, S. Kailas, A. Charlop, and C. Hyde–Wright, Phys. Rev. C **48**, 291 (1993).

[99] D. V. Shetty, A. Keksis, E. Martin, A. Ruangma, G. A. Souliotis, *et al.* Phys. Rev. C **68,** 054605 (2003).

[100] D. P. Shoemaker, C. W. Garland, and J. I. Steinfeld, *Experiments in Physical Chemistry, Third Edition* (McGraw-Hill, New York, 1974), p. 51-58.

[101] The AMD-V/GEMINI calculations are courteously implemented by Roy Wada.

[102] R. Wada, T. Keutgen, K. Hagel, Y. G. Ma, J. Wang, *et al.*, arXiv:nucl-ex/0308027, 2003.

[103] At an albeit slower pace than the Riken supercomputer, dual 2.46 GHz (1G memory) machines are used at a rate of about 5 events a day for the 35 MeV/nucleon A=128 system.

[104] W. Bauer, Phys. Rev. Lett. **61**, 2534 (1988).

[105] V.E. Viola, K. Kwiatkowski and W. A. Friedman, Phys. Rev. C **59**, 2660 (1999).

[106] The AMD-V/GEMINI calculations are courteously implemented by Roy Wada.

[107] At an albeit slower pace than the Riken supercomputer, dual 2.46 GHz (1G memory) machines are used at a rate of about 5 events a day for the 35 MeV/nucleon A=128 system.

APPENDIX

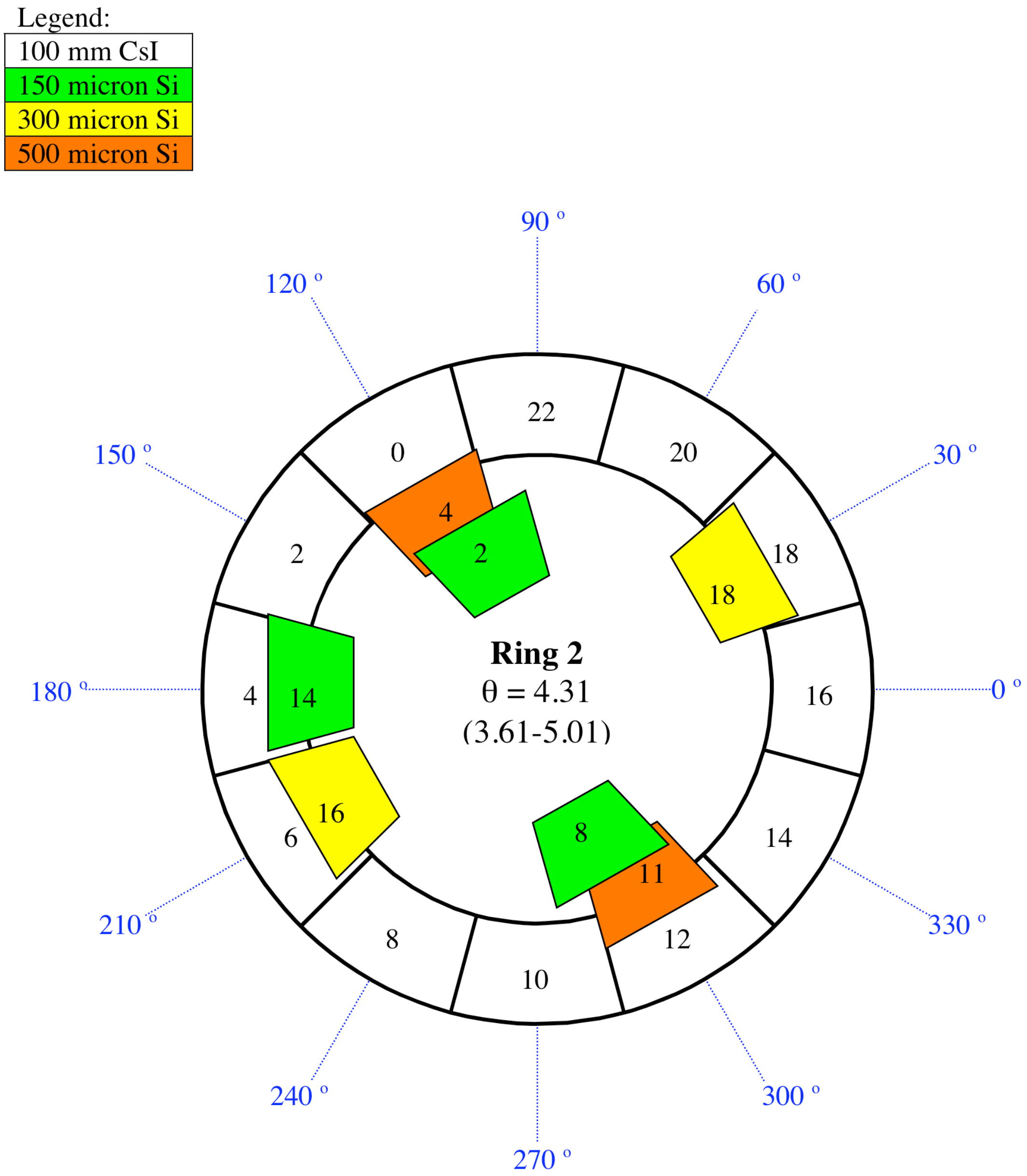

Fig. A-1. NIMROD map, ring 2.

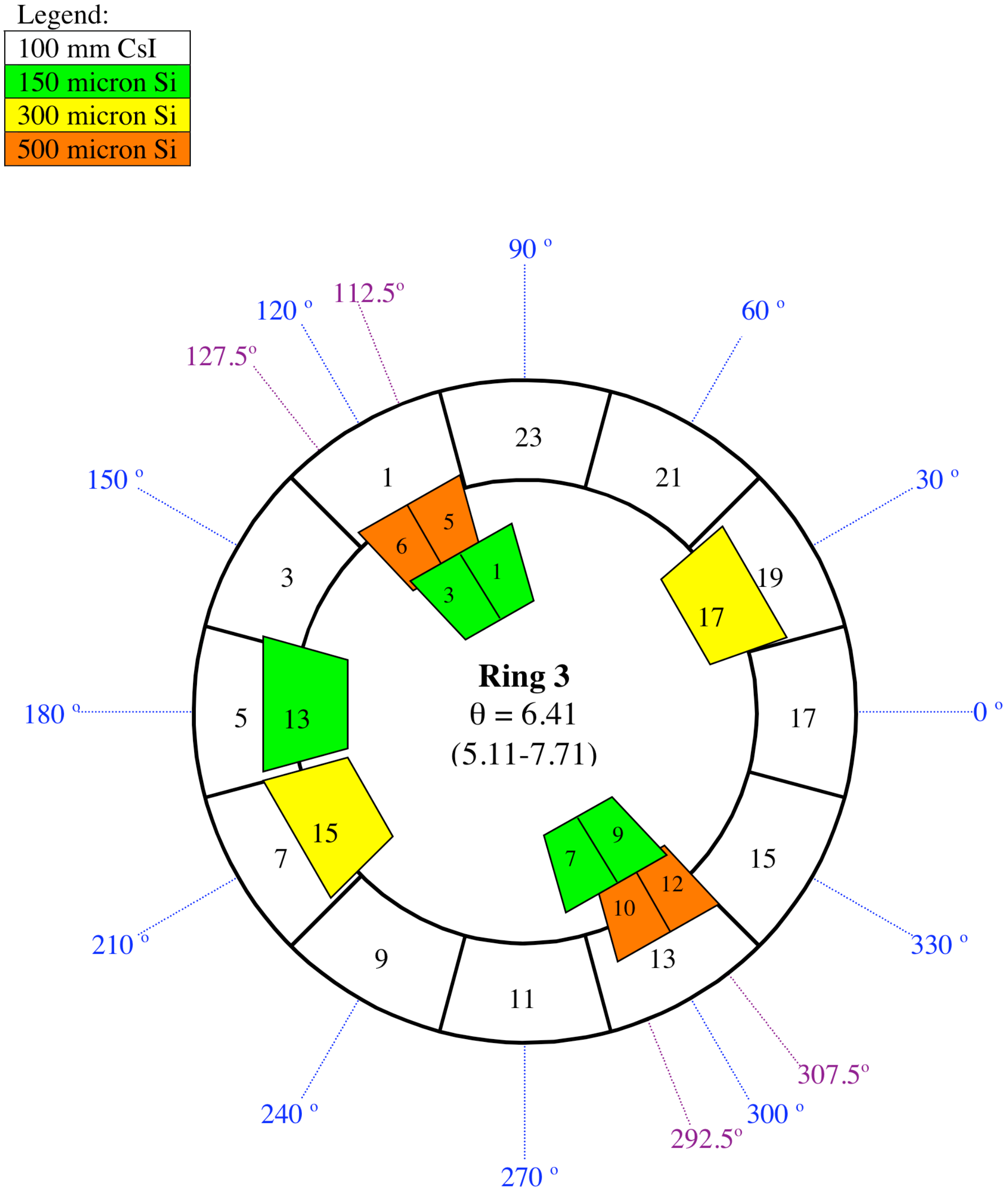

Fig. A-2. NIMROD map, ring 3.

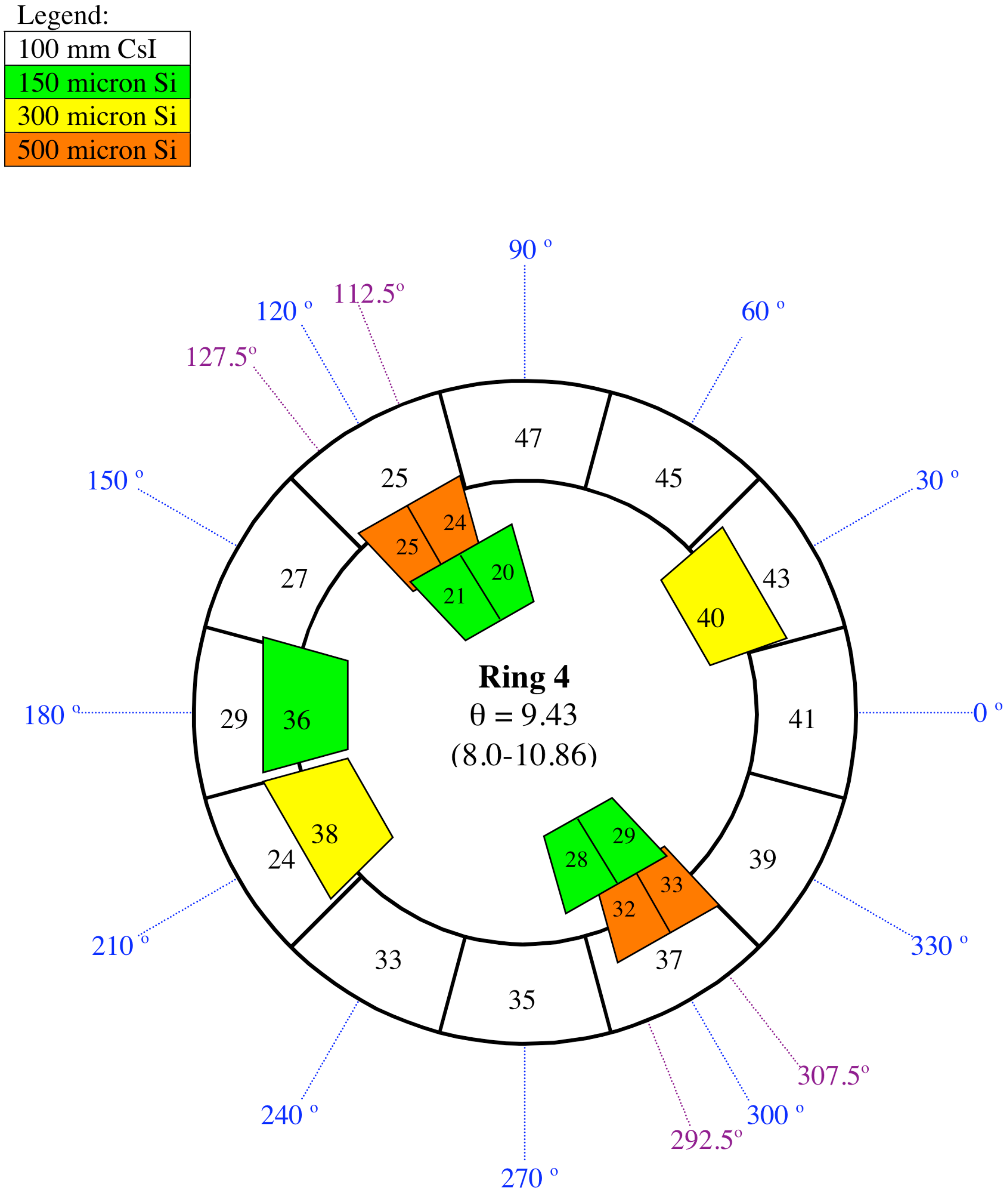

Fig. A-3. NIMROD map, ring 4.

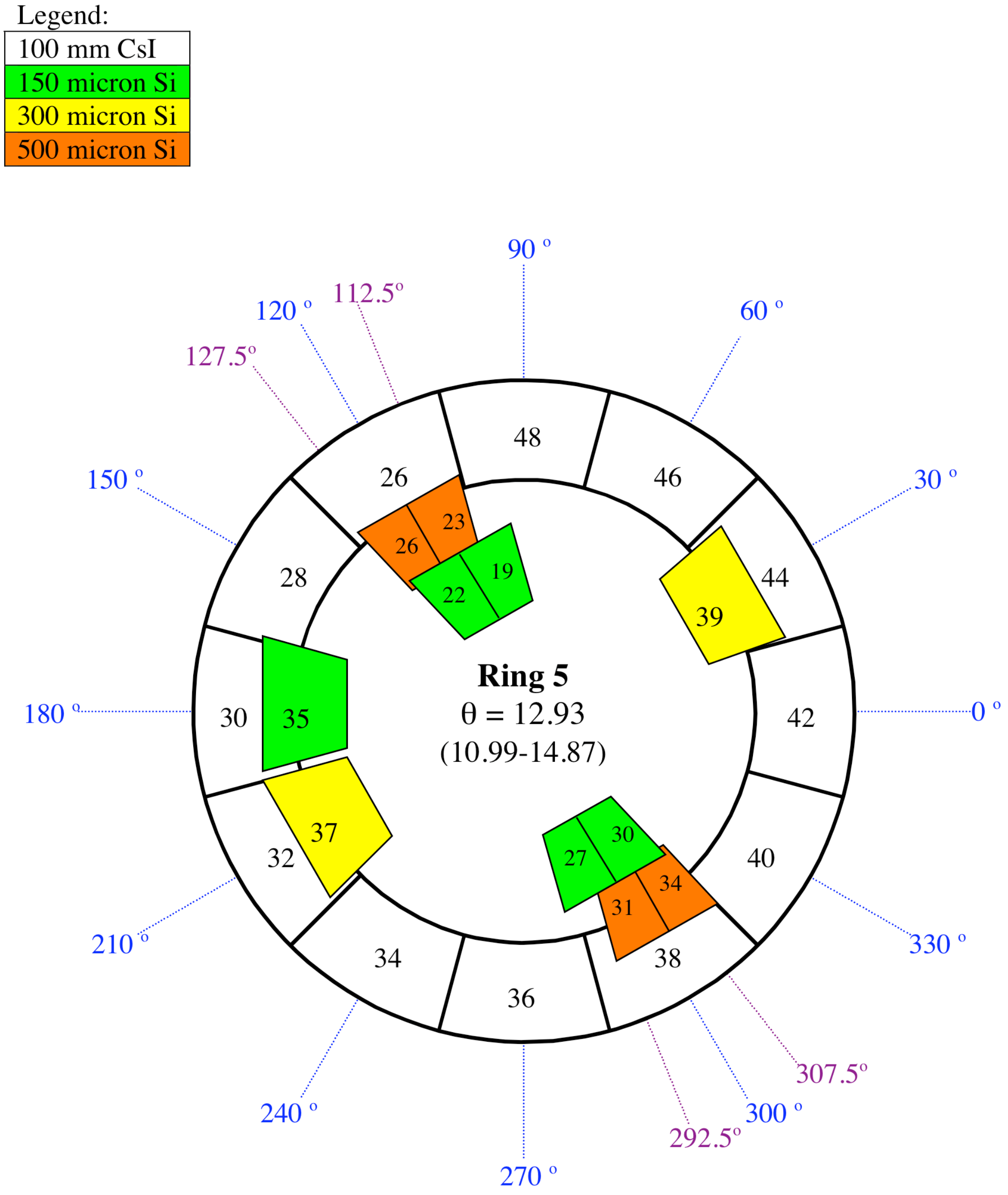

Fig. A-4. NIMROD map, ring 5.

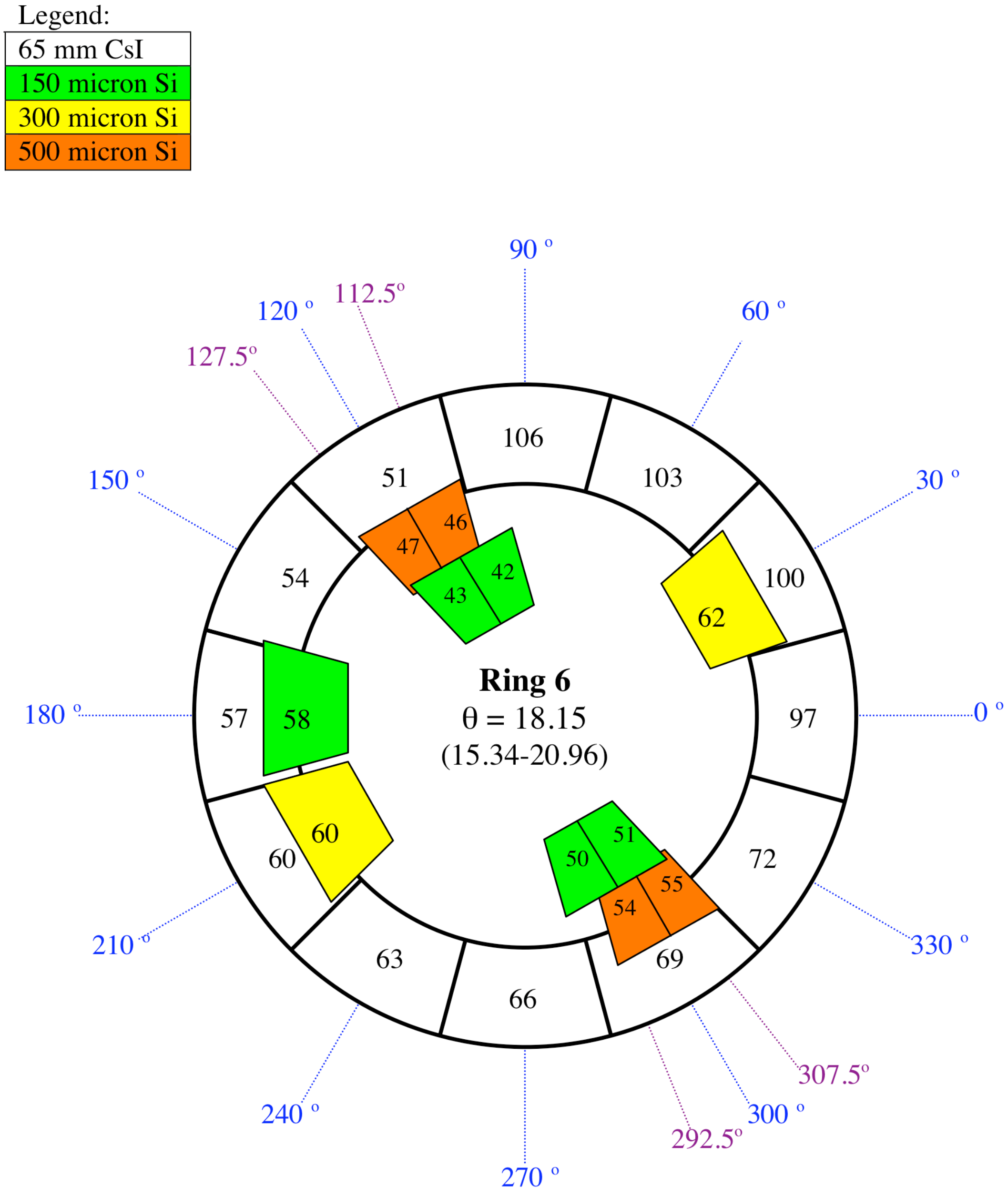

Fig. A-5. NIMROD map, ring 6.

Legend:

⬜ 65 mm CsI
🟩 150 micron Si
🟨 300 micron Si
🟧 500 micron Si

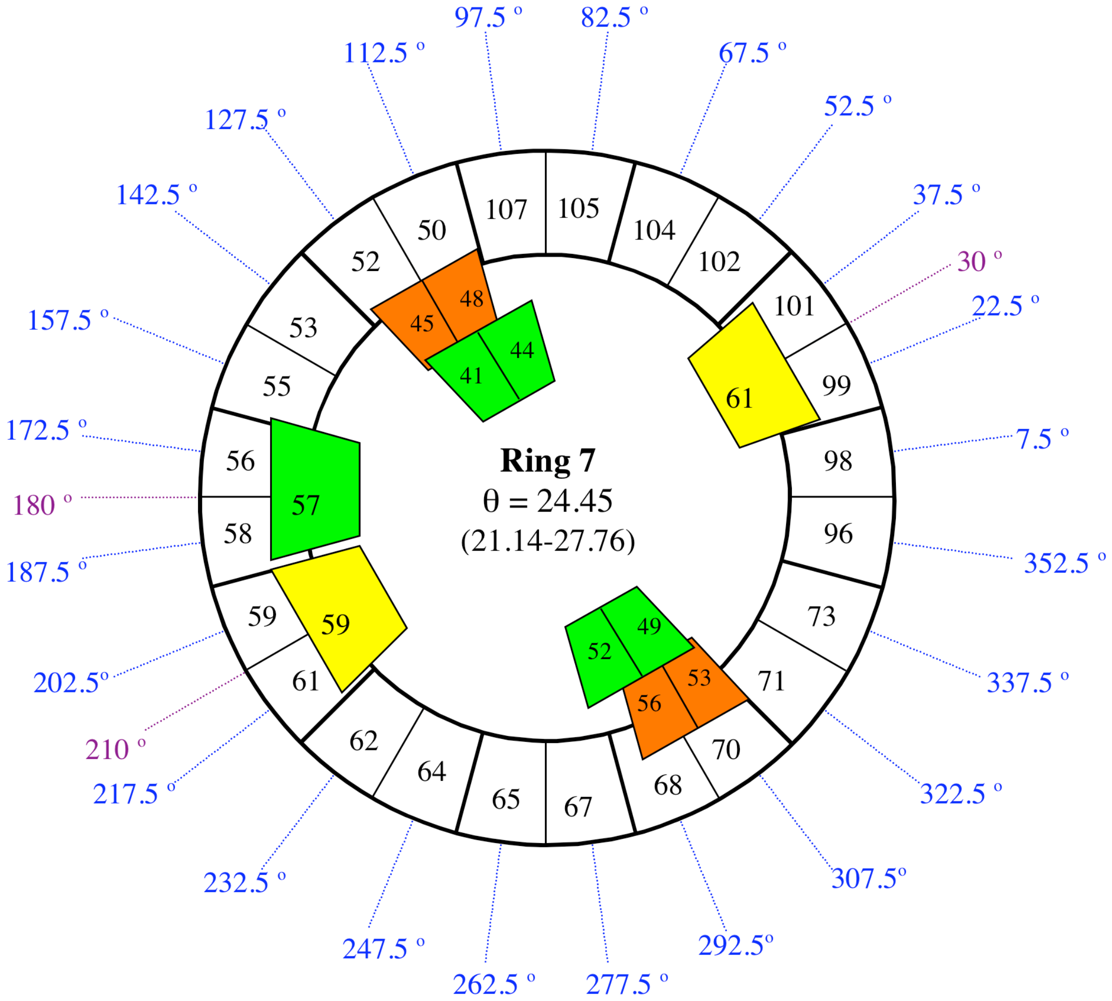

Fig. A-6. NIMROD map, ring 7.

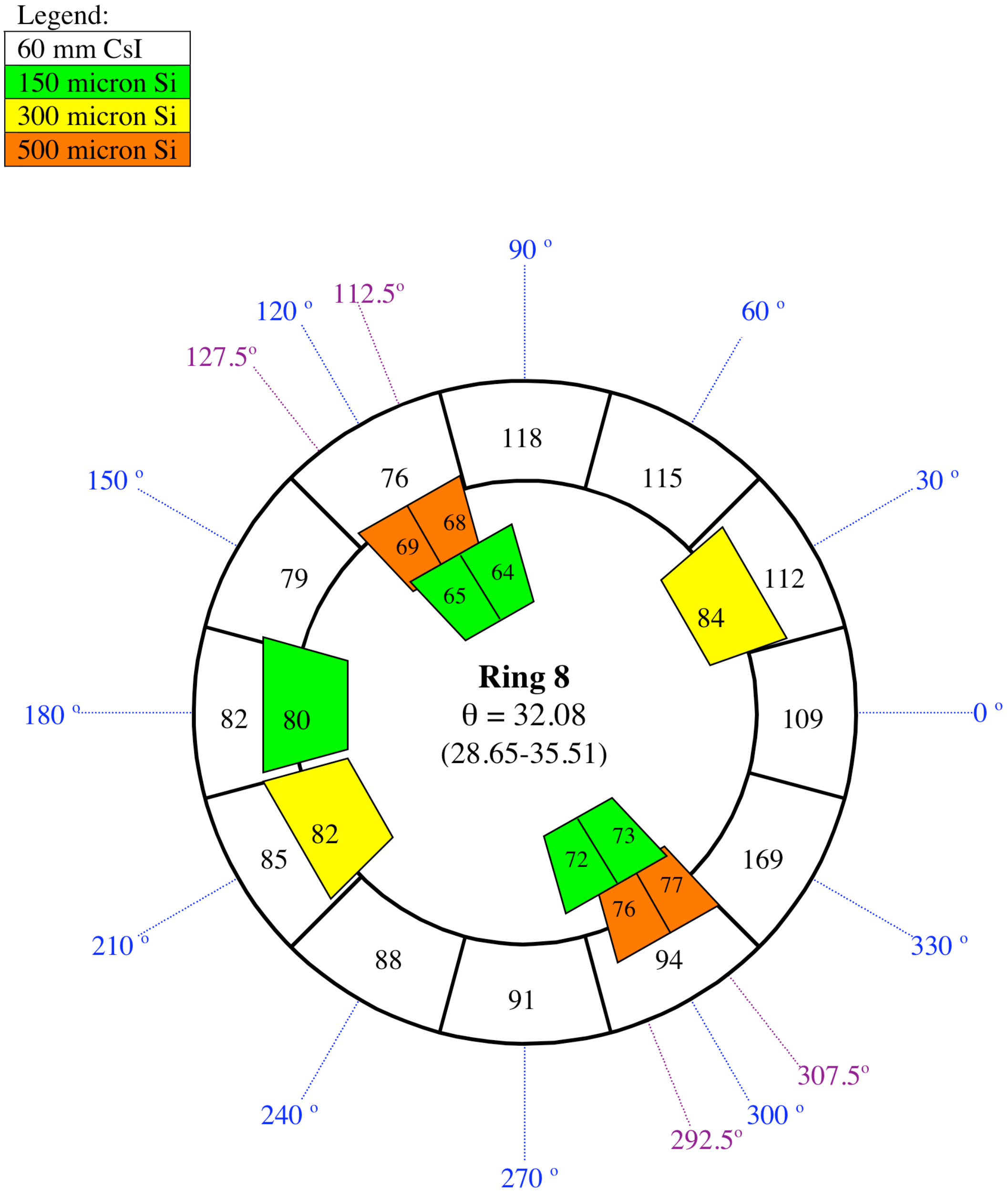

Fig. A-7. NIMROD map, ring 8.

Legend:

- ⬜ 60 mm CsI
- 🟩 150 micron Si
- 🟨 300 micron Si
- 🟧 500 micron Si

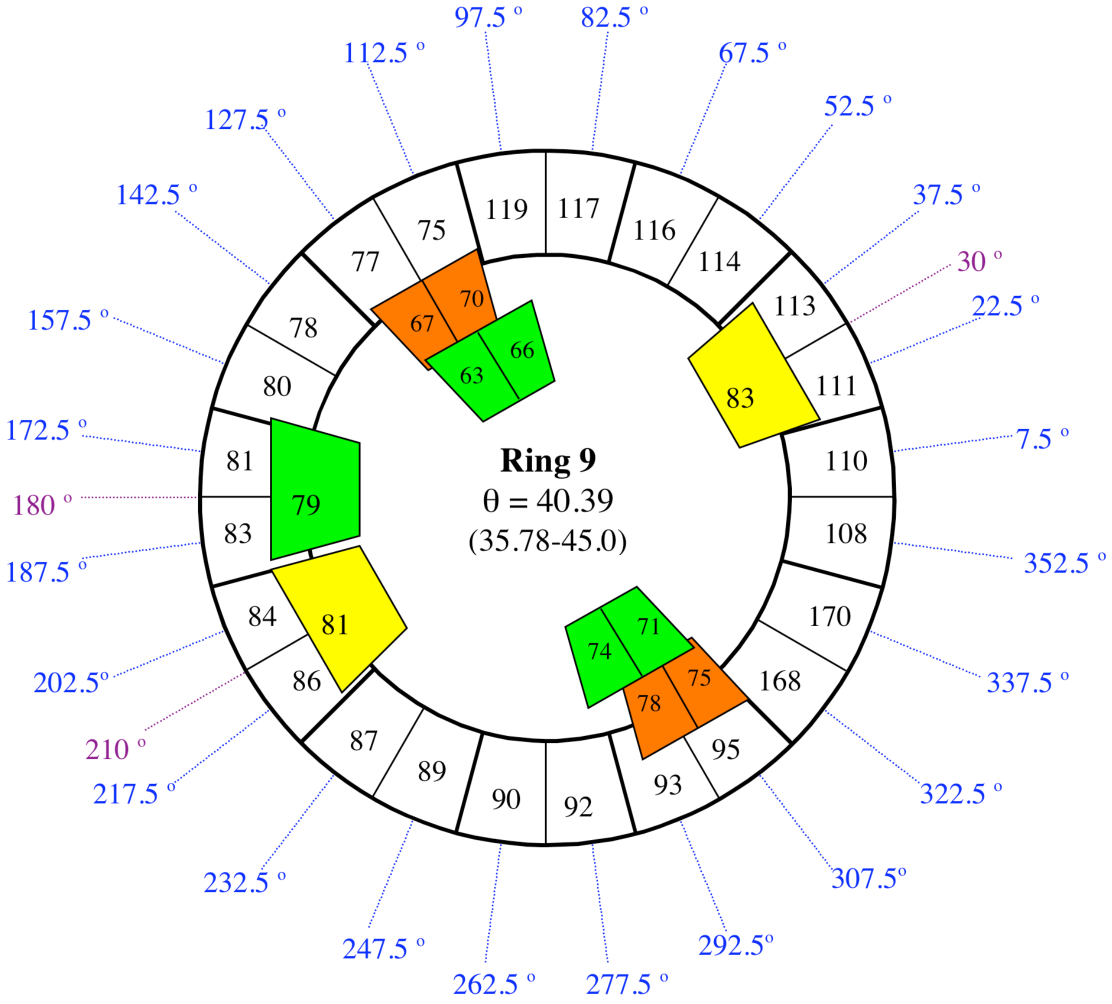

Fig. A-8. NIMROD map, ring 9.

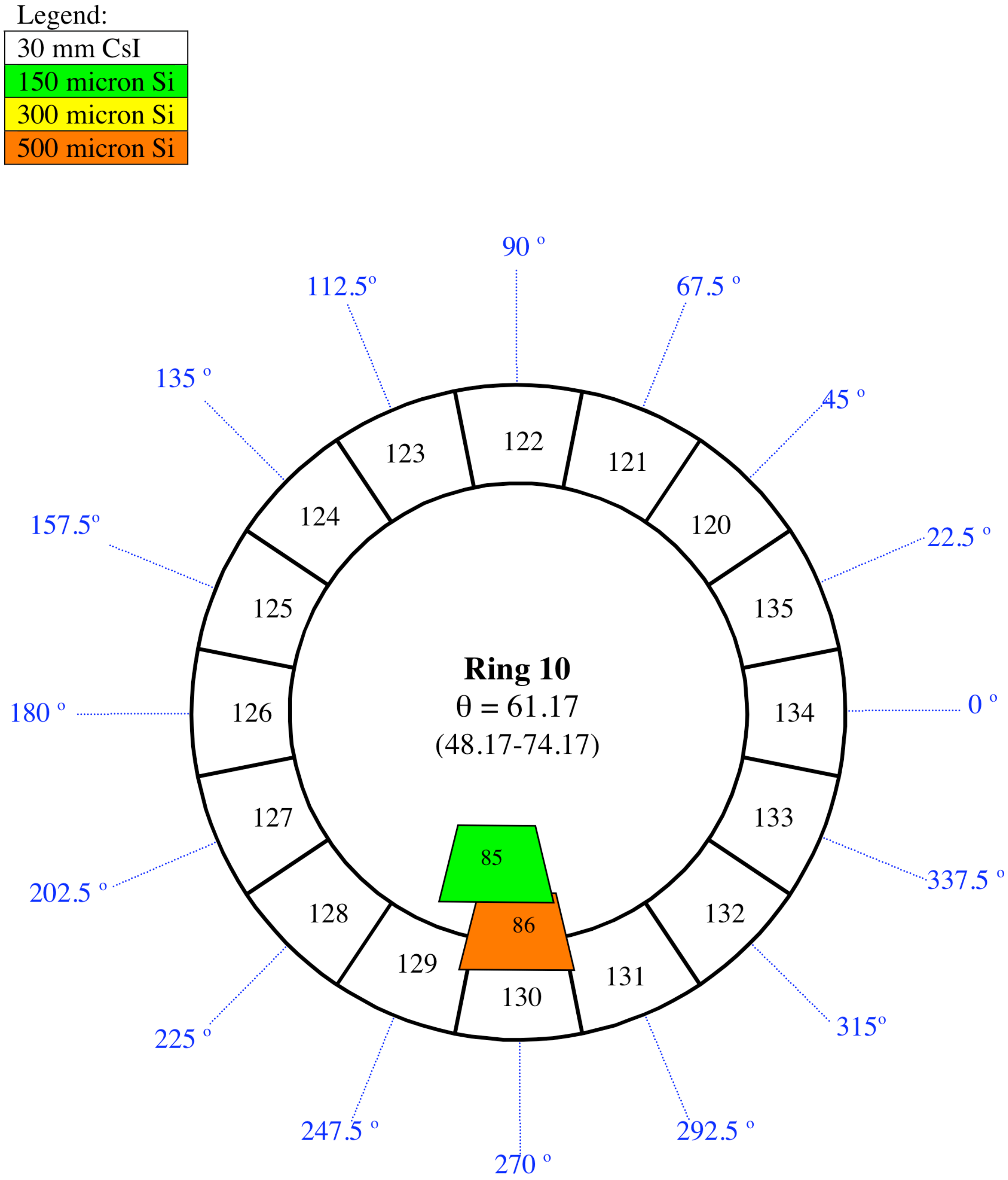

Fig. A-9. NIMROD map, ring 10.

Legend:

⬜ 10 mm CsI
🟩 150 micron Si
🟨 300 micron Si
🟧 500 micron Si

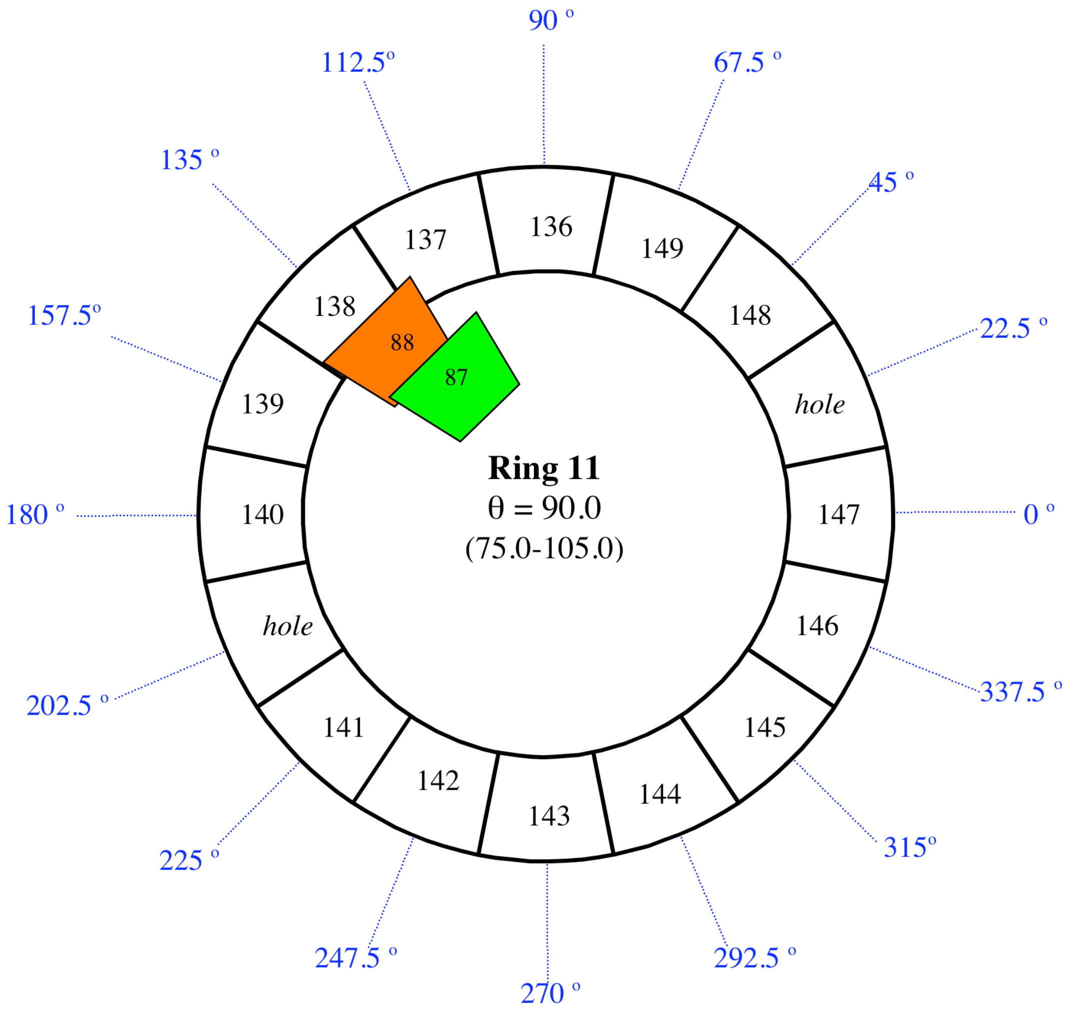

Fig. A-10. NIMROD map, ring 11.

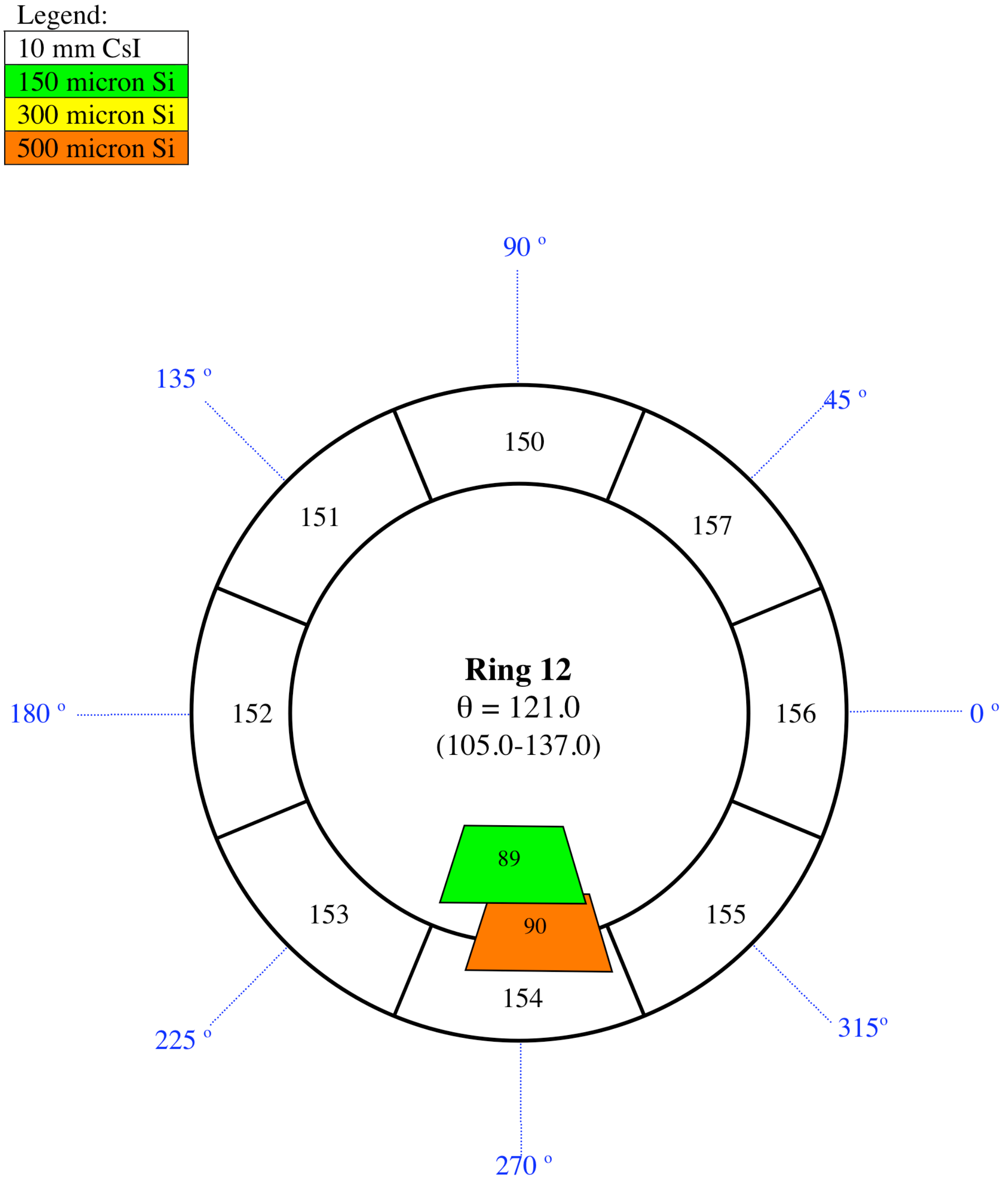

Fig. A-11. NIMROD map, ring 12.

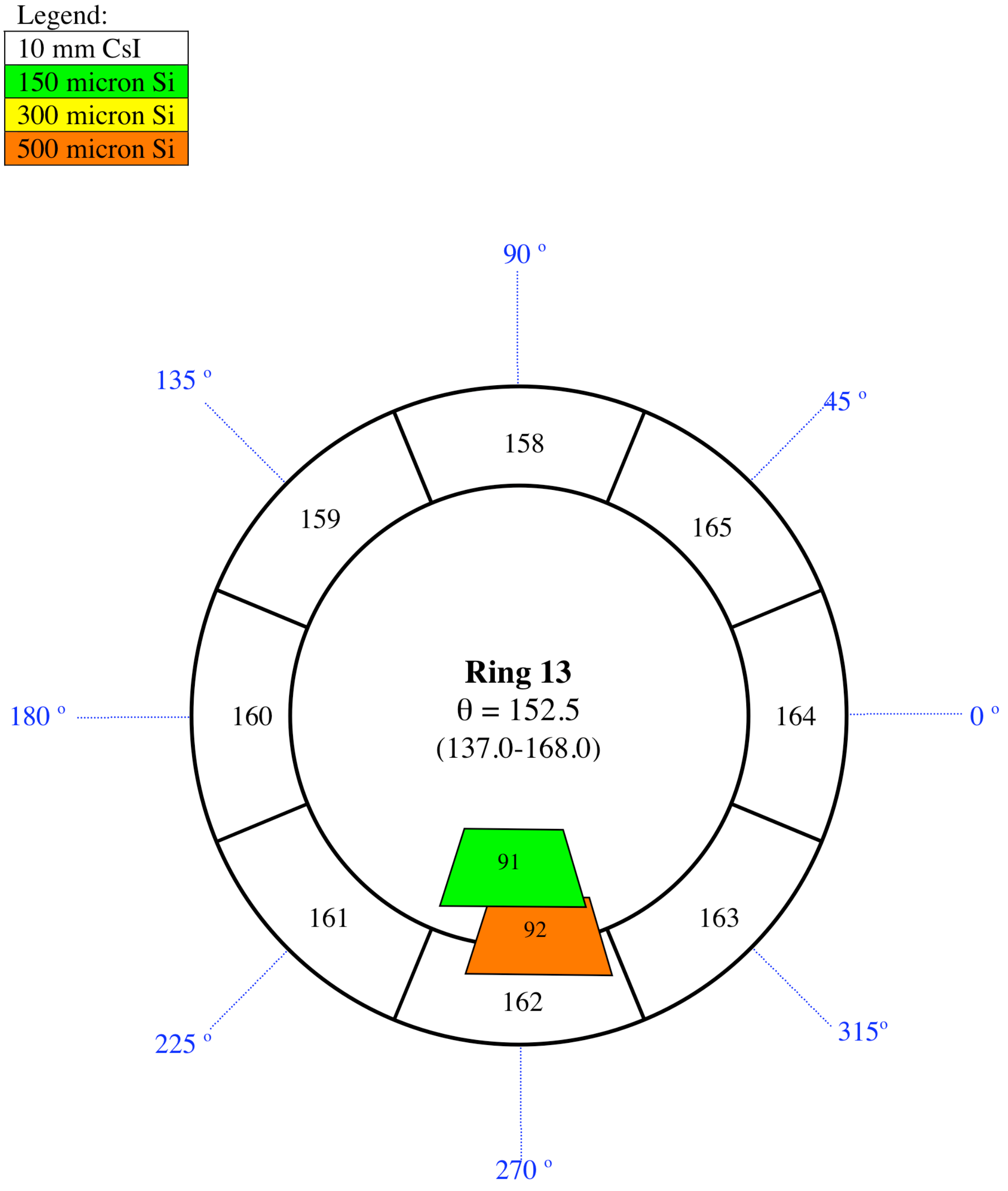

Fig. A-12. NIMROD map, ring 13.

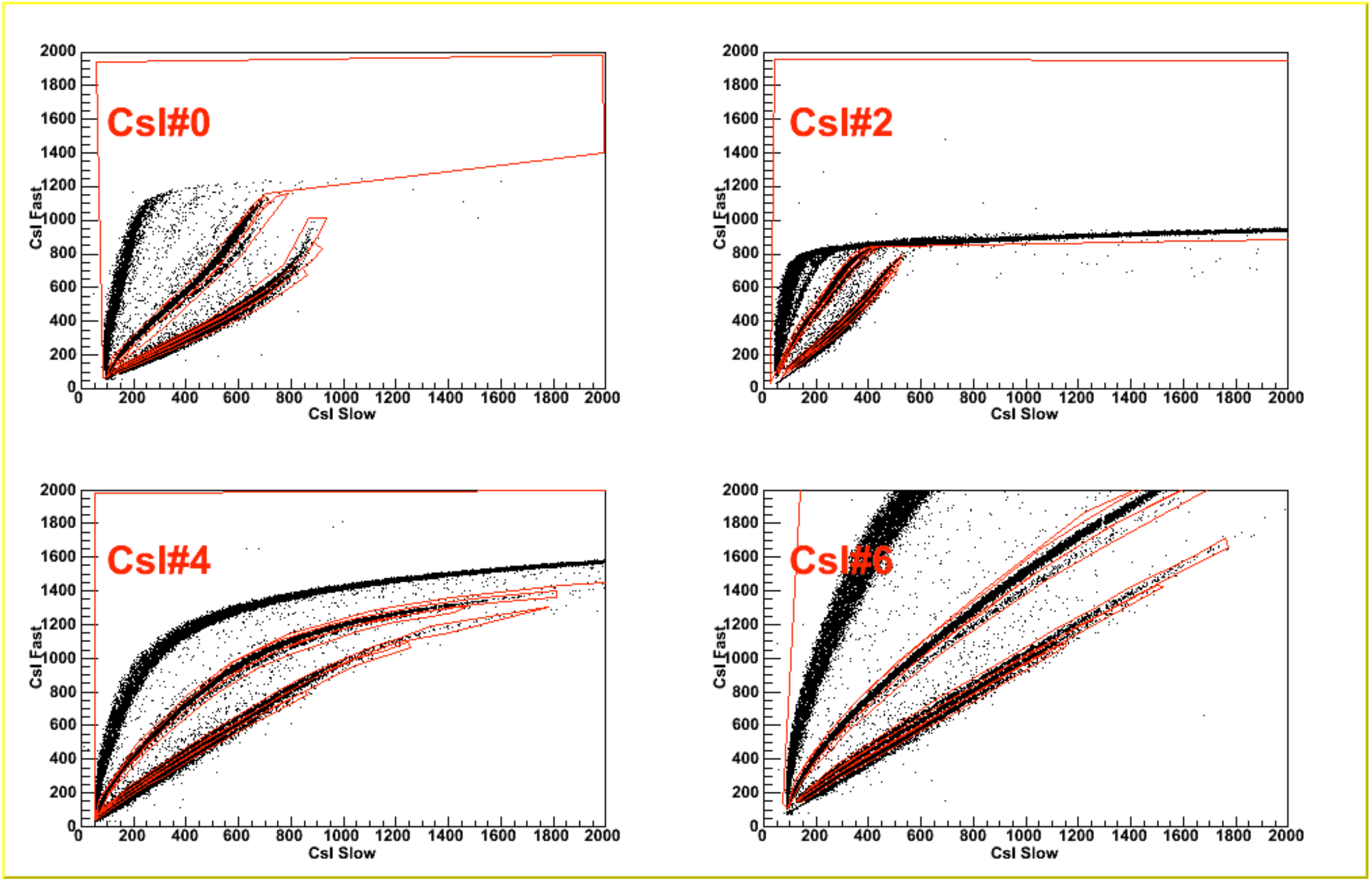

Fig. A-13. CsI slow versus fast raw spectra, ring 2, part 1.

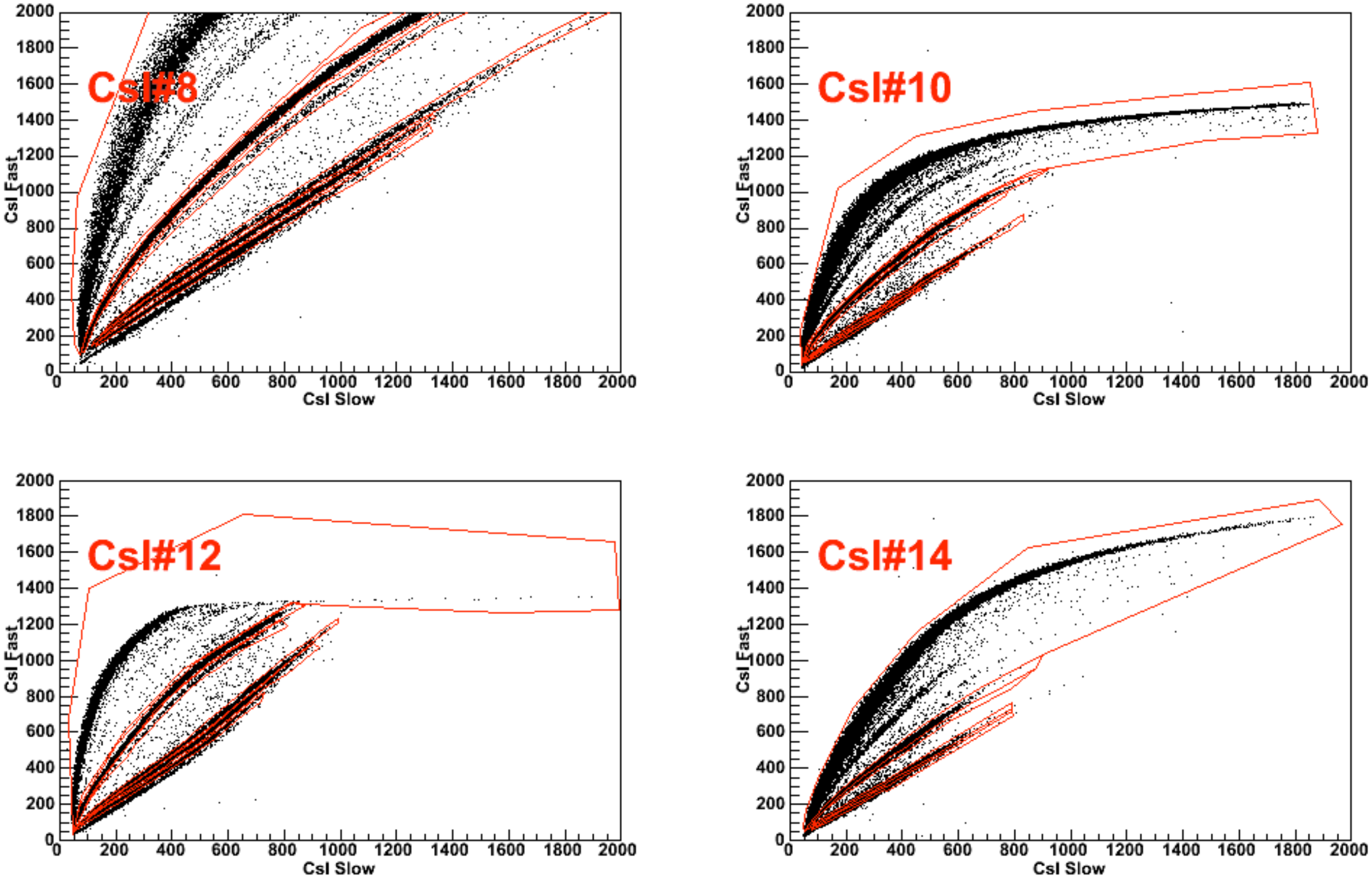

Fig. A-14. CsI slow versus fast raw spectra, ring 2, part 2.

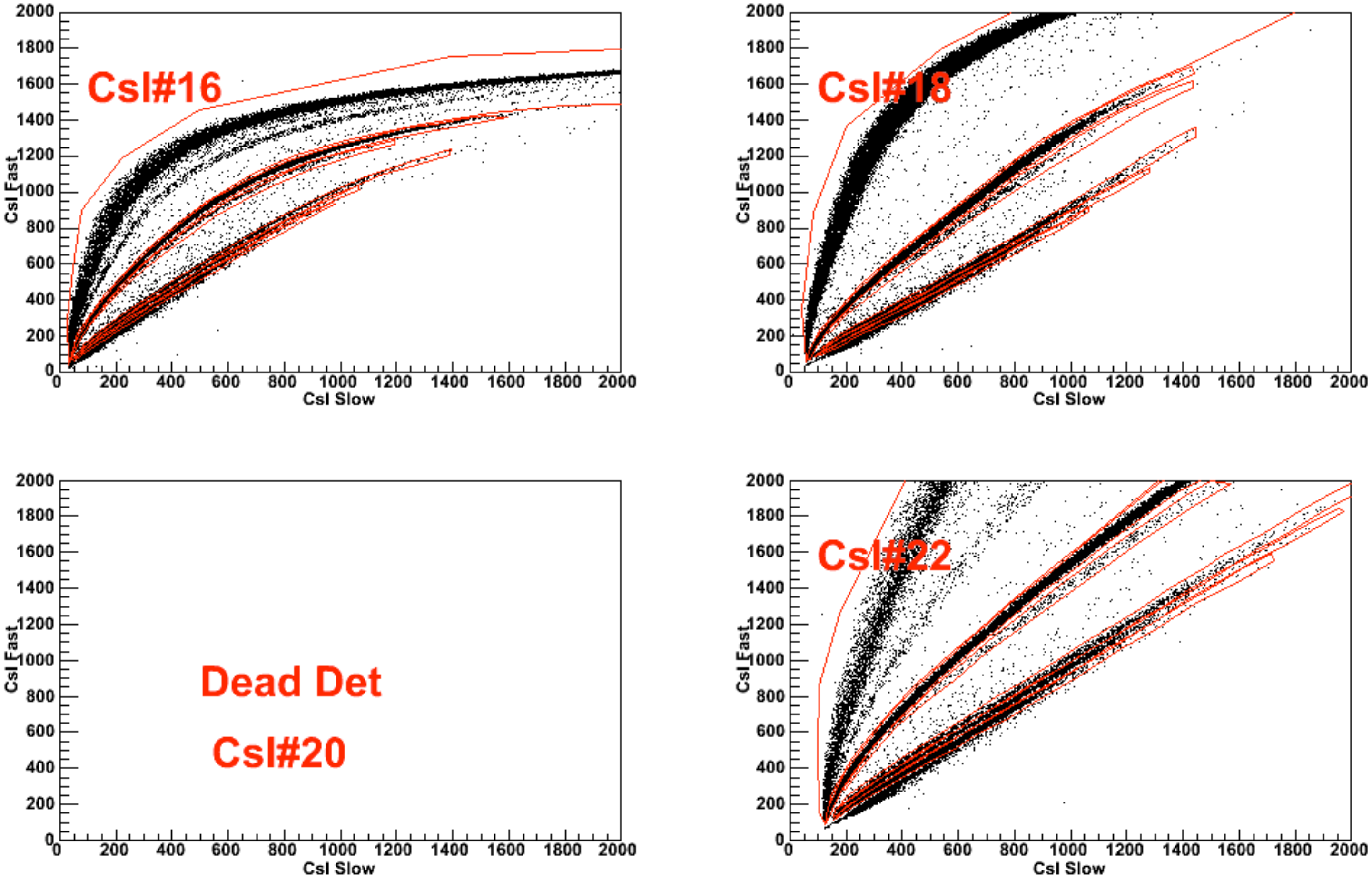

Fig. A-15. CsI slow versus fast raw spectra, ring 2, part 3.

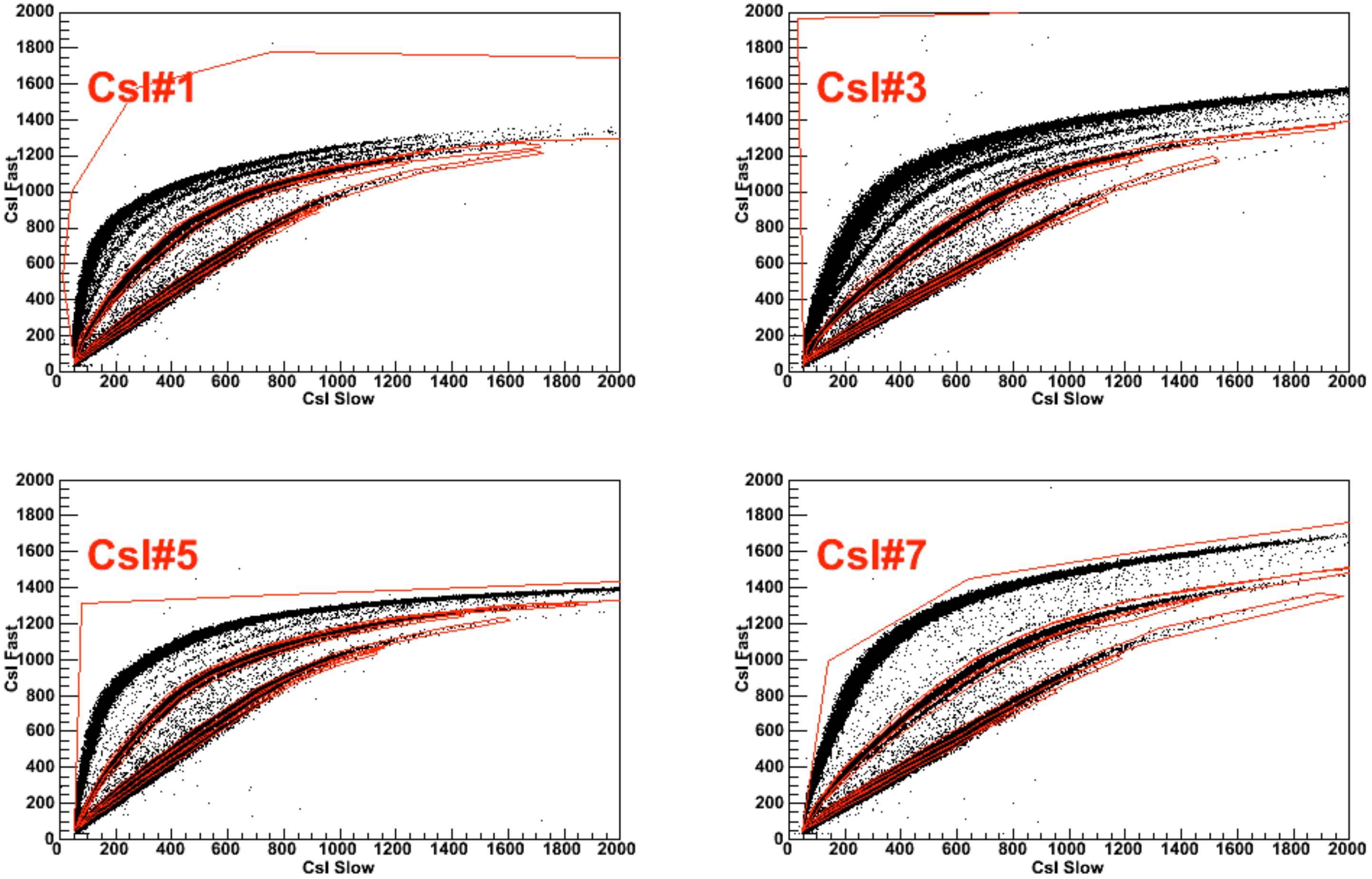

Fig. A-16. CsI slow versus fast raw spectra, ring 3, part 1.

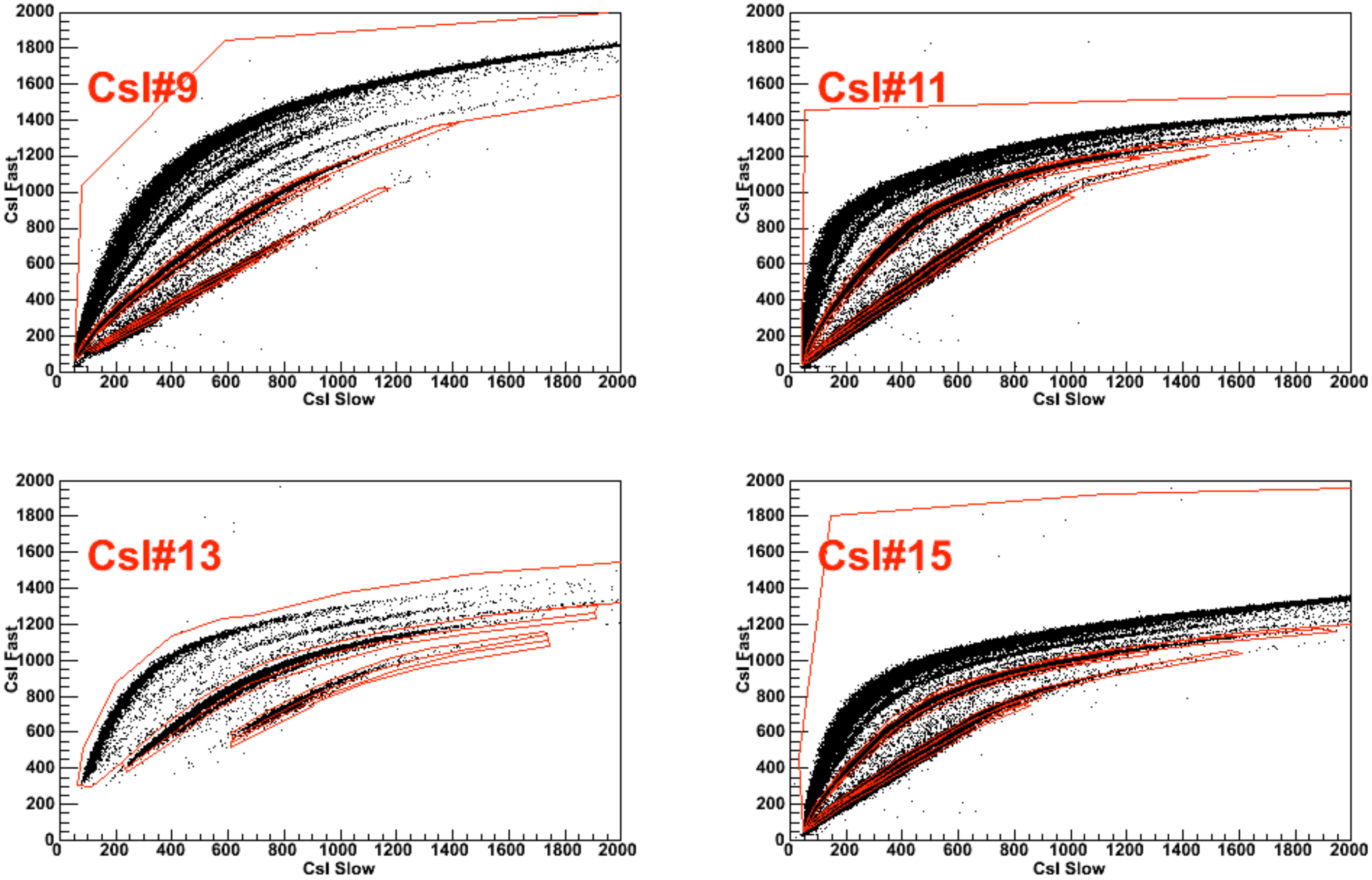

Fig. A-17. CsI slow versus fast raw spectra, ring 3, part 2.

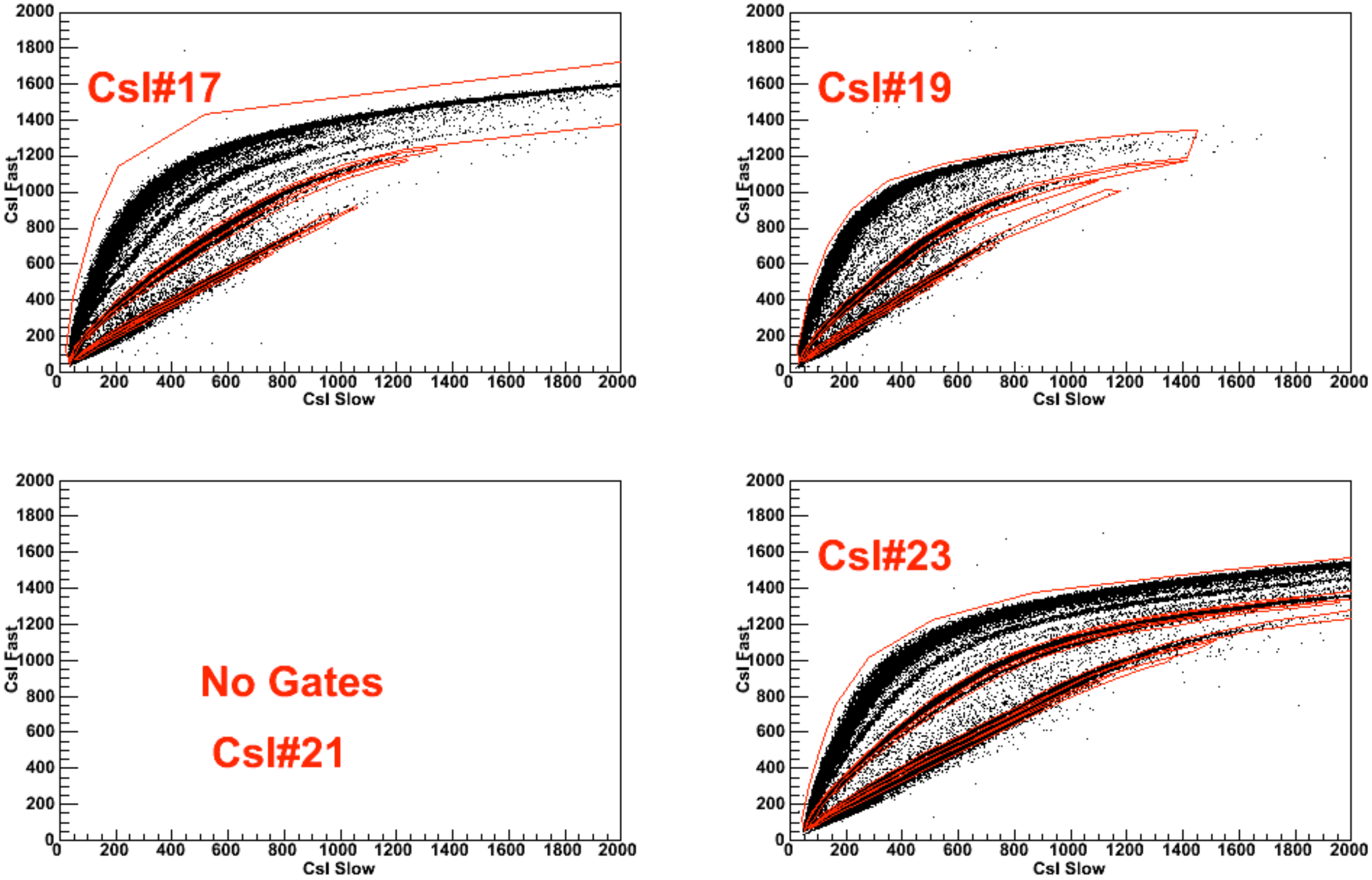

Fig. A-18. CsI slow versus fast raw spectra, ring 3, part 3.

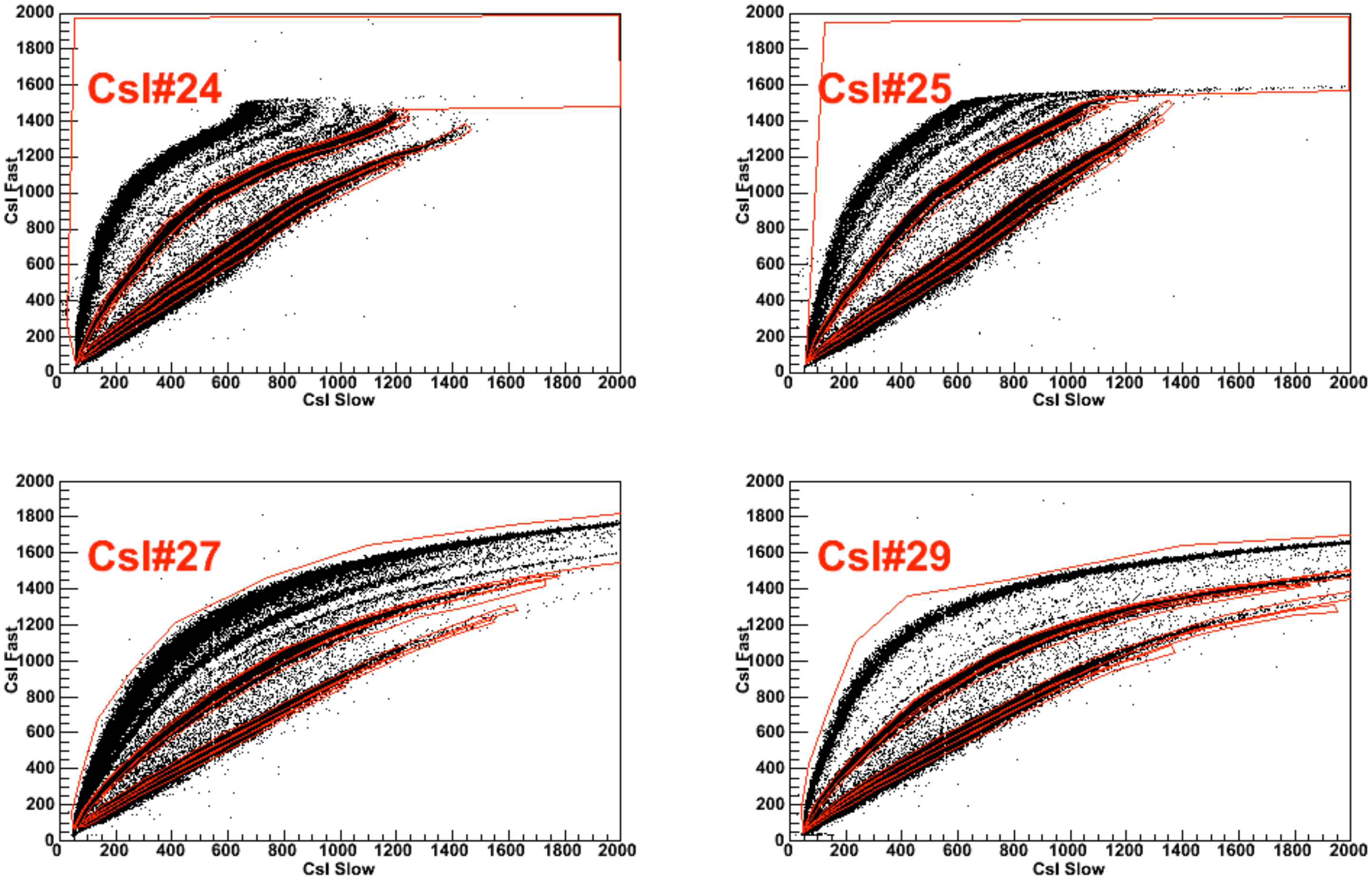

Fig. A-19. CsI slow versus fast raw spectra, ring 4, part 1.

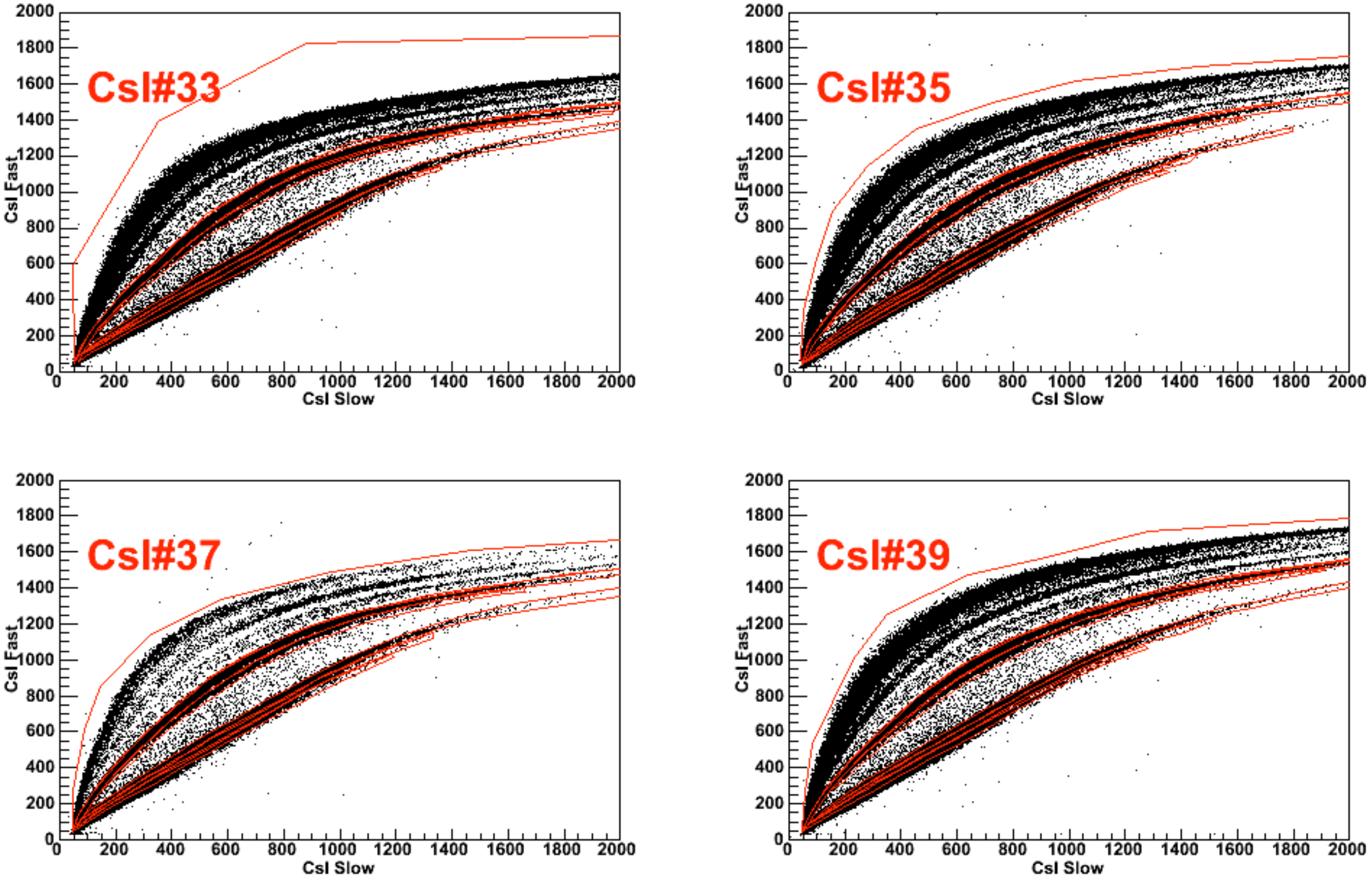

Fig. A-20. CsI slow versus fast raw spectra, ring 4, part 2.

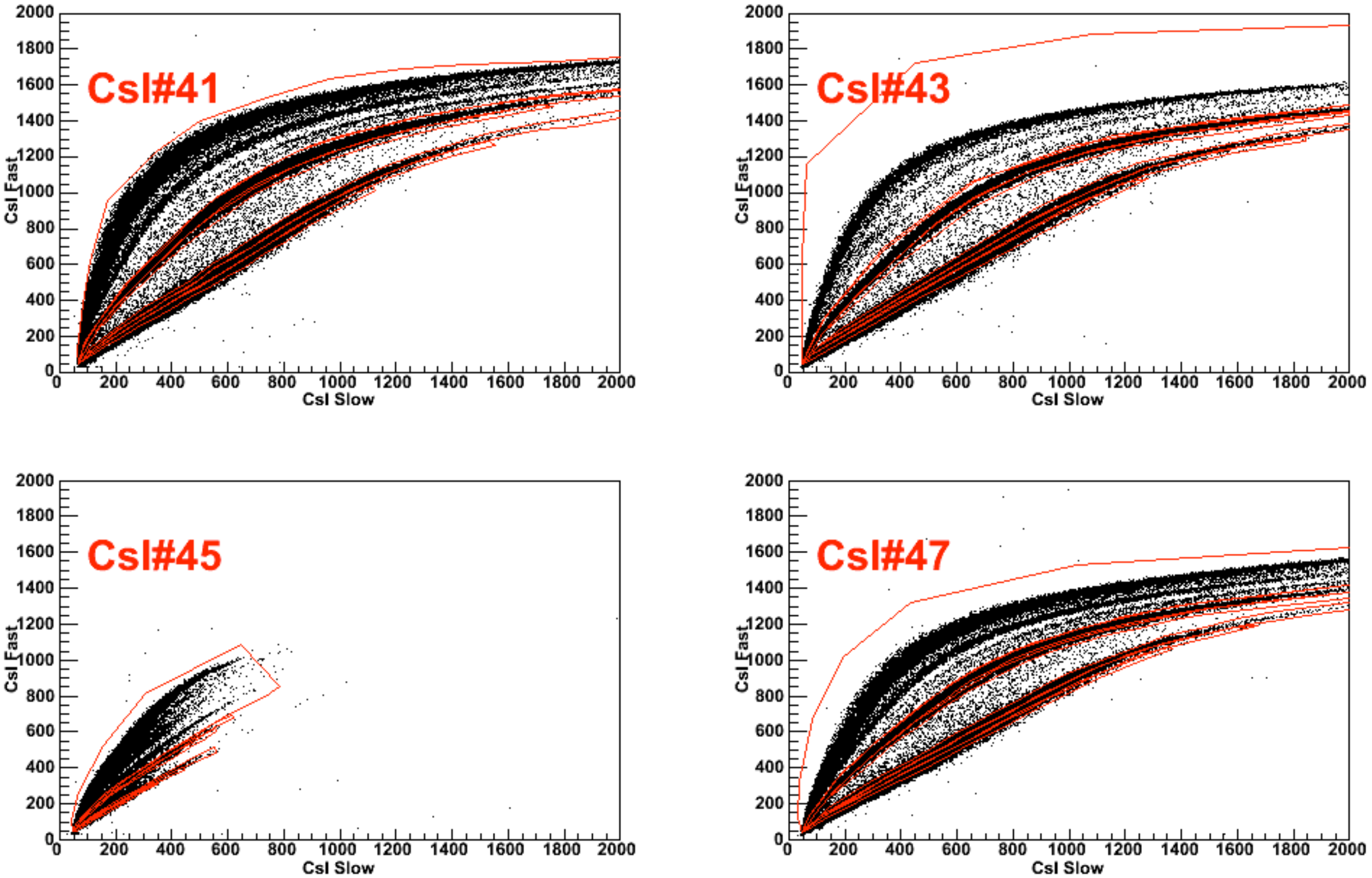

Fig. A-21. CsI slow versus fast raw spectra, ring 4, part 3.

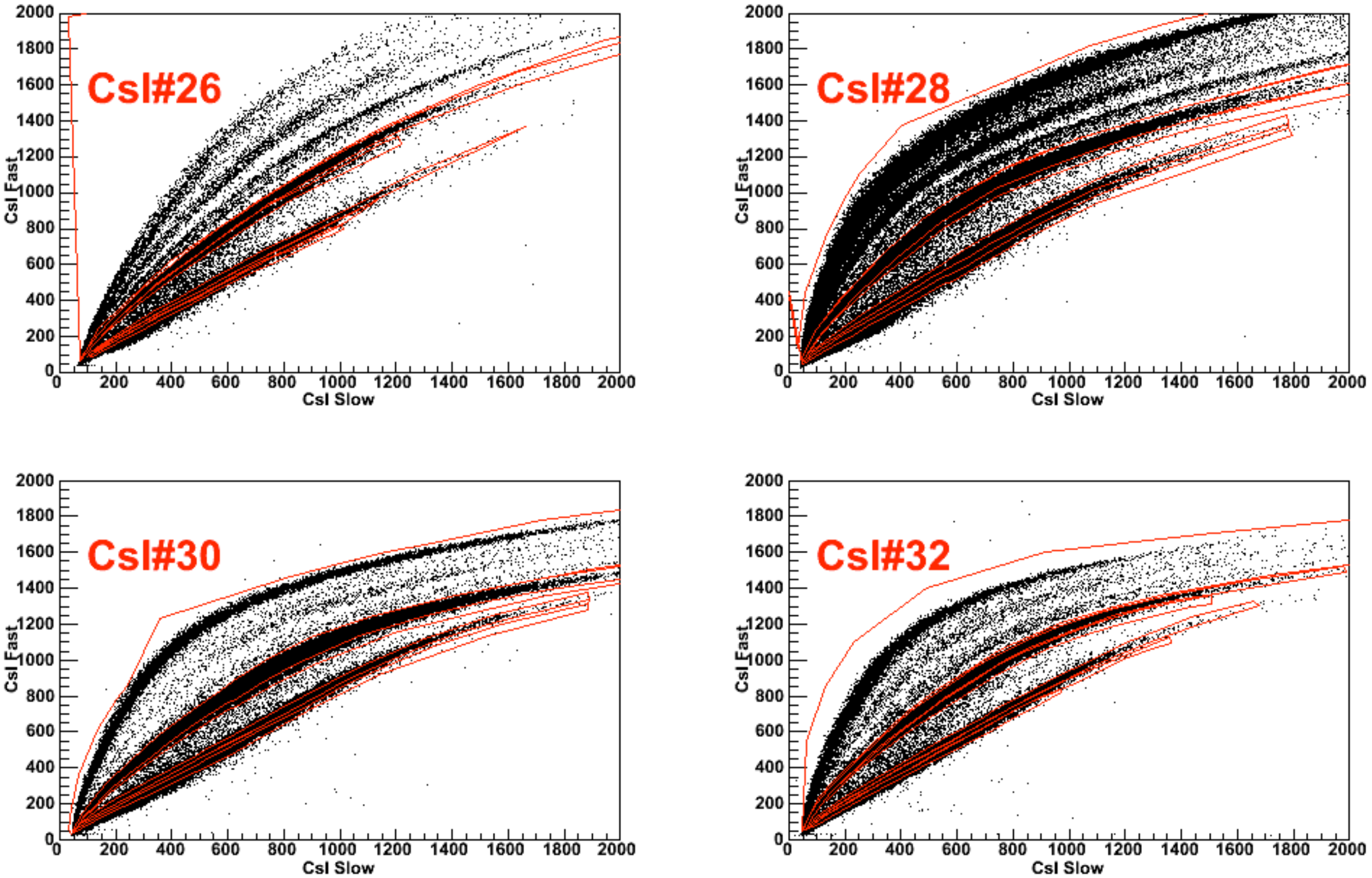

Fig. A-22. CsI slow versus fast raw spectra, ring 5, part 1.

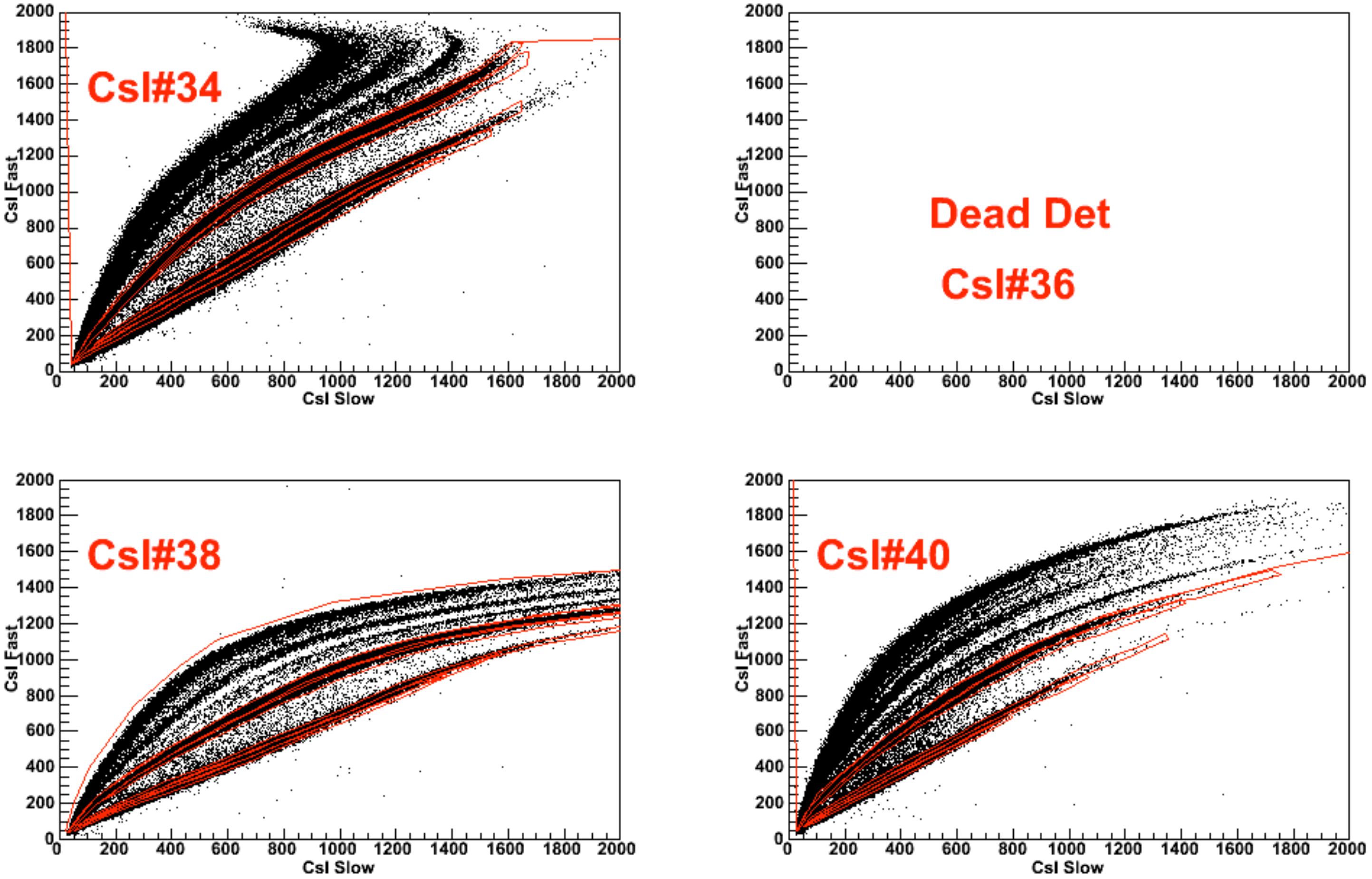

Fig. A-23. CsI slow versus fast raw spectra, ring 5, part 2.

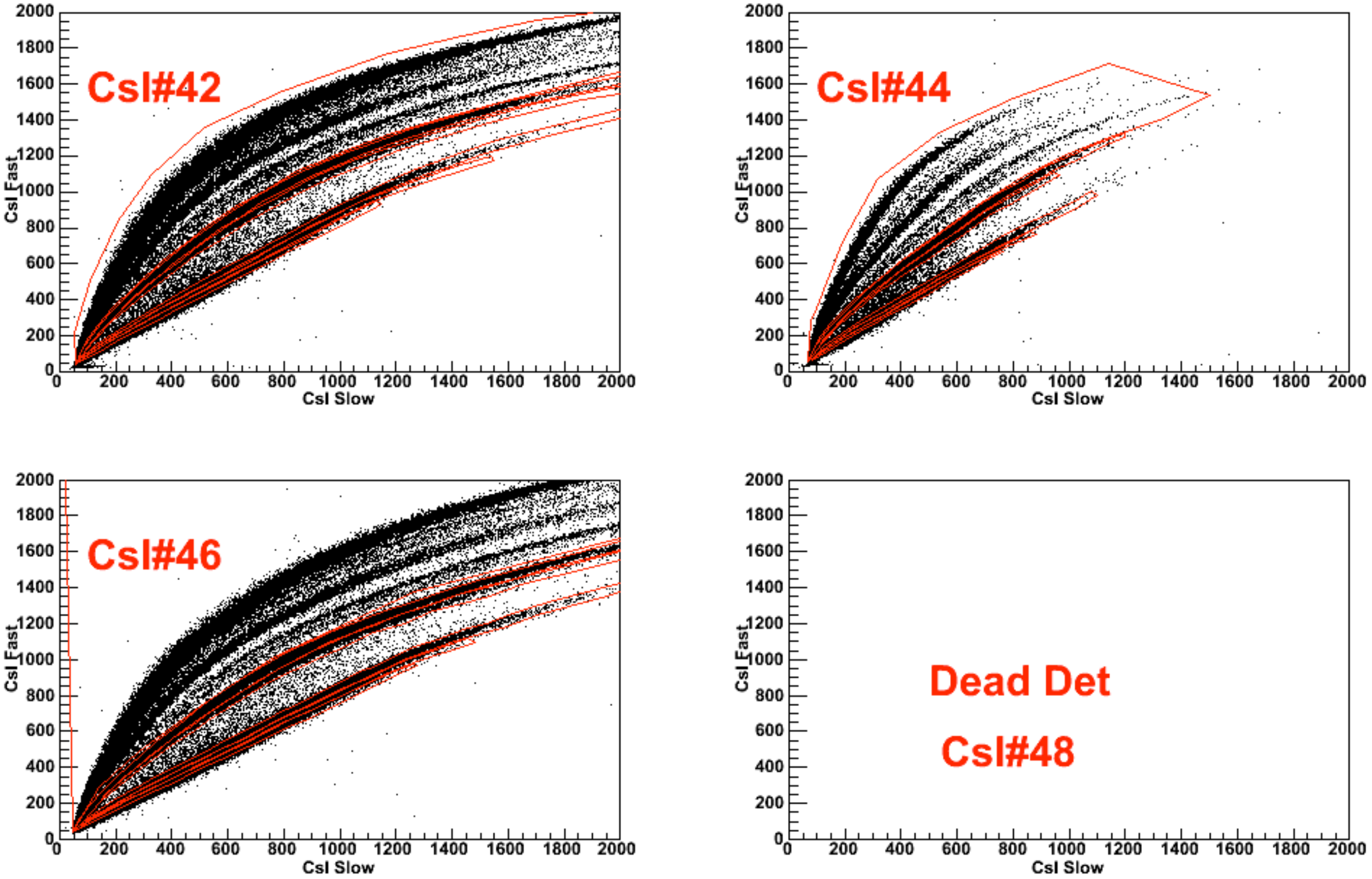

Fig. A-24. CsI slow versus fast raw spectra, ring 5, part 3.

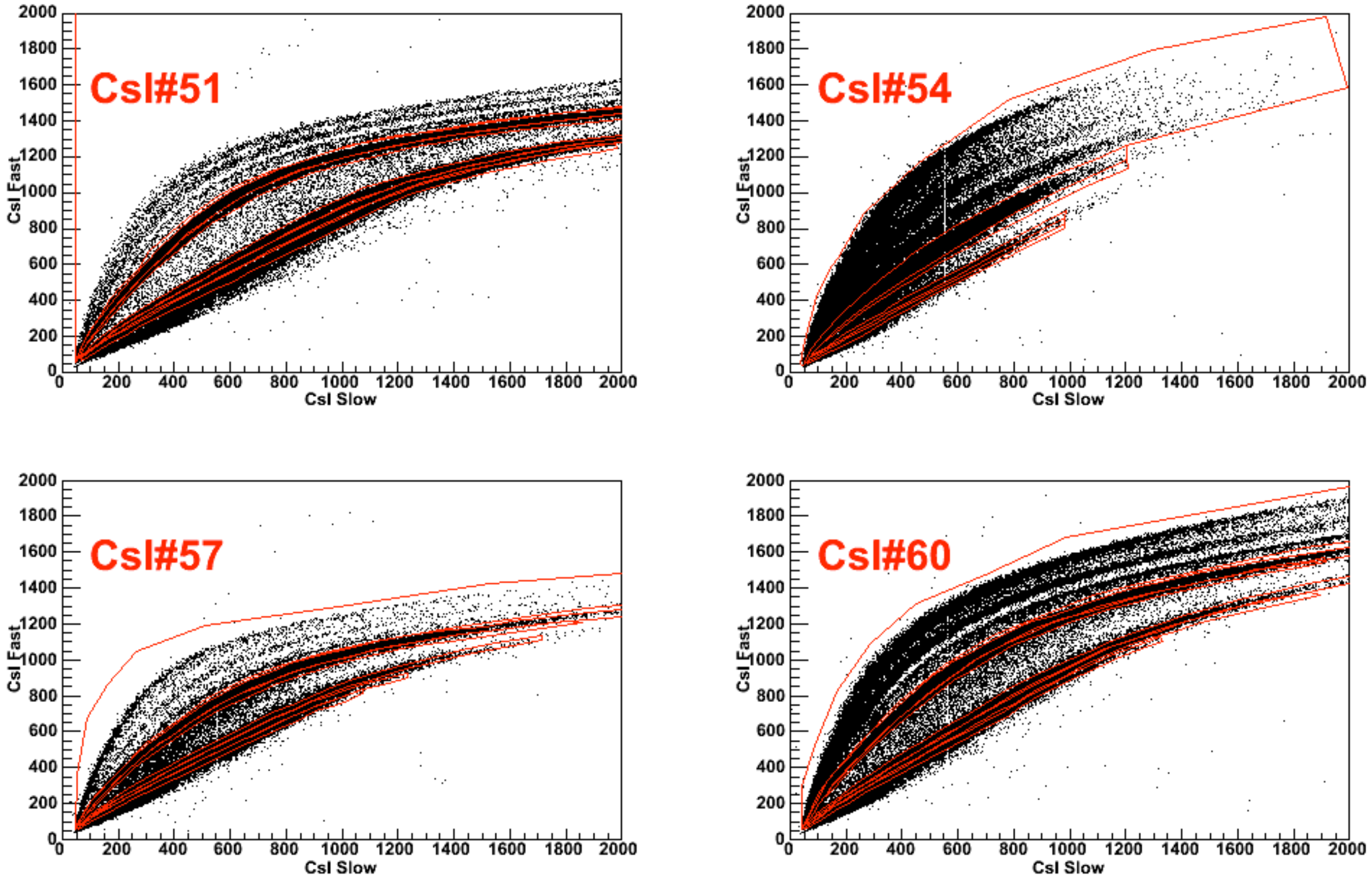

Fig. A-25. CsI slow versus fast raw spectra, ring 6, part 1.

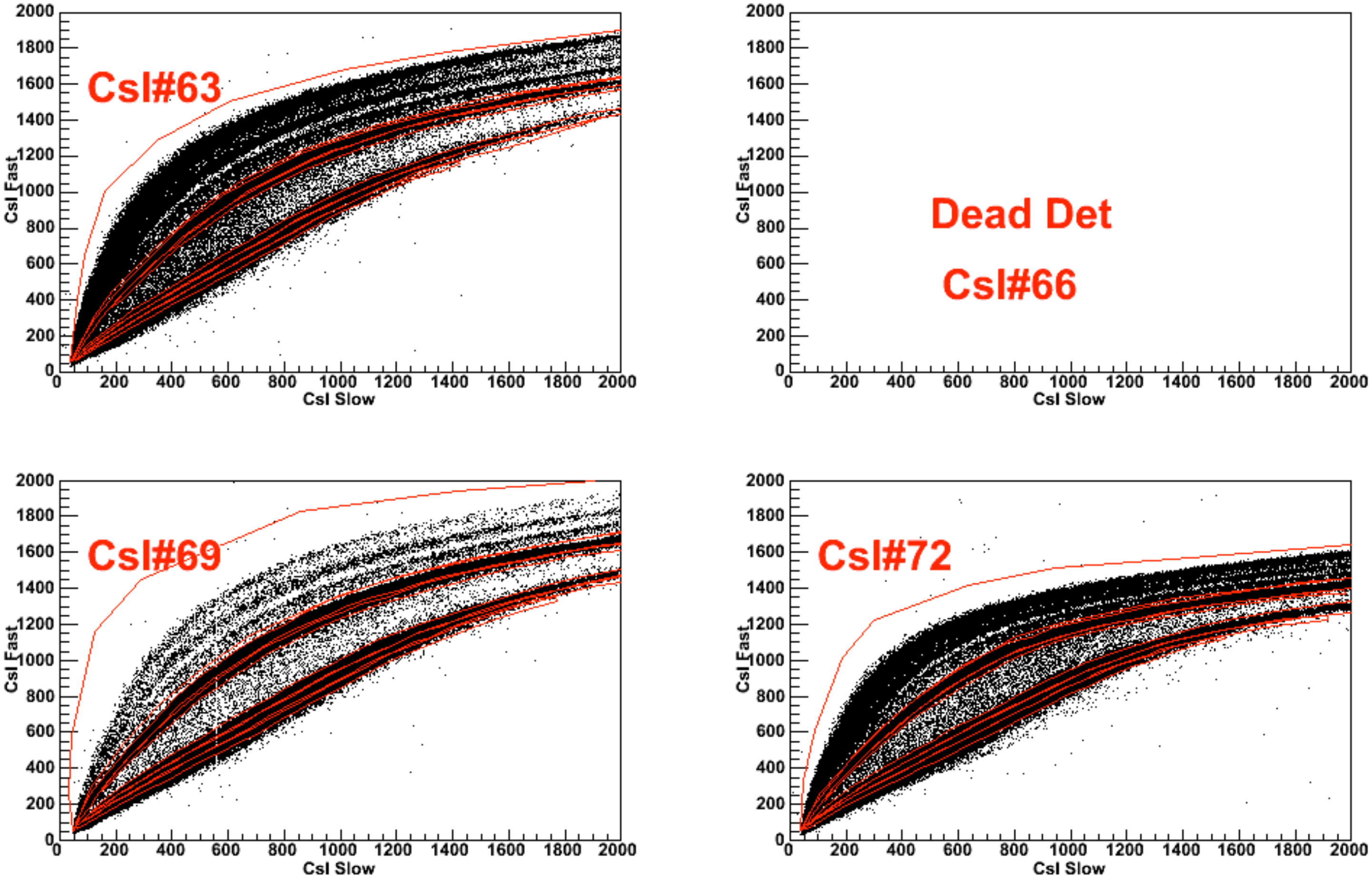

Fig. A-26. CsI slow versus fast raw spectra, ring 6, part 2.

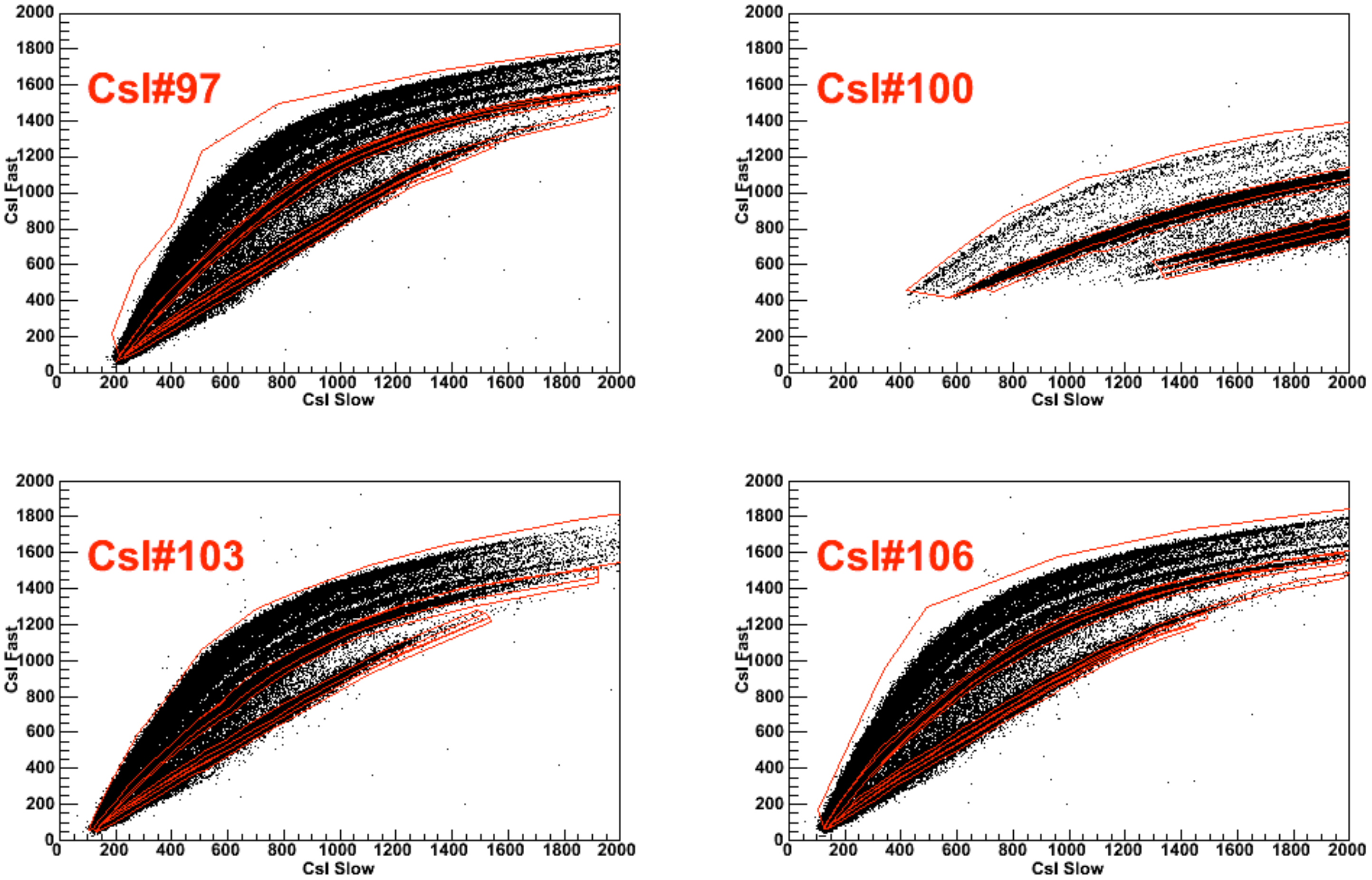

Fig. A-27. CsI slow versus fast raw spectra, ring 6, part 3.

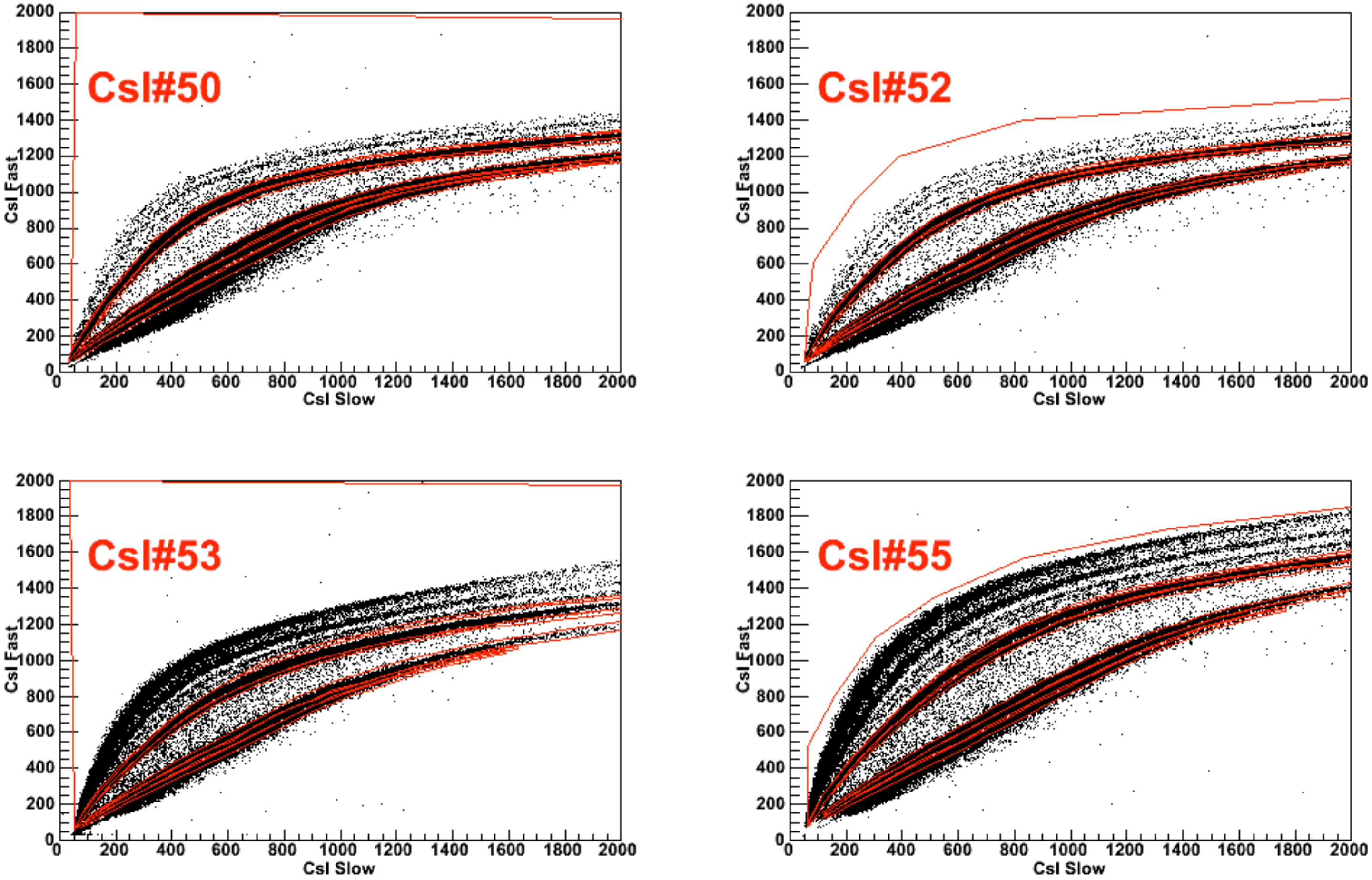

Fig. A-28. CsI slow versus fast raw spectra, ring 7, part 1.

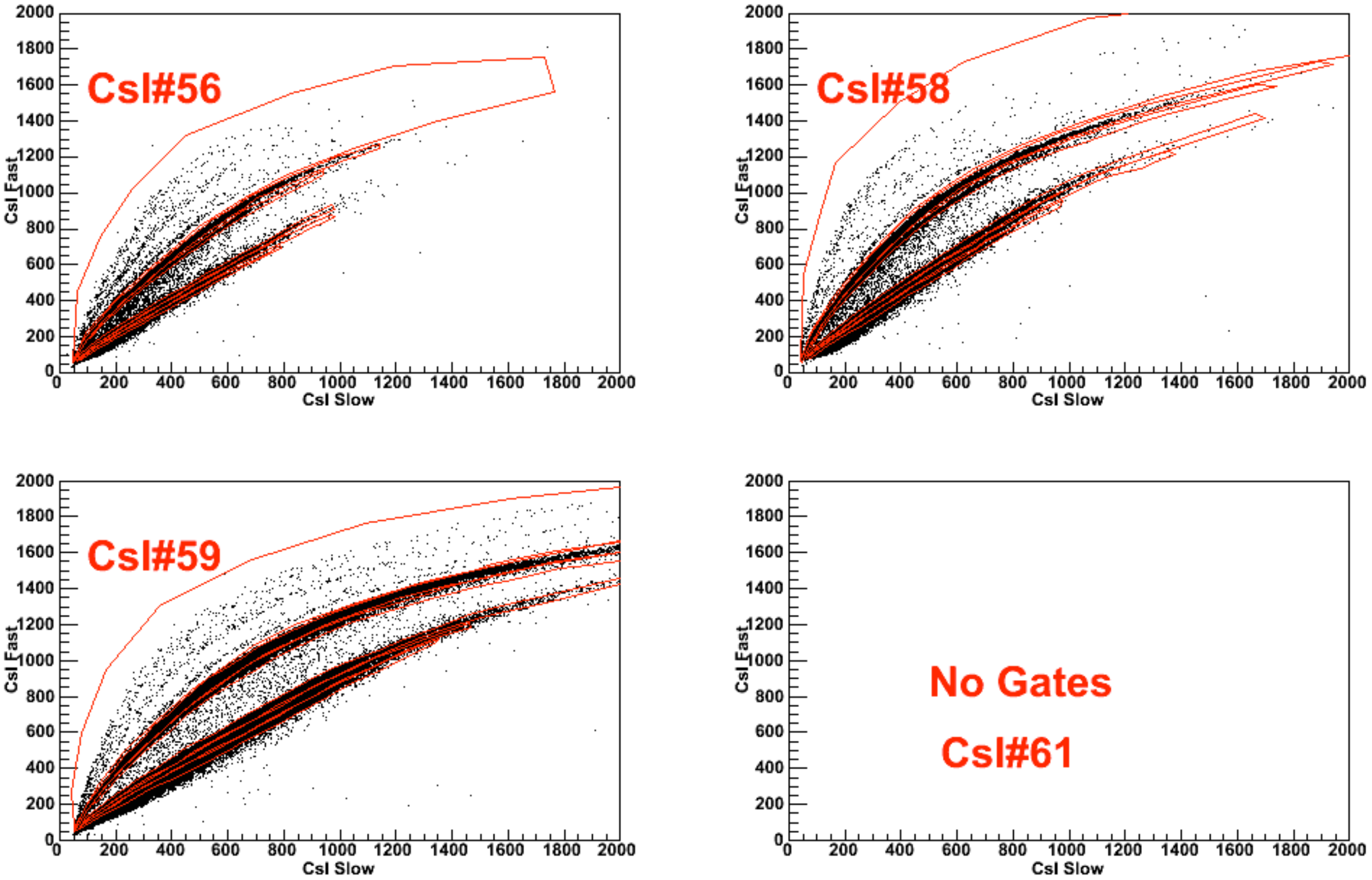

Fig. A-29. CsI slow versus fast raw spectra, ring 7, part 2.

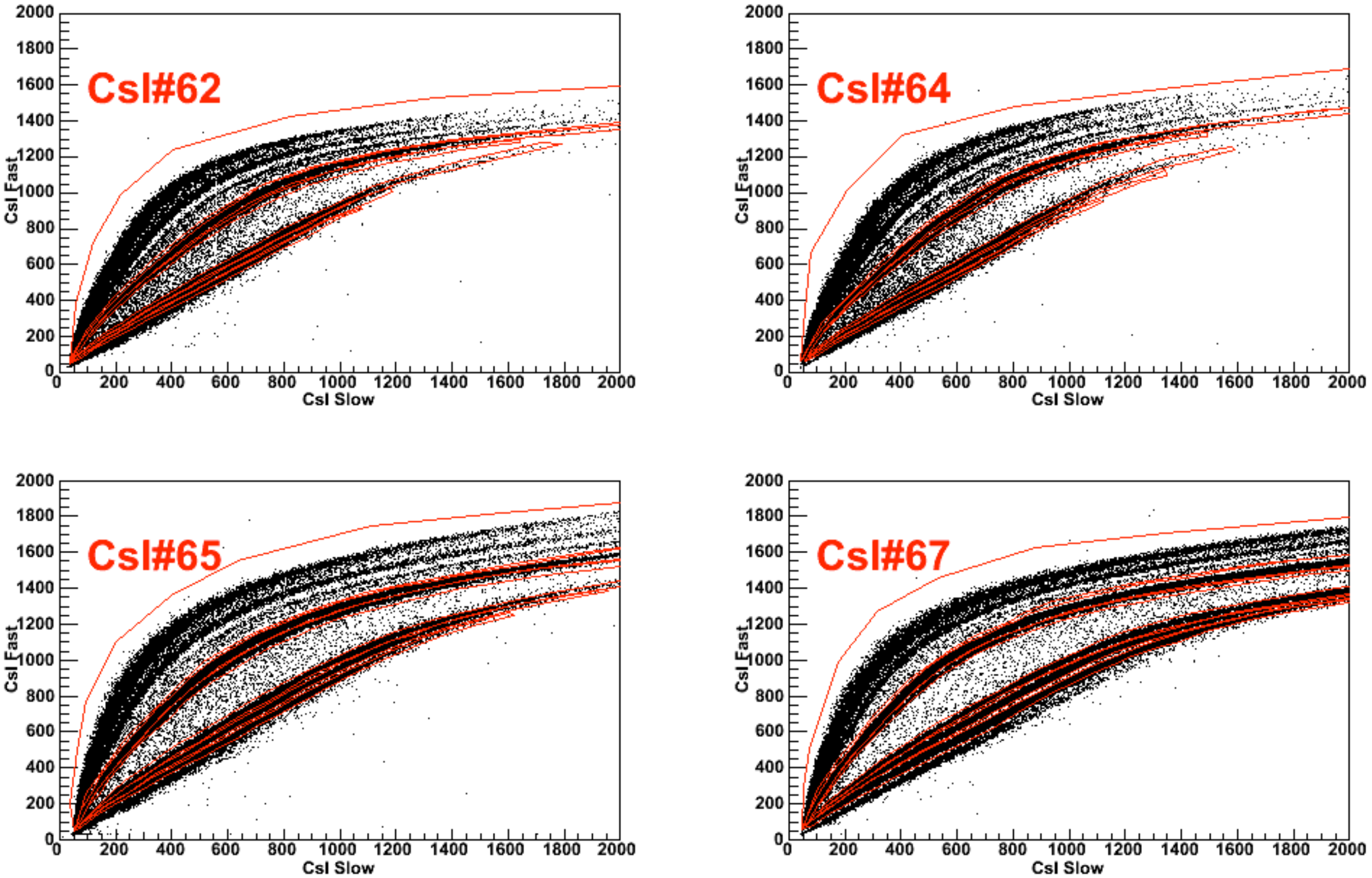

Fig. A-30. CsI slow versus fast raw spectra, ring 7, part 3.

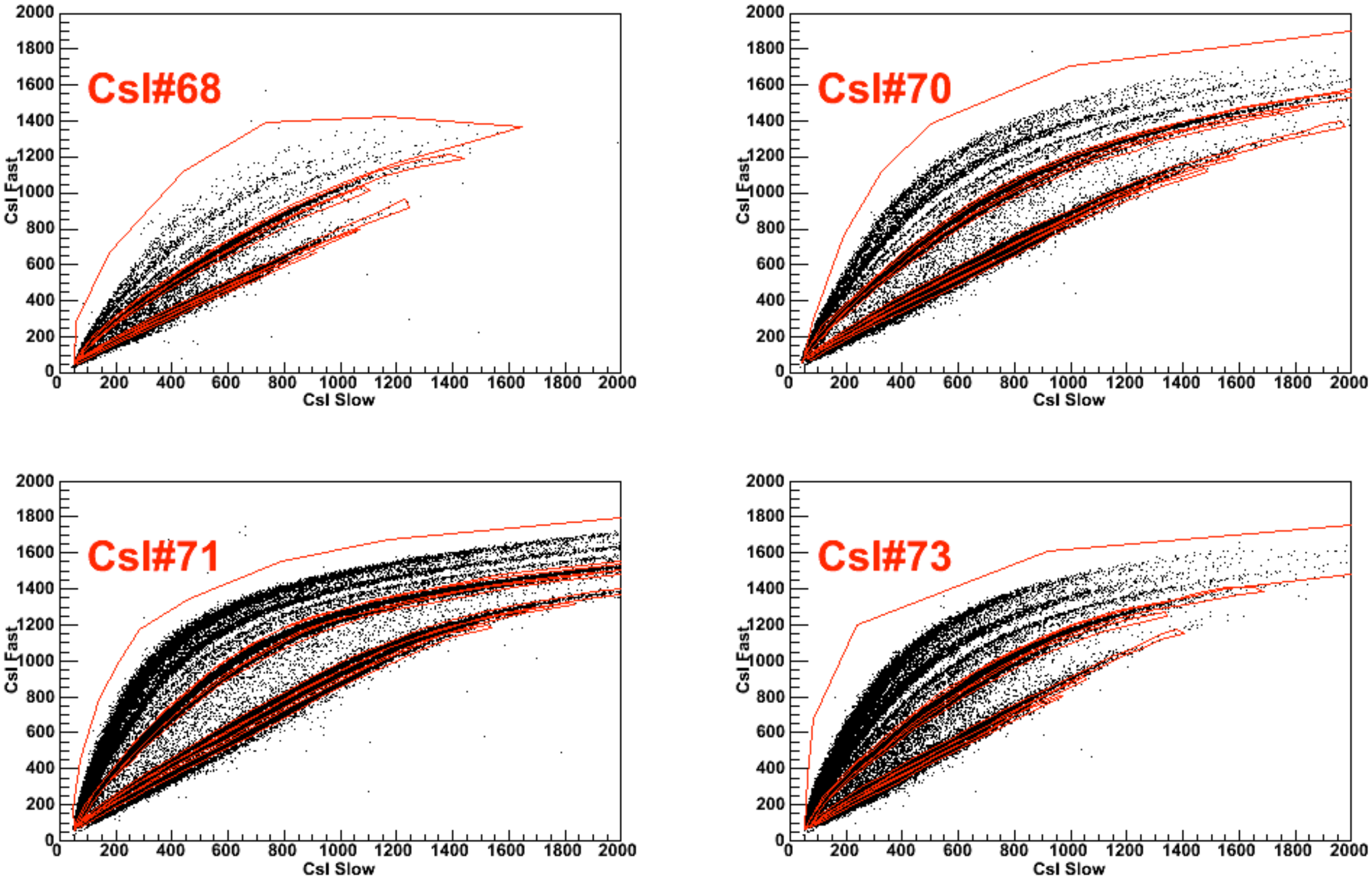

Fig. A-31. CsI slow versus fast raw spectra, ring 7, part 4.

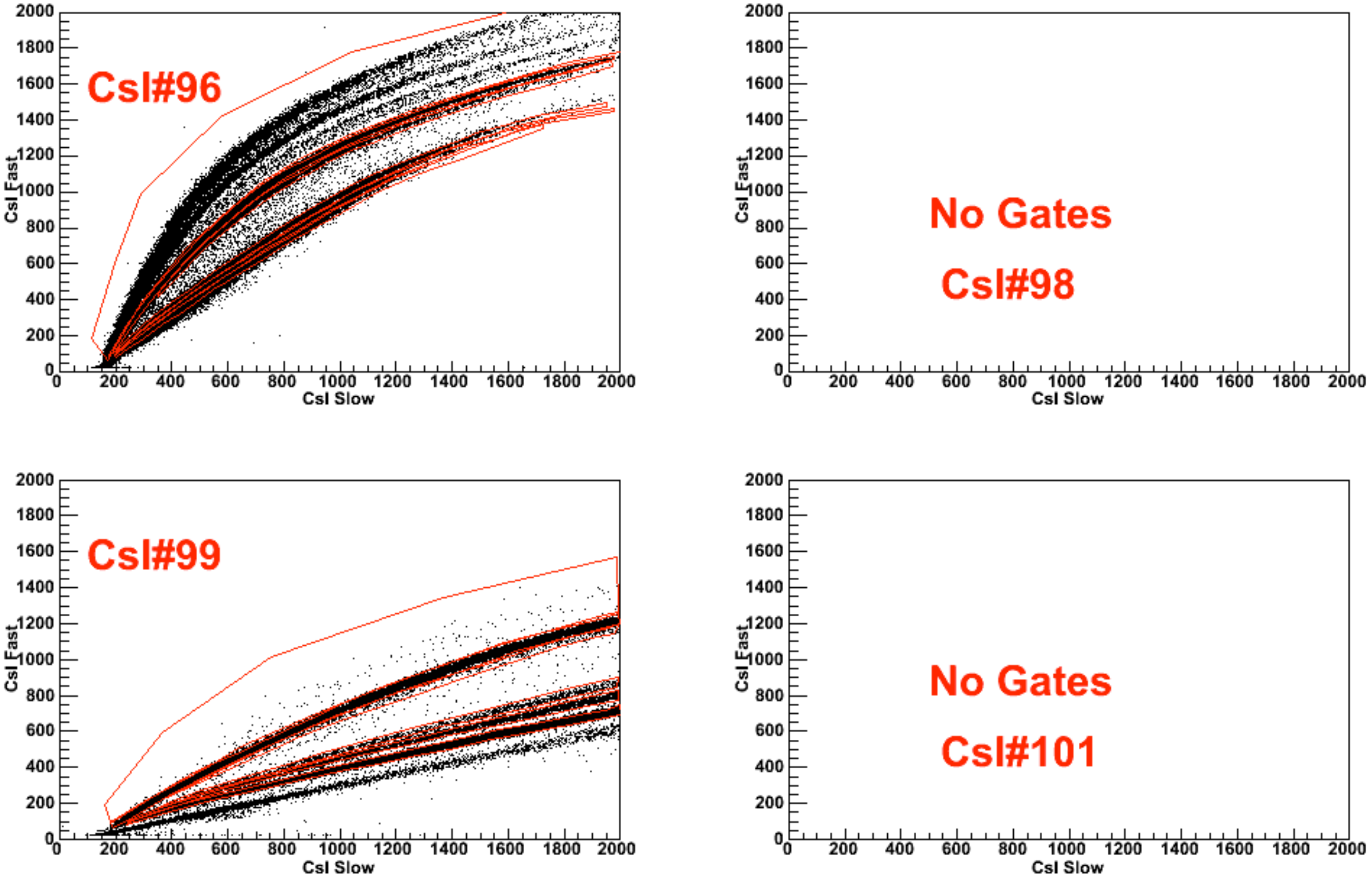

Fig. A-32. CsI slow versus fast raw spectra, ring 7, part 5.

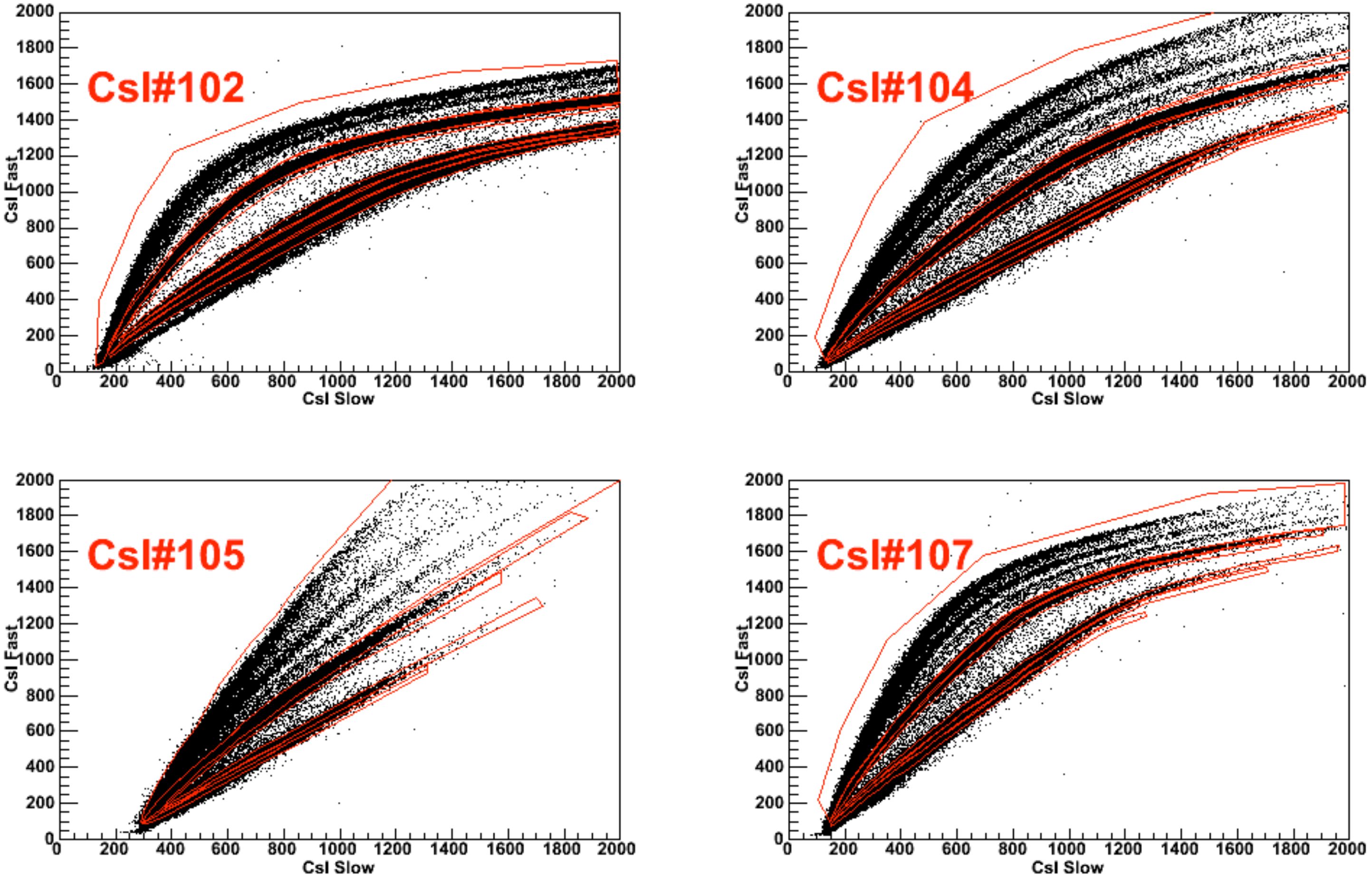

Fig. A-33. CsI slow versus fast raw spectra, ring 7, part 6.

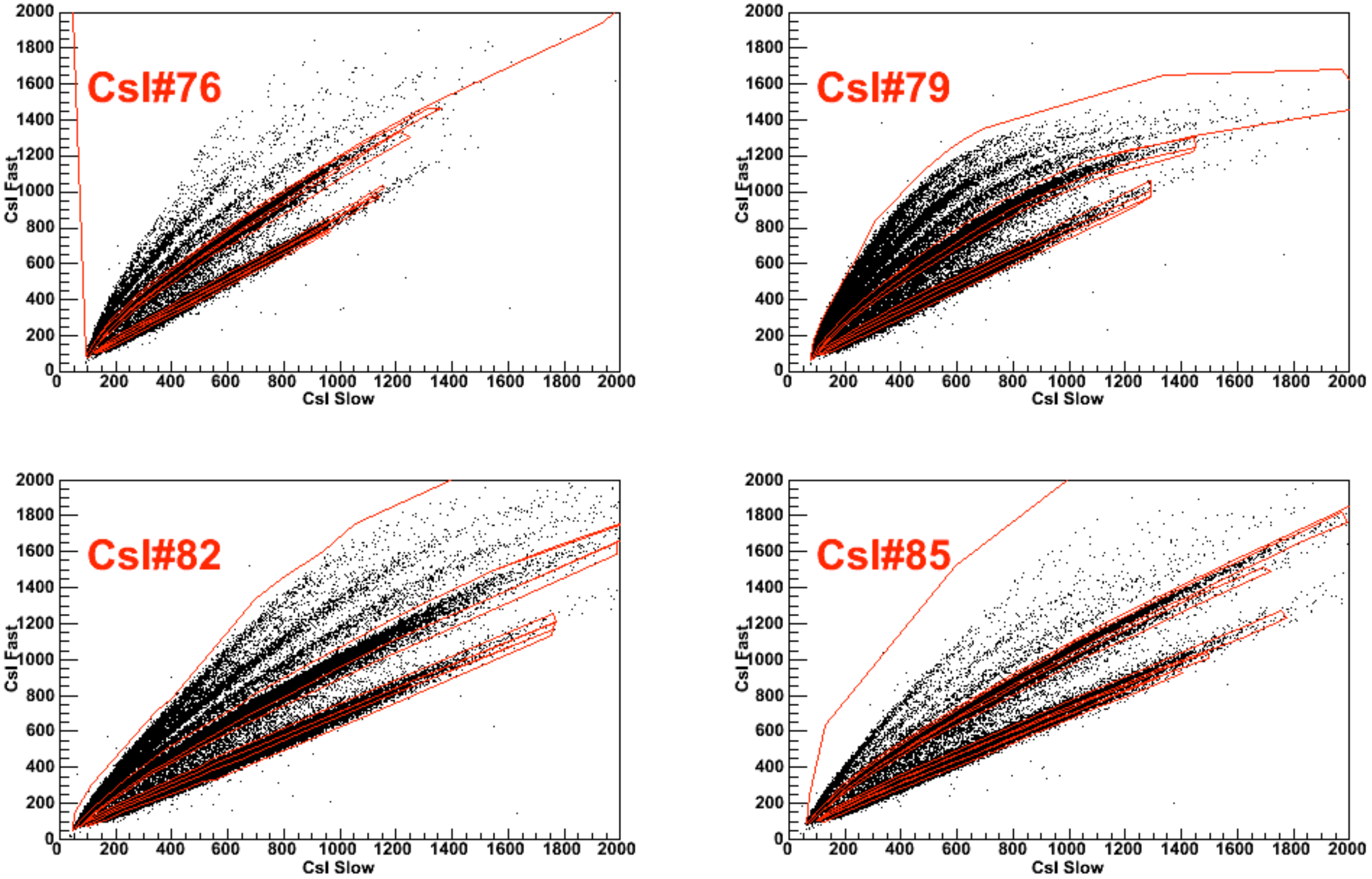

Fig. A-34. CsI slow versus fast raw spectra, ring 8, part 1.

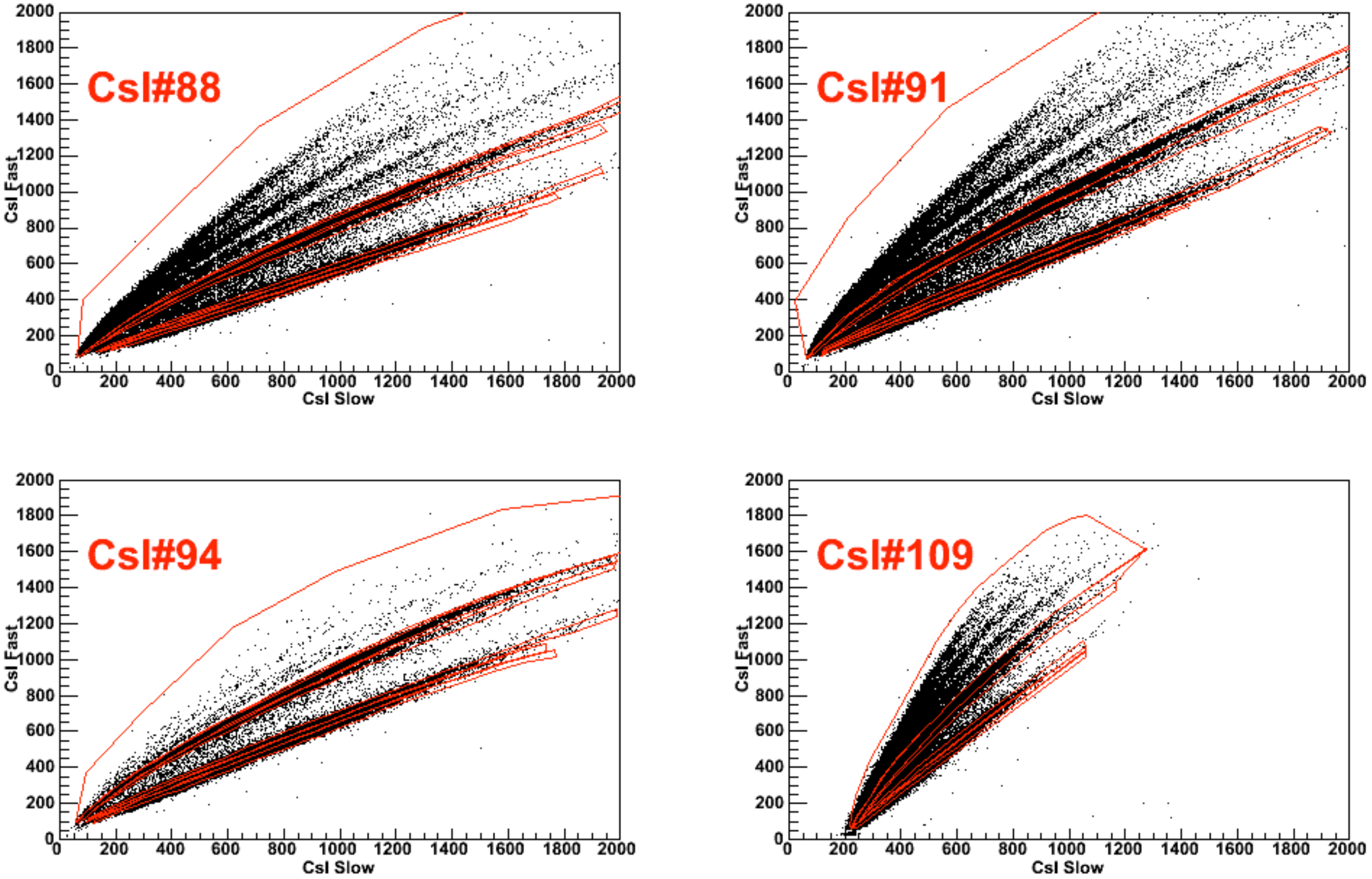

Fig. A-35. CsI slow versus fast raw spectra, ring 8, part 2.

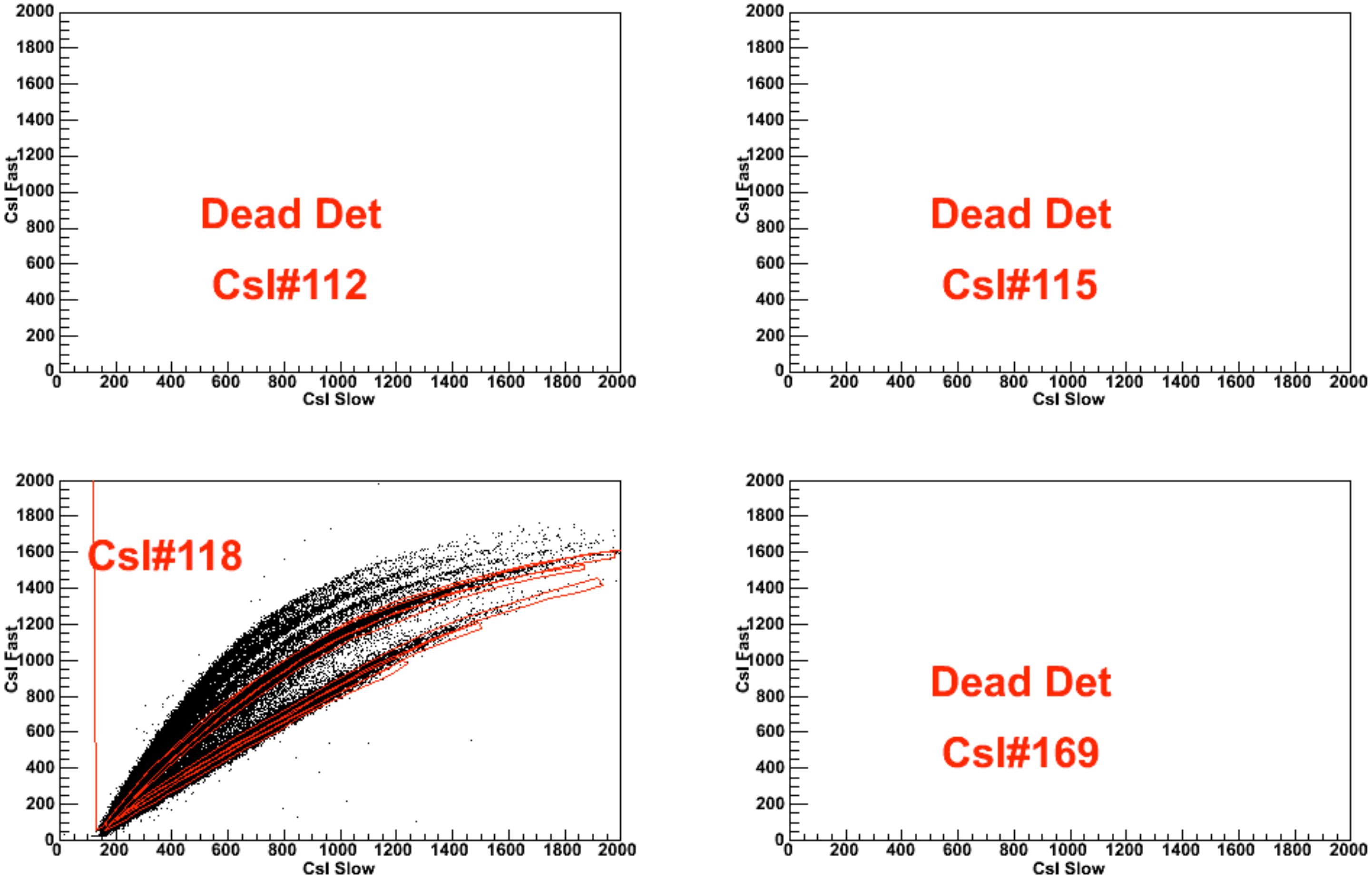

Fig. A-36. CsI slow versus fast raw spectra, ring 8, part 3.

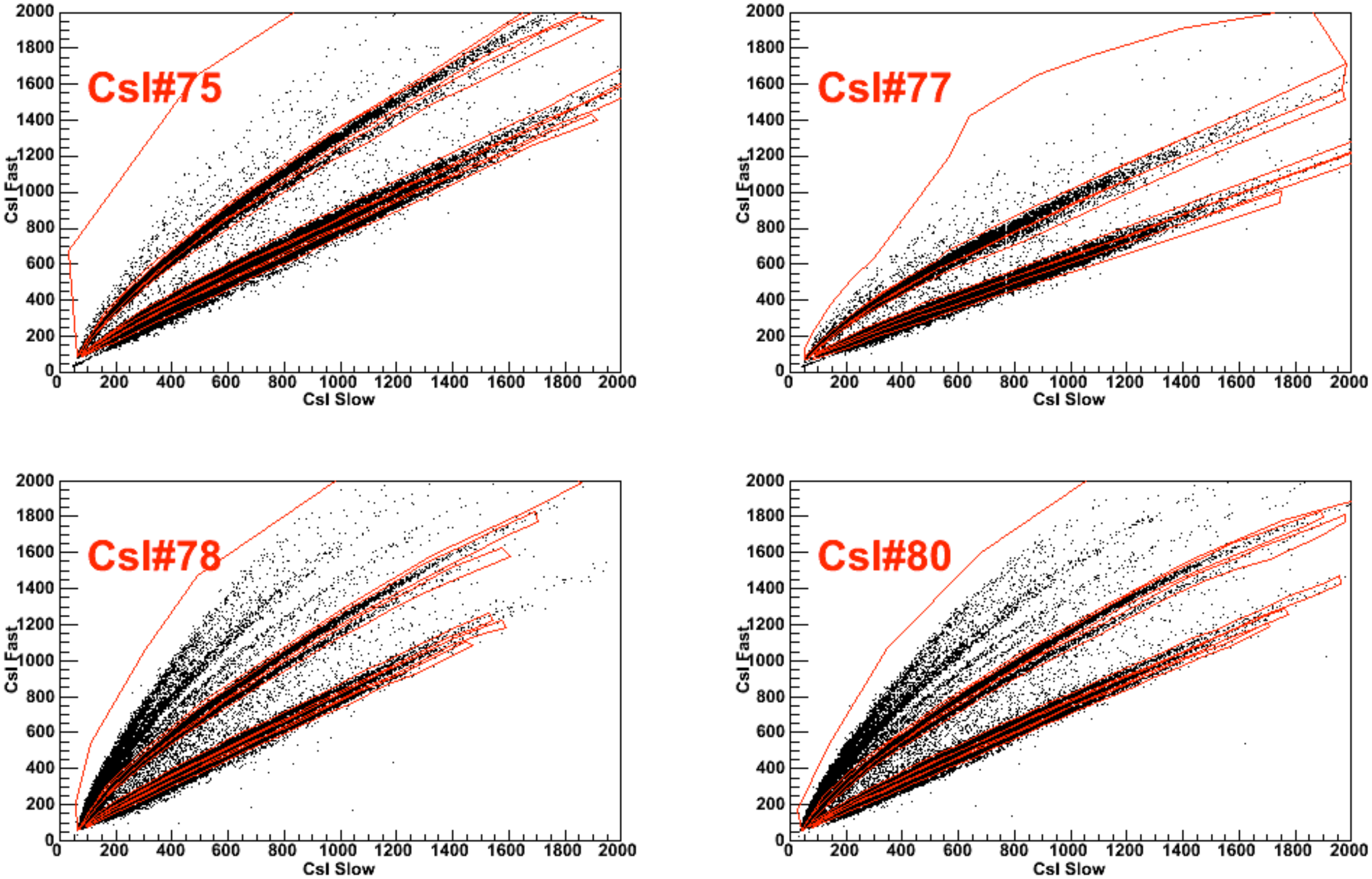

Fig. A-37. CsI slow versus fast raw spectra, ring 9, part 1.

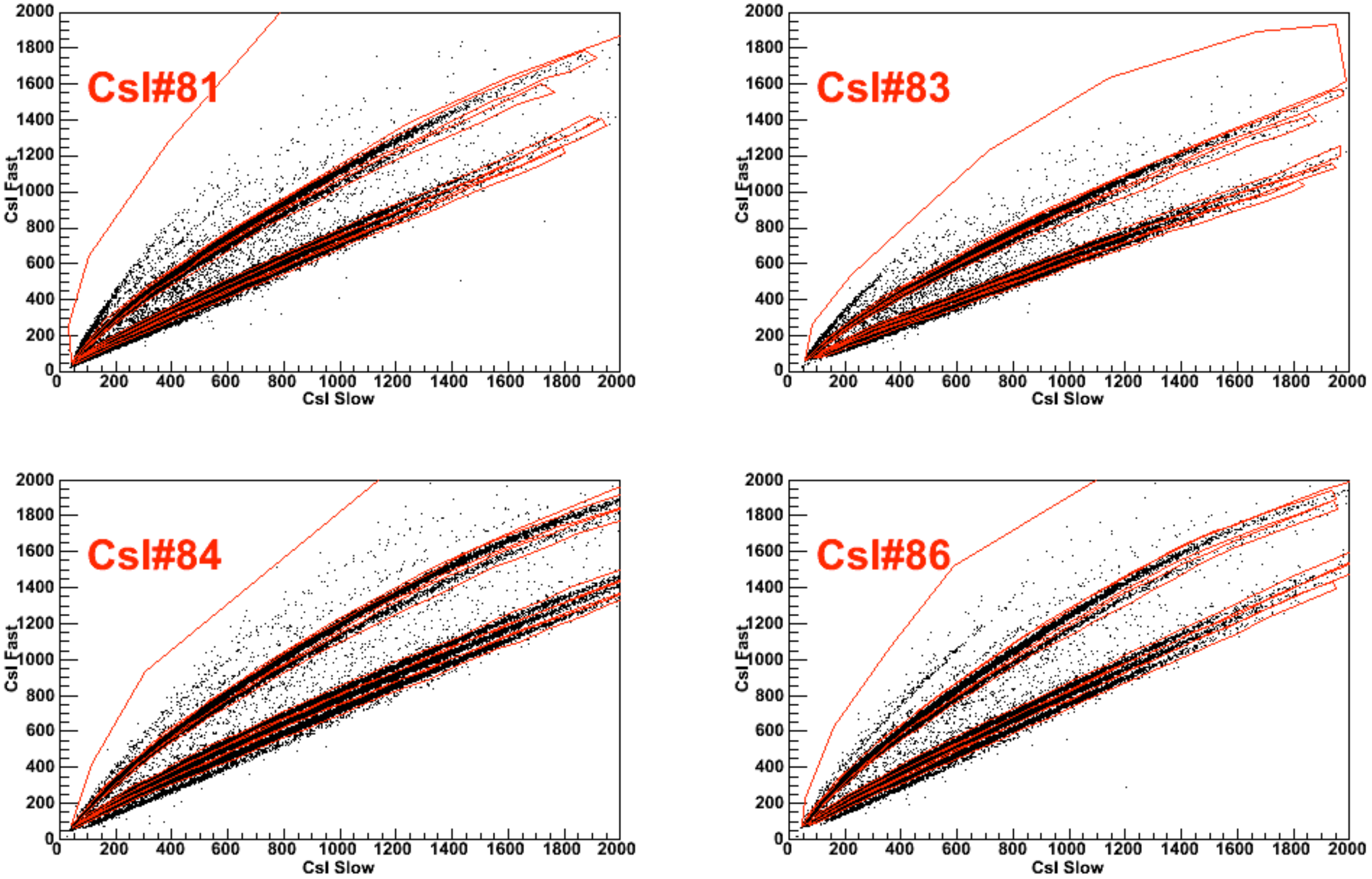

Fig. A-38. CsI slow versus fast raw spectra, ring 9, part 2.

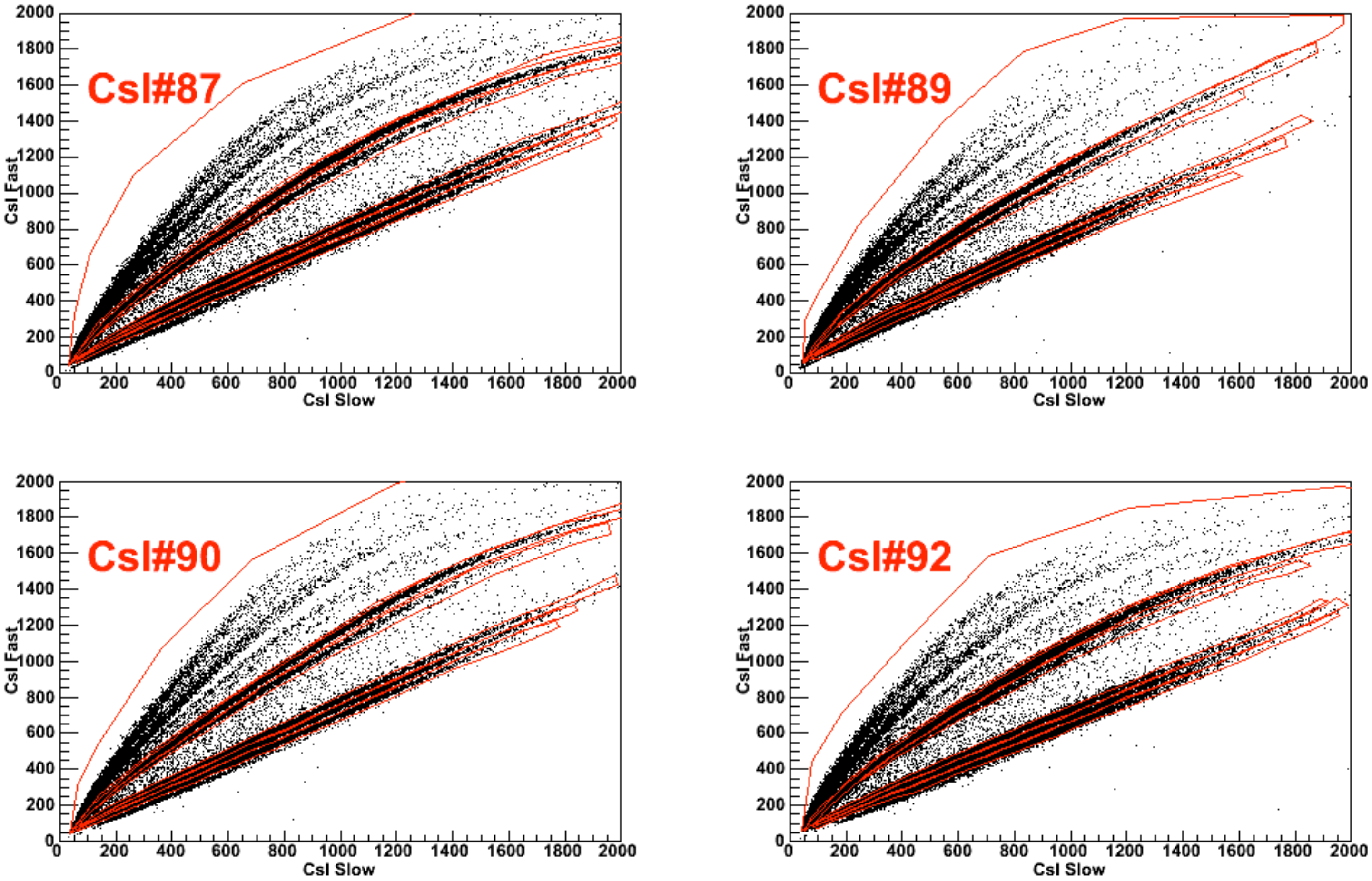

Fig. A-39. CsI slow versus fast raw spectra, ring 9, part 3.

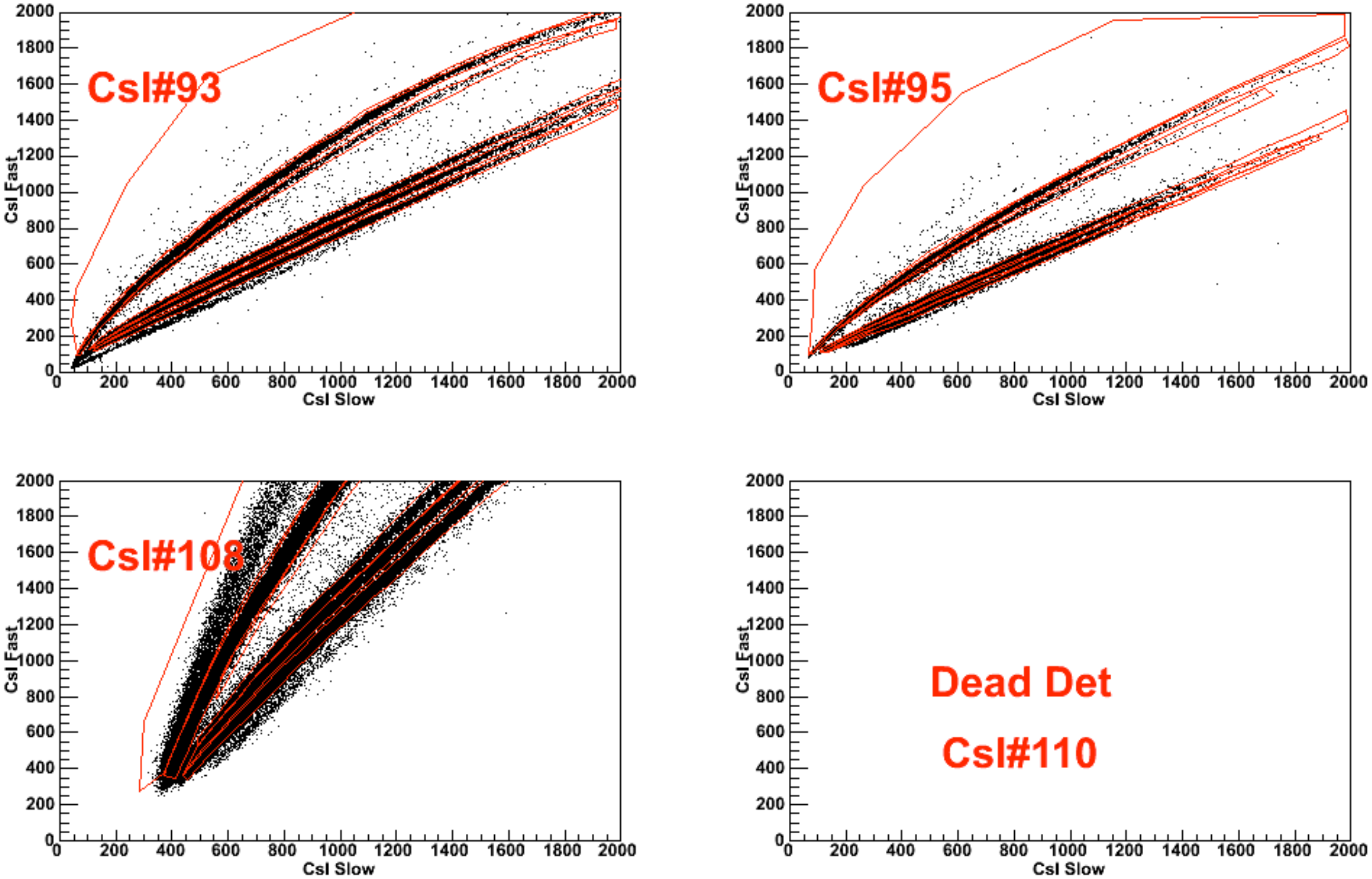

Fig. A-40. CsI slow versus fast raw spectra, ring 9, part 4.

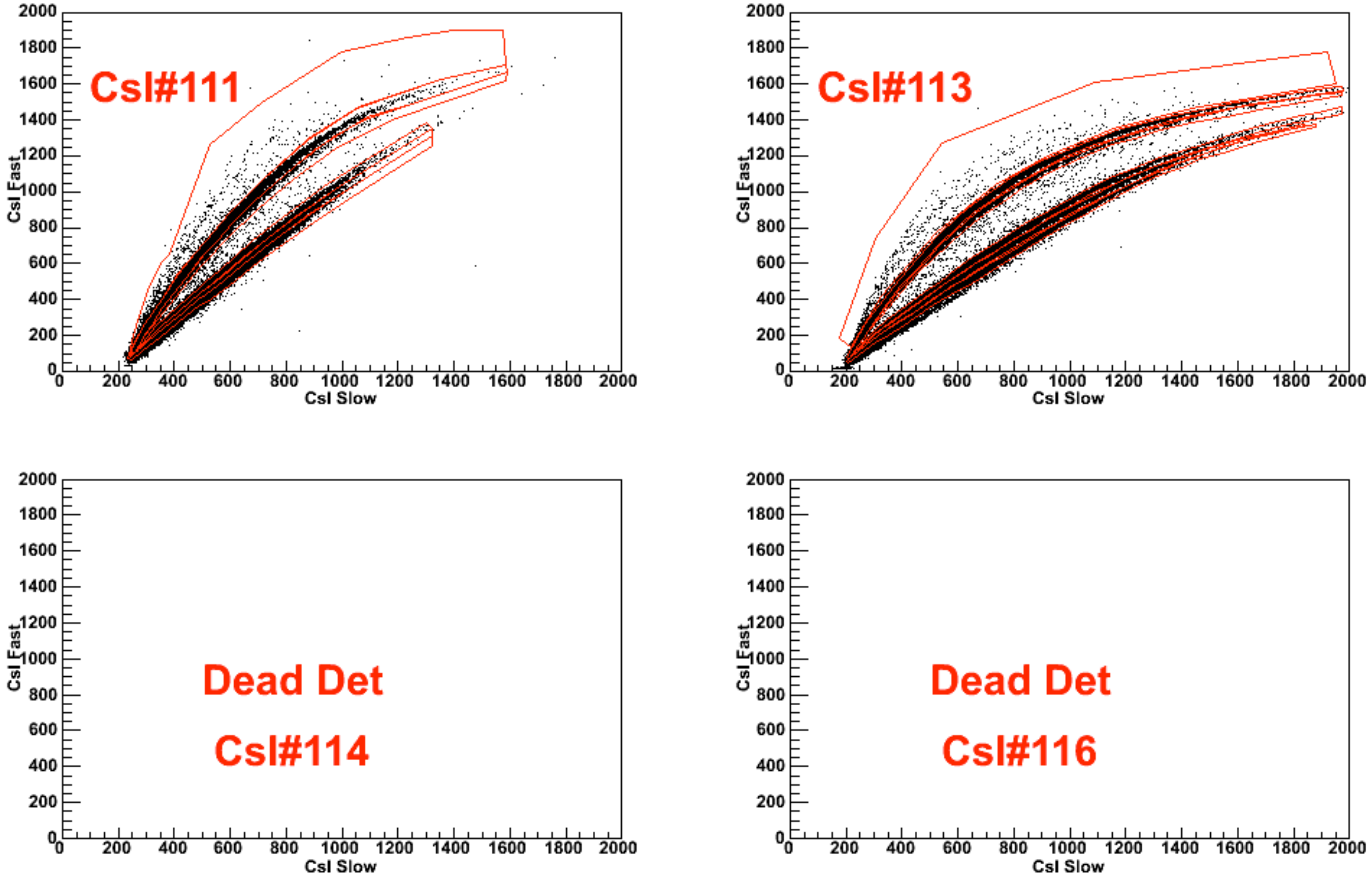

Fig. A-41. CsI slow versus fast raw spectra, ring 9, part 5.

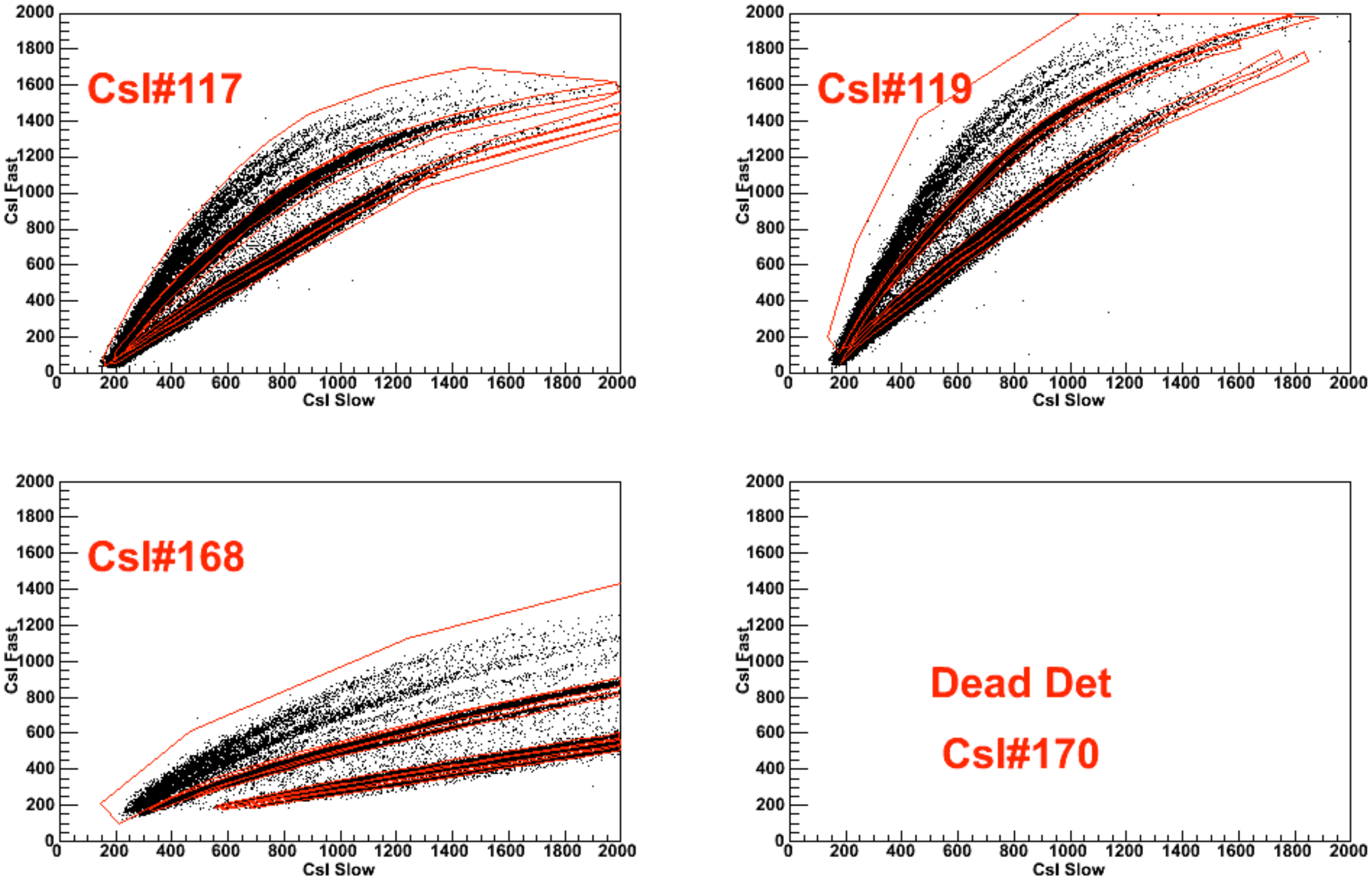

Fig. A-42. CsI slow versus fast raw spectra, ring 9, part 6.

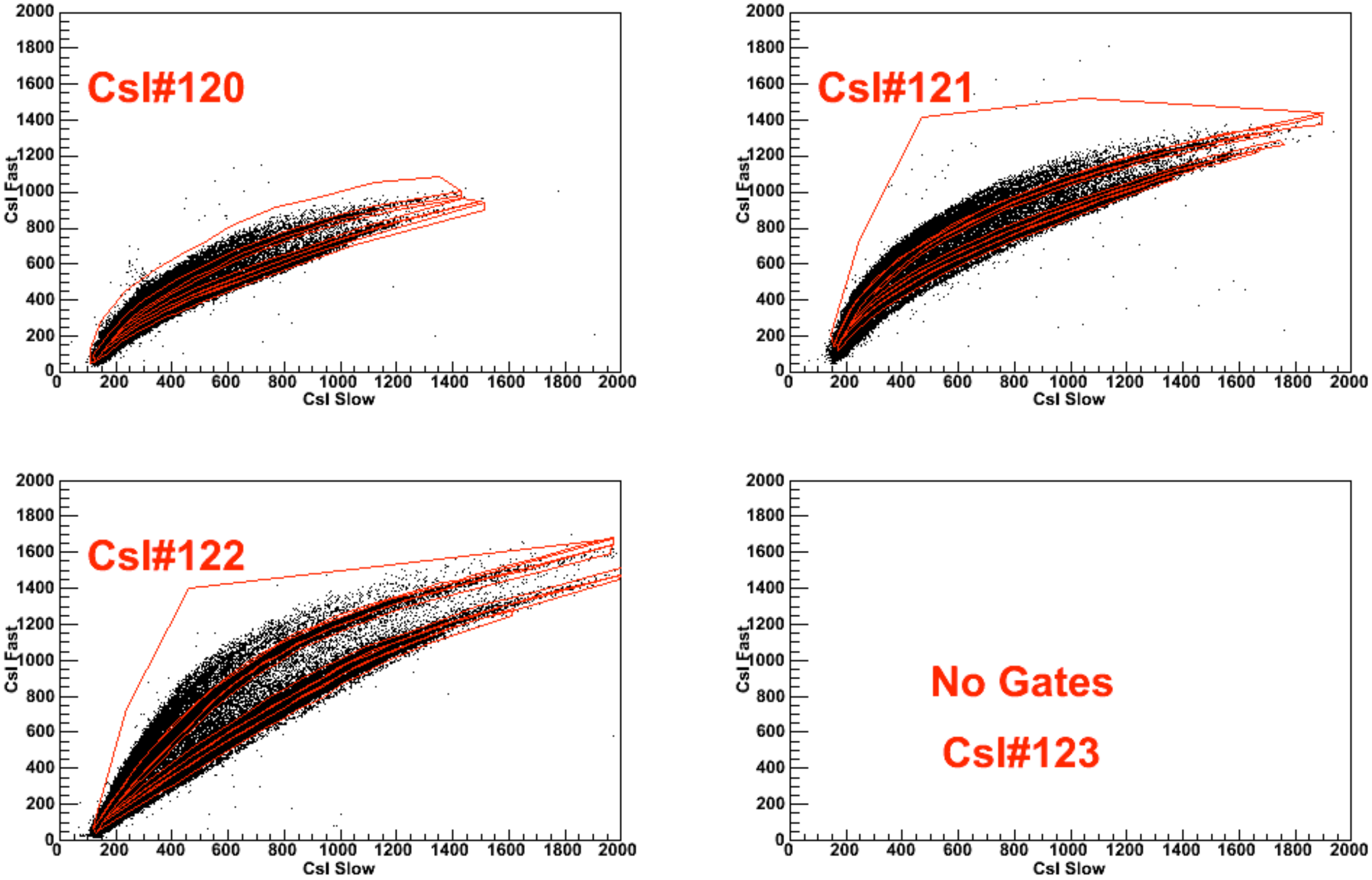

Fig. A-43. CsI slow versus fast raw spectra, ring 10, part 1.

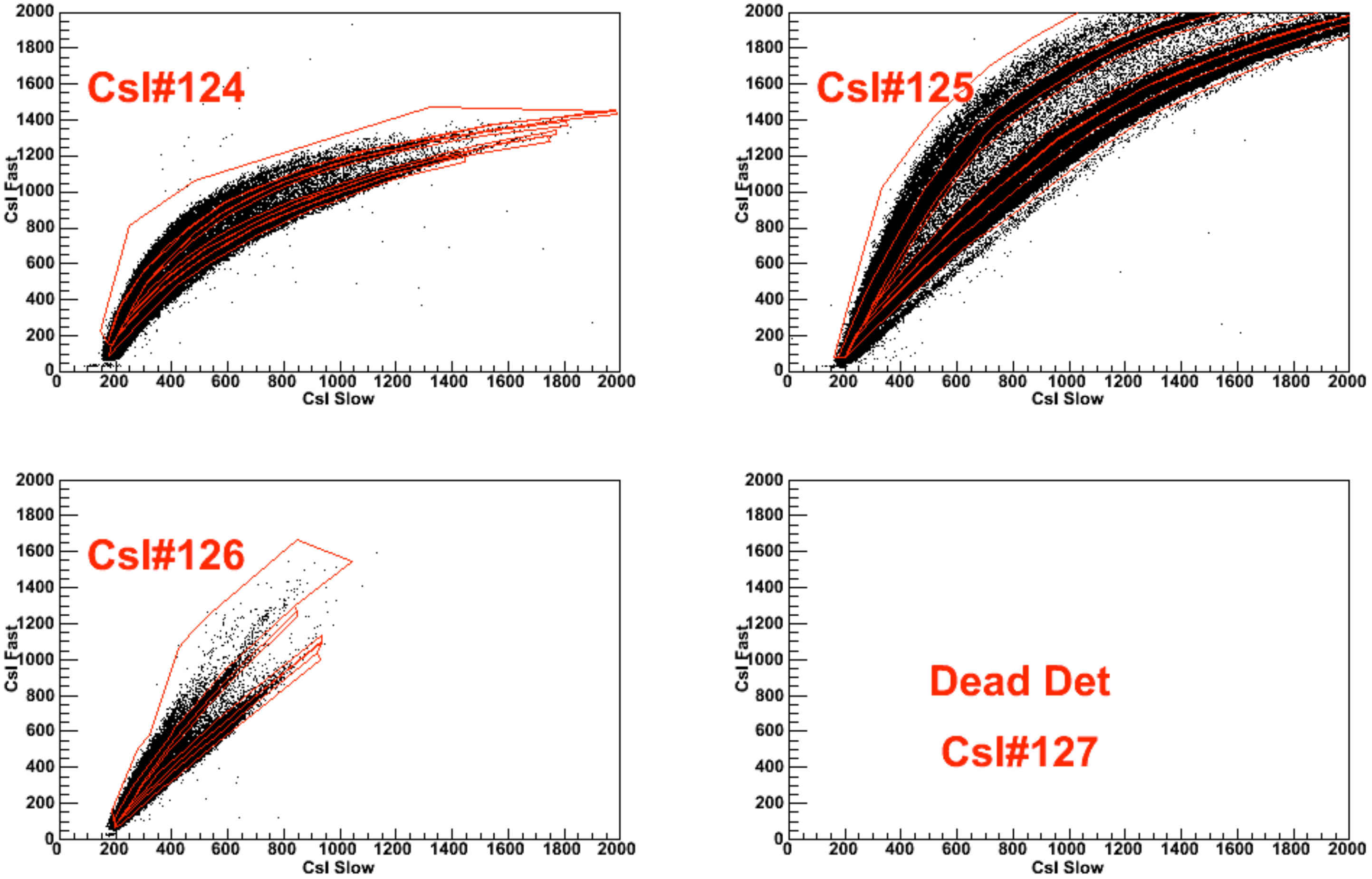

Fig. A-44. CsI slow versus fast raw spectra, ring 10, part 2.

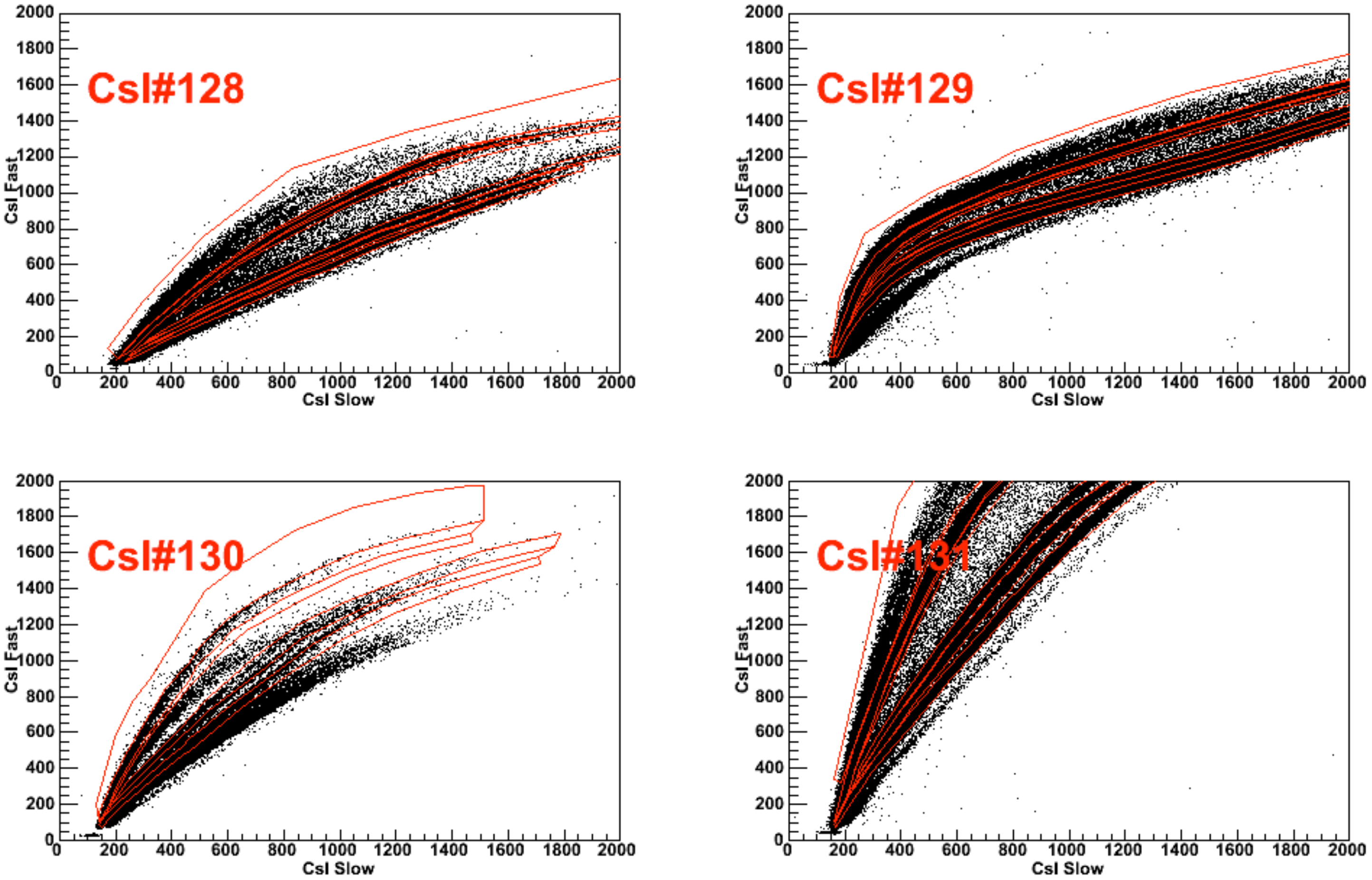

Fig. A-45. CsI slow versus fast raw spectra, ring 10, part 3.

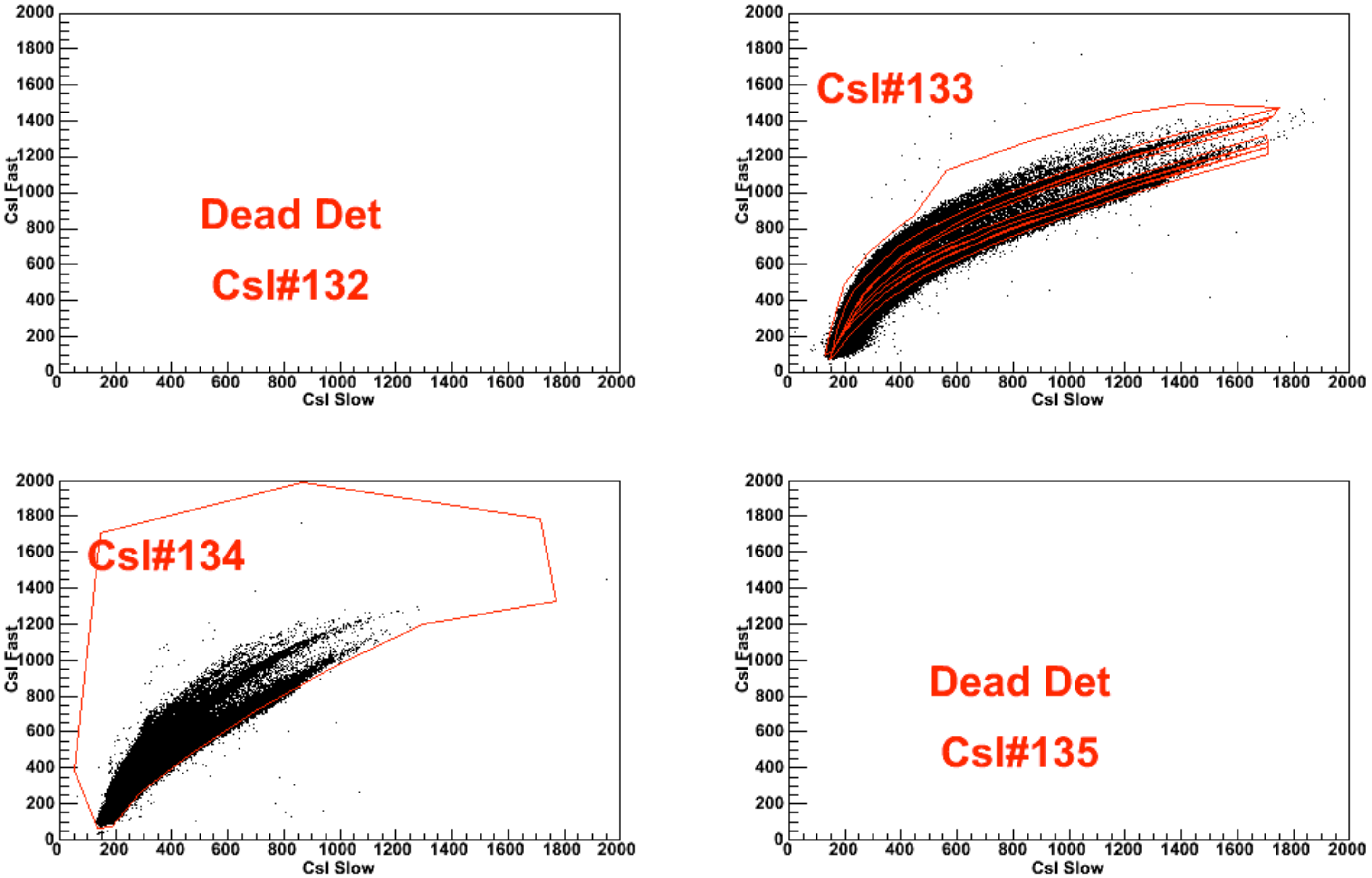

Fig. A-46. CsI slow versus fast raw spectra, ring 10, part 4.

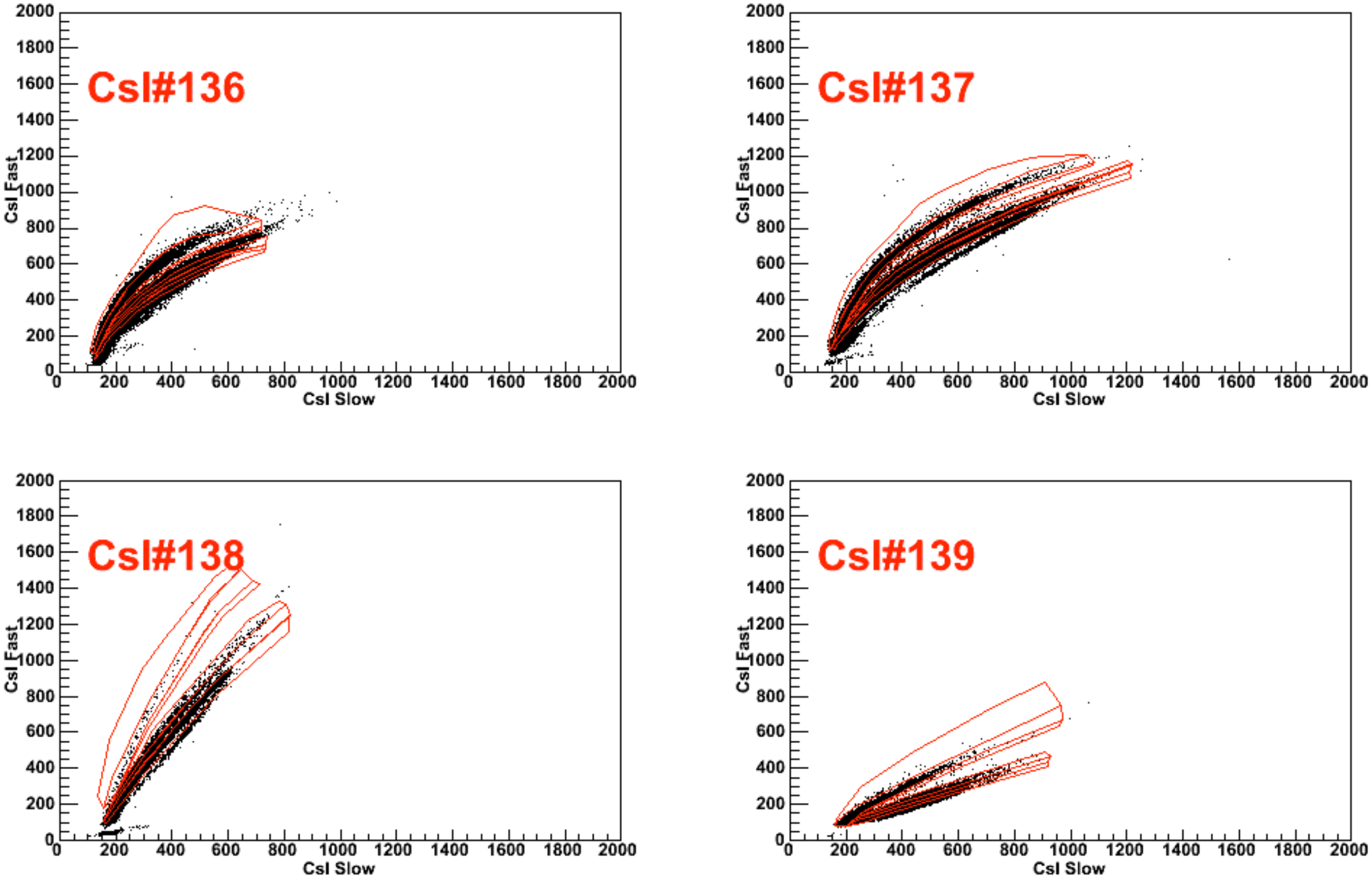

Fig. A-47. CsI slow versus fast raw spectra, ring 11, part 1.

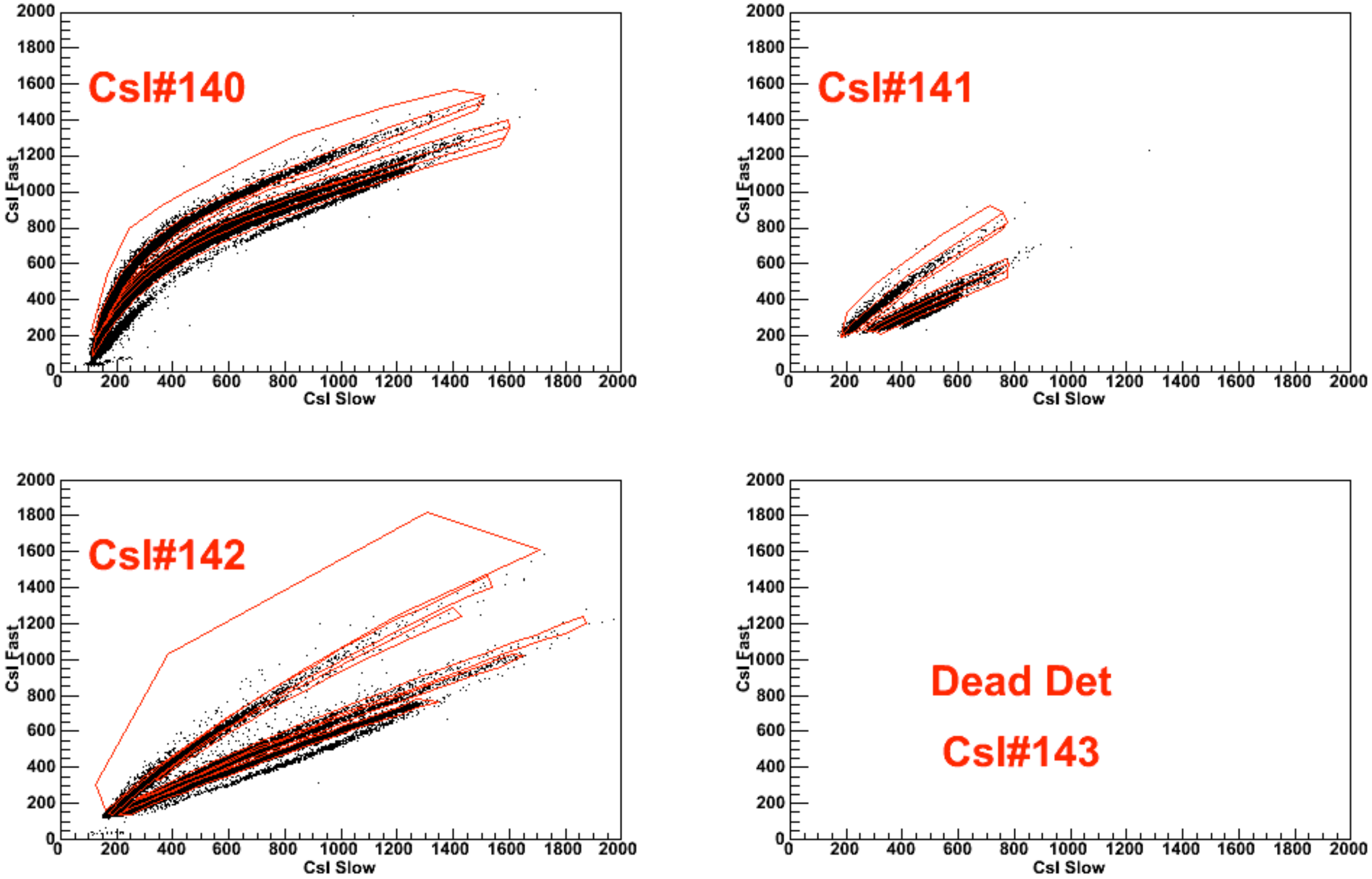

Fig. A-48. CsI slow versus fast raw spectra, ring 11, part 2.

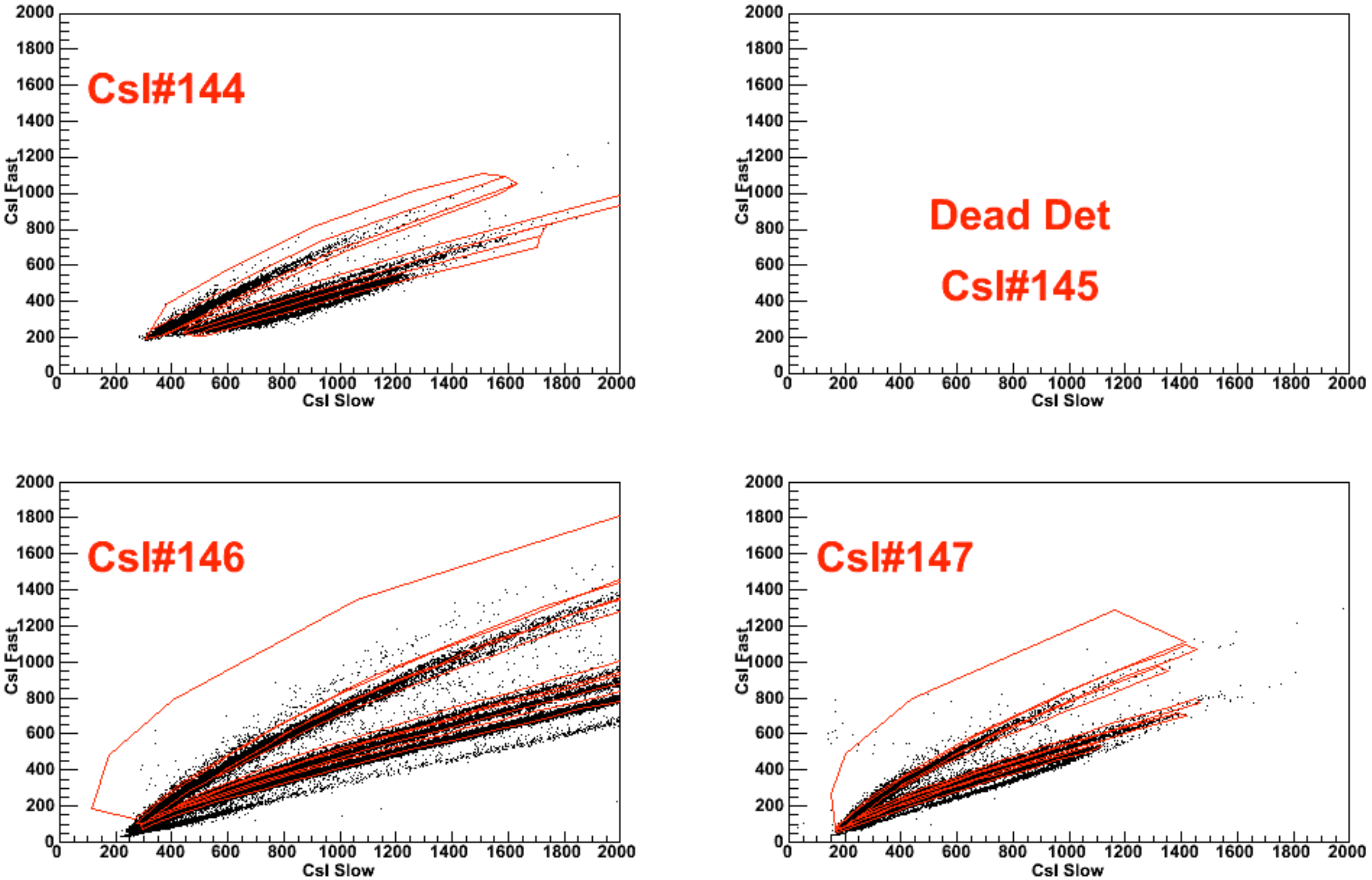

Fig. A-49. CsI slow versus fast raw spectra, ring 11, part 3.

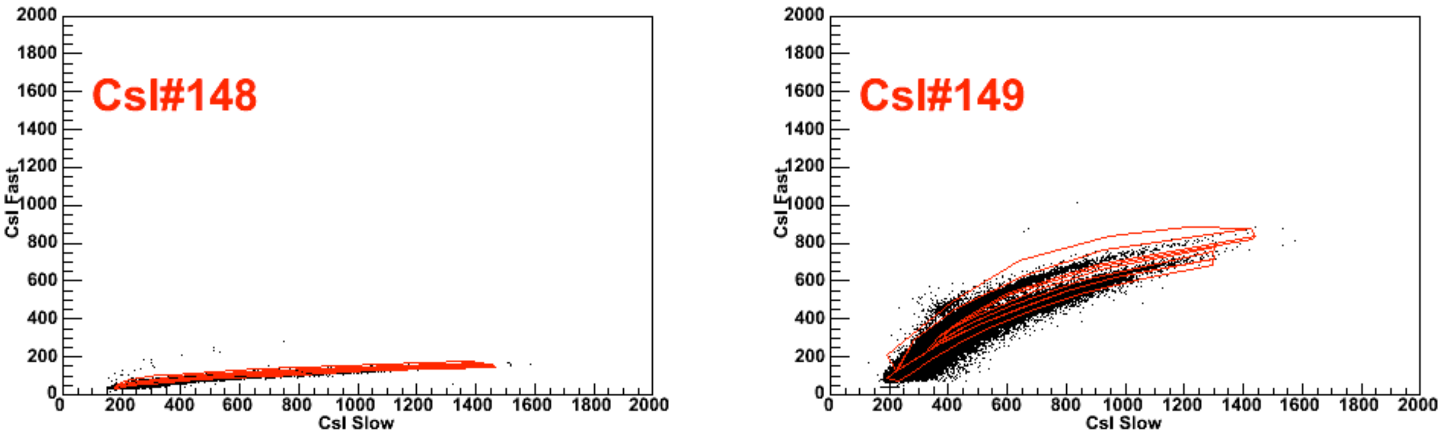

Fig. A-50. CsI slow versus fast raw spectra, ring 11, part 4.

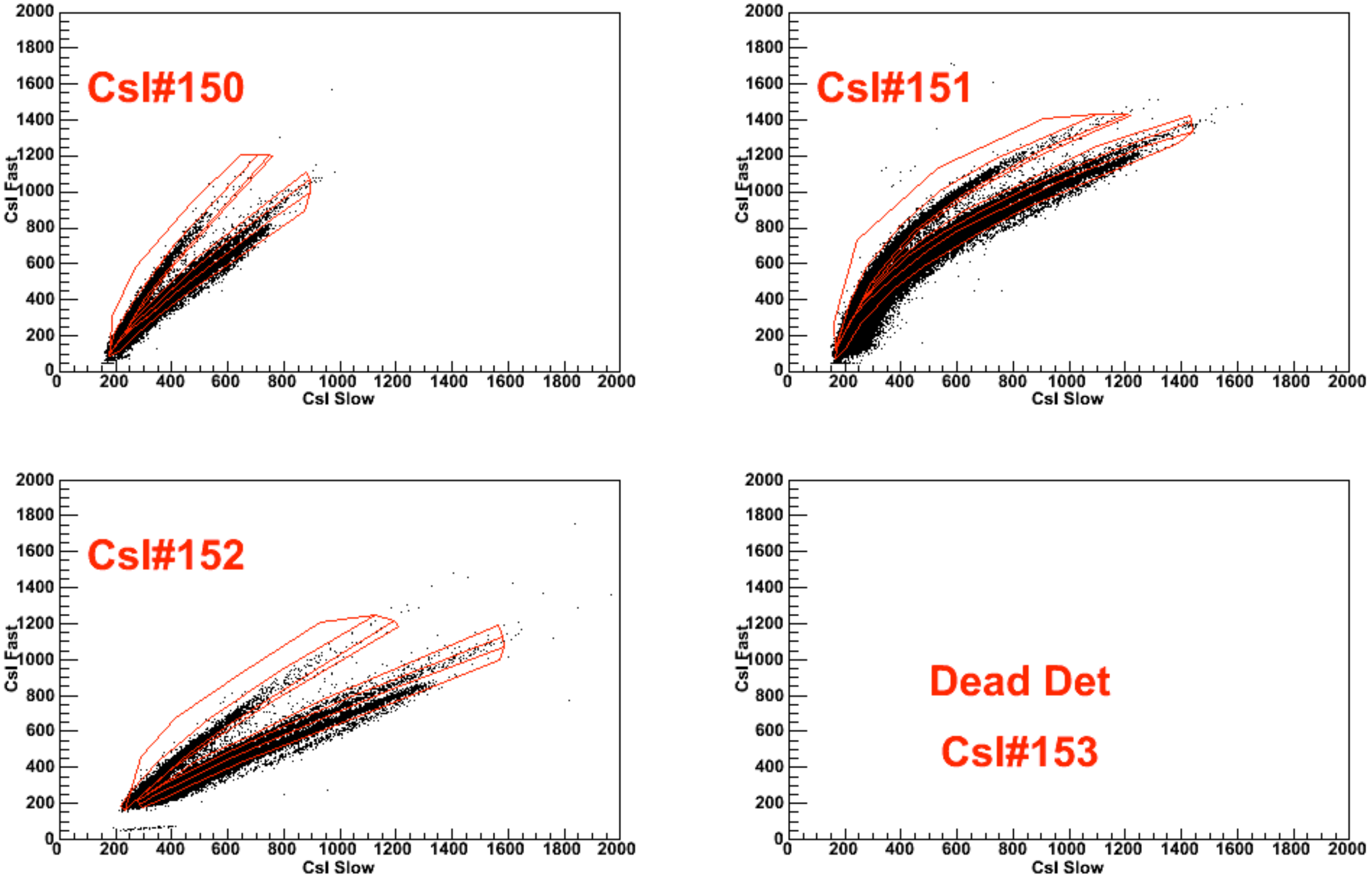

Fig. A-51. CsI slow versus fast raw spectra, ring 12, part 1.

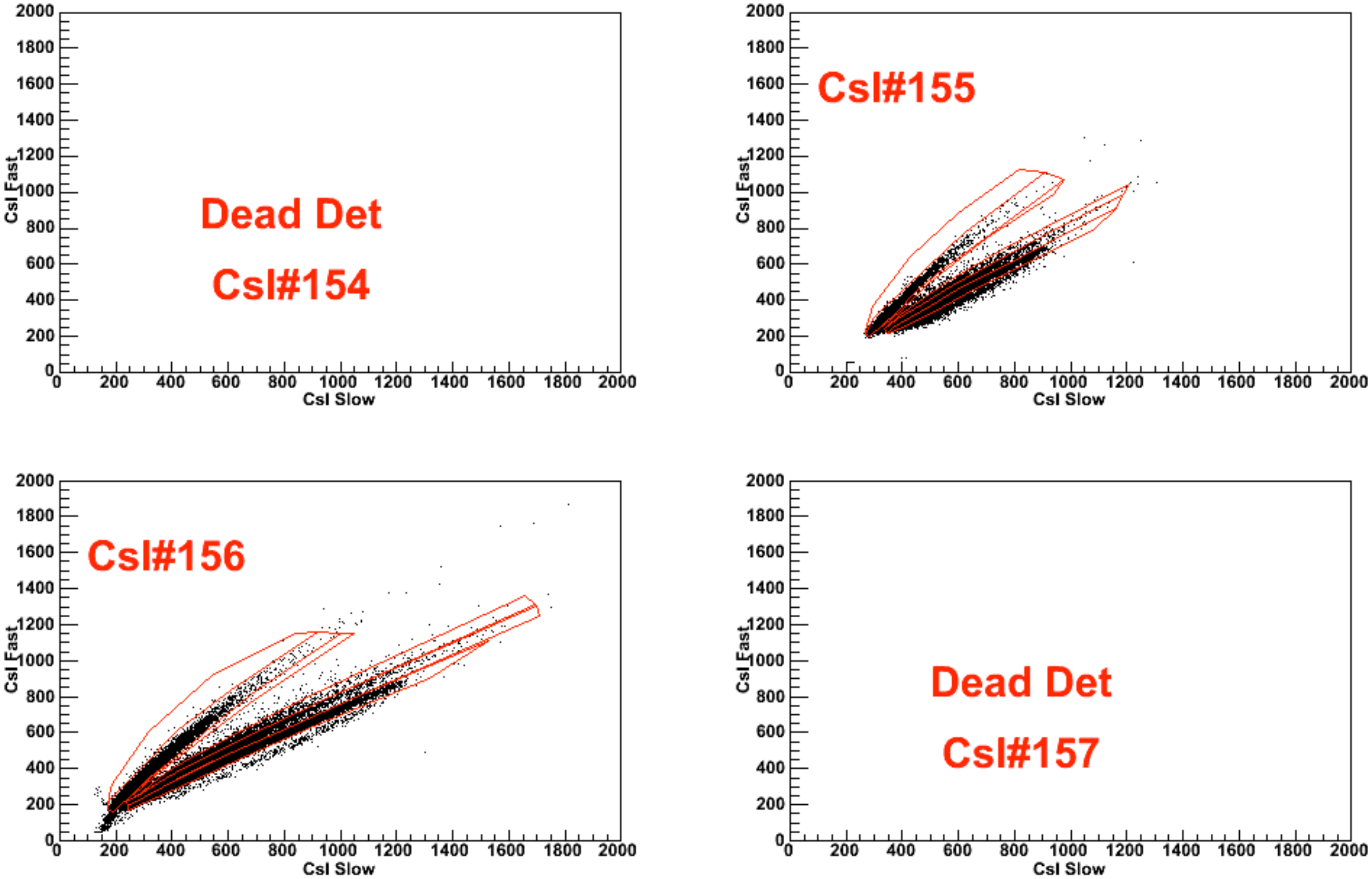

Fig. A-52. CsI slow versus fast raw spectra, ring 12, part 2.

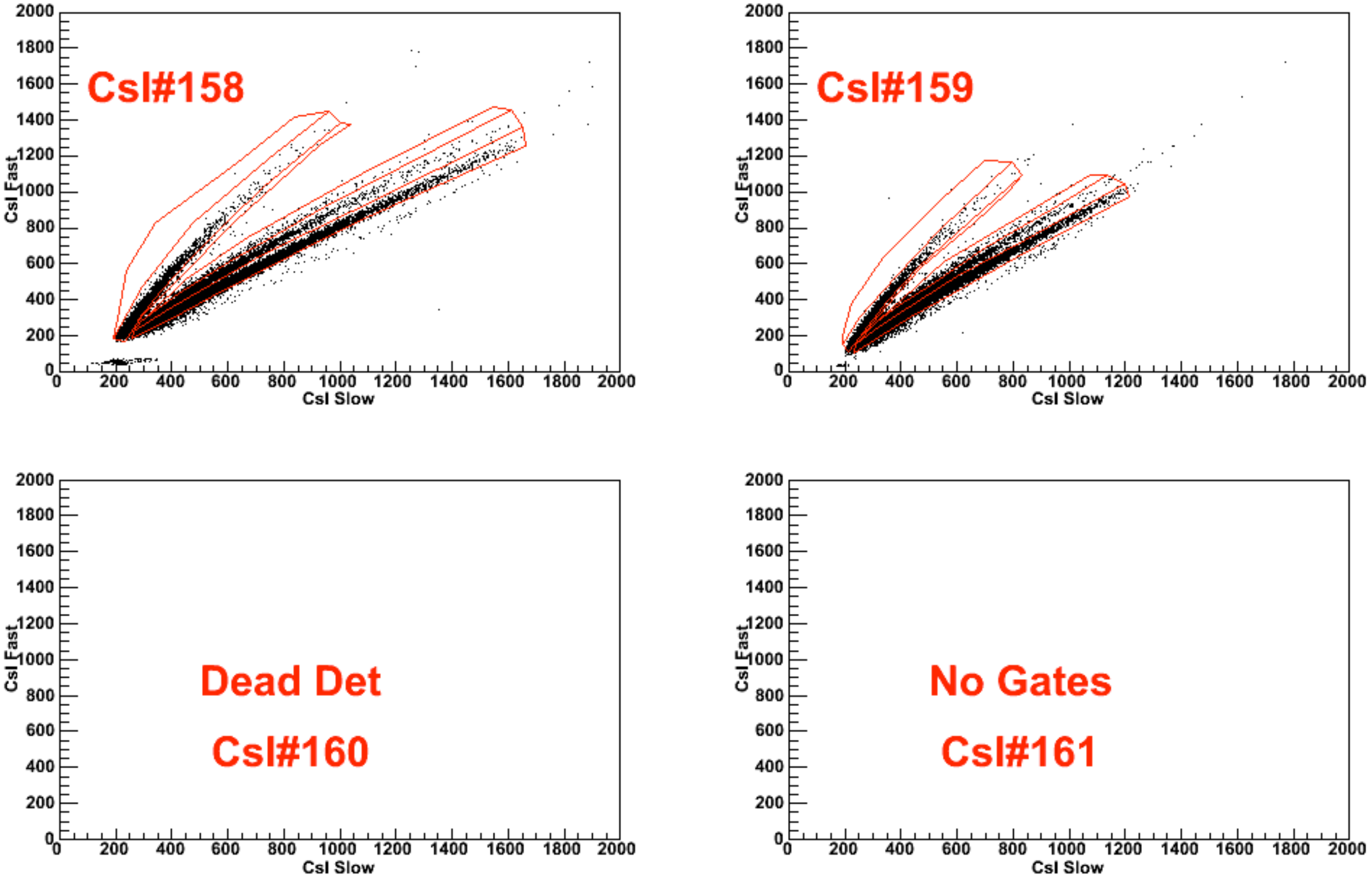

Fig. A-53. CsI slow versus fast raw spectra, ring 13.

VITA

Elizabeth Bell was born and raised in San Antonio, TX. She earned a B.S. in Chemistry from The University of Texas at San Antonio in 1996. She joined the research group of Dr. Sherry J. Yennello in the fall of 1997 and earned a Ph.D. in Nuclear Chemistry from Texas A&M University in May 2005. Work prior to April 2004 is published under the maiden name of Elizabeth Martin. Elizabeth Bell may be reached at elizabethbell@mac.com or through Sherry J. Yennello at the Cyclotron Institute, Texas A&M University, College Station, TX, 77843-3366.